Methods for Designing the Next Generation of Aircraft Architectures using Topology Optimisation

James Eves

Submitted in accordance with the requirements for the degree of
Doctor of Philosophy

The University of Leeds
School of Mechanical Engineering

September 2010

The candidate confirms that the work submitted is his own, except where work which has formed part of jointly-authored publications has been included. The contribution of the candidate and the other authors to this work has been explicitly indicated below. The candidate confirms that appropriate credit has been given within the thesis where reference has been made to the work of others.

Sections 4.3.4 and 5.3 contain work published in:

J. Eves, V.V. Toropov, H.M. Thompson, P.H. Gaskell, J.J. Doherty, J.C. Harris. "Topology Optimization of Aircraft with Non-Conventional Configurations." 8th World Congress on Structural and Multidisciplinary Optimization. Lisbon, Portugal. June 2009.

A CAD model of a conceptual aircraft design was supplied by Prof. John Doherty and Dr. John Harris. All other work in this paper is a contribution of the candidate, under the supervision of the co-authors.

Acknowledgements

The guidance and input of PhD supervisors Harvey Thompson, Vassili Toropov and Phil Gaskell are gratefully acknowledged. Their academic contributions and general supervision throughout the last four years, along with their help in preparing this manuscript, have been invaluable.

A number of people from within industry gave up their time for meetings and phone calls to exchange ideas on the direction of this research. Special thanks must go to project collaborators John Doherty and John Harris from QinetiQ. Their expertise and insight made this work possible. Thanks also go to Malcolm Nash and Bill Austin from QinetiQ, as well as Royston Jones, Martin Kemp and Sam Patten from Altair Engineering.

Countless discussions on computational analysis and optimisation with Carl Gilkeson and Rob Hewson have aided the development of many of the approaches presented in this thesis. For this the author is particularly grateful.

The author also wishes to thank Nik Kapur, Diego Angarita, Dave and Cathy Towers, and "Carl" Jian Fan, who have been colleagues in a postdoctoral project at The University of Leeds during the final year of this research. Their understanding and support have allowed the time needed for the preparation of this manuscript.

Finally, the author would like to thank the School of Mechanical Engineering for providing the PhD studentship that facilitated this research, and his family for their financial support.

Abstract

The need from energy efficient transportation has resulted in a growing interest in new aircraft configurations such as the Blended Wing Body. There is very little collective knowledge on the optimal structural layouts of these aircraft, and the paradigms applied to conventional aircraft may not be applicable. Topology optimisation is the logical tool to employ in this type of situation, as its generality removes the need for any assumption of what the structure should be. Several barriers exist that stand in the way of topology optimisation's use in designing aircraft structural architectures. Firstly, the displacements caused by spanwise bending of the wing are large compared to those caused by twisting and localised deformation of the wing. Therefore, the typical minimum compliance formulation of the topology optimisation problem favours structures that improve bending stiffness. There are also considerable difficulties associated with the implementation of buckling constraints in topology optimisation.

This thesis explores these issues, and methods are proposed for circumventing them. The effect of problem formulation on optimal topologies is demonstrated through the use of various design and manufacturing constraints, SIMP penalisation factors, and load cases. Approaches for reducing the significance of spanwise bending in the topology optimisation problem are evaluated and shown to be capable of generating designs that resist bending, torsion and localised deformation of the wing.

Methods are then proposed for including topology optimisation in a framework for designing aircraft structural architectures, along with shape and sizing optimisation. Shape optimisation is used to find optimal rib locations and orientations for structural stability. The inclusion of these ribs as non-designable structures in the topology optimisation problem is shown to have a substantial effect on the optimal material distributions, due to the load carrying capacity of the ribs. The developed methods are applied to designing the structural architecture of a Blended Wing Body UAV, and are shown to offer potential reductions in structural mass.

Contents

Figures

Tables

Abbreviations

ACARE	Advisory Council for Aeronautics Research in Europe
AoA	Angle of Attack
BWB	Blended Wing Body
CFD	Computational Fluid Dynamics
COC	Continuum-based Optimality Criteria
DCOC	Discretised Continuum-based Optimality Criteria
DoF	Degrees of Freedom
FE	Finite Element
GA	Genetic Algorithm
LP	Linear Programming
MP	Mathematical Programming
NASA	National Aeronautics and Space Administration
OC	Optimality Criteria
PLATO-N	Platform for Topology Optimisation Project
QP	Quadratic Programming
QUICK	Quadratic Upwind Interpolation for Convective Kinematics
SIMP	Solid Isotropic Material with Penalisation
SIMPLE	Semi-Implicit Method for Pressure Linked Equation
SLP	Sequential Linear Programming
SQP	Sequential Quadratic Programming
UAV	Unmanned Aerial Vehicle

Nomenclature

A	area
$\mathbf{a}$	adjoint variable vector
$\mathbf{B}$	derivative of interpolation matrix
$\mathbf{b}$	body force vector
C	compliance
C_W	weighted compliance
c	limiting values in design constraints
$\mathbf{d}$	search direction
$\mathbf{d}^0$	previous search direction
$dist$	distance
E	Young's modulus
E^0	Young's modulus of a material
E_K	modified Young's modulus used in linear stiffness matrix
E_G	modified Young's modulus used in geometric stiffness matrix
$\mathbf{E}$	elasticity matrix
$\mathbf{F}_b$	body-force load vector
$\mathbf{F}_s$	surface load vector
f	objective function
$\tilde{f}$	approximation of objective function
$\mathbf{G}$	gradients of dual function
g	inequality constraint function
$\mathbf{H}$	Hessian of dual function
$\tilde{\mathbf{H}}$	approximation of Hessian
h	equality constraint function
$\mathbf{K}$	linear stiffness matrix
$\mathbf{K}_G$	geometric stiffness matrix
L	Lagrangian function

LC	load case
l	dual function
$\mathbf{N}$	interpolation matrix
n	number of design variables
n_j	number of inequality constraints
n_k	number of equality constraints
$\mathbf{P}$	point force vector
$\mathbf{P}_{\mathrm{crit}}$	critical buckling load
P_S	surface perimeter
$\mathbf{PV}$	perturbation vector
p	penalisation factor in SIMP
$\mathbf{Q}$	matrix relating design variables to responses
$\mathbf{r}$	dual variable vector
r_{min}	minimum member radius
S	surface area
$\mathbf{t}$	surface traction vector
$\mathbf{u}$, $\mathbf{U}$	elemental and global displacement vectors
V	volume
V_{des}	volume of designable space
v	volume of an element
W	weighting factors
$\mathbf{x}$	design variable vector
$\mathbf{x}^*$	optimal design variable vector
$\mathbf{x}^0$, $\mathbf{x}^{00}$	design variable vectors for current and previous iterations
$\mathbf{x}_{nodes}$	nodal coordinates
$\mathbf{x}^0_{nodes}$	nodal coordinates of initial design
$\mathbf{Y}$	intermediate design variable vector
z_{upper}, z_{lower}	z-coordinates of nodes on upper and lower surfaces of a wing
Λ_B	bending strain energy

Λ_F	potential energy due to all applied loads
Λ_M	membrane strain energy
Λ_P	potential energy due point forces
Λ_b	potential energy due to body forces
Λ_s	potential energy due to surface traction
Λ_ε	strain energy
Π	total potential energy
ε	strain
$\bar{\varepsilon}$	small positive value
η	numerical damping factor
λ, μ	Lagrange multipliers
λ_{BLF}	eigenvalues corresponding to buckling load factors
$\lambda_{\min}$	eigenvalues of critical buckling mode
ρ	element density
ρ_L	lower limit on element density
σ	stress
σ_U	upper limit on stress
σ_{VM}	von Mises stress
ζ	move limit on design variables
ℓ	length of element interface

Nomenclature for Fluid Dynamics

To allow conventional notation, an alternative nomenclature is given for Section 2.2 and Chapter 3, which focus on fluid dynamics.

A	planform area
a	coefficients in the discretised momentum equations
C_D	coefficient of drag
C_L	coefficient of lift
C_P	coefficient of pressure
CV	cell volume
D	drag force
E	central node of neighbouring cell to the east
EE	central node of cell two cells east
e	eastern cell wall
F	mass flux across cell wall
L	lift force
N	central node of neighbouring cell to the north
n	northern cell face
P	node at cell centre
p	pressure
p^*, p'	estimated and correction components of pressure
p_∞	upstream pressure
S	central node of neighbouring cell to the south
s	southern cell face
U, u	mean and fluctuating components of velocity
$\overline{u_i u_j}$	Reynolds stresses
u, v	components of velocity vector
u^*, u'	estimated and correction components of u-velocity
V	volume
v^*, v'	estimated and correction components of v-velocity

v_∞	upstream velocity
W	central node of neighbouring cell to the west
w	western cell face
x, y	Cartesian coordinate components
μ	viscosity of fluid
μ_t	turbulent viscosity
$\tilde{v}$	modified turbulent viscosity
ρ	density of fluid

Chapter 1

Introduction

The introductory chapter to this thesis begins by stating the motivation behind the work presented here and outlines the key objectives of the research. This is followed by a review of approaches to design optimisation, with a focus on topology optimisation. In particular, this review highlights some of the current problems associated with topology optimisation, for example the difficulties of including stress and buckling constraints. Finally a detailed study of the literature reveals that the number of applications of topology optimisation to aerospace structural design problems is severely limited. The literature review indicates a number of avenues that are yet to be explored, some of which are investigated in the subsequent chapters.

1.1   Motivation

In recent years environmental issues have risen in prominence on the worlds agenda, which has had a major effect on the priorities of the aircraft industry. One of the goals set out by the Advisory Council for Aeronautics Research in Europe (ACARE) is to achieve a 50% reduction in aircraft fuel consumption and CO_2 emissions by 2020 (ACARE 2001). The design of modern commercial aircraft is now driven by an ever increasing need for efficiency. This can clearly be seen in the current generation of

airliners. The Airbus A380 is capable of carrying up to 853 passengers (Flight_International 2006) allowing greater efficiency per passenger. Boeing's 787 has tackled the problem of increasing efficiency in an altogether different way, using lightweight composites for 50% (by weight) of the aircraft in comparison to just 12% in the earlier 777 (Boeing 2010). This reduction in weight is reported to offer significant savings in fuel per passenger along with a corresponding reduction in CO_2 emissions (Hawk 2005). However, both of these aircraft are evolutionary rather than revolutionary. In fact there has been very little variation in the designs of commercial transport jets since the 1950s (Sensmeier and Samareh 2004) when aircraft such as the De Haviland Comet, the Boeing 707 and the Douglas DC-8 launched the jet transport age. Studies have shown that year-on-year improvements in aerodynamic efficiency from the 1960s until recently have been modest, with no great leaps forward with the advent of new design and manufacturing capabilities (Liebeck, Page et al. 1998). This is most likely due to the similarities in the design of all aircraft over this period. For these reasons, new aircraft configurations are increasingly attracting the attention of the aerospace community.

1.1.1 Next Generation of Aircraft Configurations

Amongst the non-conventional aircraft configurations currently being explored are the Lifting Body, Flying Wing, and Blended Wing Body concepts. Lifting Body aircraft configurations utilise an aerofoil shaped fuselage to generate additional lift. This configuration was seen as early as 1921 in the Burnelli RB-1 (Burnelli 1930) for passenger transport use, however in recent years its use has been confined to space vehicles such as the NASA X-38 and Lockheed Martin X-33. The Flying Wing concept on the other hand, has no fuselage, with the entire aircraft consisting of a fixed wing. This idea was proposed even earlier, by Hugo Junkers (1914), where the idea of containing the aircraft's payload, engines and crew within the lifting surfaces was first introduced. Flying Wings have the potential to be more aerodynamically efficient than any other fixed wing aircraft configuration and the load distributions along the wing also allow them to be very structurally efficient (Li, Seebass et al. 1998), reducing the necessary structural mass. However, a major drawback of this configuration is the small amount of space available for passengers or cargo. This is primarily why this type of

aircraft is most commonly seen in military applications, such as the Northrop B-2. Another disadvantage of the Flying Wing is its inherent aerodynamic instability, although this is less of an issue with current fly-by-wire technology.

Fig 1.1 Artist's impression of the NASA X-48 Blended Wing Body (www.nasa.gov).

Of the three non-conventional aircraft configurations mentioned earlier, the Blended Wing Body concept is attracting the most interest for use in commercial transport. This type of aircraft sits somewhere between the Lifting Body and Flying Wing concepts. It consists of a thick, aerofoil shaped fuselage which is smoothly blended into distinct, high aspect ratio wings. Most applications of this configuration currently involve military unmanned aerial vehicles (UAVs) such as the Boeing X-45, Northrop Grumman X-47, and Raytheon Killer Bee. However there are a number of research projects investigating its potential use in commercial aircraft, for example the X-48 (Figure 1.1) currently being developed as a joint venture by Boeing and NASA (Barnstorff 2006). Aircraft of this type offer some of the advantages of the Lifting Body and Flying Wing concepts. Improvements in aerodynamic efficiency when compared to conventional tube-with-wings aircraft are achieved, as the aerofoil shaped fuselage contributes to the lift. Additional improvements in efficiency are also achieved through the reduced wetted surface compared to conventional configurations, reducing viscous drag (Qin, Vavalle et al. 2004). Structural efficiency may also be improved as it is possible to achieve a near elliptical spanwise lift distribution (Qin, Vavalle et al. 2005), and the spanwise weight distribution is much more uniform than in conventional aircraft, resulting in reduced bending moments. The lift contribution from the fuselage/blended wing sections mean that the cantilever span of the high aspect ratio

outer wings can be reduced (Liebeck, Page et al. 1998). Potsdam, Page et al. (1997) compare the BWB concept for an 800 passenger aircraft to equivalent conventional aircraft and show that the BWB could increase the lift to drag ratio by 21% and reduce take-off weight by 15%. These factors offer a potential reduction in fuel consumption of 28%. A similar study by Liebeck (2004) indicates that for a smaller 480 passenger aircraft the savings in fuel costs could be even greater, around 32%.

Another reason why this aircraft configuration is attracting so much attention is the potential reductions in noise pollution. The ability to incorporate engines into or above the airframe could significantly reduce the noise impact for people on the ground (Hileman, Spakovszky et al. 2010). The main advantage that the Blended Wing Body has over true Flying Wings is the large amount of space available within the blended wing section for passengers and cargo. This makes the blended wing configuration especially advantageous for aircraft designed to carry large numbers of passengers, above and beyond what conventional aircraft are currently capable of (Mialon, Fol et al. 2002).

A major disadvantage of all these unconventional aircraft is the lack of collective knowledge on their performance, both aerodynamically and structurally. This is especially true of the Blended Wing Body configuration due the aspects of its design that have few similarities to conventional aircraft, i.e. the combined shape of the fuselage and blended wing sections . Conventional aircraft have had over 60 years to be explored and developed into the designs that exist today. However, with modern computational analysis and optimisation technology and the growing availability of high performance computing resources, it should be possible for new configurations to reach their potential and compete with conventional designs in a shorter time frame. In fact, at the current time, the majority of published research on the BWB configuration is entirely or predominantly computational, for example (Mialon, Fol et al. 2002; Mukhopadhyay, Sobieszczanski-Sobieski et al. 2004; Hansen, Heinze et al. 2008; Rodriguez 2009). Other disadvantages of the BWB configuration include the lack of access to windows for passengers, and the difficulties in evacuating a large number of passengers in an emergency. However a recent report suggests that passenger familiarity with the new configurations could play a more significant role in this problem than the configurations themselves (Galea, Filippidis et al. 2010).

1.2   Objectives, Scope and Overview

Given the growing interest in non-conventional aircraft configurations and the lack of collective knowledge on their prospective structural layouts, the advantages of employing state-of-the-art optimisation tools are evident. One such tool is topology optimisation. The generality of topology optimisation allows the generation of designs that are not based on pre-existing ideas for conventional aircraft, and can result in structures that may be un-intuitive. This makes it a logical tool for aiding the design of next-generation aircraft. The general focus of this research therefore, is on the potential uses of topology optimisation for determining the optimal structural architectures of next generation aircraft. As indicated by the paucity of literature in this field, topology optimisation technology is not yet mature enough to be applied in this role using typical problem formulations. There are several obstacles that stand in the way of it being used in this type of application; this thesis attempts to address some of them.

One such obstacle involves the high number of design variables associated with topology optimisation for real-world problems. If the structure of an aircraft is to be optimised then ideally, aerodynamic considerations should be factored in to the optimisation problem. This approach has been applied to some simple test cases (Maute and Allen 2004), however it currently requires substantial compromises in the fidelity of the structural and flow analysis. This is due to the large number of sensitivity calculations that are associated with a large number of design variables, combined with the comparatively high computational cost of flow analysis. The first objective of this research is to develop methods in which the structural optimisation problem can be formulated so that the aircraft's aerodynamic efficiency is not compromised, based on the assumption that changes to the wing's aerodynamic, cross-sectional shape will reduce this efficiency.

Another obstacle that is addressed here involves the large tip deflections of the high aspect-ratio wings seen on many aircraft. The usual way that topology optimisation problems are formulated involves the use of global compliance (or weighted global compliance) as an objective function, with a volume fraction constraint (Bendsoe and Sigmund 2004). The large deflection of these wings results in the global compliance being dominated by the spanwise bending of the wing; the displacements due to

twisting, chordwise bending, and local deformation due to control surface loads are small in comparison. The second objective of this research is to investigate how the topology optimisation problem, and the finite element models associated with it, can be adapted so that these additional considerations are accounted for.

Finally, the difficulties associated with buckling constraints in continuum-based topology optimisation are well documented. A common approach for overcoming this in real world applications is to optimise for minimum compliance, and use the interpreted material distribution for sizing and shape optimisation where buckling constraints can be applied (Schramm, Zhou et al. 2004). This approach works well in some applications, however it is not well suited to the optimisation of aircrafts' structural layouts. One main role of the ribs is to improve the critical buckling loads of the wing skin, whereas the key structures to improve stiffness are the spars. The ribs do little to improve bending stiffness which, as already mentioned, is currently the driving factor in the topology optimisation problem. Therefore, as the structural members for improving stiffness are distinct from those to improve structural stability, the typical approach is not adequate. The final objective of this research is to investigate alternative ways in which topology, shape and sizing optimisation can be combined to generate conceptual designs for the structural architectures of aircraft, with consideration of buckling requirements.

1.2.1 Synopsis

Chapter 1 gives an overview of several topics related to this research. Firstly a discussion of the prospective configurations of next generation aircraft is made. This is followed by an introduction to some of the theory of optimisation and a review of the structural optimisation methods available to engineers. Finally the use of structural optimisation in the aerospace industry is reviewed with emphasis on topology optimisation.

Chapter 2 gives a description of the analysis and optimisation tools used in this work, along with an application of these technologies. It begins by introducing a conceptual aircraft design with a Blended Wing Body (BWB) configuration. There is then an

explanation of the finite volume method of computational fluid dynamics (CFD) which is used to calculate pressure loads on the aircraft for use in the structural models, along with an overview of the finite element (FE) method of structural analysis. Finally the range of optimisation tools that are used in this work, including algorithms, material distribution models and design constraints, are described.

In Chapter 3 CFD is used to analyse the external flow over the same BWB aircraft. Firstly the results of a preliminary analysis and a mesh independency study are shown. This is followed by an investigation into effect of angle of attack on lift and drag. The results of this study are used to select an angle of attack and velocity to achieve an appropriate loading on the aircraft.

Chapter 4 addresses the first two objectives of the research. Firstly a series of parameter studies are conducted on a simple wing section. These parameters include: mesh resolution, design constraints, loadings, and penalisation. The second part of the chapter focuses on the application of topology optimisation to the internal structure of the BWB aircraft. This includes the proposal of several methods for preventing the dominance of spanwise bending in the optimisation problem. A study is also presented showing how topology optimisation can be used within the aircraft fuselage, where packaging constraints are tight.

In Chapter 5 the role that topology optimisation plays in a wider optimisation framework for this type of application is examined. The primary aim is to address the need for buckling considerations in the optimisation process, which is the third objective of this research. This begins with additional parameter studies on a wing section in order to quantify the effect of ribs and skin thickness on critical buckling loads. The use of shape optimisation for increasing these critical loads is investigated. A new approach to combining topology and shape optimisation within a multi-level framework is then proposed, which involves initial shape optimisation of rib positions for buckling requirements. Ribs are then included as non-designable members in the topology optimisation problem, which is shown to significantly affect results. Finally, techniques developed in Chapters 4 and 5 are applied to the BWB aircraft and are shown to offer potential savings in structural mass.

Chapter 6 outlines conclusions that can be drawn from the research presented in this thesis. It includes a discussion of the potential uses of topology optimisation in the design of aircraft structural architecture and the limitations that still exist. Possible directions of future work are also suggested.

1.3   Design Optimisation

1.3.1   Introduction

The purpose of optimisation is to find a set of design variables that minimise or maximise an objective function while satisfying any stated constraints. A general optimisation problem can be expressed as:

$$
\begin{aligned}
\text{minimise} \quad & f(\mathbf{x}) \\
\text{subject to} \quad & g_j(\mathbf{x}) \le 0 & j = 1,2,...,n_j \\
& h_k(\mathbf{x}) = 0 & k = 1,2,...,n_k \\
& x_i^L \le x_i \le x_i^U & i = 1,2,...,n
\end{aligned}
\tag{1.1}
$$

where $\mathbf{x}$ are the design variables, f is the objective function, and g and h are constraints.

Design Variables

In engineering optimisation problems the system to be optimised is parameterised into a set of design variables, which are defined as: $\mathbf{x}=[x_1,x_2,...,x_n]^T$. The solution to the problem is the vector of design variables, $\mathbf{x}^*$, that describe the optimal design. These design variables can be classified in several ways. One such classification is continuous or discrete. Continuous variables can take any real value between the upper and lower side constraints, x^U and x^L. Discrete variables are restricted to a selection of admissible values, for example the number of teeth on a gear must be an integer number. Optimisation problems with discrete variables are generally more difficult to solve than with continuous ones. It is common practice to disregard the discrete nature of design variables and simply round values to the nearest integer value after optimisation. However, this only works well if the admissible values are closely spaced so that rounding the variables does not make significant changes to the responses (Haftka and Gurdal 1992). If this method is not viable, there are two other options. An optimisation algorithm capable of handling discrete variables, such as integer programming or genetic algorithms, can be used. Alternatively, penalisation of inadmissible values can be introduced to the objective function, pushing the optimisation algorithm towards the admissible values of the design variables.

Another way to classify design variables is deterministic or stochastic. Optimisation using deterministic variables assumes that designs can be produced to correspond exactly to the optimised design variables. A stochastic optimisation problem is one in which uncertainties in the design variables, such as numerical noise, are accounted for. This may also cover uncertainties in known parameters as well as design variables. In stochastic optimisation the design variables and known parameters are expressed as probability density functions rather than exact values. Optimisation problems may then be formulated with an objective of minimizing the probability of failure, in order to produce robust designs.

Constraints

All optimisation problems can be classified as unconstrained or constrained. Unconstrained optimisation problems contain only an objective function, and optional side constraints. This can be expressed as:

$$
\begin{aligned}
\text{minimise} \quad & f(\mathbf{x}) \\
\text{subject to} \quad & x_i^L \leq x_i \leq x_i^U \quad i = 1,2,...,n
\end{aligned}
\qquad . \tag{1.2}
$$

In most practical problems designs are required to satisfy a series of requirements. These requirements can be included in the optimisation problem through the use of constraints. Constrained optimization problems may contain either equality or inequality constraints, or both, as stated in (1.1). Depending on the optimisation algorithm being used it may not be viable to use either equality or inequality constraints, in which case the equality constraints must be converted to inequalities or vice-versa. Equality constraints can be expressed as two inequality constraints with equal values for the upper and lower bounds. Inequality constraints can be expressed as equality constraints through the use of slack variables (Rao 2009). During the optimisation process, constraints can be described as active or inactive. A constraint is said to be active if removing that constraint alters $\mathbf{x^*}$, and the reverse for inactive constraints.

Objective Function

In order to find an optimal design, a criterion must be selected for comparing the quality of designs and selecting the best one. This criterion is known as the objective function and must be defined in terms of the design variables. Optimisation problems can be

single-objective or multi-objective. In the case of multi-objective problems it is common to have conflicting objectives. For example, maximising the stiffness of a structure conflicts with minimising its weight. There are several ways to deal with this. The optimisation problem can be solved as a single-objective problem by using only the most significant objective function, and converting the others to constraints. Alternatively the objective functions can be combined into a single function, either using weighting factors, W_I, on the individual objective functions:

$$\text{minimise } f(\mathbf{x}) = \sum_{I=1}^{N} W_I f_I(\mathbf{x}) , \qquad (1.3)$$

where the weightings represent the relative significance of each objective, or with a minmax formulation:

$$\text{minimise } \max(f_I(\mathbf{x})) \qquad I = 1,2,...,N \quad . \qquad (1.4)$$

Another possibility is to calculate the Pareto-optimal set. A design is Pareto-optimal if any changes to the design variable vector results in at least one objective function worsening. The Pareto-optimal set describes the trade-offs between the various objective functions, which allows a compromise to be chosen without the need to pre-define weighting factors.
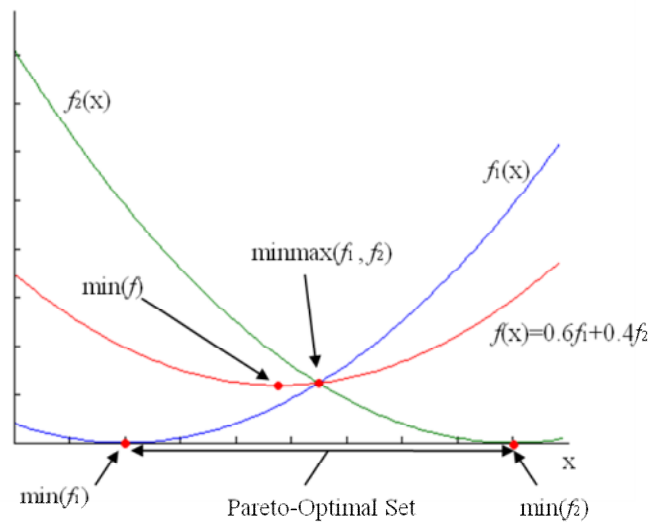
Figure 1.2 Depiction of the various solutions to a multi-objective optimisation problem with a single design variable.

Design Space

The design space is the domain defined by the design variables and their side constraints. A part of the design space bounded by the constraints is known as the feasible space. Any point in the feasible space satisfies all constraints in the optimisation problem, and is therefore a feasible design. This is illustrated in Figure 1.3. An optimal design must therefore be the point within the feasible space which has the best value of the objective function.
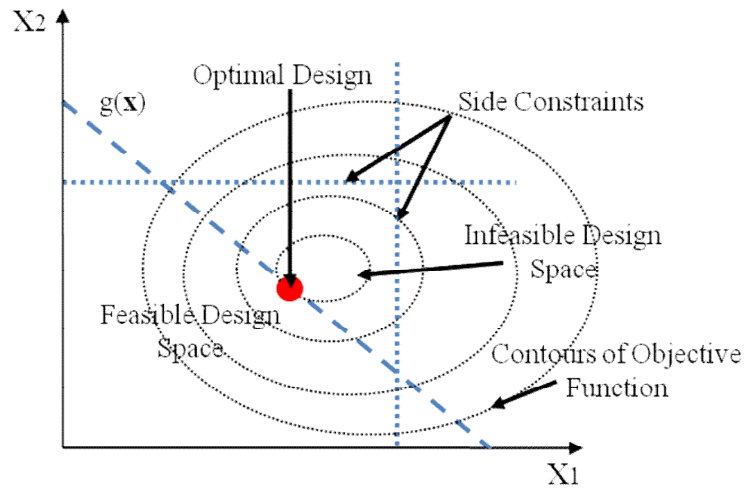
Figure 1.3 2D design space with constraints and objective function.

Conditions for Optimality

In classical analytical optimisation, problems are solved using calculus to define the conditions for optimality. For the unconstrained optimisation problem (1.2) these are:

$$\frac{\partial f(x)}{\partial x_1} = \frac{\partial f(x)}{\partial x_2} = \ldots = \frac{\partial f(x)}{\partial x_n} = 0 .$$

(1.5)

As is evident from these condition, the analytical approach to unconstrained optimisation is easy to implement so long as f is differentiable. The conditions for optimality of a constrained problem, known as the Kuhn-Tucker conditions, can be expressed as:

$$\frac{\partial f}{\partial x_i} + \sum_{j=1}^{n_j} \lambda_j \frac{\partial g_j}{\partial x_i} + \sum_{k=1}^{n_k} \mu_k \frac{\partial h_k}{\partial x_i} = 0,$$

$$\lambda_j g_j = 0, \qquad g_j \le 0, \tag{1.6-1.10}$$

$$h_k = 0, \qquad \lambda_j \ge 0.$$

For a design variable vector to be a local optimum a set of Lagrange multipliers, λ_j, μ_k, must exist that satisfy these conditions. The need for differentiability of both the objective function and constraints remains, and finding solutions to this system of equations can be difficult for all but the simplest functions, represented by *f*, *g* and *h*. It is therefore necessary to implement numerical optimisation techniques in most large scale, real-world applications.

1.3.2 Optimisation Algorithms

There is no universally superior method of optimisation, and the best approach is problem dependent (Onwubiko 2000). It is therefore beneficial to categorise optimisation problems in a number of ways. These can include:

- Constrained or unconstrained problems;
- Single or multi-variable problems;
- Single or multi-objective problems;
- Linear or non-linear problems;
- Continuous or discrete problems;
- Separable or non-separable problems;
- Deterministic or stochastic problems.

Just from these classifications, the large range of optimisation problems that exist is quickly apparent. It therefore makes sense that there is an equally large range of ways in which to solve these problems. These can be broadly classified as: mathematical programming methods; optimality criteria methods; or metaheuristic methods. Encyclopaedic textbooks exist, covering the numerous algorithms available within these classes, see (Rao 2009). It is therefore outside the scope of this work to review these methods in any detail, however a brief overview of the three general classes is provided.

1.3.2.1 Mathematical Programming Methods

Mathematical programming methods were the earliest form of numerical optimisation. The majority of work in this field came about in the mid-twentieth century along with the computers capable of implementing them. These methods involve defining an initial design variable vector, and iteratively moving towards an optimum.

Unconstrained Descent Methods

One of the simplest and most intuitive approaches to mathematical programming is the steepest descent method for unconstrained optimisation problems. This involves finding a search direction, **d**, such that:

$$\mathbf{d} = -\nabla f(\mathbf{x}^0),\tag{1.11}$$

where $\mathbf{x}^0$ is the current point in the design space. A simple line search method is then used to locate the minimum objective function value in this direction. The process is repeated from the located minimum until convergence. This method can be inefficient in poorly scaled problems as the search direction is orthogonal to that of the previous iteration. This is alleviated in the conjugate gradient method (Fletcher and Reeves 1964), where the search direction is determined by:

$$\mathbf{d} = -\nabla f(\mathbf{x}^0) + \left(\frac{\left|\nabla f(\mathbf{x}^0)\right|}{\left|\nabla f(\mathbf{x}^{00})\right|} \right)^2 \mathbf{d}^0,\tag{1.12}$$

where $\mathbf{x}^{00}$ is the previous point in the design space, $\mathbf{d}^0$ is the previous search direction, and the step-size is determined in the same way as the steepest decent method.

Linear Programming

Linear programming (LP) is a mathematical programming method that can be used to solve constrained optimisation problems where the objective function and constraints are linear functions of the design variables. A general linear program can be stated as:

minimise $\quad f(\mathbf{x}) = \mathbf{c}^T\mathbf{x}$

subject to $\quad \mathbf{Ax} = \mathbf{b}$. $\hfill$ (1.13)

$\qquad\qquad \mathbf{x} \geq 0$

This class of problem can be solved efficiently even for large numbers of design variables using the simplex method (Onwubiko 2000). Of course many practical engineering problems do not have linear objectives and constraints. However, linear programming can be implemented as an intermediate step in other optimisation algorithms, for example the method of feasible directions. Sequential linear programming (SLP) also allows most non-linear problems to be solved using a series of linear approximations, as follows:

$$f(\mathbf{x}) \approx f(\mathbf{x}^0) + \nabla f(\mathbf{x}^0)^T (\mathbf{x} - \mathbf{x}^0) \quad ,$$
$$h_k(\mathbf{x}) \approx f(\mathbf{x}^0) + \nabla h_k(\mathbf{x}^0)^T (\mathbf{x} - \mathbf{x}^0) \quad , \qquad (1.14\text{-}1.16)$$
$$g_j(\mathbf{x}) \approx f(\mathbf{x}^0) + \nabla g_j(\mathbf{x}^0)^T (\mathbf{x} - \mathbf{x}^0),$$

where move limits are imposed to account for the decreasing accuracy of the approximations at increasing distances from $\mathbf{x}^0$. These approximated sub-problems can be solved using LP methods which will converge to the exact solution of the non-linear problem (Haftka and Gurdal 1992).

Quadratic Programming

Likewise, quadratic problems can be solved using quadratic programming (QP). Quadratic problems are a specific class of non-linear problem where the objective function is a quadratic function of the design variables and the constraints are linear functions. A general quadratic problem can be stated as:

minimise $\quad f(\mathbf{x}) = \mathbf{c}^T\mathbf{x} + \frac{1}{2}\mathbf{x}^T\mathbf{D}\mathbf{x}$

subject to $\quad \mathbf{Ax} \leq \mathbf{b}$. $\hfill$ (1.17)

$\qquad\qquad \mathbf{x} \geq 0$

This problem can be reduced to a linear programming problem through the use of Lagrange multipliers and the Kuhn-Tucker conditions (Rao 2009). As in SLP, most non-linear problems can be approximated with a series of QP problems. This method is

known as sequential quadratic programming (SQP). The quadratic sub-problem used to find a search direction can be stated as:

$$
\begin{aligned}
\text{minimise} \quad & \nabla f(\mathbf{x})^T \mathbf{d} + \tfrac{1}{2} \mathbf{d}^T \tilde{\mathbf{H}} \mathbf{d} \\
\text{subject to} \quad & g_j(\mathbf{x}) + \nabla g_j(\mathbf{x})^T \mathbf{d} \leq 0 \qquad j = 1,2,...,n_j \quad, \\
& h_k(\mathbf{x}) + \nabla h_k(\mathbf{x})^T \mathbf{d} = 0 \qquad k = 1,2,...,n_k
\end{aligned}
\tag{1.18}
$$

where $\tilde{\mathbf{H}}$ approximates the Hessian of the Lagrangian function:

$$
L(\mathbf{x}, \lambda, \mu) = f(x) + \sum_{j=1}^{n_j} \lambda_j g_j(x) - \sum_{k=1}^{n_k} \mu_k h_k(x) \quad .
\tag{1.19}
$$

The resulting search direction vector and Lagrange multipliers are then used to find the optimum by minimising the function:

$$
f(\mathbf{x}) + \sum_{j=1}^{n_j} \lambda_j \max[0, g_j(\mathbf{x})] + \sum_{k=1}^{n_k} \mu_k |h_k(\mathbf{x})| \quad .
\tag{1.20}
$$

$\tilde{\mathbf{H}}$ is updated and a new quadratic subproblem is constructed at the new $\mathbf{x}$. Haftka and Gurdal (1992) state that the additional work required to solve the quadratic problem is often outweighed by the increased convergence speeds compared to SLP.

1.3.2.2 Optimality Criteria Methods

Optimality criteria (OC) methods are methods of optimisation which attempt to mimic the analytical approaches to solving optimisation problems using the conditions for optimality. According to Haftka and Gurdal (1992) their use is mostly confined to structural applications, where they have been shown to be effective for very large scale problems due to their relationship with duality. This can make them highly advantageous for problems where the number of design variables is large compared to the number of constraints, for example topology optimisation. The use of MP methods

in these cases can be prohibitively computationally expensive due to the number of gradient calculations required (Zhou and Rozvany 1992). A drawback of these approaches is that they rely on the ability to derive the optimality criteria for a specific class of problem (Rozvany and Zhou 1992). These criteria can be used to formulate a heuristic scheme for updating the design variables. Some of the earliest OC methods used intuitively derived optimality criteria, such as the fully stressed design (FSD) concept. For example, the optimality criteria for a fully stressed design are simply:

$$\sigma_i = \sigma_U \quad , \tag{1.21}$$

where σ_i is the stress in each member or element and σ_U is an upper limit on the stress. For a truss structure the updating scheme could then be:

$$A_i^{new} = A_i^{old} \frac{\sigma_i}{\sigma_U} \quad , \tag{1.22}$$

where A_i are the cross sectional areas of each truss. Extending this method to a wider variety of problems requires optimality criteria to be derived from the Kuhn-Tucker conditions. There are a variety of OC based algorithms designed for use in structural optimisation. One such method that enables the use of both stress and displacement constraints is the iterative continuum-based optimality criteria (COC) method (Rozvany and Zhou 1991; Zhou and Rozvany 1991). An extension of this, known as the discretised continuum-based optimality criteria (DCOC) method, was developed specifically for use with finite element (FE) based structural analysis and offers further improvements in efficiency to the OC methods for large scale problems (Zhou and Rozvany 1992; 1993).

1.3.2.3 Metaheuristic Methods

Recent years have seen rapid growth in the application of optimisation algorithms that are fundamentally different to MP and OC methods of optimisation. These methods, known as metaheuristic algorithms, are often inspired by physical or biological processes. Their heuristic nature and the fact that they implement stochastic search

methods often means that an optimal solution cannot be guaranteed. However they have become popular in large scale problems, where MP methods are impractical, and in situations where gradient information is unavailable. They are also advantageous in problems with multi-modal responses due to the way they search the design space (Rao 2009).

One widely used metaheuristic method is the genetic algorithm (GA), developed by Holland (1992). GAs are based on the theory of evolution and natural selection, where design variables are encoded as binary 'chromosomes'. A GA usually consists of: creation of an initial population of designs; evaluation of the fitness (objective function with penalisation of constraint violations) of each member of the population; selection of members to act as parents for the next generation; creation of the next generation through reproduction of the parents with random mutations. Due to the way the design variables are encoded in binary form, GAs are ideally suited to problems with both discrete and continuous design variables (Haftka and Gurdal 1992). The growing interest in metaheuristic methods is evident in the number of algorithms that exist. Two of the more frequently used algorithms are simulated annealing (Metropolis, Rosenbluth et al. 1953) and particle swarm optimisation (Kennedy and Eberhart 1995), although currently neither can compete with the GA in terms of popularity.

1.3.3 Metamodelling Methods

In problems where the computational costs of calculating response values of a design are high, or where the analysis is performed using a black-box that prevents sensitivity analysis, it is often undesirable to extract responses directly from the analysis tools. In this case empirical models can be developed that describe the behaviour of the design responses as a function of the design variables. These models are known as metamodels or surrogate models. The building of these models allows cheap function evaluations which can be highly beneficial for any optimisation technique that requires a large number of these evaluations. They also provide engineers with a better understanding of the design problem, and allow the optimisation problem to be reformulated and repeated without the need for further expensive analyses (Wang and Shan 2007). The process of constructing a metamodel consists of: design of experiments (DoE) for selecting the

design points that will be used for building the model; evaluating the responses at those design points; fitting a curve to the points.

The design of experiments can be performed in a number of ways. Full factorial sampling produces uniform DoEs but is highly inefficient due to many design points existing at the same value of a design variable. The use of Latin Hypercubes ensures that a wide range of values is covered for each design variable, but can produce highly non-uniform DoEs. This problem can be alleviated by optimising the uniformity of the DoE, as implemented by Bates, Sienz et al. (2004). Likewise, there are numerous methods for fitting curves to the design points. Some methods attempt to model the entire design space, such as polynomial regression and Kriging, whereas others construct new models based on the position in the design space to be evaluated, such as trust region methods and moving least squares. For a more thorough review of the variety of approaches available for both design of experiments and curve fitting the reader is directed to Keane and Nair (2005).

A major drawback of the metamodelling method is the exponentially increasing number of sampling points required for increasing numbers of design variables. Even so, the metamodelling approach to optimisation has been shown to be well suited to problems that require expensive analysis calculations, such a computational fluid dynamics (CFD), and have low numbers of design variables. This is demonstrated by the author for a real-world, industrial application in Fan, Eves et al. (2011).

1.4   Topology Optimisation

1.4.1   Introduction to Structural Optimisation

One application of the optimisation techniques described in the previous section is in the determination of optimal structures, where responses such as mass, stresses, displacements, and buckling loads can be used. The earliest forms of structural optimisation involved the optimisation of continuous functions that described structural properties, such as the moment of inertia of a beam (Haftka and Gurdal 1992). However the advent of high performance computing allowed structural analysis to be performed using the finite element method, which allows the structural responses to be defined in terms of a discrete set of design variables. Structural optimisation can be split into three distinct classes; sizing; shape; and topology optimisation. The differences between these classes of structural optimisation problem are illustrated in Figure 1.4.
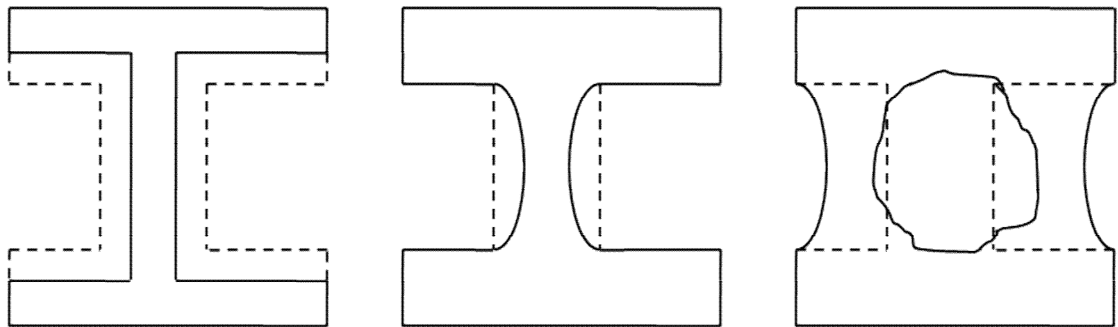
Figure 1.4 Three classes of structural optimisation illustrating the difference in generality between sizing (left), shape (middle), and topology (right) optimisation.

The earliest and simplest form of structural optimisation is sizing, where the cross-sectional areas of structural members are design variables but the shape of the structure remains constant (Haftka and Grandhi 1986). In shape optimisation the shape (and size) of the structure is optimised, but the topology remains constant. This class of structural shape optimisation is more complex than sizing optimisation as the changing shape of the structure requires alternations to the finite element mesh (Ding 1986). The simplest way in which the shape of a structure can be defined by a set of design variables is using the discrete approach. In this method the nodal coordinates of each element in a

finite element mesh are used as design variables. This approach can lead to designs that are not properly captured by the original finite element approximation, resulting in the optimiser converging to false optima (Haftka and Gurdal 1992). There is also the problem of the manufacturability of designs produced in this manner (Braibant and Fleury 1984). Basis and perturbation vector approaches describe the shape or change in shape of a structure with a linear combination of vectors (Pickett, Rubinste et al. 1973), however these approaches limit the complexity of the shapes that can be defined. Numerous other methods of shape parameterisation exist, and a review of these techniques is given in the paper by Samareh (2001). The final class of structural optimisation, and the focus of this work, is topology optimisation. Topology optimisation is the most general of the three classes, where the design variables in describe the connectivity or layout of a structure, along with its shape and size. Ways in which this is achieved and the problems this poses are discussed below.

1.4.2 Introduction to Topology Optimisation

Topology optimisation is a relatively new area of research that is attracting increasing attention within the structural optimisation community. This is clearly demonstrated by the large number of papers featuring topology optimisation presented at both the 2007 and 2009 World Congresses on Structural and Multidisciplinary Optimisation (Rozvany 2009). As already mentioned, the advantage of topology optimisation lies in its generality. Sizing and shape optimisation require the connectivity of a structure to be determined before optimisation. This is not an issue for applications where there is a high level of collective knowledge on what the optimal structures should be. However, for new applications where there is little or no collective knowledge on the optimal structures, assumption as to this connectivity have to be made. It is often impossible to guarantee that such assumptions result in an optimal structure. In this type of application, topology optimisation is the logical approach as no such assumptions have to be made.

As with shape optimisation, there are many different ways in which the topology optimisation problem can be represented in terms of a discrete set of design variables. Olhoff and Enschenauer (2001) state that approaches within this field of research can

also be divided into two distinct classes, discrete and continuous, which are illustrated in Figure 1.5.
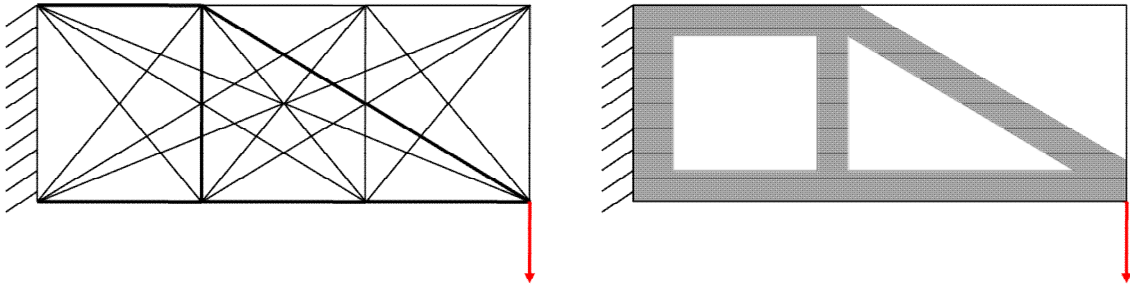
Figure 1.5 Discrete (left) and continuum-based (right) topology optimisation.

Discrete topology optimisation involves the optimisation of systems with discrete structural members, for example truss structures. This begins with the definition of a ground structure made up of a network of potential members, as proposed by Dorn, Gomory et al. (1964), an example of which is shown in Figure 1.5 (left). Sizing can then be carried out on the trusses with the size of non-optimal members approaching zero (Zhou 1996). Alternatively, trusses can be removed entirely using a genetic algorithm (Deb and Gulati 2001) or the evolutionary methods that are discussed later in this chapter (Steven, Querin et al. 2000). This approach can be extended to more complex applications, for example the structural layouts of aircraft wings (Lencus, Querin et al. 2002).

1.4.3   Topology Optimisation of Continuum Structures

Topology optimisation of continuum structures begins with the definition of a design domain, as shown in Figure 1.5 (right). The design domain is then meshed to create a finite element model, which may also include non-designable structures and non-designable voids. The topology optimisation problem can then be formulated by relating each of these finite elements to a design variable. The most basic and intuitive way of doing this is as a material-void or 0-1 distribution. The implementation of this in the finite element method is simple as the elemental material properties are constant. A drawback of this approach is that it is not always well-posed which can result in the non-existence of solutions (Stadler 1986). This problem can be overcome by using a material distribution model, where the binary problem is converted to a sizing problem

using element densities that vary continuously from zero to one. This type of problem can then be solved using any number of optimisation algorithms, although due to the typically large number of design variables, optimality criteria and dual methods are usually employed (Rozvany 2009). Optimality criteria can be derived from the Kuhn-Tucker conditions, or alternatively a heuristic approach can be used such as that of the fully stressed design. Bulman, Sienz et al. (2001) propose updating element densities based on either stresses or strain energy density. This hybrid approach adopts aspects of both the material distribution and evolutionary methods discussed in the following sections.

1.4.3.1   Material Distribution Models

The first method proposed for modelling the material distribution problem were homogenisation methods, originally suggested by Bendsoe and Kikuchi (1988). These approaches involve the periodic distribution of small voids throughout the designable space to create a composite material, or microstructure, as shown in Figure 1.6. The density of an element can then be related to the size of the void within it, and the dimensions and orientation of these voids can be used as design variables. Both the size and orientation of these voids effect the macroscopic properties of the material, and therefore the stiffness matrix. The effects of the microstructure on element properties must be calculated using the theory of homogenisation.
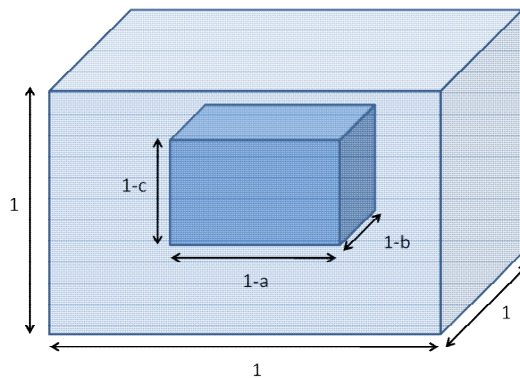
Figure 1.6 Homogenisation approach to material distribution modelling. Dimensions of inner void are used as design variables.

The most common implementation of the microstructure with homogenisation approaches is the Optimal Microstructures with Penalisation (OMP) method (Allaire, Belhachmi et al. 1996). This method uses the dimension of the voids as design variables, while the optimal orientation of the voids is derived from the constraints and objective function defined in the topology optimisation problem. Initially optimisation is performed without additional penalisation, although the existence of voids naturally penalises intermediate densities to some degree. Upon convergence optimisation continues with the density updated as a function of the computed optimal density, which introduces additional penalisation of intermediate values. An alternative method applies penalisation through the use of a Non-Optimal Microstructure (NOM). In this approach the elements are intentionally orientated in a non-optimal way which further penalises intermediate element densities (Bendsoe and Kikuchi 1988).

An alternative, and currently the most common, method of formulating the material distribution problem is the Solid Isotropic Material with Penalisation (SIMP) approach (Bendsoe 1989). In this model the element densities, ρ, are related to the Young's modulus, E. This can be compared to the optimisation of a plate thickness, which can vary continuously between upper and lower limits, as suggested by Rossow and Taylor (1973). However, this results in large areas with thicknesses in between these limits, whereas in topology optimisation it is desirable to approach a material-void distribution. For this reason, penalisation of elements with intermediate densities is introduced in the following way:

$$E = \rho^{p} E_{0},$$
(1.23)

where E_0 relates to the material properties and p is known as the penalisation factor, with $p > 1$ (Figure 1.7). Because of the apparent un-physical nature of this relationship justification for it is given in a number of ways. Bendsoe and Sigmund (1999) show that microstructures can be derived that mimic the SIMP relationship for various values of p. Rozvany, Zhou et al. (1992) relate SIMP to the plate thickness problem with a consideration of manufacturing costs, where intermediate thicknesses must be machined and are therefore undesirable.
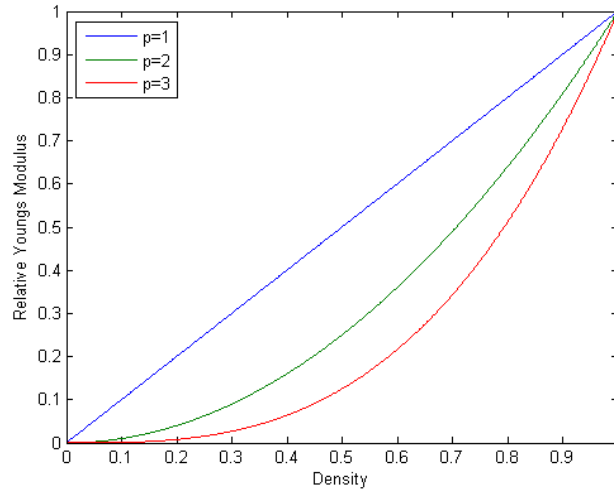
Figure 1.7 Relationship between density and Young's modulus for various penalisation factors in SIMP.

Each of these approaches have their relative advantages and disadvantages. SIMP is more computationally efficient than the homogenisation methods as there is only one design variable for each element. It can potentially be used for any type of design constraint as no knowledge of the microstructure is needed, although there are difficulties associated with applying stress and buckling constraints due to the phenomena of singular topologies which are discussed later. Conversely the homogenisation methods require knowledge of the optimal microstructure for a given set of design constraints (Rozvany 2001). Another advantage of SIMP is there is no need for homogenisation of the microstructure. On the other hand the use of additional penalisation can result in optimal solutions that are dependent on the value of p used (Svanberg and Stolpe 2000) and there are cases where material-void designs are not approached for any value of p (Stolpe and Svanberg 2001). However the fixed penalisation used in NOM is often insufficient to find optimal solutions that approach a material-void distribution (Rozvany 2000). Bendsoe (1989) points out the possible non-existence of solutions to the SIMP formulation which lead to mesh dependency, although this can be alleviated in a number of ways which are discussed later in this chapter.

1.4.3.2   Topology Optimisation without Material Distribution Models

Other methods of topology optimisation avoid the need for a material distribution model by adopting the material-void approach described earlier. One of these methods, developed by Xie and Steven (1993), is known as Evolutionary Structural Optimisation (ESO). However it should be noted that this is not related to the evolutionary methods used in genetic algorithms (Rozvany 2009). ESO is similar in nature to the concept of fully stressed design, described by Haftka and Gurdal (1992). In ESO elements with the lowest criterion value, which may be stress or compliance for example, are removed and the criterion value of each remaining element is recalculated. This is known as a hard-kill approach. An improvement on this is the Bi-directional Evolutionary Structural Optimisation (BESO) approach (Querin, Steven et al. 1998), where material can be added next to elements with a high criterion value. The main advantage of ESO-based optimisation is that it is conceptually simple, and implementation is easy. There is also no need for gradient calculations which can be beneficial in cases where structural analysis is performed by a black-box solver. However, this method has been shown to break down in specific cases where the removal of material with a low criterion value can dramatically increase compliance, as shown by Zhou and Rozvany (2001). Suggested methods for improving ESO in these cases include; numerical comparison of a performance index, e.g. a function of compliance and mass, for designs throughout the optimisation process (Ling and Steven 2002); and adapting the original hard-kill approach so that the removed elements are replaced with low density material. Stresses are still calculated in the low density material and therefore any element can be replaced (Zhou and Rozvany 2001; Rozvany and Querin 2002). A major criticism of ESO methods is that they are entirely heuristic in nature, and in fact can often lead to non-optimal designs. There are also severe limitations on the number and type of constraints that can be used. For a thorough critique of ESO and comparison with SIMP the reader is directed to the review paper by Rozvany (2009).

A relatively recent approach to topology optimisation is the level set method, as implemented by Sethian and Wiegmann (2000). Level set methods for moving interface problems were first proposed by Osher and Sethian (1988) for representing flame fronts, however it is becoming increasing popular for structural optimisation (Allaire, Jouve et al. 2004; Challis 2010). In this approach the moving boundaries of a structure are

described by a level set function, where negative values represent material and positive values represent void. The movement of the boundary can then be determined either based on stresses in the structure (as in ESO) (Sethian and Wiegmann 2000), or by shape sensitivity analysis (Allaire, Jouve et al. 2004). Another method of topology optimisation, where the boundaries of a structure can be described independently of the spacial discretisation and without the need for a material distribution model, is the bubble method (Eschenauer, Kobelev et al. 1994). This involves iteratively inserting a void (or bubble) into the material followed by shape optimization.

1.4.4 Known Issues and Recent Developments in Material Distribution Based Topology Optimisation

The primary method of topology optimisation used in this work is the SIMP model. It is therefore worthwhile discussing some of the issues associated with SIMP and the available methods for overcoming them. Two of these issues can be tackled in very similar ways. The first is mesh dependency, which has already been mentioned, and the second is checkerboarding. An example of the checkerboarding problem is illustrated in Figure 1.8. Checkerboarding is a problem associated with the finite element discretisation of a structural model, or more specifically the overestimation of checkerboard stiffnesses made in this approximation (Bendsoe and Sigmund 2004). In the majority of cases, methods that ensure mesh independence will eliminate the problem of checkerboarding. These methods can also be used to enforce minimum member sizes to aid manufacturability.
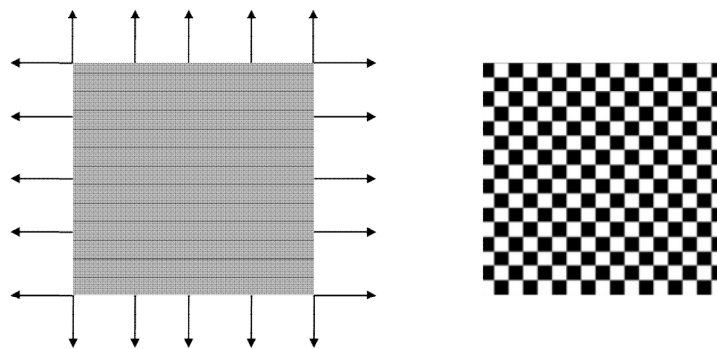
Figure 1.8 Designable region under uniform, in plane stress (left) and resultant material distribution suffering from the checkerboard phenomena (right).

The first of these methods is perimeter control. This places an upper limit on the perimeter of the structure, which is defined as:

$$P_S = \sum_{k=1}^{K} \ell_k \left(\sqrt{(\rho_i - \rho_j)^2 + \bar{\varepsilon}^2} - \bar{\varepsilon} \right) , \qquad (1.24)$$

where ℓ_k is the length of the interface between adjacent elements i and j, and $\bar{\varepsilon}$ is a small positive number to ensure the sensitivity of P_S can be computed (Haber, Jog et al. 1996). Another method is to control local density gradients. In its simplest form this consist of placing constraints on the gradient of density between adjacent elements, as implemented by Petersson and Sigmund (1998). This approach has been extended by Zhou, Shyy et al. (2001), through the use of adaptive lower limits on element densities,

$$\rho_i \geq \max\left[\rho_L, \rho_{j\,max} - (1.0 - \rho_{min}) \text{dist}(i,\, jmax)/ r_{min} \right] , \qquad (1.25)$$

where ρ_{min} is the density below which is interpreted as void, ρ_L is a lower limit on element densities, $jmax$ is the number of the highest density element from the previous iteration that is adjacent to i, dist($i,jmax$) is the distance between elements i and $jmax$, and r_{min} is a constraint on the minimum member radius. Other methods of ensuring mesh independence and removing checkerboarding consist of filtering, either of the densities or sensitivities. Filtering the densities results in checkerboard distributions and very fine structures being interpreted as intermediate densities, which are penalised in both the SIMP and OMP approaches. Sensitivity filtering involves modifying the sensitivities as follows (Bendsoe and Sigmund 2004):

$$\frac{\partial \hat{f}}{\partial \rho_j} = \frac{1}{\rho_j \sum_{i=1}^{N} H_i} \sum_{i=1}^{N} H_i \rho_i \frac{\partial f}{\partial \rho_i} , \qquad (1.26)$$

where:

$$H_i = r_{min} - dist(i, j), \qquad \{ i \in N \,|\, dist(i, j) \leq r_{min} \} . \qquad (1.27\text{-}1.28)$$

A comparison of these approaches is made by Zhou, Shyy et al. (2001), and can be summarised as follows: Problems exist in the perimeter method as there is no clear

definition of what the perimeter constraint should be to achieve the required simplicity of the material distribution. Standard gradient control introduces a large number of constraints to the optimisation problem making it impractical for large scale problems. This problem is removed by the adaptive method in Equation (1.25), but it requires the optimisation algorithm to allow temporary violations of the constraints and it is not clear how altering the limits will affect convergence. The filtering of densities results in a 'blurred' stiffness matrix which effects the fidelity of the structural analysis (Bendsoe and Sigmund 2004). Filtering sensitivities is highly efficient, but problems exist in applications with multiple constraints where the altering of sensitivities can jeopardise the accuracy of local approximations. This demonstrates that there is no single preferable approach for all applications, and the choice of the best method to use is problem dependent.

The use of stress constraints in material distribution based topology optimisation problems poses some important challenges. The intuitive way to impose stress constraints is:

$$\left(\sigma_{VM}\right)_i \leq \rho_i^p \sigma_U \;, \tag{1.29}$$

where σ_{VM} is the von Mises stress and σ_U is the stress constraint. However, this implementation can result in a phenomenon known as singular topologies. This is a result of the constraints tightening as densities approach zero. Vanishing members, when elemental densities reach zero, can cause the globally optimal solution to exist in a part of the feasible space confined to an m-dimensional hyperplane in the n-dimensional design space, where $m < n$. This is illustrated for a simple 2D design space in Figure 1.9. Singular topologies can make finding the global optimum incredibly difficult and usually results in solutions converging to local optima (Rozvany and Birker 1994). Although non-zero minimum density constraints are usually placed on elements in material distribution based topology optimisation, this phenomena can still cause global optima to exist in sharp peaks of the design space, making them difficult to reach.
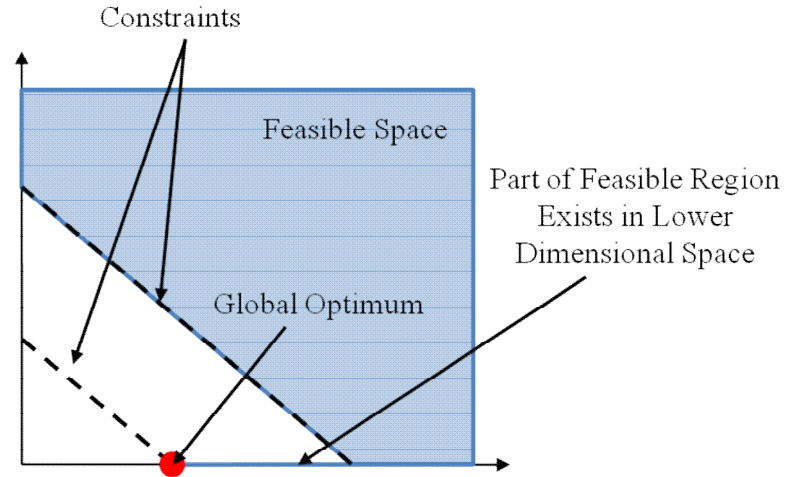
Figure 1.9 2D design space illustrating the singular topology phenomena (Cheng and Guo 1997).

Cheng and Guo (1997) propose the ε-relaxed method for dealing with this problem. This consists of relaxing the stress constraints at lower densities in the following way:

$$\frac{(\sigma_{VM})_i}{\rho_i^p \sigma_U} - \frac{\bar{\varepsilon}_i}{\rho_i} + \bar{\varepsilon}_i \leq 1 \ , \qquad \bar{\varepsilon}_i^2 = \rho_L \leq \rho_i \ . \qquad (1.30\text{-}1.31)$$

Although effective in overcoming the singular topology issue, this approach still requires considerable computational effort for large scale problems due to the large number of constraints. Duysinx and Sigmund (1998) suggest a global stress constraint:

$$\left[\frac{1}{n} \sum_{i=1}^{n} \left(\max\left\{ 0, \frac{(\sigma_{VM})_i}{\rho_i^P \sigma_U} - \frac{\bar{\varepsilon}_i}{\rho_i} + \bar{\varepsilon}_i \right\} \right)^q \right]^{1/q} \leq 1 \ . \qquad (1.32)$$

This method reduces the problem to a single constraint which, although not able to ensure local stresses do not exceed their limit, can provide reasonable results. Bendsoe and Sigmund (2004) suggest using a value of 4 for q.

The inclusion of buckling constraints in topology optimisation problems also poses significant difficulties, and is therefore not widely practiced. One of these problems is artificial modes occurring as a result of high geometrical stiffness compared to linear stiffness in low density elements. Neves, Rodrigues et al. (1995) propose that the geometrical stiffness in these low density elements should be neglected. Bendsoe and

Sigmund (2004) suggest that this approach may cause oscillations in the convergence of the optimiser due to step changes in the constraints or objective function. They propose a smooth version of this approach with:

$$E_K = \left[\rho_L + (1 - \rho_L)\rho^P \right] E^0,$$ (1.33)

$$E_G = \left[\rho^P \right] E^0,$$ (1.34)

where E_K and E_G are the elastic moduli corresponding to the (linear) stiffness matrix and the geometrical stiffness matrix, respectively. This is reported to eliminate the problem of oscillation. Another issue is that of the singular topology phenomena resulting from 'vanishing' members (Rozvany 1996). More recently Zhou (2004) has suggested that topology optimisation with buckling considerations is not yet mature enough to generate useful solutions for general applications. There are a subset of problems where buckling responses can be included. These involve optimisation of shells with non-zero minimum thicknesses, for example laminated composite structures (Lund 2009).

Pressure loads can also present problems in topology optimisation because the position and direction of these loads are dependent on the shape and topology of the structure. Problems of this type exist in a number of applications such as for aeroplanes and submerged structures subjected to aerodynamic or hydrostatic loads, respectively. There have been several approaches suggested for dealing with this type of problem. Hammer and Olhoff (2000) use an iso-density surface to calculate the pressure loads on the designable elements. Other methods include using splines to model the pressure loads based on the element densities (Fuchs and Shemesh 2004) and defining the fluid region (void) as incompressible (Sigmund and Clausen 2007). This problem is more easily dealt with in the level-set approach to topology optimisation as the boundaries of the structure are already defined by the level set function (Allaire, Jouve et al. 2004). Obviously these problems do not exist if pressures are only applied to non-designable structures or shells with non-zero minimum thicknesses, such as the skin of an aircraft wing.

As demonstrated with the mesh dependency and checkerboarding problems already discussed, the manufacturability of designs produced using topology optimisation can be an issue. A variety of additional constraints in the topology optimisation problem

have been suggested to aid manufacturability. One such constraint allows the topology optimisation of cast parts, where the die or dies must be able to slide off the part in a specified direction. Zhou, Shyy et al. (2002) implement this by specifying that:

$$\rho_i \leq \rho_j \leq ... \leq \rho_n \; , \qquad\qquad\qquad (1.35)$$

where *i, j, n*, are aligned in the draw direction of the die. This can be extended to include two dies with a specified die splitting point. In ESO-based approaches there is also the possibility of ensuring global connectivity of the part by checking whether rejecting elements effects this, and preventing rejections that do (Harzheim and Graf 2006); however, this is not possible in SIMP due to the step-function response that would define the connectivity of the structure as either global or non-global. Zhou, Shyy et al. (2002) also apply extrusion constraints to ensure structures with constant cross-sections, which is implemented by specifying:

$$\rho_i = \rho_j = ... = \rho_n \; , \qquad\qquad\qquad (1.36)$$

where *i, j, n*, are aligned in the extrusion direction. This method of coupling element densities has been extended to two further applications. Pattern grouping allows the design of multiple components with the same topology, e.g. a series of aircraft wing ribs, and pattern repetition allows the design of symmetrical structures without the need for symmetrical loadings, e.g. car wheels (Altair 2009 ii).

Reliability Based Topology Optimisation (RBTO) is another recent development in this field. The usual method of topology optimisation is deterministic with no consideration for uncertainties in the design variables (i.e. the element densities). Kharmanda, Olhoff et al. (2004) propose a method of RBTO where the loads applied to a deterministic topology optimisation problem are updated iteratively, based on uncertainties in the variables and a required reliability index. This demonstrates the significant differences in optimal topologies when reliability is considered compared to the usual deterministic approach. This method has also been successfully implemented with multiple load cases and a system-wide reliability requirement, and applied to large-scale 3D problems (Silva, Tortorelli et al. 2010).

Applications of continuum-based topology optimisation to problems with dynamic loads are uncommon, although there has been some research in this area (Min, Kikuchi et al. 1999). However the computational costs associated with large scale problems are prohibitive (Kang, Park et al. 2006). Very recently the use of the Equivalent Static Load (ESL) method, developed by Kang, Choi et al. (2001) has been extended to topology optimisation. This method uses FE analysis of the transient problem to derive a series of equivalent static loads that replicate displacements in the structure at different time steps. These equivalent loads are used to define multiple load cases in the topology optimisation problem. The optimised material distribution is then used to update the transient model and the process is repeated iteratively (Park 2010). The approach has also been extended to include damage constraints, which involves integrating load induced stresses with respect to time (Sherif, Witteveen et al. 2010).

1.5   Topology Optimisation of Aerospace Structures

1.5.1 Introduction

In the preface to their book, Haftka and Gurdal (1992) point out the historic imbalance between research into structural optimisation and real world applications. Fortunately, this is no longer true, and one of the industries in which structural optimisation has become part of everyday operations is the aerospace sector. As discussed in the introduction to this chapter, the need for energy efficient air transport is now a key driver in the design of aircraft. One way in which this increase in efficiency can be achieved is by reducing the mass of aircraft, of which a significant proportion is made up of its load bearing structure (Roskam 2003).

Structural optimisation in the aerospace industry has its roots in airframe sizing. Finite element based structural sizing has been practiced in this industry for as long as the necessary computational technology has allowed it. The earliest uses of this approach involved global finite elements models to extract local loadings on structural components, represented as simple 1D and 2D members with estimated sizes. Sizing of these components could then be performed using empirical methods and simple stress analysis tools. Engineers then had the option to update the global FE model with these new sizes for further iterations (Niu 1997; Grihon and Krog 2009). This approach is similar to the fully stressed design principle on which ESO is based. Due to the limitations of this type of sizing associated with statically indeterminate structures, as discussed by Haftka and Gurdal (1992), and with the increasing availability of computational resources, the industry moved towards numerical optimisation techniques, i.e. mathematical programming (Petiau 1991). However, semi-empirical tools are still employed in the sizing process for phenomena that FE technology is not considered mature enough to properly model, for example de-lamination (Grihon and Krog 2009). Even so, aerospace engineers have a wider array of structural optimisation tools available to them than ever before, and of these topology optimisation is becoming increasingly popular.

1.5.2   Literature Review

The use of topology optimisation within the aerospace industry is still in its infancy, although this is rapidly changing. The PLATO-N project (PLATO-N 2010) is currently developing a software platform for topology optimisation, with a specific focus on aeronautical applications. It is hoped that the tools developed as part of the project will extend the role of topology optimisation within the aerospace industry, allowing the cost and environmental impact of both conventional and non-conventional aircraft to be reduced. Even so, there is still very little literature on aerospace applications available in the public domain. Stanford and Ifju (2009) suggest that approaches to topology optimisation in aerospace applications can be divided into three classes. The first of these covers approaches where aerodynamic loadings are calculated using fluid dynamics analysis. These loads are then applied to a structural model on which optimisation can be performed with consideration of only structural responses such as mass, compliance, stress and displacements. This method ignores the effect of changes to the wings shape due to elastic deformation on aerodynamic loadings. The second class covers approaches where aerodynamic quantities such as lift and drag are included as responses in the optimisation problem. Deformation of the wing and aerodynamic loadings are linked through aeroelastic coupling. The third class of aerospace topology optimisation that is suggested involves the topology optimisation of fluid domains. It is outside the scope of this work to discuss this third class in any depth, but descriptions and applications of this approach can be found in (Borrvall and Petersson 2003; Pingen, Evgrafov et al. 2007; Pingen, Waidmann et al. 2010). A fourth class could be added to this method of classification, as there are a variety of aerospace applications where aerodynamic loads are not required in the structural model, such as landing gear (Schramm 2009) and even aircraft seats (Altair 2010).

It seems logical to divide the first approach into two types of application; those that aim to optimise the general structural layout of aircraft or wing sections; and those that aim to optimise individual aircraft components, e.g. ribs, aileron hinges, etc. The earliest use of topology optimisation in an aerospace application falls into the first category, and corresponds to the earliest form of topology optimisation. Balabanov and Haftka (1996) use a ground structure of discrete trusses, as proposed by Dorn, Gomorov et al. (1964), to represent the internal structure of a wing. The cross-sectional areas of these members

are used as design variables to allow compliance to be minimised as a sizing problem. Since then there has been little attention to this specific field, with the small amount of academic research focussing on aeroelastic topology optimisation problems, and industrial research focussing on individual aircraft components. There are, however, some papers worth noting.

Lencus, Querin et al. (1999) employ the ESO approach to optimise the structural layout of an aircraft spoiler. This is applied in two ways, both using an initial ground structure of structural members. The first uses a binary representation of the members, while the second allows for continuous thicknesses of the members. This approach is extended to an entire aircraft wing by Lencus, Querin et al. (2002), where the topology is optimised using the binary representation followed by sizing of the remaining members. Ledermann, Ermanni et al. (2006) use CAD-based parameterisation with an upper limit on the permissible number of structural members. This approach bypasses the need for either a ground structure or a material distribution model by allowing the number and location of spars and ribs to be defined without the existence of a finite element model. The ground structure approach is adopted by Inoyama, Sanders et al. (2007; 2008) for the optimisation of morphing wing structures, where the structural member, actuator and joint types are linked to the design variables in the optimisation problem. This approach allows three wing configurations to be achieved, while reducing the required number of actuators compared to a baseline design. Rao, Kiran et al. (2008) optimise the material distribution in a continuum representation of a commercial transport wing, and show that the use of high mesh resolution can produce structures similar to bird wings. A second study using manufacturing constraints to determine optimal spar locations is shown to yield a single spar. Additional spars are only seen as a result of dividing the design domain, with separate volume constraints on each. Krog, Grihon et al. (2009) present a similar study using a combination of flight and ground loads. This is shown to result in a curved, truss-like spar, with additional structures linking the landing gear rib to the root. It is suggested that the resulting material distribution could be used as a guide for designers, although the lack of buckling considerations and the questionable manufacturability are highlighted. Finally in a paper by the author (Eves, Toropov et al. 2009), the layout of a Blended Wing Body aircraft is optimised using continuum based topology optimisation. An approach for preserving the wing's aerodynamic shape is suggested, details of which are included in Chapters 4 and 5 of this thesis.

In their review paper, Olhoff and Enschenauer (2001) demonstrate how the bubble method of topology optimisation can be applied to the optimisation of an aircraft's wing rib. A similar study by Krog, Tucker et al. (2004) compares three approaches to optimising wing ribs. Topology optimisation of a rib as part of a wing box is shown to result in structures suited to withstand locally applied loads but not loads applied globally to the wing box. Applying only local loads based on an initial free body analysis is shown to give more favourable results. It is also proposed that compliances from the initial analysis should be used as constraints on compliances for individual load cases, with mass as the objective function. This ensures that a critical load case drives the design, whereas the weighted sum formulation favours a material distribution that improves stiffness for all load cases, and a minmax formulation encourages equal stiffness for each load case. Buchanan (2007) also demonstrates how the material distribution from topology optimisation can be interpreted for size and shape optimisation, where buckling and stress considerations can be included. Other applications of topology optimisation to aerospace structural components include the leading edge ribs of the Airbus A380 (Krog, Tucker et al. 2002) and a vertical stabiliser component (Saleem, Yuqing et al. 2008; Saleem, Hu et al. 2009). Topology optimisation has also been applied in aerospace applications other than aeroplanes, for example missile bodies with vibration considerations (Luo, Yang et al. 2006). The moment of inertia of space vehicles, which has been linked to the requirements for altitude control, can also be minimised using topology optimisation (Kang, Wang et al. 2009).

Literature on aeroelastic topology optimisation of aircraft structures is even scarcer. This is probably due to the large number of design variables involved in topology optimisation, coupled with the relatively high computational costs of flow analysis compared to structural analysis. These two factors make this type of approach very computationally expensive, and compromises are required in terms of the fidelity of fluid solvers. The first work in this field came from Maute and Allen (2004), however the low number of papers citing this important work (23 on Google Scholar as of August 2010) perhaps demonstrates how under-explored this field is. Topology optimisation is used to locate stiffeners within a wing in two ways. Firstly with consideration for only structural responses, and secondly for both aerodynamic and structural responses where aerodynamic responses are determined using an Euler flow

analysis. The benefits of accounting for fluid-structure interaction are demonstrated by a substantial decrease in drag compared to the pure structural approach. The developed approaches are also extended to the optimisation of compliant structures for adaptive aerofoil design (Maute and Reich 2004; Maute and Reich 2006), where the benefits of coupling aerodynamic and structural responses are confirmed. Gomes and Suleman (2008) use a level set method for topology optimisation of the reinforcement layout on the skin of a wing box to maximise aileron reversal speed. Results of this approach are shown to be independent of the initial configuration of the reinforcements. However, in more recent work by Stanford and Ifju (2009), this is shown not to be true for all cases. In this study, topology optimisation of reinforcements to a micro air vehicle wing for improvements in a number of aerodynamic responses is shown to be highly sensitive to the initial layout. The approach uses low fidelity aerodynamic and structural models, which are shown to be capable of improving aerodynamic performance. This is confirmed by experimental validation. This method is extended to the optimisation of the thicknesses of plate like wings with a number of planform shapes and consideration of aeroelastic stability (Stanford and Beran 2010). Although this is strictly speaking a free-size problem, penalisation is applied to intermediate thicknesses, so in practice it bears more resemblance to SIMP-based topology optimisation. Pareto-fronts describing the trade-off between mass and critical flutter speed are calculated, which demonstrates potential improvements over plates with uniform thickness.

As indicated by the literature reviewed in this section, there is definite scope for improvements in the way topology optimisation is applied to aerospace structural design problems. Consideration of aeroelastic effects is prohibitively computationally expensive, especially for large-scale problems such as optimising entire structural layouts of aircraft. It is therefore necessary to explore ways in which topology optimisation problems can be formulated for the design of such layouts without the need for numerous, expensive flow analyses. Methods for achieving this, along with the results of applying them to a conceptual aircraft design, are presented in the following chapters.

Chapter 2

Application and Methodology

Chapter 1 introduced the potential role of topology optimisation in aerospace applications, along with a variety of approaches available for solving topology optimisation problems. This chapter begins with the description of an example application, in the form of a Blended Wing Body UAV, followed by an overview of the analysis and optimisation tools that are used for optimising the structural architecture of the aircraft. This includes an explanation of the approaches used for external flow analysis, structural analysis, topology optimisation and shape optimisation. The results from applying these approaches to the proposed structural optimisation problem are then presented in the subsequent chapters.

2.1 Application: An Unmanned Aerial Vehicle

In order to assess the usefulness of topology optimisation as a tool for determining optimal layouts of aircraft architecture a conceptual design for a Blended Wing Body UAV was provided by QinetiQ Ltd. (Figure 2.1). As discussed in Chapter 1, very little is known about the optimal structural layouts for this type of aircraft, making the use of topology optimisation potentially advantageous.
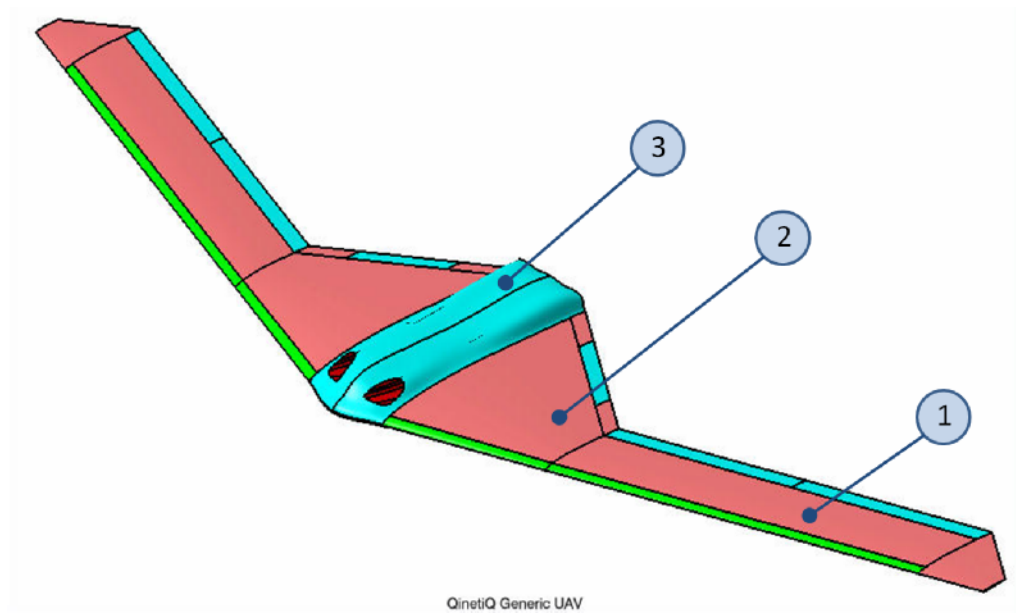
Figure 2.1 Conceptual design of a Blended Wing Body UAV, showing un-tapered (1) and tapered (2) wing sections and fuselage (3).

The choice of this aircraft configuration can be justified by the number of different challenges it provides for topology optimisation. Despite the blended wing design, the aircraft's body can be split into three distinct sections. The un-tapered, aft-swept wing section (Figure 2.1(1)) is of similar shape and size to that found on many commercial aircraft. As this type of wing has been meticulously studied over many years the optimal positions and orientations of structural members within it are well understood, allowing a good benchmark for comparison with the results from topology optimisation. The second partition is the tapered, blended wing section (Figure 2.1(2)). This part of the wing is becomes much thicker than usual aircraft wings as it blends into the fuselage. This makes the wing especially susceptible to deformation of its shape under aerodynamic loading. There is little collective knowledge on this type of wing or of how it should connect to either a fuselage or to a more slender un-tapered wing section. Topology optimisation can be used to determine how best to stiffen this part of the wing to maintain its aerodynamic profile.

Finally the fuselage section (Figure 2.1(3)) provides an altogether different and more usual test for topology optimisation. Within the fuselage there are numerous packaging constraints. Spaces for two engines along with their intakes and exhausts are situated in

the upper half of the fuselage (Figure 2.2), leaving only a small amount space above them for structural members. The bottom half of the fuselage contains non-designable spaces for a cargo bay and front landing gear (Figure 2.2). Accordingly there are only three areas in which structural members such as spars can connect to the centreline of the aircraft along its lower surface. These areas are situated in the nose and at the rear of the aircraft, and in between the landing gear and cargo bay. There is also very limited space between the engines and cargo bay. Topology optimisation has been successfully applied to this type of problem before and shown to be useful in finding optimal spaces to add material in order to improve structural performance (Sigmund 2000).
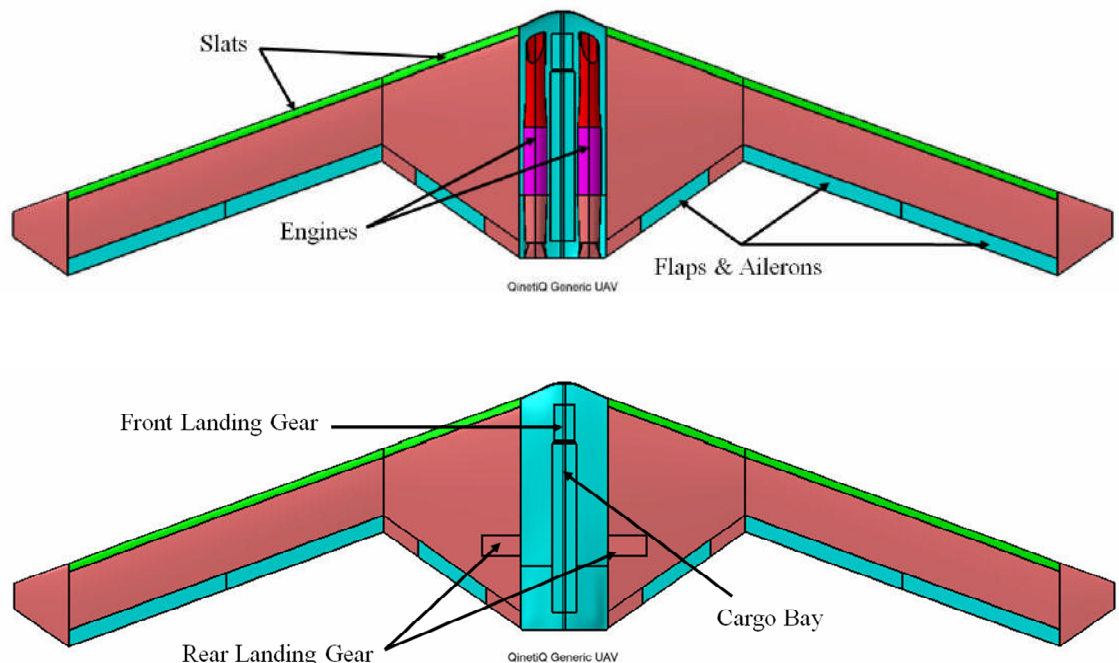
Figure 2.2 Planform views of UAV showing non-designable spaces for engines, intakes, exhausts, landing gear and cargo bay.
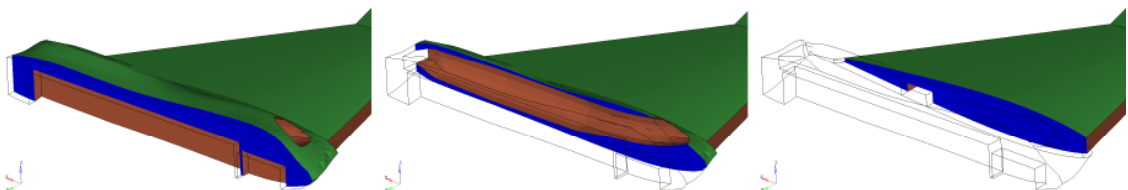
Figure 2.3 Section cuts of UAV geometry showing designable and non-designable spaces.

2.1.1 Selection of Load Cases, Design Requirements and Materials

In consultation with QinetiQ, several key flight conditions were identified for the derivation of loadings on the UAV,. The first of these was a 3.5g loading resulting from pulling out of a dive, the next was a -1g loading resulting from pulling out of a climb, and a third was a 1g loading for steady level flight. All of these loadings are based on an initial estimation of the aircraft's mass, also provided by QinetiQ. An initial topology optimisation study using these three load cases showed material distributions to be almost entirely dependent on the most severe of the load cases, which in this study was 3.5g. There was little variation in the distributions resulting from the combined load cases and the single 3.5g load case. The 3.5g case contributes significant levels of both bending and twisting of the wing and represents the highest loading the aircraft would be expected to endure. Due to the almost symmetrical nature of the aircraft and the isotropic materials used, a negative load case is not necessary. For these reasons, the 3.5g 'pull out of a dive' load case is used for all optimisation involving aerodynamic pressure loadings.

For the purpose of this work five key design requirements were also identified. The first three of these relate to improving the overall stiffness of the aircraft's structure. They are: the maximum displacement of the wing must not exceed a defined upper value; the twist angle of the wing must be kept to a minimum as twisting of the wing results in higher loadings at the tip, increasing bending moments which require increased structural mass (Desktop_Aeronautics 2007); and the wing must maintain its aerodynamic cross-sectional shape to maintain aerodynamic performance. The other two requirements are that the stresses in the structure should not exceed the yield strength of the material, and the structure's critical buckling load should not exceed the loadings from the 3.5g load case.

The material used for all structural components is aluminium with an elastic modulus of 70 GPa, a Poisson's ratio of 0.33 and a density of 2700 kg/m^3. The wetted surface of the aircraft is defined by a skin with a thickness of 2mm unless otherwise stated. The skin allows pressure loads to be applied to the aircraft without any of the problems discussed in Section 1.4.4, however its thickness is small in order to reduce its effects on topology optimisation.

2.2   Computational Fluid Dynamics

In this work the pressure loadings used in structural analysis and optimisation are calculated using the commercial CFD package Fluent (ANSYS 2009). Fluent solves the Navier-Stokes equations governing fluid flow numerically, using the finite volume method (FVM). Three-dimensional flow over the aircraft is modelled, however the methods used are presented in 2D for simplicity.

2.2.1   Finite Volume Discretisation of the Navier-Stokes Equations

The Navier-Stokes equations governing the conservation of momentum for steady state, incompressible flow can be written as:

$$\nabla \cdot (\rho \mathbf{u} u) = -\frac{\partial p}{\partial x} + \mu \nabla^2 u \ , \quad \nabla \cdot (\rho \mathbf{u} v) = -\frac{\partial p}{\partial y} + \mu \nabla^2 v \ , \qquad (2.1\text{-}2.2)$$

with mass conservation ensured via the continuity equation, given as:

$$\nabla \cdot (\rho \mathbf{u}) = 0 \ , \qquad (2.3)$$

where x and y are the Cartesian coordinates, u and v are the x and y components of velocity, $\mathbf{u}$ is the velocity vector, p is pressure, and ρ and μ are the density and viscosity of the fluid, respectively.
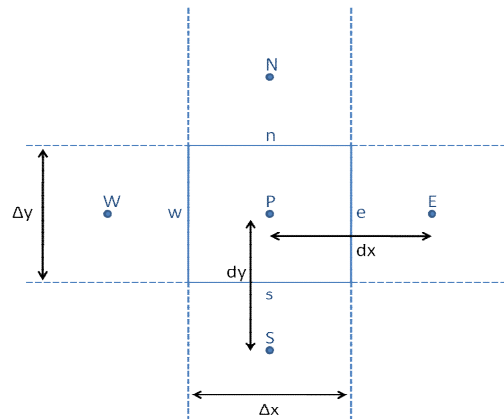
Figure 2.4 2D CFD grid arrangement with uniform, structured cells, showing north, south, east and west cell faces (lower-case), and neighbouring nodes (uppercase).

These are discretised via the finite volume approach for incompressible flow on the grid shown in Figure 2.4:

$$\int_{CV} \nabla \cdot (\rho \mathbf{u}u)dV = (\rho uu)_e \Delta y - (\rho uu)_w \Delta y + (\rho uv)_n \Delta x - (\rho uv)_s \Delta x, \qquad (2.4)$$

$$\int_{CV} \nabla^2 u \, dV = (\mu \frac{\partial u}{\partial x})_e \Delta y - (\mu \frac{\partial u}{\partial x})_w \Delta y + (\mu \frac{\partial u}{\partial y})_n \Delta x - (\mu \frac{\partial u}{\partial y})_s \Delta x, \qquad (2.5)$$

$$\int_{CV} \frac{\partial p}{\partial x} dV = \frac{(p_E - p_W)}{2dx} \Delta x \Delta y \;, \qquad (2.6)$$

$$\frac{\partial u}{\partial x}\bigg|_e = \frac{u_E - u_P}{dx}, \quad \frac{\partial u}{\partial x}\bigg|_w = \frac{u_P - u_W}{dx}, \quad \frac{\partial u}{\partial y}\bigg|_n = \frac{u_N - u_P}{dy}, \quad \frac{\partial u}{\partial y}\bigg|_s = \frac{u_P - u_S}{dy} \;, \qquad (2.7)$$

for the u-momentum equation (2.1), and similarly for v-momentum (2.2). The convection terms (Equation 2.4) can be linearised by initialising the problem with a flux term, F, at the cell faces, calculated as the product of the density and the velocity at and normal to the cell face. The CFD problem is solved iteratively, and these flux terms are updated based on the flow field from the previous iteration.

2.2.2 Numerical Scheme

A suitable numerical scheme is required to interpolate the face velocities from the node velocities. In this work the Quadratic Upwind Interpolation for Convective Kinematics (QUICK) scheme of Leonard (1979) is used. In QUICK these face values are obtained from a quadratic function passing through two nodes immediately upstream and one node immediately downstream. For example, the east cell face velocity is calculated as:

$$u_e = \begin{cases} \frac{3}{4}u_P + \frac{3}{8}u_E - \frac{1}{8}u_W & \text{if} \quad F_e > 0 \\ \frac{3}{4}u_E + \frac{3}{8}u_P - \frac{1}{8}u_{EE} & \text{if} \quad F_e < 0 \end{cases}, \qquad (2.8)$$

where F is the flux term at the cell faces, calculated from the previous iteration.

2.2.3 Solution Method

The SIMPLE (Semi-Implicit Method for Pressure Linked Equations) algorithm (Patankar and Spalding 1972) employed in Fluent introduces an equation for pressure correction based on the discretised continuity equation:

$$\int_{CV} \nabla \cdot (\rho \mathbf{u}) dV = (\rho u_e \Delta y) - (\rho u_w \Delta y) + (\rho v_n \Delta x) - (\rho v_s \Delta x) = 0 . \tag{2.9}$$

Pressure and velocity are split into a guessed part (*) and a correction part ('):

$$p = p^* + p' , \qquad u = u^* + u' , \qquad v = v^* + v' . \tag{2.10-2.12}$$

Face velocities are computed using a simplified form of the momentum equations:

$$u_e = u_e^* + \frac{p'_P - p'_E}{a_e} \Delta y , \tag{2.13}$$

for the east face, and similarly for the others. This yields a further system of linear equations for correction of the pressure field based on a velocity field calculated in the way described in Section 2.2.1.

2.2.4 Turbulence Model

The Reynolds Averaged Navier-Stokes (RANS) equations (Equation 2.14) are derived from decomposing flow variables into mean (U) and fluctuating (u) parts. This introduces the Reynolds Stresses, $\overline{u_i u_j}$, which can then be computed individually or accounted for via the solution of a turbulence model.

$$\frac{\partial}{\partial x_j}(U_i U_j) = -\frac{1}{\rho}\frac{\partial P}{\partial x_i} + \frac{\mu}{\rho}\frac{\partial}{\partial x_j}\left(\frac{\partial U_i}{\partial x_j} + \frac{\partial U_j}{\partial x_i}\right) + \frac{\partial \overline{u_i u_j}}{\partial x_j} . \tag{2.14}$$

The Spalart-Allmaras model (Spalart and Allmaras 1994) is used in this work as it was

developed specifically for modelling turbulent external flows in aerospace applications. This uses a single transport equation for a modified turbulent kinematic viscosity, $\tilde{v}$:

$$\frac{\partial}{\partial x_i}(\rho \tilde{v} u_i) = C_{b1} \rho \tilde{S} \tilde{v} + \frac{1}{\sigma_{\tilde{v}}} \left[\frac{\partial}{\partial x_j} \left\{ (\mu + \rho \tilde{v}) \frac{\partial \tilde{v}}{\partial x_j} \right\} + C_{b2} \rho \left(\frac{\partial \tilde{v}}{\partial x_j} \right)^2 \right] - C_{w1} \rho f_w \left(\frac{\tilde{v}}{d} \right)^2 ,$$

(2.15)

where:

$$\tilde{S} = \sqrt{2 \Omega_{ij} \Omega_{ij}} + \frac{\tilde{v}}{\kappa^2 d^2} f_{v2}, \qquad \Omega_{ij} = \frac{1}{2} \left(\frac{\partial u_i}{\partial x_j} - \frac{\partial u_j}{\partial x_i} \right) .$$

(2.16-2.17)

This modified turbulent viscosity is related to the turbulent viscosity, μ_t, via the relationship:

$$\mu_t = \rho \tilde{v} f_{v1} ,$$

(2.18)

which in turn can be related to the Reynolds stresses in the RANS equations via the Boussinesq hypothesis. In Equations (2.15-2.16) f_{v1}, f_{v2}, f_w are wall damping functions and d is the distance to the wall. The Fluent default values for the constants used in the transport equation are (ANSYS 2009):

$$C_{b1} = 0.1355, \quad C_{b2} = 0.622, \quad \sigma_{\tilde{v}} = 2/3, \quad C_{v1} = 7.1,$$
$$C_{w1} = \frac{C_{b1}}{\kappa^2} + \frac{(1 + C_{b2})}{\sigma_{\tilde{v}}}, \quad C_{w2} = 0.3, \quad C_{w3} = 2.0 \quad \kappa = 0.4187.$$

(2.19)

2.3 Finite Element Analysis

The responses for all optimisation problems are derived from structural analysis based on the finite element method (FEM), as described below. Finite element analysis is performed using Altair's RADIOSS solver via their optimisation tool, OptiStruct (Altair 2009 ii). Despite the large displacements present in the aircraft's wing, all structural analyses performed here are considered geometrically linear. The number of design variables, and therefore the necessary number of sensitivity calculations involved in topology optimisation is so high, the use of non-linear analysis is prohibitively computationally expensive. Linear analysis provides an adequate first approximation for use in large scale, industrially relevant topology optimisation.

2.3.1 Linear Static Analysis

The finite element model can be derived from the principle of minimum potential energy, which states that a system will be stable if its displacement minimises its total potential energy. For a more detailed explanation of this the reader is referred to Szabo and Babuska (1991). The total potential energy of the system is:

$$\Pi = \Lambda_\varepsilon - \Lambda_b - \Lambda_s - \Lambda_P \ , \tag{2.20}$$

where Λ_b is the potential of body forces; Λ_s is the potential of surface traction; and Λ_P is the potential of point forces acting on the structure. The strain energy of the structure is given by:

$$\Lambda_\varepsilon = \tfrac{1}{2}\int_V \sigma^T \varepsilon \, dV \ . \tag{2.21}$$

The volume is discretised into n elements with the elemental displacement vectors given by:

$$\mathbf{u}_i^T = \left(u_1, u_2, ..., u_m\right)_i \ , \tag{2.22}$$

where *m* is the number of degrees of freedom of the element. Assuming the structure has no initial strain, Equation (2.20) can then be rewritten as:

$$\Pi = \sum_{i=1}^{n} \left(\frac{1}{2} \int_V \mathbf{u}_i^T \mathbf{B}^T \mathbf{E} \mathbf{u}_i \, dV - \int_{V_i} \mathbf{b}^T \mathbf{N} \mathbf{u}_i \, dV_i - \int_{S_i} \mathbf{t}^T \mathbf{N} \mathbf{u}_i \, dS_i \right) - \mathbf{P}^T \mathbf{U} , \qquad (2.23)$$

where **b** is the body force vector, **t** the surface traction vector, and **P** is the point force vector; **E** is the elasticity matrix that relates stress to strain. The **B** matrix is the derivative of the interpolation matrix **N** that relates discrete nodal displacements to continuous displacements. Differentiating (2.23) with respect to the nodal displacements gives:

$$\sum_{i=1}^{n} \left(\mathbf{k}_i \mathbf{u}_i - \left(\mathbf{f}_b \right)_i - \left(\mathbf{f}_s \right)_i \right) - \mathbf{P} = \mathbf{K} \mathbf{U} - \mathbf{F}_b - \mathbf{F}_s - \mathbf{P} = 0 , \qquad (2.24)$$

where **K** is the stiffness matrix, $\mathbf{F}_b$ the body force vector, and $\mathbf{F}_s$ the surface load vector. Therefore, for a known set of forces the resulting displacements can be calculated with a system of linear equations. Elemental stresses can then be easily calculated via:

$$\sigma_i = \mathbf{E} \mathbf{B} \mathbf{u}_i . \qquad (2.25)$$

2.3.2 Buckling Analysis

Buckling occurs when a structure converts its membrane strain energy into bending strain energy with no change in applied loadings. The total potential energy of the structure can be defined by:

$$\Pi = \Lambda_B - \Lambda_M - \Lambda_F , \qquad (2.26)$$

where *B* and *M* denote the contributions from bending and membrane strain energies respectively and *F* denotes the potential from all the applied loadings. The bending strain energy is given by the first term in Equation (2.23) and the membrane strain

energy is defined as:

$$\Lambda_M = \tfrac{1}{2}\mathbf{U}^T\mathbf{K}_G\mathbf{U}.$$ (2.27)

To satisfy the principle of minimum potential energy:

$$\frac{\partial\Pi}{\partial\mathbf{U}} = (\mathbf{K} + \lambda_{BLF}\mathbf{K}_G)\mathbf{U} = 0, \quad \text{or} \quad \det\left|\mathbf{K} + \lambda_{BLF}\mathbf{K}_G\right| = 0,$$ (2.28-2.29)

where $\mathbf{K}_G$ is the geometric stiffness matrix which is derived from the stresses calculated in the linear static case. The eigenvalues are the buckling load factors, with the lowest value relating to the critical load, as such:

$$\mathbf{P}_{crit} = \lambda_{min}\mathbf{P}.$$ (2.30)

2.3.3 Finite Element Types

The finite element meshes employed are generated using Altair's HyperMesh software (Altair 2009 i). Within HyperMesh the types of finite element required must be specified for passing to OptiStruct and RADIOSS. Firstly the shape of the element is specified. Three node tria (TRI3) and four node quad (QUAD4) elements were used for defining surfaces. Four node tetra (TETRA4), six node penta (PENTA6) and eight node hex (HEX8) elements were used for defining volumes. These are illustrated in Figure 2.5.

| TRIA3 | QUAD4 | TETRA4 | PENTA6 | HEX8 |
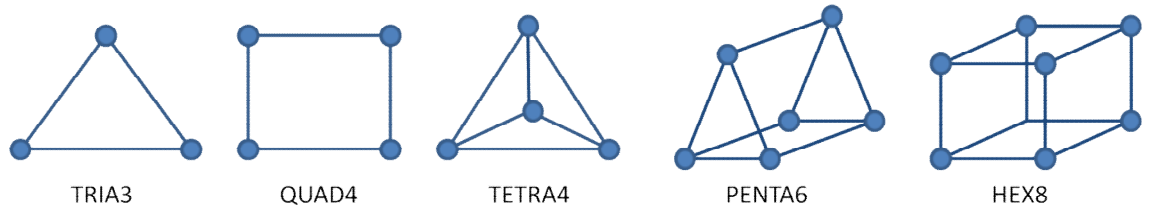
Figure 2.5 Configurations of various 2D and 3D finite elements.

The degrees of freedom (DoF) of nodes in each element type has to be specified. All 3D elements are solid elements which have three translational DoF at each node. They have no rotational stiffness in any direction. The 2D elements used are always shells. Shells are a combination of membrane elements, with two in-plane translational DoF at each node, and plate elements, with two in-plane rotational DoF and a normal translational DoF at each node (Figure 2.6). A shell element has no rotational stiffness about the axis normal to its surface.
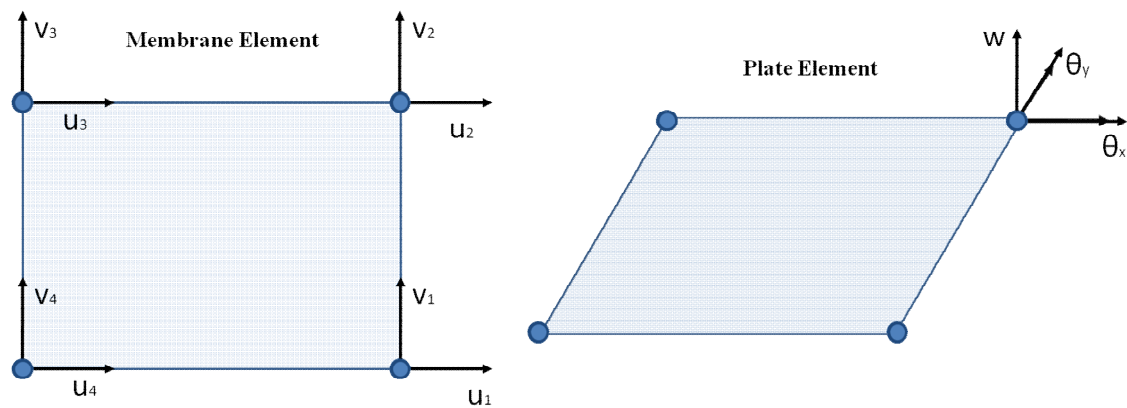
Figure 2.6 Membrane and plate elements that are combined to create a QUAD4 shell element.

2.4 Optimisation

Optimisation is performed using Altair's OptiStruct (Altair 2009 ii) in order to iteratively solve optimisation problems of the following form:

$$
\begin{aligned}
\text{minimise} \quad & f(\mathbf{x}) = f(x_i) \\
\text{subject to} \quad & g_j(\mathbf{x}) \le c_j \qquad j = 1, ..., n_j \\
& x_i^L \le x_i \le x_i^U \quad i = 1, ..., n
\end{aligned}
\tag{2.31}
$$

where $f(\mathbf{x})$ is an objective function, $g_j(\mathbf{x})$ are constraints and x_i are the design variables. OptiStruct has various methods for achieving this which are selected automatically depending on the type of problem. The methods used and the situations in which they are usually selected are described here.

2.4.1 Design Variables

Topology Optimisation

Design variables for topology optimisation are defined using the density method, also known as the Solid Isotropic Material with Penalisation (SIMP) model (Bendsoe 1989), which relates the stiffness of an element directly to the relative density of that element:

$$
E_i = \rho_i^p E^0 \; ,
\tag{2.32}
$$

where E_0 is the material properties of a given material and ρ_i are the relative densities of each element, and therefore the design variables. p is the penalisation factor, which is greater than one in order to penalise intermediate densities.

Shape Optimisation

For shape optimisation, design variables must be related to nodal coordinates of the finite element mesh. This is achieved using a perturbation vector approach which interpolates shape changes at the boundaries to nodal displacements in the interior mesh:

$$\mathbf{x}_{nodes} = \mathbf{x}^0_{nodes} + \sum_{i=1}^{n} \mathbf{x_i} . \mathbf{PV}_i \quad , \tag{2.33}$$

where $\mathbf{x}_{nodes}$ is the vector of nodal coordinates, $\mathbf{x}^0_{nodes}$ the vector of nodal coordinates for an initial design; $\mathbf{x}$ and $\mathbf{PV}$ are design variable and perturbation vectors respectively.

2.4.2 Responses

In topology optimisation the objective function used is typically the compliance. Compliance is the strain energy of the structure and can be considered as the inverse of the stiffness. It is defined as:

$$C = \Lambda_\varepsilon = \tfrac{1}{2} \mathbf{U}^T \mathbf{F} = \tfrac{1}{2} \mathbf{U}^T \mathbf{K} \mathbf{U} \quad . \tag{2.34}$$

For multiple load cases a weighted compliance can also be used:

$$C_w = \tfrac{1}{2} \sum_{k=1}^{N} W_k \mathbf{U}_k^T \mathbf{K}_k \mathbf{U}_k \quad , \tag{2.35}$$

where W are the weighting factors and N is the number of load cases that contribute to the weighted compliance. The other key response in topology optimisation problems is the volume fraction, which is defined as:

$$\text{volume fraction} = \frac{V}{V_{des}}, \quad \text{where} \quad V = \sum_{i=1}^{n} \rho_i v_i \quad , \tag{2.36-2.37}$$

and V_{des} is the volume of the designable space and v_i are the volumes of each element in the designable space. Responses for certain nodal displacements can be extracted easily from the displacement vector. Several other types of response can also be included such as stresses and buckling load factors, however there are some limitations on the use of these in topology optimisation. These limitations are discussed in Section 2.4.6.

2.4.3 Sensitivity Analysis

Responses for static analysis and their derivatives can be expressed as a function of the nodal displacements as follows:

$$f_j(\mathbf{x}) = \mathbf{Q}_j^T \mathbf{U}, \qquad \frac{\partial f_j}{\partial x_i} = \frac{\partial \mathbf{Q}_j^T}{\partial x_i} \mathbf{U} + \mathbf{Q}_i^T \frac{\partial \mathbf{U}}{\partial x_i} \quad , \qquad\qquad\qquad (2.38\text{-}2.39)$$

There are two methods of sensitivity analysis available in OptiStruct, direct and adjoint. In the direct method the stiffness equation $\mathbf{KU} = \mathbf{F}$ is used to derive:

$$\mathbf{K}\frac{\partial \mathbf{U}}{\partial x_i} = \frac{\partial \mathbf{F}}{\partial x_i} - \frac{\partial \mathbf{K}}{\partial x_i}\mathbf{U} \quad . \qquad\qquad\qquad (2.40)$$

In the adjoint method $\mathbf{U}$ is substituted for an adjoint vector $\mathbf{a}$ such that:

$$\mathbf{Ka} = \mathbf{Q} \; , \qquad\qquad\qquad (2.41)$$

and:

$$\frac{\partial f_j}{\partial x_i} = \frac{\partial \mathbf{Q}^T}{\partial x_i}\mathbf{U} + \mathbf{a}^T\left(\frac{\partial \mathbf{F}}{\partial x_i} - \frac{\partial \mathbf{K}}{\partial x_i}\mathbf{U}\right) \; . \qquad\qquad\qquad (2.42)$$

Most of the computational effort in the direct approach is used calculating the derivative of the displacements with respect to the design variable, which must be done for each design variable. In the adjoint method there is no such derivative, however the adjoint vector must be computed for each response. For this reason OptiStruct uses the direct method when the number of constraints is large and design variables small, and the adjoint method when the opposite is true (Altair 2009 ii).

2.4.4 Local Approximations

The problem in Equation (2.31) is solved by constructing and solving a series of approximate problems as described by Schmit and Farshi (1974). The approximations used in OptiStruct are convex (conservative) approximations (Haftka and Starnes 1976) and advanced approximations such as those described by Zhou (1989). The convex approximations of the responses is:

$$
\tilde{f}_j(\mathbf{x}) = f_i(\mathbf{x}^0) + \sum_{i=1}^{n} \alpha \frac{\partial f_j}{\partial x_i}(x_i - x_i^0), \qquad \alpha = \begin{cases} 1 & \text{if } \partial f_j / \partial x_i \geq 0 \\ x_i^0 / x_i & \text{otherwise} \end{cases}, \qquad (2.43)
$$

where $\tilde{f}_j(\mathbf{x})$ is the approximation of $f_j(\mathbf{x})$ and $\mathbf{x}^0$ is the current design point. The advanced approximations, generally used for sizing problems, introduce a set of geometrical properties as intermediate variables:

$$
\mathbf{Y}_i = \{Y_1, Y_2 ... Y_M\}_i^T, \qquad (2.44)
$$

where the size of $\mathbf{Y}_i$ will depend on the type of element. For instance for 2D shell elements:

$$
\mathbf{Y}_i = \{t, D, t_s, m_{ns}\}_i^T, \qquad (2.45)
$$

where t, D, t_s and m_{ns} are the thickness, bending stiffness, shear thickness and non-structural mass respectively (Zhou, Pagaldipti et al. 2004). These intermediate variables can be expressed as a function of the sizing variables $\mathbf{x}$. Then applying reciprocal approximations gives:

$$
\tilde{f}_j(\mathbf{x}) = \tilde{f}_j(Y(\mathbf{x})) = f_j^0 - \sum_{i=1}^{n} \frac{\partial f_j}{\partial y_i}(y_i^0)^2 \left(\frac{1}{y_i} - \frac{1}{y_i^0} \right). \qquad (2.46)
$$

2.4.5 Optimisers

As with many of the other options mentioned earlier, OptiStruct automatically selects the algorithm to solve the optimisation problem based on the problem type. The numbers of design variables and constraints often determine the best method to use.

2.4.5.1 Primal Feasible Directions Method

When the number of constraints exceeds the number of design variables the primal problem, Equation (2.31), can be solved using an implementation of the method of feasible directions based on the CONMIN algorithm of Vanderplaats (1973), see Zhou, Pagaldipti et al. (2004). Here, the following subproblem is solved:

$$
\begin{aligned}
\text{maximise} \quad & \beta \\
\text{subject to} \quad & \mathbf{d}^T \nabla f(\mathbf{x}) + \beta \leq 0 \\
& -\mathbf{d}^T \nabla g_j(\mathbf{x}) - \theta_j \beta \leq 0 \qquad j = 1,2,...,n_j \\
& -1 \leq \mathbf{d} \leq 1
\end{aligned}
\qquad (2.47)
$$

where θ_j determines how far $\mathbf{x}$ should move from the constraint boundaries. The primal design variables are updated via:

$$
\mathbf{x}^{new} = \mathbf{x} + \eta \mathbf{d} \; ,
\qquad (2.48)
$$

where η provides numerical damping. Therefore, assuming the initial set of design variables gives a feasible solution, The optimisation problem in Equation (2.47) ensures that $\mathbf{d}$ is in a feasible direction and is in a descent direction.

2.4.5.2 Optimality Criteria Method

Topology optimisation problems posed in the conventional 'minimum compliance with a volume fraction constraint' way shown below, can be solved using an Optimality Criteria (OC) method.

$$\text{minimise} \quad f(x_i) = \mathbf{U}^{\mathbf{T}}\mathbf{K}\mathbf{U} = \sum_{i=1}^{n} (x_i)^p u_i^T k_i^0 u_i$$

$$\text{subject to} \quad g_1(x_i) = \frac{V(x_i)}{V_{des}} = c_1 \tag{2.49}$$

$$\mathbf{K}\mathbf{U} = \mathbf{F}$$

$$0 < x^L \leq x_i \leq 1$$

Bendsoe and Sigmund (2004) and Sigmund (2001) give the following example of an updating scheme using the OC approach:

$$x_i^{new} = \begin{cases} \max\{(1-\zeta)x_i, x^L\} & \text{if} \quad x_i B_i^\eta \leq \max\{(1-\zeta)x_i, x^L\} \\ \min\{(1+\zeta)x_i, 1\} & \text{if} \quad \min\{(1+\zeta)x_i, 1\} \leq x^L B_i^\eta \\ x_i B_i^\eta & \text{otherwise} \end{cases} \tag{2.50}$$

where ζ is a move limit on the new solution and η is for numerical damping. B can be derived from the optimality conditions:

$$B_i = \frac{-\partial f / \partial x_i}{\lambda \, \partial V / \partial x_i} \tag{2.51}$$

where, in the same paper, the sensitivity of compliance is shown to be:

$$\frac{\partial f}{\partial x_i} = -p(x_i)^{p-1} u_i^T k_i^0 u_i \tag{2.52}$$

and λ is a Langragian multiplier that can be adjusted in an inner iteration loop until the volume fraction constraint is satisfied.

2.4.5.3   Dual Method with Sequential Quadratic Programming

Topology optimisation problems with different formulations and other classes of optimisation problem when the number of design variables exceeds the number of constraints can be solved using a dual approach based on the CONLIN algorithm of Fleury (1989), see Zhou, Pagaldipti et al. (2004). The solution to Equation (2.31) can be found in the following way:

$$
\begin{array}{ll}
\text{maximise} & l(r) \\
\text{subject to} & r_j \geq 0
\end{array}
\tag{2.53}
$$

where $l(r)$ is the dual function, r_j are the dual variables, and $l(r)$ can be found by minimising the Langragian function. If the objective and constraint functions are expressed as:

$$
\mathbf{c} = \{c_0, c_1, c_2, ..., c_m\} = \{f, g_1, g_2, ..., g_m\} ,
\tag{2.54}
$$

the convex approximations used in CONLIN give:

$$
\begin{array}{ll}
\text{maximise} & l(r) = \sum_{j=0}^{m} r_j \left[\sum_{+} \frac{\partial c_j}{\partial x_i} x_i(r) - \sum_{-} \frac{\partial c_j}{\partial x_i} \frac{1}{x_i(r)} - \bar{c}_j \right] , \\
\text{subject to} & r_j \geq 0
\end{array}
\tag{2.55}
$$

where:

$$
\bar{c}_j = \sum_{i=1}^{n} \left| \frac{\partial c_j}{\partial x_i} \right| x_i^0 - c_j(x_i^0) .
\tag{2.56}
$$

$\sum_{+}$ refers to a summation over terms where the derivative term is positive and $\sum_{-}$ where negative; x_i are defined in terms of the dual variables r_j as:

$$x_i = \begin{cases} x_i^L & \text{if } \quad b_i/a_i \leq \left(x_i^L\right)^2 \\ \left(b_i/a_i\right)^{1/2} & \text{if } \quad \left(x_i^L\right)^2 \leq b_i/a_i \leq \left(x_i^U\right)^2 \\ x_i^U & \text{if } \quad \left(x_i^U\right)^2 \leq b_i/a_i \end{cases} \quad , \tag{2.57}$$

where:

$$a_i = \sum_+ \frac{\partial c_j}{\partial x_i} r_j \, , \qquad b_i = -\sum_- \frac{\partial c_j}{\partial x_i} r_j \, , \tag{2.58-2.59}$$

and in the same paper the derivatives of the dual function are shown to be:

$$G_j = \frac{\partial l}{\partial r_j} = \sum_+ \frac{\partial c_j}{\partial x_i} x_i(r) - \sum_- \frac{\partial c_j}{\partial x_i} \frac{1}{x_i(r)} - \overline{c}_j \, , \tag{2.59}$$

$$H_{jk} = \frac{\partial^2 l}{\partial r_j \partial r_k} = \sum_+ \frac{\partial c_j}{\partial x_i} \frac{\partial x_i}{\partial r_k} + \sum_- \frac{\partial c_j}{\partial x_i} \frac{1}{x_i^2} \frac{\partial x_i}{\partial r_k} \, . \tag{2.60}$$

A solution to the problem in dual space can then be found using sequential quadratic programming (SQP). The quadratic subproblem takes the form:

$$\begin{array}{ll} \text{maximise} & \frac{1}{2} \mathbf{d}^T \mathbf{H} \mathbf{d} + \mathbf{d}^T \mathbf{G} \\ \text{subject to} & -1 \leq \mathbf{d} \leq 1 \end{array} \quad , \tag{2.61}$$

where $\mathbf{d}$ is the search direction. The problem is linearised with a set of initial values for r_j and the solution to Equation (2.61) is found. Dual variables are then updated in the same way as in Equation (2.48) via:

$$\mathbf{r}^{new} = \mathbf{r} + \eta \mathbf{d} \, . \tag{2.62}$$

The updated design variables are used to re-linearise the problem and the process is repeated until $\mathbf{d}$ reaches some predefined lower limit.

2.4.6 Additional Considerations for Continuum-Based Topology Optimisation

In order to overcome the difficulties associated with the use of stress constraints in topology optimisation, a single global stress constraint approach is adopted. This can be introduced to the optimisation problem in the following way (Duysinx and Sigmund 1998):

$$\left[\frac{1}{n}\sum_{i=1}^{n}\left(\max\left\{0,\frac{(\sigma_{VM})_i}{\rho_i^P\sigma_U}-\frac{\rho_L^{0.5}}{\rho_i}+\rho_L^{0.5}\right\}\right)^q\right]^{1/q}\leq 1 \ , \tag{2.63}$$

where σ_{VM} is the von Mises stress, σ_C is the global stress constraint and ρ_L is the lower limit on relative density. Bendsoe and Sigmund (2004) suggest that a value of 4 for q is suitable. This method does not guarantee that local stresses will be below the constraint value, but acts more like a maximum stress guideline. Even so, it is capable of producing reasonable results.

Due to the difficulties associated with calculating buckling modes discussed in Section 1.4.4, OptiStruct does not allow the inclusion of buckling constraints in topology optimisation. The only exception to this is for topology optimisation of shell structure with non-zero base thicknesses.

Limits on the dimensions of structural members are frequently imposed to aid manufacturability. Placing a lower limit on member size also controls the issue of checkerboarding and ensures mesh-independent solutions. This is achieved by using adaptive lower bounds on the elemental densities, as developed by Zhou, Shyy et al. (2001), in the following way:

$$\rho_i \geq \max\left[\rho_L,\rho_{jmax}-\left(1.0-\rho_{\min}\right)\text{dist}(i,jmax)/r_{\min}\right] \ , \tag{2.64}$$

where ρ_L is the predefined lower limit on density, $\rho_{\min}$ is the density below which is interpreted as void, dist($i,jmax$) is the distance between adjacent elements i and $jmax$, and r_{min} is the constraint on the minimum member radius. Here $jmax$ is the highest density element from the previous iteration that is adjacent to i, such that:

$$\rho_{jmax} = \max(\rho_k \mid k \in \Omega_i) \; .$$
(2.65)

This dynamic constraining of element densities means that no additional constraints are needed in optimisation problems and the only additional computations are the adjustments of the design variable constraints. The main disadvantage of this approach is that the boundaries of the members are defined by a density gradient changing from 1 to ρ_L which introduces additional elements with intermediate densities. To avoid this the optimisation problem is solved using an initial penalisation factor, p. The default value for this is 2.0 for shell and solid elements (Altair 2009 ii). The penalisation factor is then increased by 1.0 and the solution is recalculated, and finally the constraints on the density slopes in Equation (2.64) are relaxed and the solution is calculated once more (Zhou, Shyy et al. 2001).
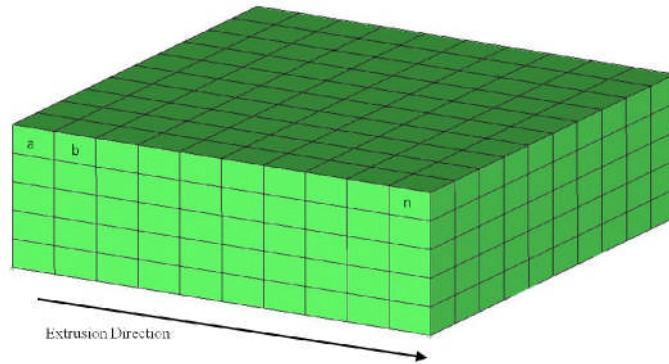
Figure 2.7 Extrusion direction and linked design variables resulting from extrusion constraints.

Extrusion constraints are applied by the specification of an extrusion direction. The constraint is then implemented simply by the linking of design variables so that the optimisation problem is reformulated as in Zhou, Fleury et al. (2002):

minimise $\quad f(\boldsymbol{\rho})$

subject to $\quad g_j(\boldsymbol{\rho}) \le c_j \qquad\qquad\qquad j = 1,...,m \qquad$, (2.66)

$\qquad\qquad (\rho_L \le \rho_a = \rho_b = ... = \rho_n \le 1)_k \qquad k = 1,...,n_k$

where n_k is the number of sets of elements aligned with the extrusion direction. A useful

by-product of this implementation is the significant reduction in the number of independent design variables

2.5 Conclusion

The variety of methods for structural optimisation used in this research are described in this chapter. Many of these methods are selected automatically and are dependent on the type of optimisation problem, number of design variables and number of constraints. There are also a number of manufacturing constraints available to aid the design process. The wide variety of tools available make it advantageous for the range of optimisation problems involved in finding optimal structural layouts of entire aircraft, as is intended in this thesis. Structural responses required in the optimisation problems can be calculated using finite element analysis and aerodynamic loadings on an aircraft can be calculated using the finite volume method of computational fluid dynamics. These methods of analysis and optimisation are applied to a Blended Wing Body UAV in order to find the optimal layout of its structural architecture, the results of which are presented in subsequent chapters.

Chapter 3

External Flow Analysis using CFD for Calculation of Flight Loads

Chapter 2 introduced the analysis and optimisation tools used in this investigation. A conceptual aircraft design on which to apply these tools was also proposed,. This chapter presents the results from analysis of the external flow over the aircraft. Firstly a numerical model of the flow is developed and preliminary analysis is performed. This is followed by a parameter study, investigating the effect of mesh density on global metrics, such as lift and drag. A suitable mesh size is selected and used in the development of a series of models, with the aircraft at varying angles of attack. Lift curves are generated to determine the stall angles of the aircraft's wing, and an angle of attack is chosen that provides both bending and torsional forces on the aircraft, without the wing stalling. In order to derive the necessary total force on the aircraft, an appropriate velocity is calculated for this angle of attack. Pressure loads from this configuration are interpolated onto a finite element model of the aircraft, to be used for structural optimisation in the subsequent chapters.

3.1 Preliminary Analysis and Mesh Dependency Study

In order to calculate the pressure distributions on the aircraft, a CFD model of the UAV was developed. Initially the UAV is positioned with no angle of attack (AoA) within a domain that extends five times the semi-span upstream and ten times the semi-span downstream, as shown in Figure 3.1. The size of the flow domain is based on earlier studies in which the domain size was gradually increased until there was no longer a noticeable effect on the aircraft's lift and drag. For simplicity, the engines intakes and exhausts are incorporated into the aircraft's wetted surface, shown in red in Figure 3.2. A finite volume mesh is generated using unstructured tetrahedral cells in the area closely surrounding the aircraft, to allow for the complexities of the geometry, along with a prismatic boundary layer mesh 6 cells thick on the aircraft's wetted surface. Structured hexahedral cells are then used to define the remaining flow domain.
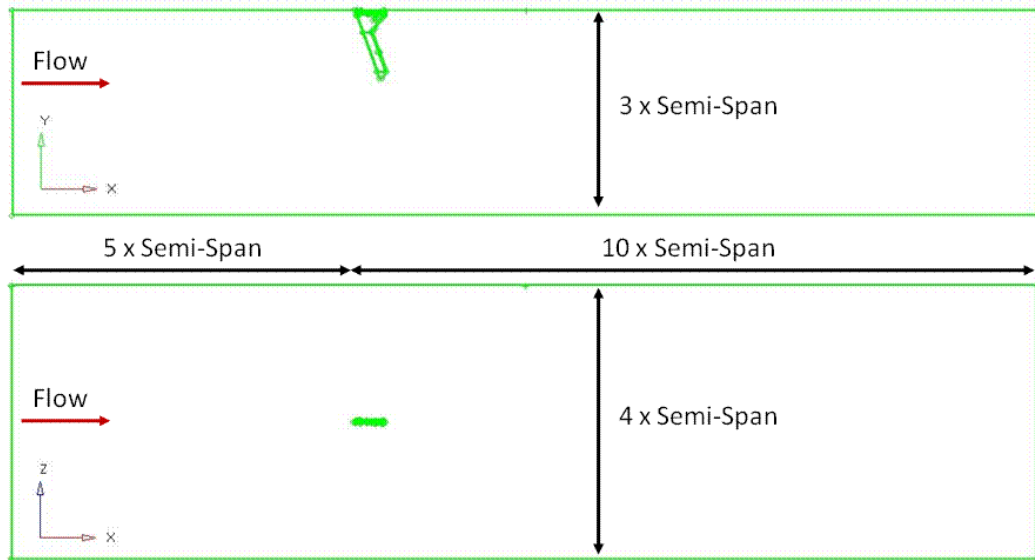
Figure 3.1 Top-down (top) and side (bottom) views of the flow domain used for CFD analysis of the external flow over a UAV.
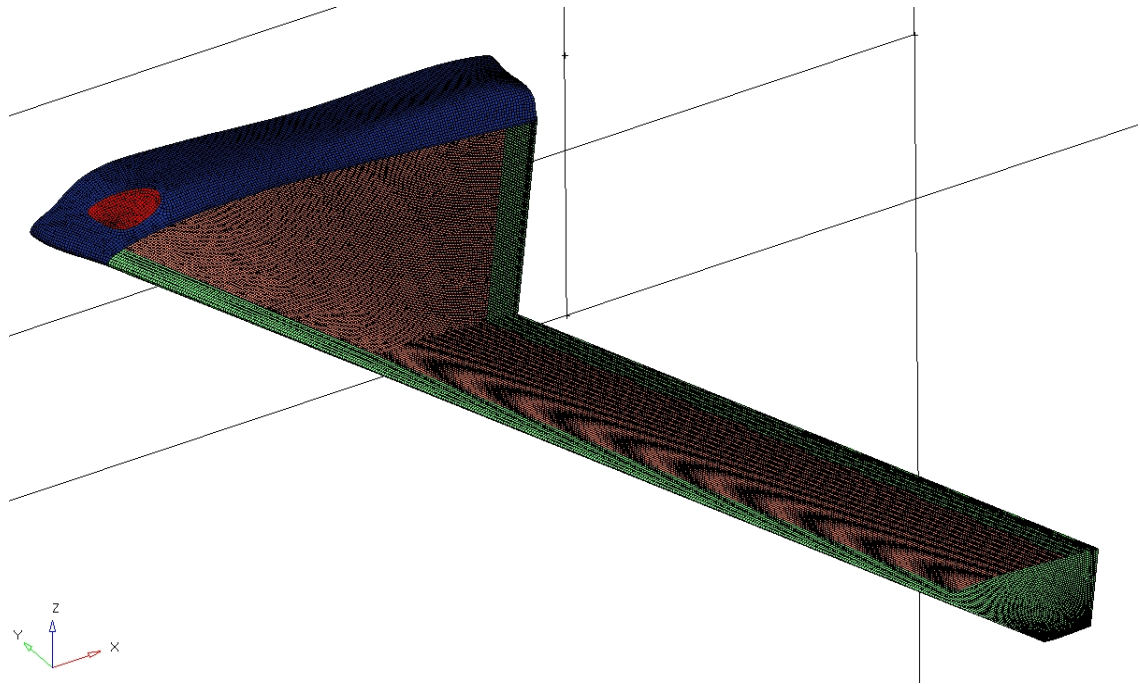
Figure 3.2 CFD mesh of the wetted surface of a BWB UAV.

The boundary conditions applied to the CFD model are shown in Figure 3.3 and given in Table 3.1. No-slip conditions are applied at all walls. Turbulence boundary conditions at the velocity inlet are calculated based on the hydraulic diameter of the boundary, with the Fluent default value of 10% used for turbulence intensity. The large solution domain ensures the flow is fully developed before reaching the UAV so a highly accurate choice of the turbulence boundary conditions is not essential. The flow is assumed to be incompressible and isothermal so temperatures at the boundaries need not be defined. Flow analysis is performed using the commercial CFD software Fluent (ANSYS 2009). The QUICK scheme is used for interpolating flow variables at cell faces. Turbulence is modelled using the single transport equation Spalart-Allmaras model and solutions obtained using the iterative SIMPLE algorithm. These approaches are discussed in detail in Section 2.2.
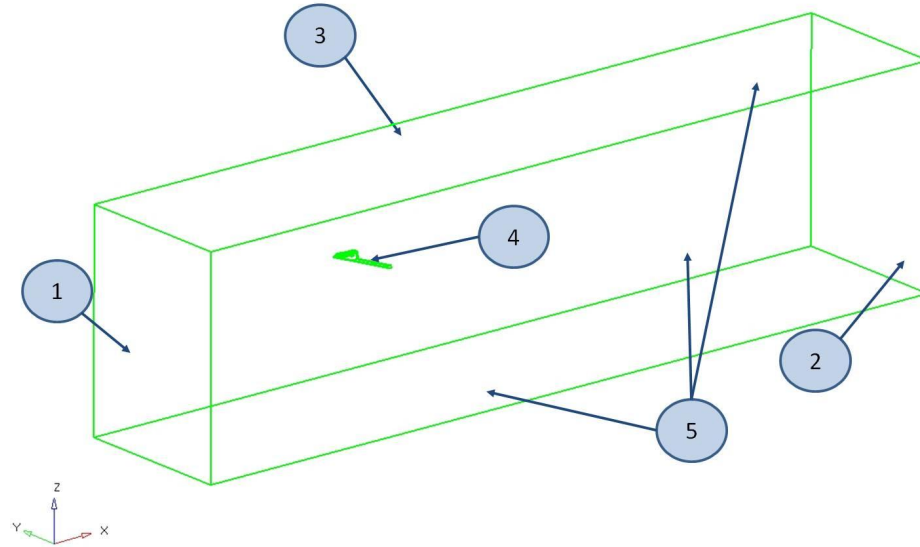
Figure 3.3 Boundaries of the flow domain, with numbers referring to the boundary conditions summarised in Table 3.1..

Table 3.1 Boundary conditions applied for preliminary flow analysis.

Boundary	1	2	3	4	5
Type	Velocity Inlet	Pressure Outlet	Symmetry	Wetted Surface	Walls
Value	100 m/s	101325 Pa	N/A	No-slip	Zero-shear
Direction	(1 0 0)	N/A	N/A	N/A	N/A

Lift, drag and pressure are non-dimensionalised in order to compare CFD results for varying upstream velocities. This is achieved using coefficients which are calculated via:

$$L = \tfrac{1}{2}\rho v_\infty^2 A C_L, \qquad D = \tfrac{1}{2}\rho v_\infty^2 A C_D, \qquad p - p_\infty = \tfrac{1}{2}\rho v_\infty^2 C_p, \qquad (3.1\text{-}3.3)$$

where L, D and p are the lift, drag and pressure respectively, C_L, C_D, C_P are their respective coefficients and ∞ denotes an upstream value. A is a reference area, which for an aircraft is given by the planform area. The pressure coefficients on the UAV's wetted surface are shown in Figure 3.4. From preliminary analysis, areas of high pressure can be seen to exist along the leading edge of the wing, and more so on the nose of the aircraft. Most of the aircraft's surface has a negative pressure coefficient as the flow is

accelerated over it. A region of very low pressure also exists above the engine intakes, at the thickest point of the fuselage.
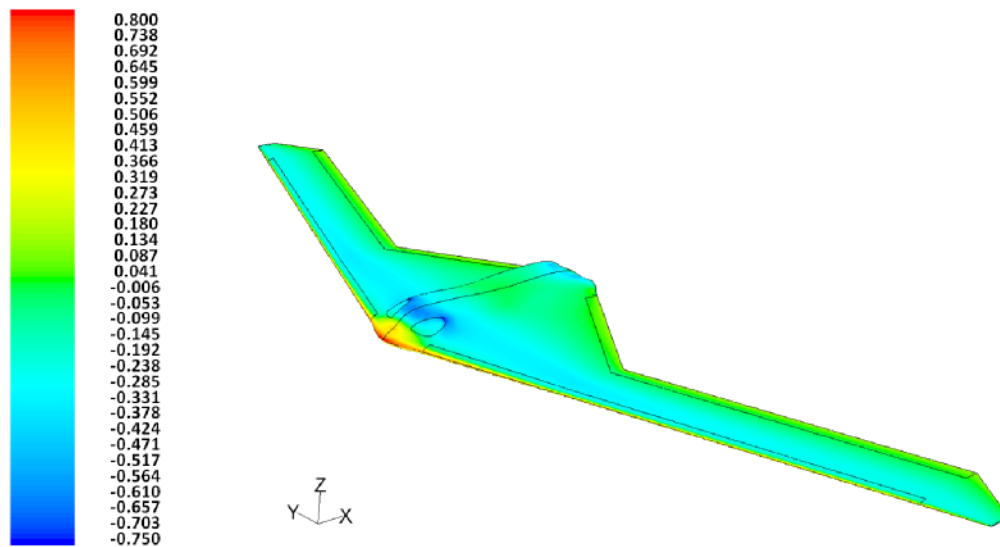
Figure 3.4 Contours of pressure coefficient resulting from preliminary flow analysis of a UAV flying at 100m/s with AoA=0.0.

The next stage in the development of a CFD model of the UAV was a study of mesh dependency. Five additional meshes were produced, maintaining the same angle of attack of the aircraft. Mesh sizes range from 227153 cells to 1073067 cells. In all cases a 6 cell boundary layer mesh is used with a growth rate of 1.2 and a first layer thickness approximately one quarter of the surrounding tetrahedron size. The same boundary conditions and solution methods from the preliminary analysis are prescribed, and the results of the mesh independency study are shown in Figure 3.5. At smaller mesh sizes there is significant variation in the lift and drag coefficients obtained however there is very little variation in these global quantities at mesh sizes above 800000 cells. Figure 3.6 shows that even for the coarser meshes, the pressure distribution is quite similar to that at higher mesh densities. Higher mesh densities may be required to properly capture flow phenomena such as wing tip vortices, however the purpose of this study is purely to extract aerodynamic loadings. For this reason mesh sizes of 800000 to 900000 are used subsequently, as these appear to be of an adequate fidelity for this purpose.
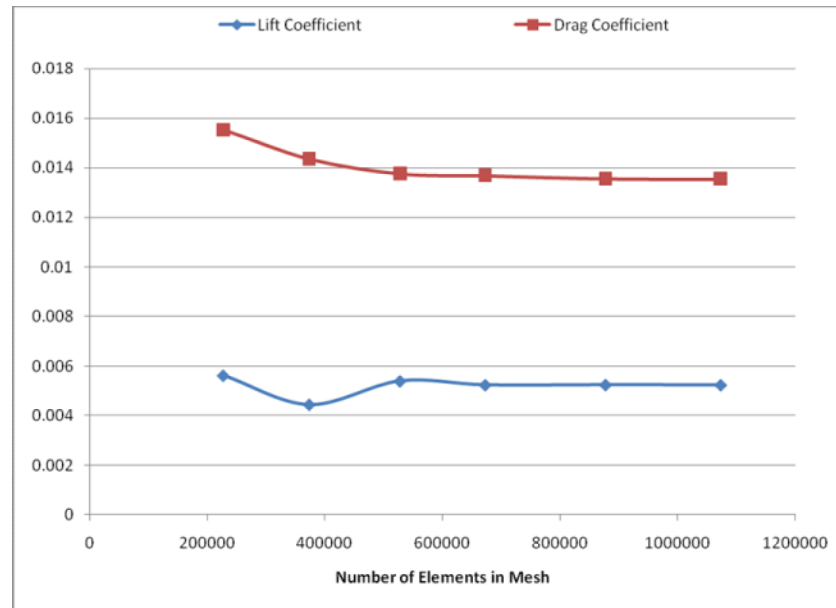
Figure 3.5 Effect of mesh density on a UAV's lift and drag coefficients, with sufficient mesh independence reached at 800000 cells.
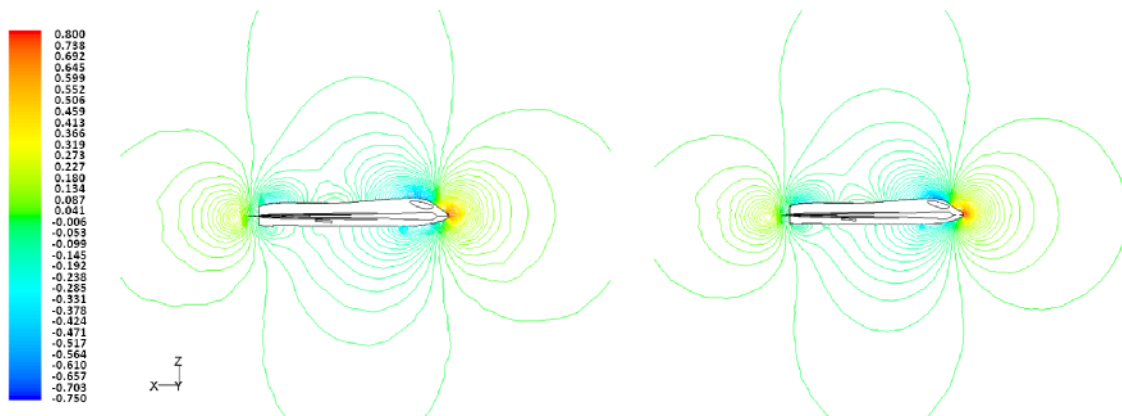
Figure 3.6 Contours of pressure coefficient on the symmetry plane for meshes containing 373388 cells (left) and 1073076 cells (right).
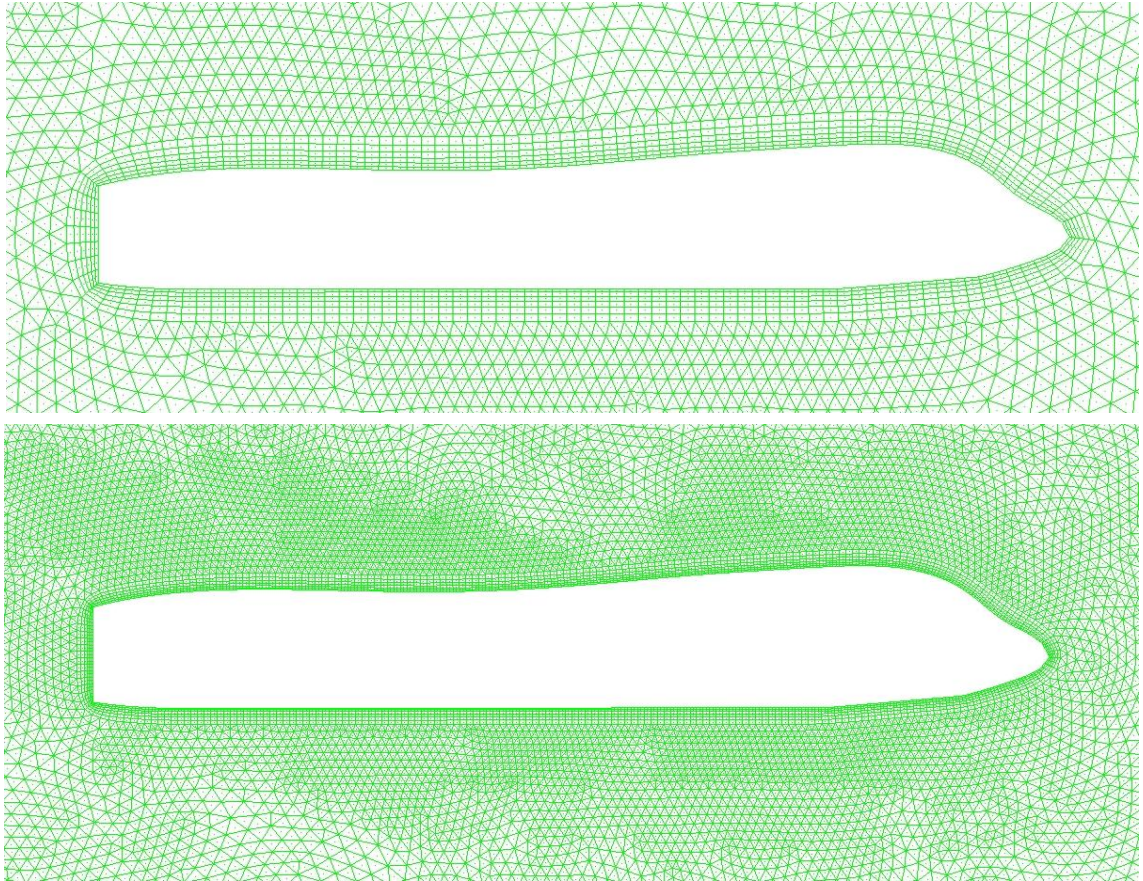
Figure 3.7 CFD meshes on the symmetry plane showing boundary layer mesh on the wetted surface transitioning into an unstructured tetrahedral mesh. Total cell count is 373388 (top) and 1073076 (bottom).

3.2   Calculation of Flight Loads

As discussed in Section 2.1.1, the primary load case to be used for structural optimisation is derived from a 3.5g 'pull out of a dive' manoeuvre. In order to determine the necessary angle of attack and velocity of the UAV to achieve this loading, a study of the effects of the UAV's angle of attack on lift and drag is performed. This is achieved by rotating the domain about the spanwise axis while keeping the UAV aligned with the global coordinate system, as shown in Figure 3.8. Analysis is performed with the same solver, numerical schemes and turbulence model used in the previous study. The angle of attack is varied from 0° to 20°. In each case the CFD meshes are rebuilt using mesh densities similar to those that achieved a sufficient level of mesh independence above. In this study an upstream velocity of 50m/s is specified at the inlet boundary. All other boundary conditions remain the same.
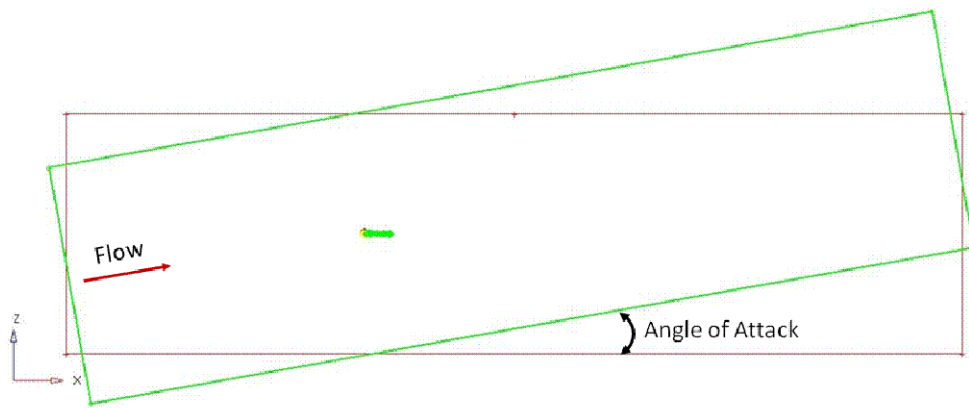
Figure 3.8 Side view of the flow domain, rotated to vary the UAV's angle of attack.

The effect of the angle of attack on lift and drag coefficients is shown in Figure 3.8. The lift coefficient varies linearly with angle of attack up to 7.5°. Beyond this the gradient of the lift curve begins to decrease and at 20° lift begins to decrease. Figure 3.10 illustrates the flow over two cross-sections of the wing at an angle of attack of 15°. In Figure 3.10 (left) the flow is attached over the entire chord length of this part of the tapered wing section. However in Figure 3.10 (right) the flow is separating from the upper surface of the un-tapered wing section at the quarter-chord, resulting in reversed and re-circulating flow. Figure 3.11 shows the same wing sections at a 20° angle of attack. Here the flow is entirely separated from the wing at both points, with large areas of re-circulating flow above the wing that explains the large increases in drag coefficient. Together, Figures

3.10-3.11 explain the gradual decreasing of the gradient of the lift curve. The wing appears to be stalling at different points along its span at differing angles of attack, so that as the angle is increased less of the wing is contributing to the lift.
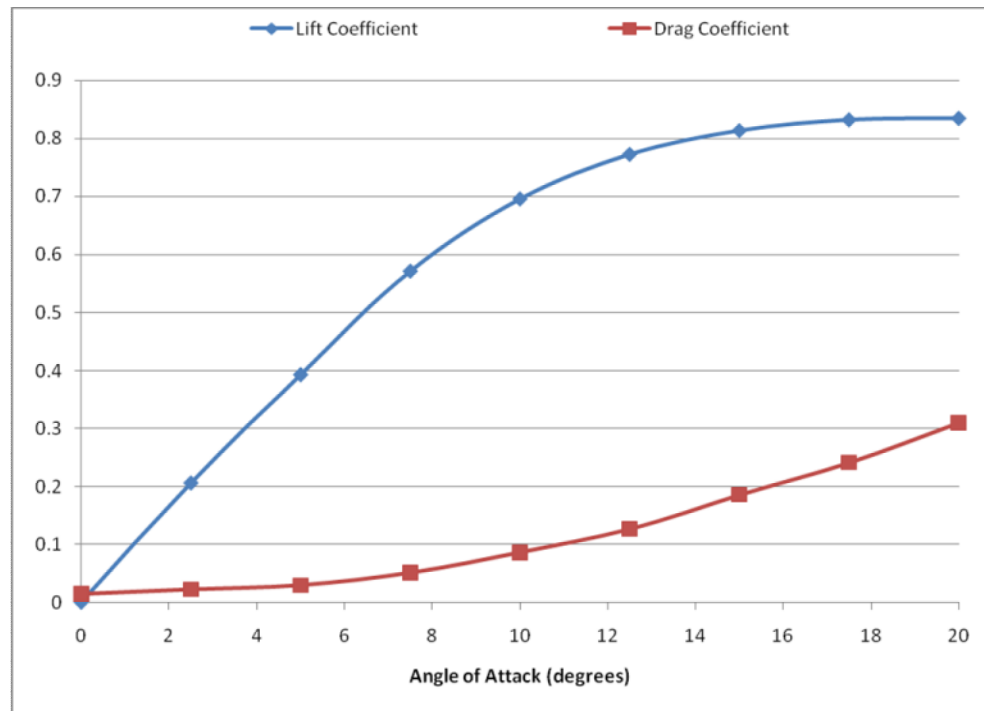
Figure 3.9 Lift and drag coefficient curves, showing increasing losses in lift-drag ratio at angles of attack greater than 10°.
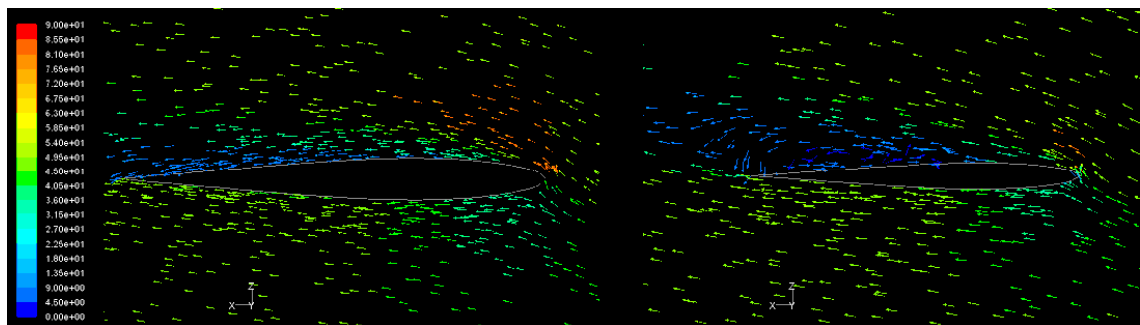
Figure 3.10 Velocity vectors of equal size, coloured by velocity magnitude (m/s), in planes located at the centres of the tapered (left) and un-tapered (right) wing sections. Flow is beginning to separate on the upper surface of the un-tapered wing section at AoA=15°.
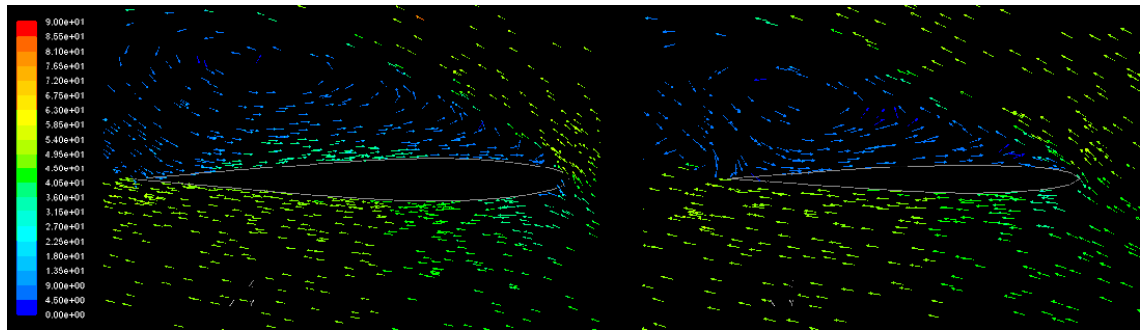
Figure 3.11 Velocity vectors of equal size, coloured by velocity magnitude (m/s), in planes located at the centres of the tapered (left) and un-tapered (right) wing sections. Flow is separated along the entire length of the wing at AoA=20°.

Before the wing begins to stall the relationship between lift and drag coefficients can be described using the drag polar equation, which for this aircraft is calculated as:

$$C_D = 0.014 + 0.108C_L^2 \ .$$

(3.4)

From the above data, an angle of attack of 10° was selected for use in calculating the flight loads for structural analysis and optimisation. At this angle the majority of the wing has not begun to stall, however it is high enough to provide significant torsional forces on the wing. The high loadings at the leading edge of the wing are demonstrated in Figure 3.12.
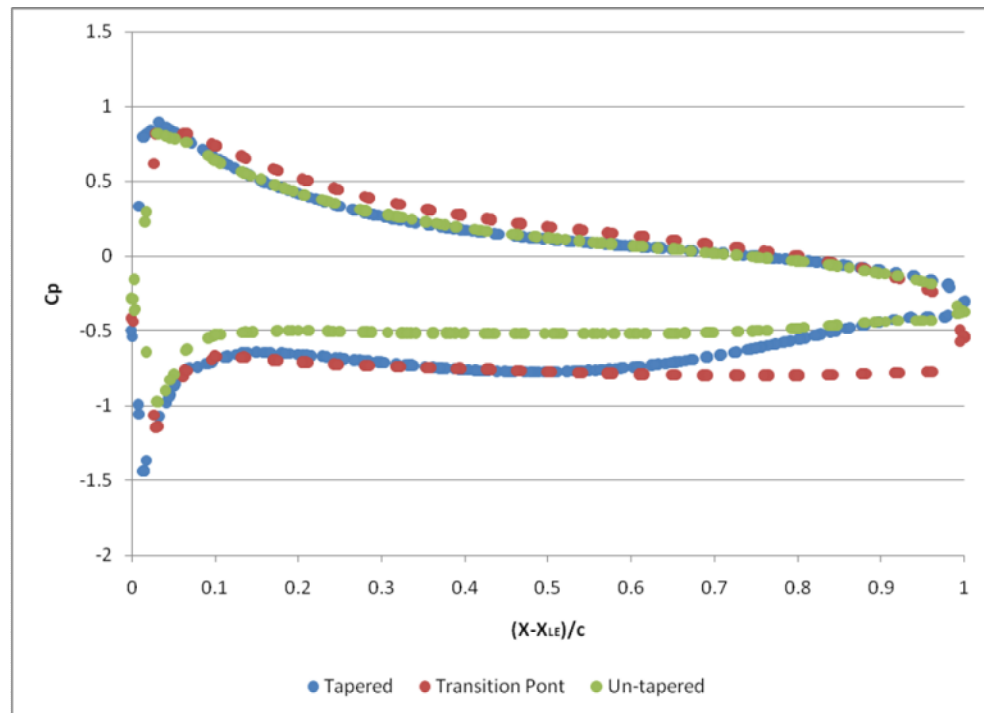
Figure 3.12 Coefficients of pressure taken at three cross sections of the UAV wing (centres of the tapered and un-tapered wing section, and transition point between the two) at AoA=10°, showing higher loadings towards the leading edge.

To produce the correct pressure distribution needed to acheive a lift equivalent to 3.5g at 10° AoA , a corresponding upstream velocity needs to be calculated. The required lift is calculated based on an approximation of the UAV's total design mass, also provided by QinetiQ Ltd. The lift coefficient is assumed to be constant with respect to velocity, so that the velocity can be calculated using Equation (3.1), giving a velocity of 78m/s. A CFD analysis was repeated for a 10° AoA using the new velocity inlet boundary condition. The pressure distribution on the UAV's wing resulting from this velocity and angle of attack are shown in Figure 3.13. The total lift of the aircraft is calculated to be equivalent to 3.52g, which is sufficiently close to the intended loading for use as a load case in the structural analysis and optimisation.
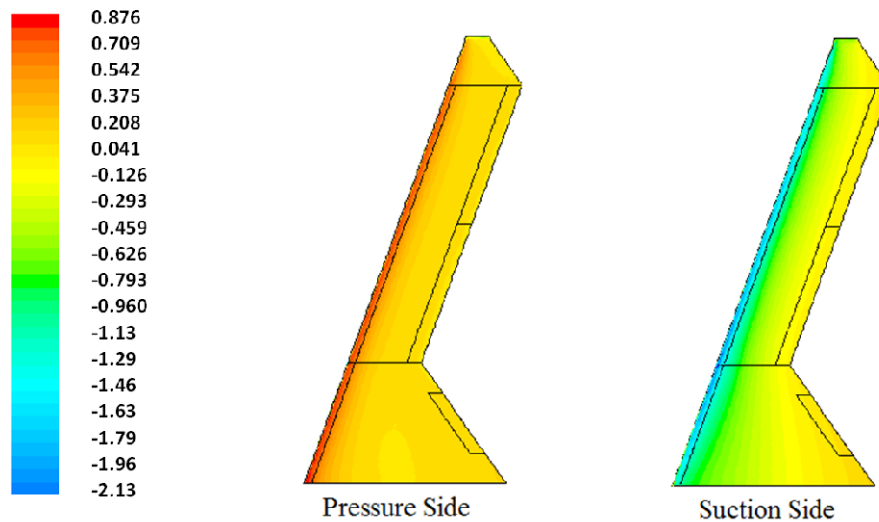
Figure 3.13 Contours of pressure coefficient on lower (left) and upper (right) surfaces of the wing for a UAV flying at 78m/s with AoA=10°.

Finally pressure loads from the CFD analysis have to be interpolated onto the finite element meshes used in structural analysis. Viscous shear stresses are ignored for simplicity as at this high angle of attack they are very small in comparison to the pressures. Figure 3.14 shows that viscous forces account for only 4.9% of the aircraft's drag, although it is noted that at lower angles of attack the viscous stresses would be more significant. Because of the large size of elements in the finite element mesh compared to the CFD mesh, pressures are interpolated using a search radius of 120mm corresponding to three times the average element size in the CFD mesh. This is constant for all finite element meshes in order to be consistent. At each element in the finite element mesh the three pressures in the CFD output file closest to the centroid of the element and within the search radius are found, and linear interpolation is used to calculate the pressure on that element (Altair 2009 ii). This results in a small loss in the fidelity of the pressure data. The total lift force generated by the interpolated pressures is recalculated and found to range from 3.62 to 3.67 times the UAV's mass, depending on the density of the finite element mesh. This level of inaccuracy and range is deemed acceptable for this application.
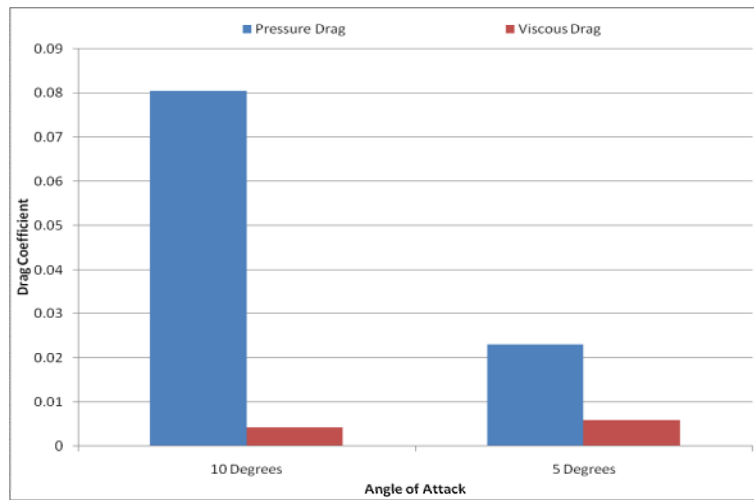
Figure 3.14 Contributions of pressure and viscous effects to the total drag coefficients for two angles of attack.

3.3   Conclusion

In this chapter a CFD model of a conceptual UAV design is utilised in order to calculate the pressure loads required for structural analysis and optimisation purposes. An initial finite volume mesh is produced and an appropriate combination of boundary conditions, numerical scheme, turbulence model and solution algorithm is proposed. A mesh dependency study is performed with the aim of finding the minimum mesh size required to predict reasonably the total lift and drag acting on the aircraft. The pressure distributions at different mesh sizes are also shown to be similar.

The effect of the aircraft's angle of attack is investigated. Different sections of the UAV wing are shown to have different stall angles as is common in aircraft with aft-swept wings (Wakayama and Kroo 1995). This results in the gradient of the lift curve slowly decreasing at increasing angles of attack rather than dropping off suddenly. A 10° angle of attack is selected for use in calculating load cases as this is the largest angle achievable without the wing beginning to stall. This high angle of attack exerts high bending and twisting loads on the wing. For this angle a corresponding velocity of 78m/s is calculated in order to achieve the required 3.5g of lift.

Finally a method for interpolating the pressures from the CFD model into the FEM of the UAV's structure is discussed. This involves linear interpolation of the pressures from three CFD nodes onto a single finite element. The resultant forces from the interpolated pressures are shown to be reasonably close to the original CFD values. The load cases are used and further developed in the following two chapters.

Chapter 4

Application of Topology Optimisation to Aircraft Architecture Design

Chapter 3 presented a study of the external flow over a conceptual UAV design. This study allowed the generation of aerodynamic pressure loads which are then applied to a structural model of the aircraft. In this chapter structural models of the UAV, as well as some simple wing sections, are used to investigate the potential uses of topology optimisation in determining the optimal structural architectures of aircraft. This begins with a series of parameter studies, in which the effects of mesh resolution, design constraints and SIMP penalisation factors are explored. A typical minimum compliance formulation of the topology optimisation problem is found to result in single spar structures that improve bending stiffness of the wing, with little consideration for torsional stiffness or maintaining the wing's cross-sectional shape. Therefore, several methods for overcoming this problem are proposed and evaluated.

4.1 Topology Optimisation of Wing Sections

An initial test case was developed in order to investigate the effects of design constraints, load cases and mesh densities in the finite element model. The test case used is shown in Figure 4.1 (left). It consists of a two metre, un-tapered section of an aircraft wing with no sweep. The cross-sectional profile is a NACA0012 aerofoil with a chord length of 1975mmm, truncated 200mm from the leading edge and 395mm from the trailing edge. A finite element model of the wing section was built using three dimensional solid elements to define the designable space within the wing. The wetted surface of the wing is represented by a layer of two dimensional shell elements around the exterior of the solid elements, on which aerodynamic pressure loads can be applied (Figure 4.1 (right)).
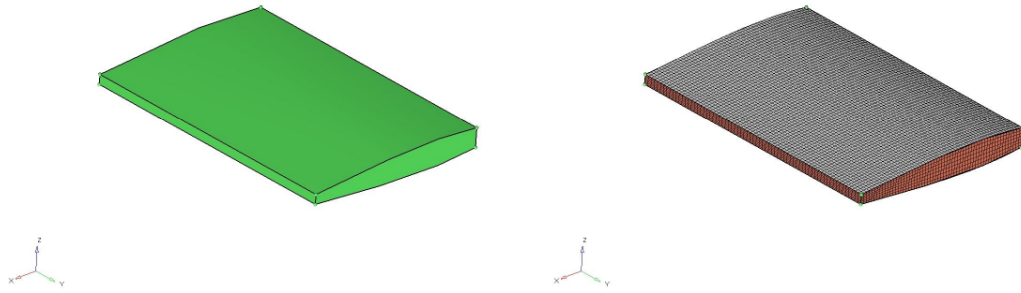
Figure 4.1 Wing section with no taper or sweep angle used as a test case (left). Finite element model of the wing section with resolution of 60x70x7 elements. (right).

Three distinct and relevant load cases were selected for an initial study of topology optimisation in this type of application. These load cases are spanwise bending, torsion and compression of a wing section. In all load cases the wing section is constrained in all degrees of freedom at its root. The topology optimisation problem is formulated as follows:

$$
\begin{aligned}
\text{minimise} \quad & \text{compliance} \\
\text{subject to} \quad & \text{volume fraction} \leq c_1 \\
& \rho_L \leq \rho_i \leq 1 \qquad i = 1, 2, ..., n
\end{aligned}
\qquad , \qquad (4.1)
$$

where ρ_i is the relative density of each solid element in the designable space, and c_1 is the maximum allowed volume fraction.

4.1.1 Wing Section in Bending

The first load case studied is the spanwise bending of the wing section. This was achieved by connecting all nodes at the free end of the wing section to a single point, midway between leading and trailing edges, using rigid elements. A 4kN point force is selected based on the mass of the aircraft and the length of the wing section, and is applied to this point in the z-direction, as indicated in Figure 4.2.
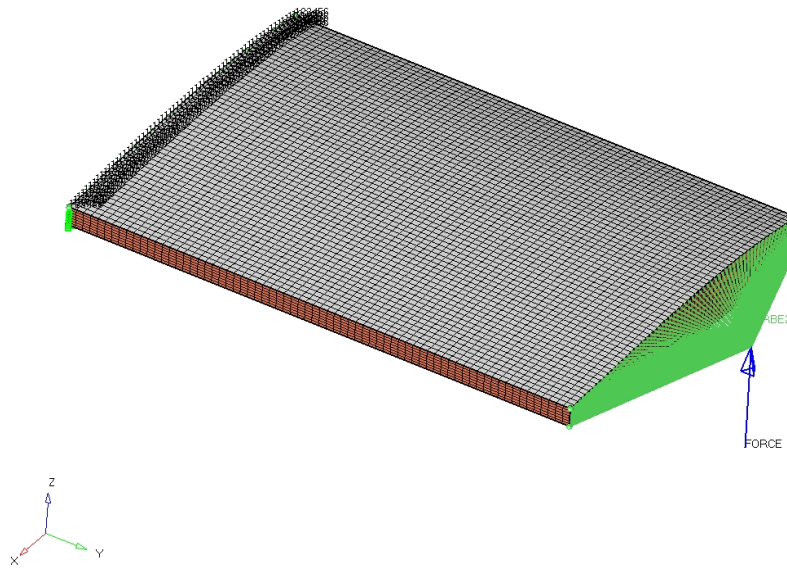
Figure 4.2 First load case, with a single bending force applied to the wing section.

The first study carried out on this test case is an investigation of the effects of mesh density on the optimised topology and final values of compliance. Five finite element meshes were produced. The number of 3D designable elements, and therefore the number of design variables, in each mesh vary from 5200 to 51000. Topology optimisation is performed using the formulation in (4.1) with c_1 equal to 0.25 and a value of 1.5 for the penalisation factor in the SIMP formulation (2.32). Figures 4.3 to 4.5 show that there is very little difference in the resultant material distribution for all mesh densities. All show that the majority of material is distributed at the wing section's upper and lower surfaces. This configuration would clearly maximise the wings second moment of inertia and therefore improve stiffness. The other thing to note from these results is the tapered profile of the distributed material, wider at the root and narrower at the tip. This agrees with what would be expected if the structure was to distribute stress

evenly along the wingspan, showing a clear link between minimised compliance and uniform stress distribution. Figure 4.6 shows the final value of compliance after optimisation for the five meshes. The value approaches convergence; however, as mentioned in Section 1.4.4, results of topology optimisation are rarely completely mesh independent without the application of some sort of minimum member size control.
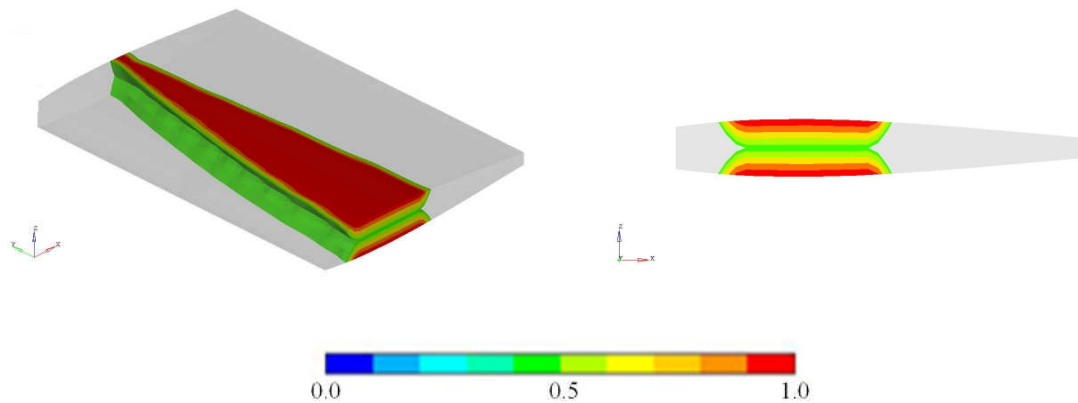
Figure 4.3 Contours of element density resulting from a 5200 elements mesh. Material distribution shows spar size decreasing from root to tip in isometric view (left).
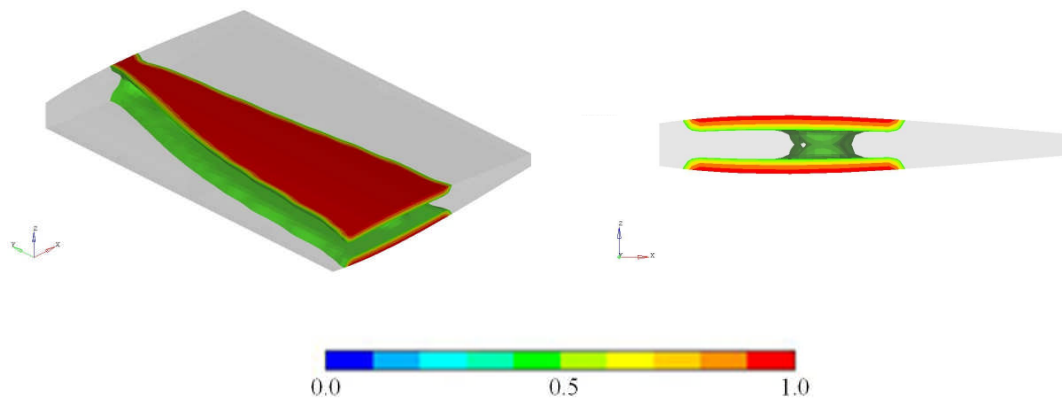
Figure 4.4 Contours of element density resulting from a 21500 elements mesh. Material distribution shows spar size decreasing from root to tip in isometric view (left).
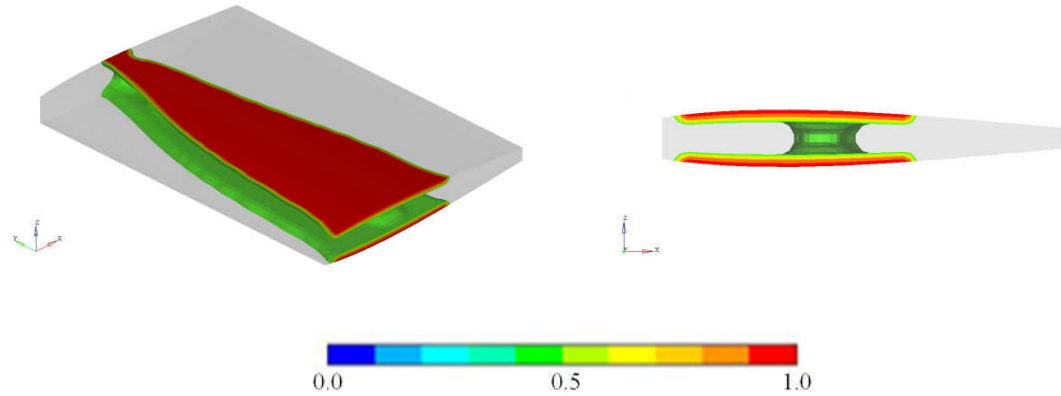
Figure 4.5 Contours of element density resulting from a 51000 elements mesh. Material distribution shows spar size decreasing from root to tip in isometric view (left).
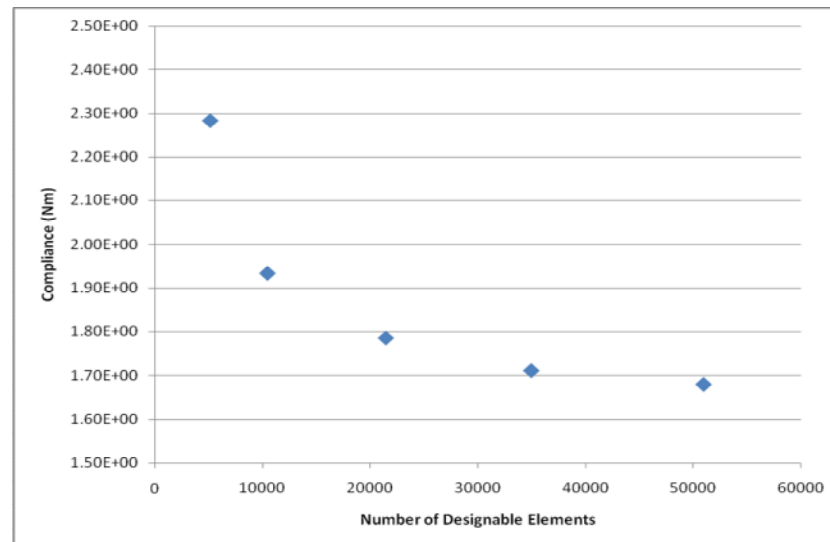
Figure 4.6 Decreasing compliance with increasing mesh resolution indicating mesh dependency of topology optimisation without minimum members size constraints.

Three additional studies were carried out on the spanwise bending test case. Firstly the value of c_1 is varied from 0.15 to 0.4 to investigate the effect this constraint has on the final structure. Figures 4.7 and 4.8 show that when this value is increased or decreased the size of the optimised structure increases or decreases accordingly. However there is little change to the topology. Note that though this is true for this basic structure, it may not be so for more complex structures with many more structural members. Figure 4.9 shows the reduction in compliance as volume fraction is increased.
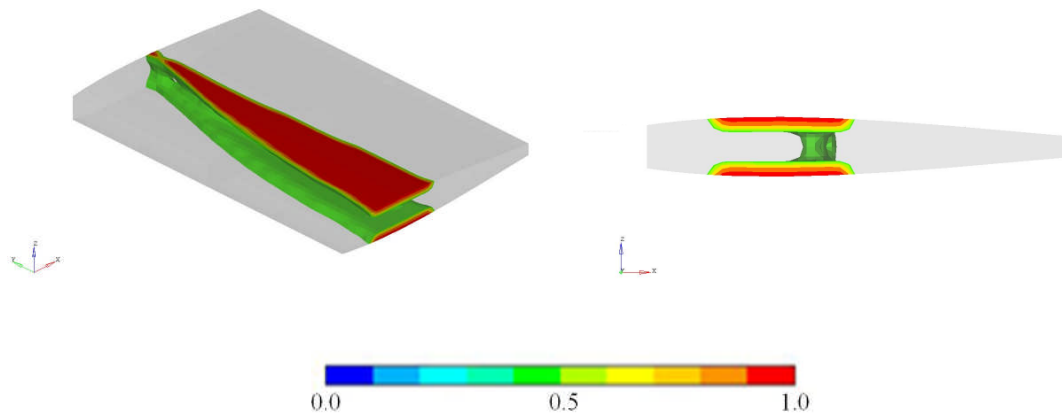
Figure 4.7 Contours of element density resulting from a 0.15 volume fraction constraint. Material distribution shows spar size decreasing from root to tip in isometric view (left).

Figure 4.8 Contours of element density resulting from a 0.35 volume fraction constraint. Material distributions shows larger spar, decreasing in size from root to tip.
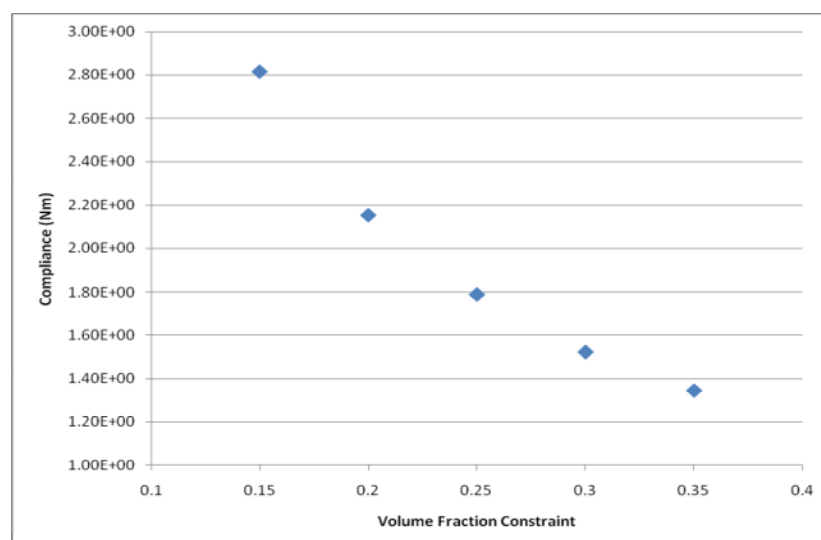
Figure 4.9 Optimised compliance reducing with higher allowable volume fractions. Higher volume fractions result in lower structural efficiency due to material being distributed further from the optimal locations.

Varying the penalisation factor in the SIMP formulation, from 1.0 to 3.0 is considered next. The first thing to note, in Figure 4.10, is a small reduction in the number of elements with intermediate densities when penalisation is increased from 1.5 (top left) to 2.5 (top right), which is exactly what penalisation is supposed to achieve. This reduction in intermediate density elements makes the material distributions easier to interpret as discrete designs and improves manufacturability. Figure 4.11 shows the increase in optimised compliance with increased penalisation factors. This is expected as there is a constraints of 0.1 on minimum relative element densities in the topology optimisation problem. Therefore, even with a structure that appears to have a completely 0-1 material distribution, all elements representing the void contribute a little to the volume fraction, but high penalisation makes any contribution of these elements to the global compliance negligible. A penalisation factor of 3.0 is found to result in sub-optimal designs (Figure 4.10 (bottom)) indicated by the sudden increase in compliance, shown in Figure 4.11. A penalisation factor of 2.0 is used in all subsequent studies unless otherwise stated. This value gives a near-0-1 material distributions without converging to sub-optimal solutions.
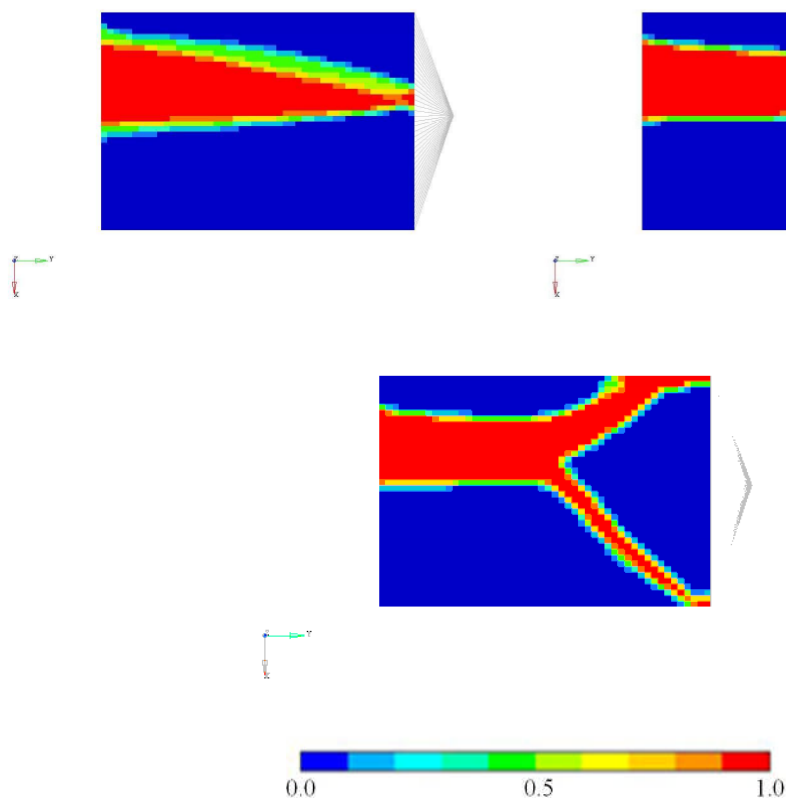
Figure 4.10 Contours of element density resulting from penalisation factors of 1.5 (top left) 2.5 (top right) and 3.0 (bottom), all showing the wing root on the right and tip on the left. High penalisation factors results in non-optimal designs.
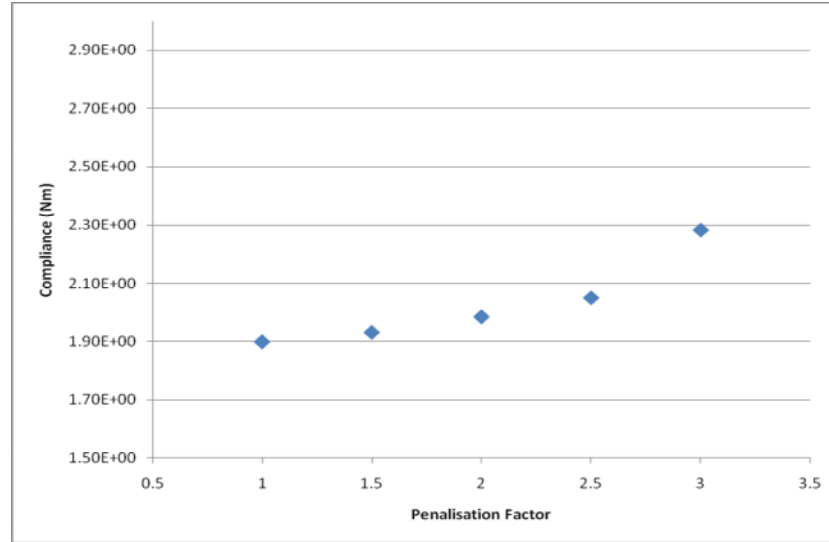
Figure 4.11 Increasing compliance at higher penalisation factors, with a sudden increase at p=3.0 due to non-optimal topology.

Finally, the implementation of stress constraints in topology optimisation is considered. As described in Section 1.4.4, the way in which stress constraints are applied to the topology optimisation problem makes them more like guidelines rather than actual constraints. The use of the test case enables the effectiveness of these constraints to be assessed. To achieve this, the problem is formulated in a different way. The usual constraining of volume fraction alongside the stress constraint could easily lead to infeasible designs, where the prescribed volume of material is insufficient to satisfy the constraint. Therefore the problem is redefined as such:

$$
\begin{aligned}
&\text{minimise} &&\text{volume fraction} \\
&\text{subject to} &&\text{displacement}_{\text{wing tip}} \le c_1 \\
& &&\text{stress} \le c_2 \\
& &&\rho_L \le \rho_i \le 1 &&i = 1,2,...,n
\end{aligned}
\qquad (4.2)
$$

This new formulation allows designs to be driven by the stress constraint assuming high values of c_1 and low values of c_2. In this case c_1 is maintained at 1mm while c_2 is varied from 2MPa to 3MPa. These values are selected to demonstrate the driving design constraint changing from stress to displacement, while maintaining a reasonable volume fraction, based on preliminary studies. A penalisation factor of 2.0 is also used. Figures 4.12 to 4.14 show the increasing size of structural members as the stress constraint is

tightened (left), and the reduction in stress concentrations are clearly demonstrated (right). Figure 4.15 shows that the way in which the stress constraints are implemented is a little conservative as the specified constraint is never quite reached. Also note that in this case, for c_2 of 2-2.5MPa, topology optimisation is driven by the stress constraint and the constraint on wing tip displacement is not reached. At a stress constraint of 2.75MPa the constraints are of similar importance, and at higher values tip displacement becomes the driving factor.
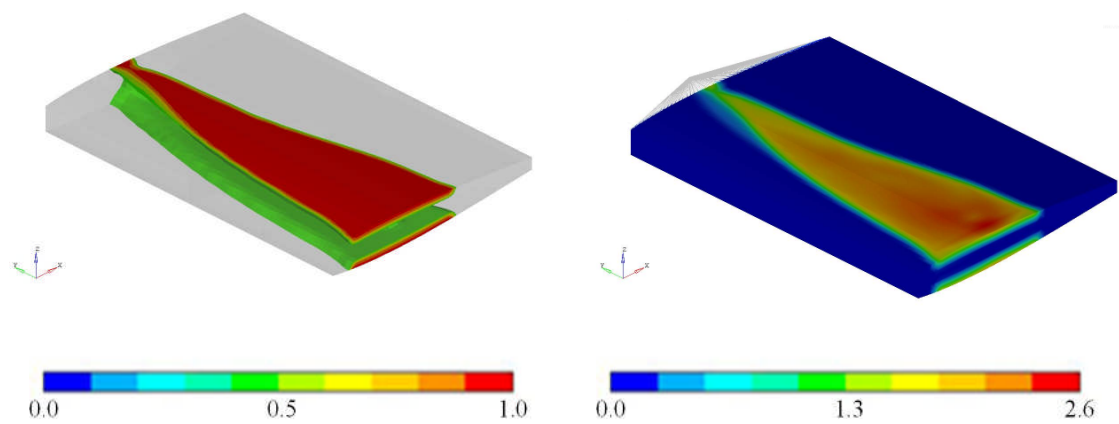
Figure 4.12 Contours of element density (left) and contours of von Mises stress (right) resulting from a 3MPa stress constraint. Material distribution shows spar size decreasing from root to tip.
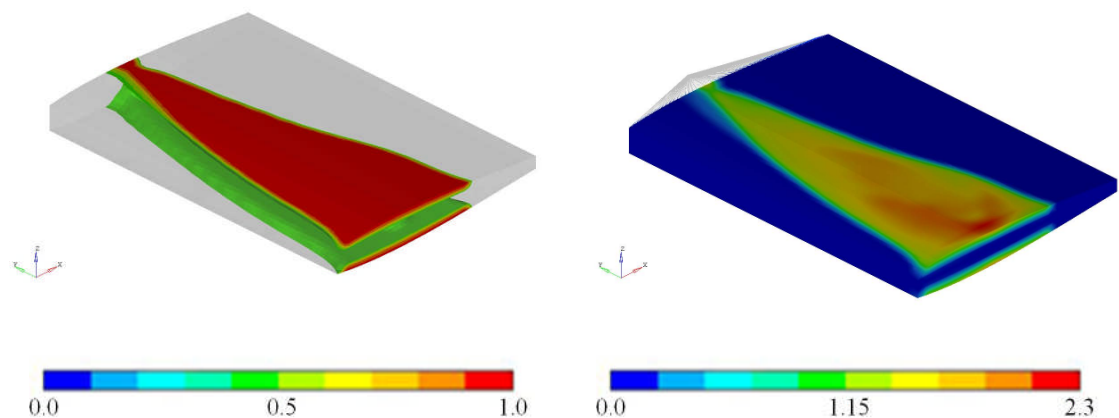
Figure 4.13 Contours of element density (left) and contours of von Mises stress (right) resulting from a 2.5MPa stress constraint. Material distribution shows spar size decreasing from root to tip.
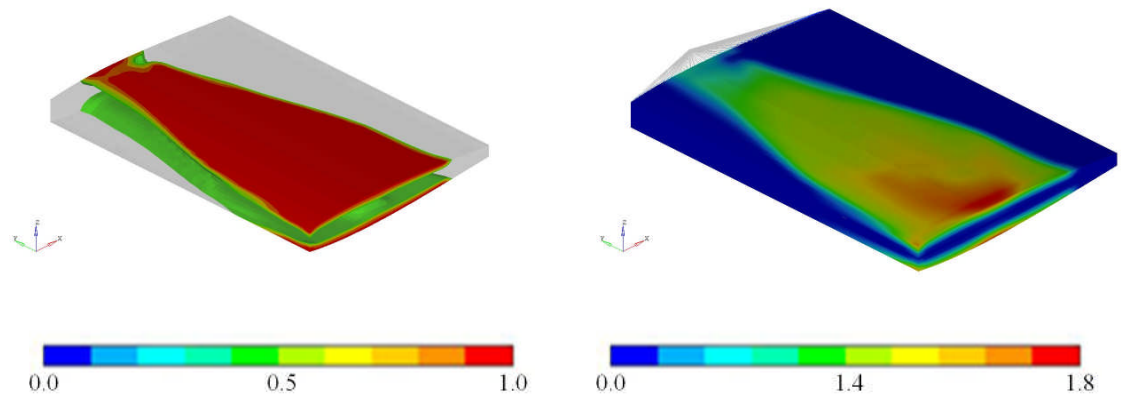
Figure 4.14 Contours of element density (left) and contours of von Mises stress (right) resulting from a 2MPa stress constraint. Material distribution shows spar size decreasing from root to tip.
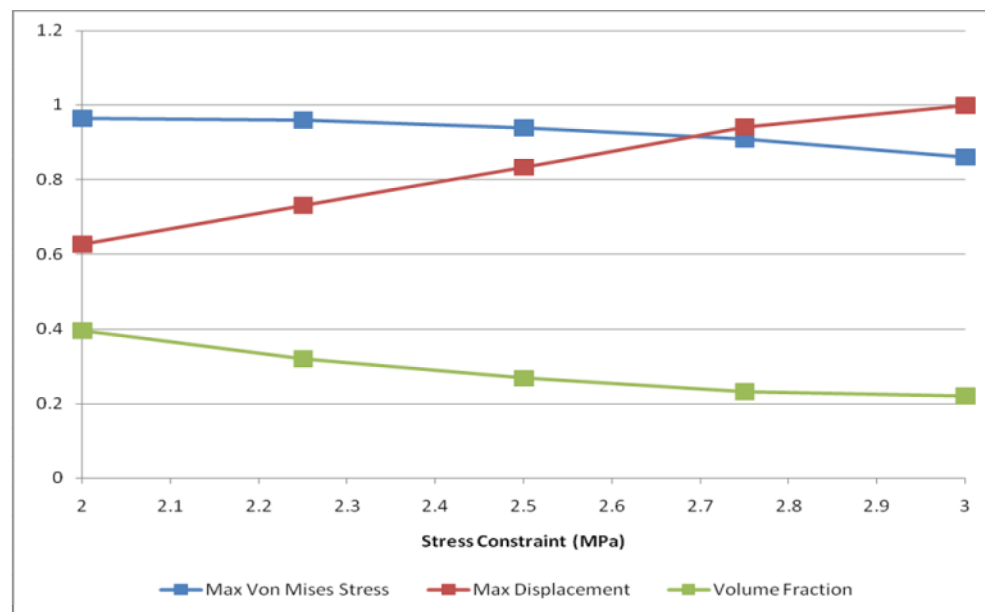
Figure 4.15 – Effects of stress constraints on maximum von Mises stress, displacements and volume fractions. Stresses and displacements shown normalised by their allowable values.

4.1.2 Wing Section in Torsion

The second test case investigates a wing section in torsion. This is achieved in a similar manner to the bending case. The nodes at the free tip of the wing section are joined to a point in space using rigid elements. However, this time a 4kNm moment is applied to the point about the spanwise axis, representing a similar magnitude of loading to the bending test case, as shown in Figure 4.16.
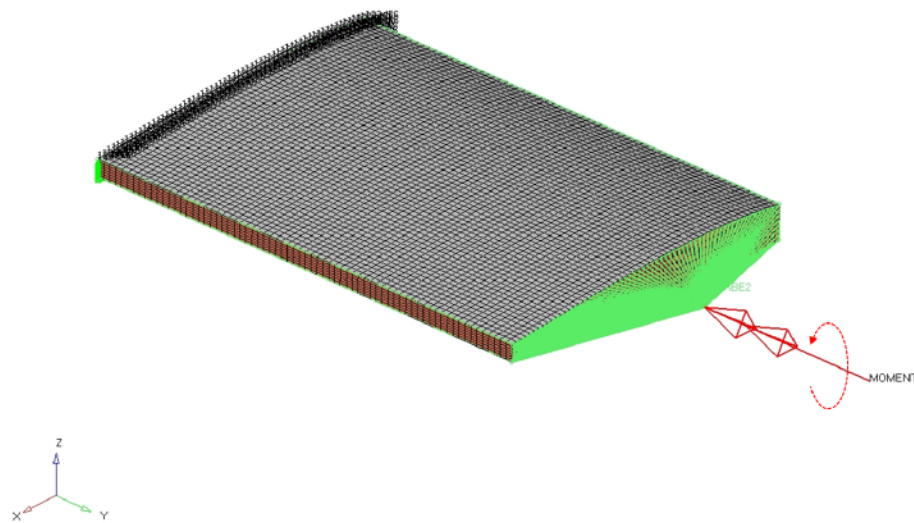
Figure 4.16 Second load case, with a single moment applying torsion to the wing section.

A mesh independency study was carried out using the same meshes used previously and a penalisation factor of 1.5. In this test case the mesh density required for a satisfactory level of mesh independency appears to be higher. At low mesh densities the topology of the optimised structures is noticeably different from those at higher densities (Figures 4.17 to 4.19). Despite this, designs appear to reach some level of mesh independency, at least as far as the topology of the structure is concerned, at approximately 21500 elements. In Figure 4.17 material is distributed at the leading and trailing edges and at the upper and lower surfaces. This is expected to increase the polar moment of inertia which would decrease compliance for this torsional loading. In Figures 4.18 and 4.19 the majority of material is positioned at the leading edge and upper and lower surfaces which is also expected for maximising torsional stiffness. However there appears to be diagonal spar structures developing to further reduce twisting of the wing section.
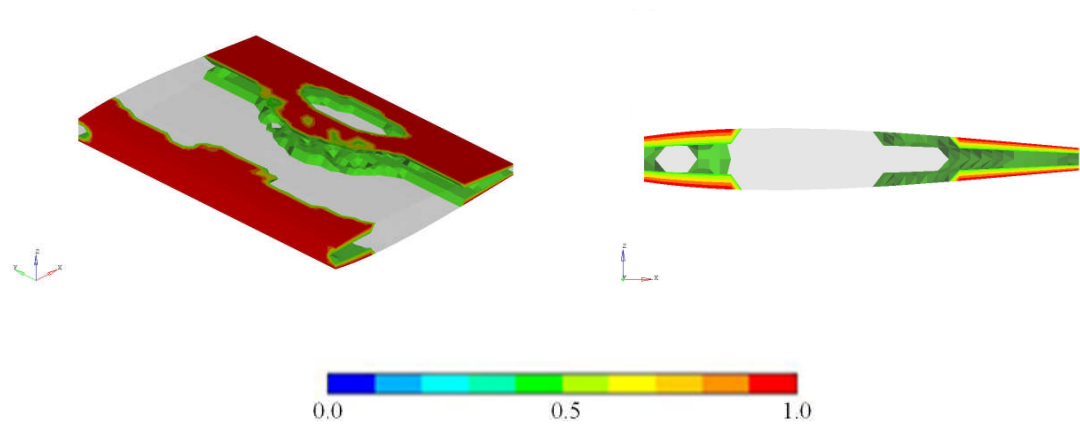
Figure 4.17 Contours of element density resulting from a 5200 element mesh.
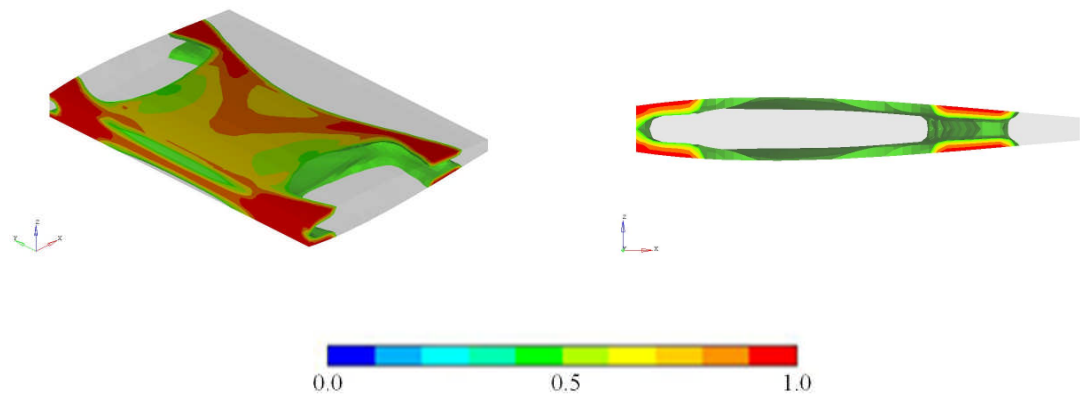
Figure 4.18 Contours of element density resulting from a 21500 element mesh.
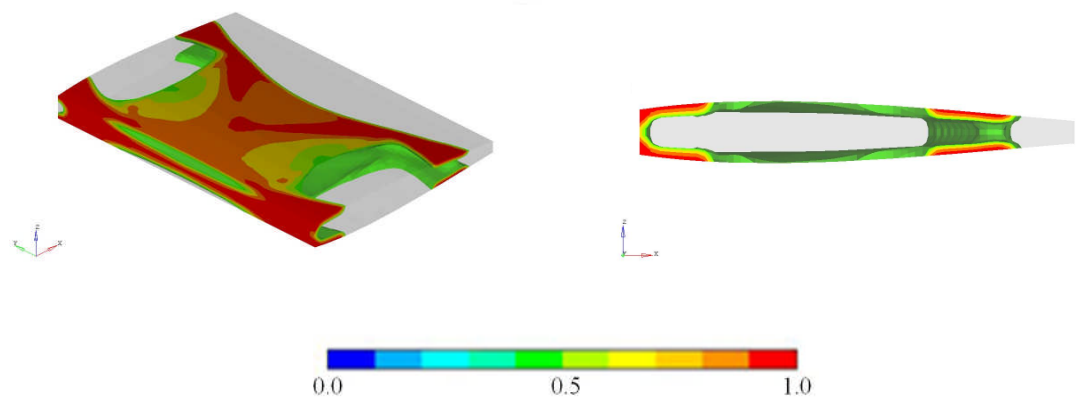
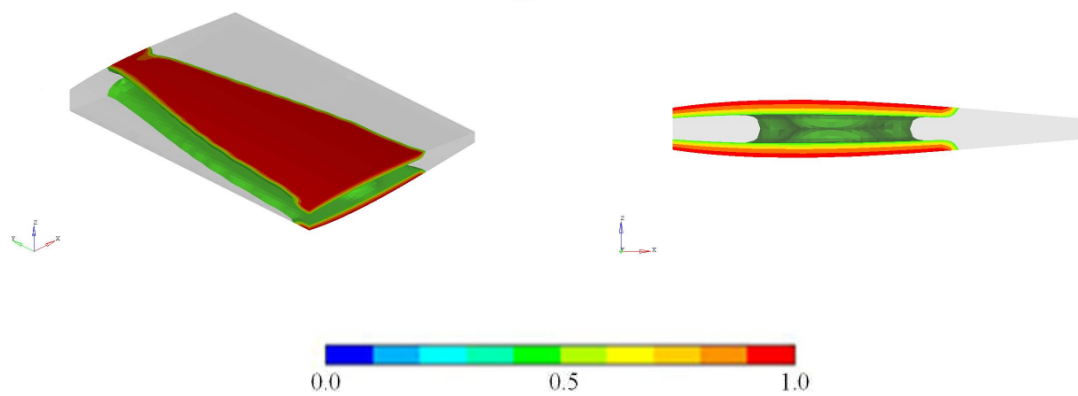**Figure 4.19** Contours of element density resulting from a 51000 element mesh.
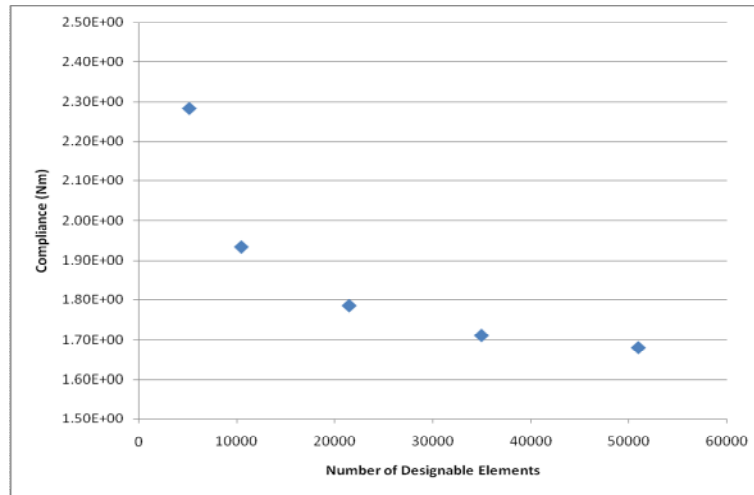
Figure 4.20 Decreasing compliance with increasing mesh resolution indicating mesh dependency of topology optimisation without minimum members size constraints.

Due to the large volume of elements with intermediate densities in some of the designs produced, the study of sensitivity to penalisation performed on the bending test case is repeated for the torsion case. As before, increasing penalisation results in reducing the use of intermediate element densities, giving a material distribution that is much easier to interpret as a manufacturable design, along with a corresponding increase in optimised compliance (Figures 4.21 & 4.22). Figure 4.21 shows that increasing penalisation factors cause further development of the diagonal spars that were appearing at lower values. It would appear that these diagonal structures are an alternative to a thick walled tube for improving torsional stiffness when mass restrictions are tight. All of the optimised topologies involve large volumes of material in one area. In order to try and produce designs with individual stuctural members a maximum member size control is added to the problem formulation:

$$
\begin{aligned}
\text{minimise} \quad & \text{compliance} \\
\text{subject to} \quad & \text{volume fraction} \leq c_1 \\
& \text{member size} \leq 250 \, \text{mm} \\
& \rho_L \leq \rho_i \leq 1 \qquad i = 1,2,...,n
\end{aligned}
\qquad . \qquad (4.3)
$$

The results of this combined with a penalisation value of 2.5 results in the distribution shown in Figure 4.23. Inclusion of this additional constraint in the problem results in an increase in the compliance of the optimised structure. However, at this stage it starts to become clear how the results from topology optimisation might be interpreted as

structural members such as spars and stiffeners.
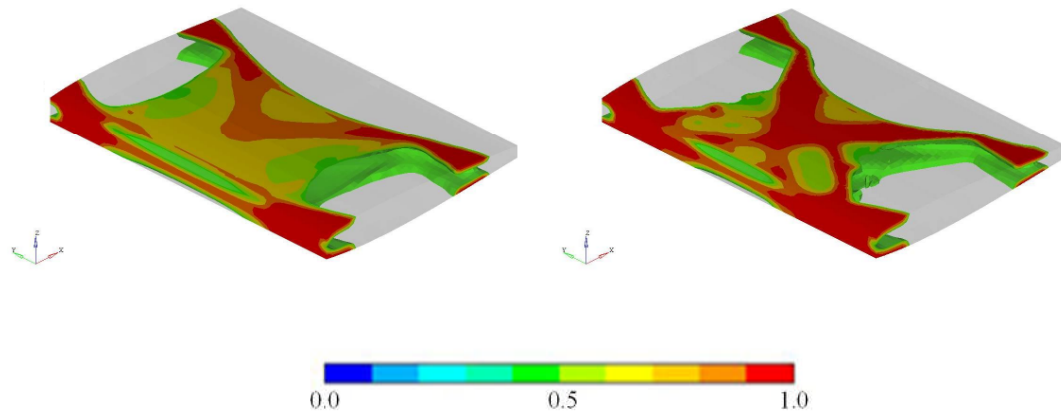
Figure 4.21 Contours of element density resulting from penalisation factors of 1.5 (left) and 2.5 (right).
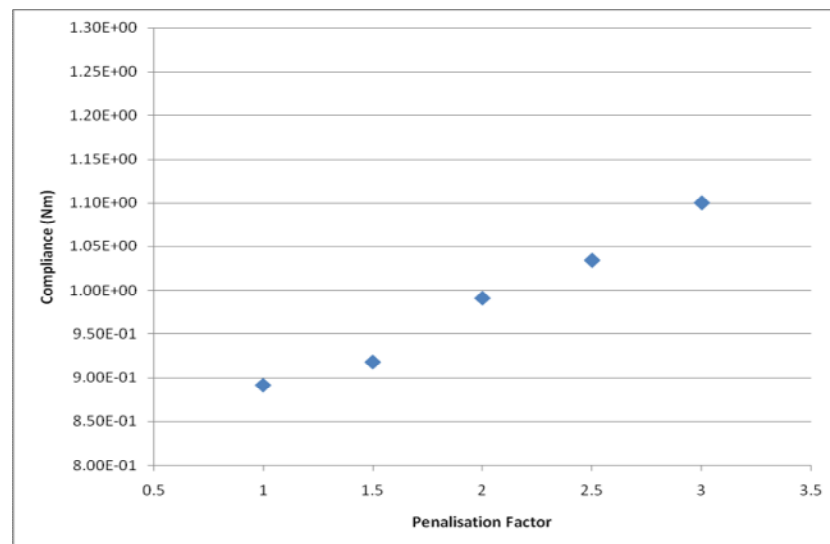
Figure 4.22 Increasing compliance at higher penalisation factors.
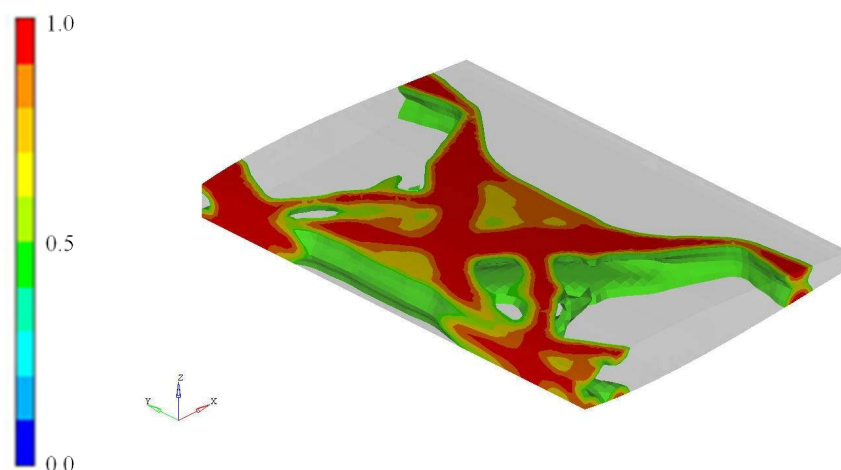
Figure 4.23 Material distributions resulting from the application of member size control and a

penalisation factor of 2.5.

The final study using this test case investigates the optimised topology's sensitivity to the wing section's length. Wing sections with lengths of 2m, 3m and 4m are used and the mesh density is kept constant for the three models. The penalisation is given as 2.5 with c_1 equal to 0.25 and no manufacturing constraints. Figure 4.21 shows the resultant material distributions for the 4m section, which can be compared to the 2m section in Figure 4.21 (right). The diagonal spars running from the trailing edge to leading edge maintain a similar orientation in all cases and therefore do not always connect opposite corners as they do in the 2m section.
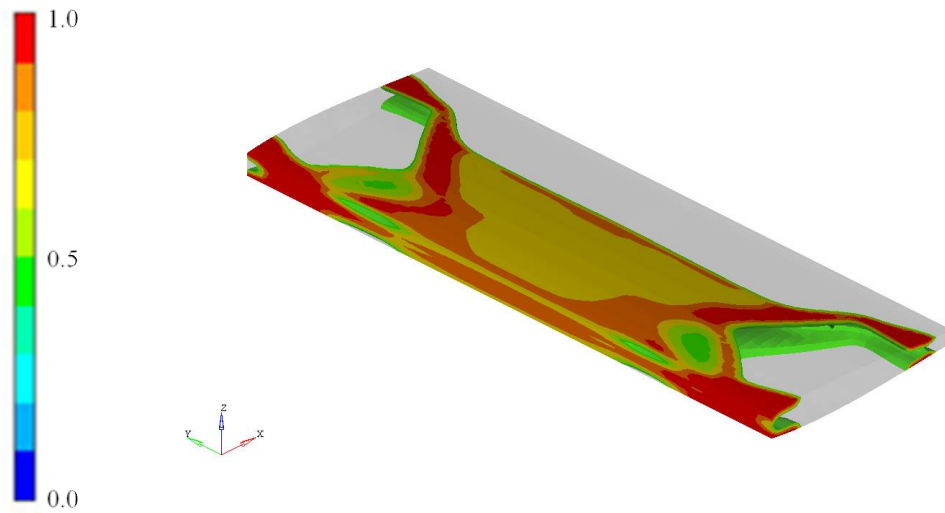
Figure 4.24 Contours of element density in a 4m wing section with a torsional loading.
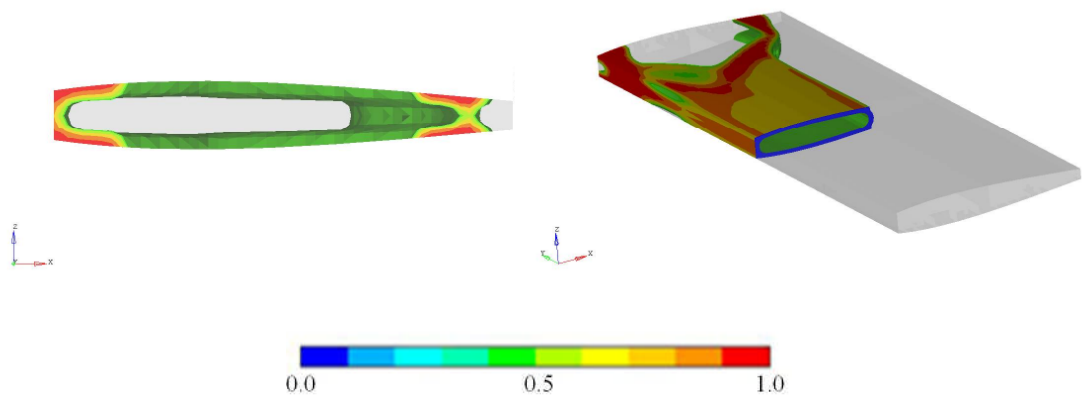
Figure 4.25 Contours of element density in a 4m wing section showing the attachment points for the diagonal members (left) and the central box structure (right).

4.1.3 Symmetrically Loaded Wing Section

The third load case involves examining the compression of the wing section due to pressure loading. In this case a rectangular cross section is used instead of the aerofoil section used previously. This allows the local deformation of the wing skin to be investigated without the influence of any bending or twisting of the wing in the minimum compliance formulation. The behaviour of the wing structure under this type of loading is of great importance, as the deformation of the wing's cross-sectional shape under pressure loadings will affect its aerodynamic performance. A rectangular section with dimensions 100mm x 100mm x 20mm is constrained in all degrees of freedom at the root with equal and opposing pressures loads applied to its upper and lower surfaces (Figure 4.26). It is important to note that this test case only considers changes in cross-sectional shape due to the pressure loads. Compressive brazier loads resulting from the global bending of the wing are not considered. The effects of such brazier loads are difficult to isolate as this type of loading is highly dependent on the internal structure of the wing, such as the location of ribs. As the internal structure is not yet known, these loads cannot be applied.
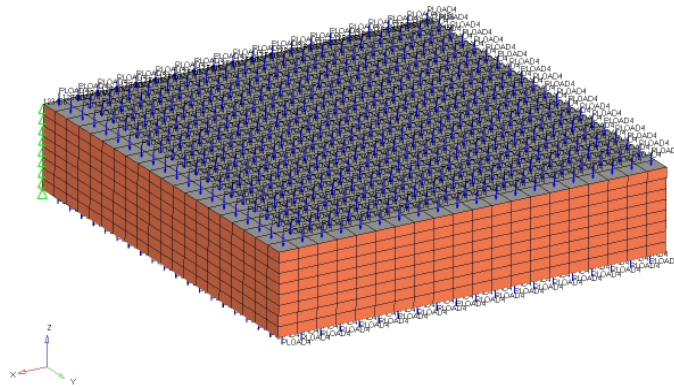
Figure 4.26 Symmetrically loaded finite element model, with equal and opposite pressure loads on upper and lower surfaces.

The topology optimisation problem is formulated as in the previous two test cases and with the same 0.25 constraint on volume fraction and a penalisation factor of 2.0. Initial computations are performed with 3200 designable elements. This combination of boundary conditions and problem formulation results in a seemingly random distribution of material within the design space. In order to avoid this, manufacturing constraints are used to try and achieve coherent structures. Firstly an extrusion

constraint is introduced in the *z*-direction. This results in the material distribution shown in Figure 4.27(left). It is clear that this result suffers from a problem similar to that of checkerboarding, as discussed in Section 1.4.4. Therefore, a checkerboarding constraint is applied to the problem. Topology optimisation with these two additional constraints results in the much more manufacturable structure shown in Figure 4.27 (right). A mesh independency study was then completed using this new formulation for mesh sizes from 3200 to 17150 elements. The topology of structures in this study remained the same as Figure 4.27 (right). Note that Figure 4.28 shows that with the checkerboard control, the compliance of the optimised design does not achieve the same minimum as it does without it. This highlights the need for manufacturing constraints as Figure 4.27 (right) is much more desirable than Figure 4.27 (left) for any real world application even though Figure 4.27 (left) is a less compliant design.
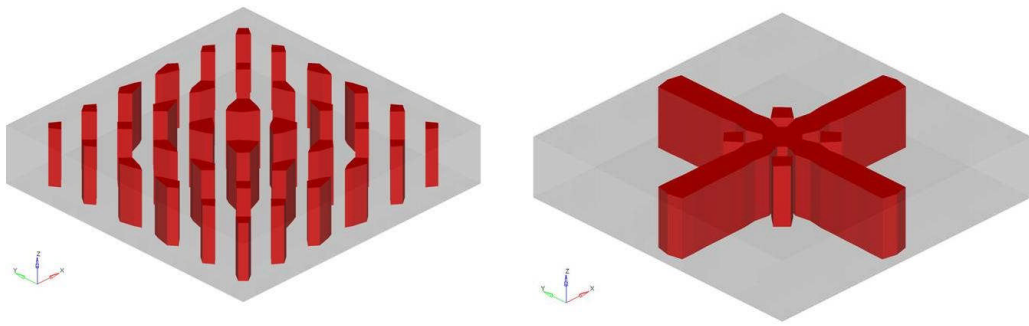
Figure 4.27 Material distribution of elements with ρ > 0.5, resulting from symmetrical loading with extrusion constraint (left) and additional checkerboard control (right).
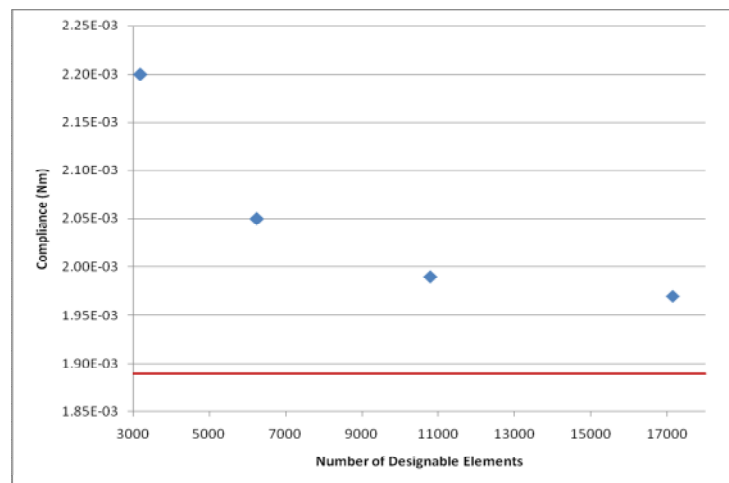
Figure 4.28 Decreasing compliance with increasing mesh resolution. Red lines shows compliance of the structure without checkerboard control on a 3200 element mesh.

4.2   Preliminary Topology Optimisation Study of Entire Aircraft

4.2.1   Problem Formulation

A finite element model of half of the UAV was developed, as shown in Figure 4.29. Again, this consists of 3D solid elements covered in a layer of 2D shell element to represent the aircraft's wetted surface. The model contains spaces for engines, cargo bay and landing gear. Three individual load cases, shown in Figure 4.30, were devised for a preliminary study. The first to investigate bending of the aircraft wing, achieved using two equal point forces at the leading and trailing edges of the wing tip. The second for investigating twisting of the aircraft wing, achieved using two equal and opposite point forces at leading and trailing edges of the wing tip. The use of these point forces is a highly simplified representation of the loading of the wing. The position at the wing tip is used to load the wing along its entire span. They are placed at the leading and trailing edges to represent high loads generated by the control surfaces. Finally, pressures calculated from CFD are applied on the wetted surface, for a 3.5g 'pull out of dive' manoeuvre. The latter represents a more realistic loading than the first two load cases, however at this stage forces from slats and flaps are not included in the problem, for simplicity. In all cases the aircraft is constrained in all degrees of freedom along its centreline. Unless otherwise stated, the topology optimisation problem is formulated in the same way as was used in previous test cases:

$$
\begin{array}{lll}
\text{minimise} & \text{compliance} & \\
\text{subject to} & \text{volume fraction} \leq c_1 & \qquad . \qquad (4.4)\\
& \rho_L \leq \rho_i \leq 1 & \qquad i = 1,2,...,n
\end{array}
$$

A penalisation factor of 2.0 is employed along with a volume fraction constraint of 0.25. At this stage no manufacturing constraints are included in the formulation.
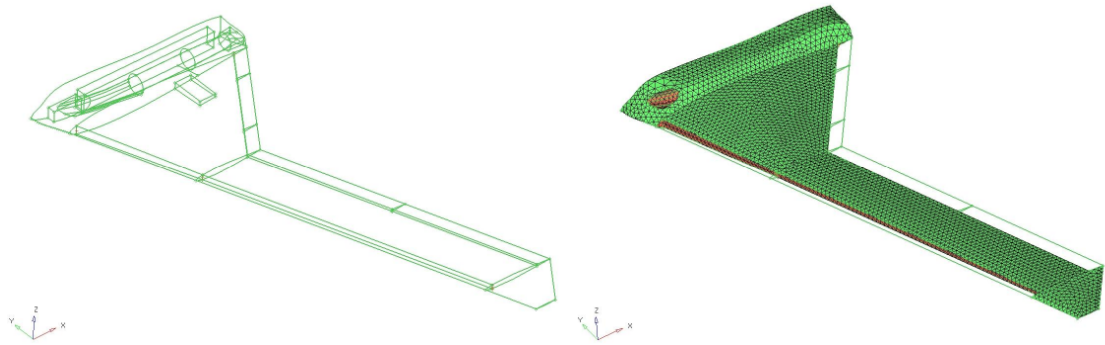
Figure 4.29 Half model of the UAV geometry (left) and a finite element model defining the designable space and wetted surface of the UAV with control surfaces removed (right).
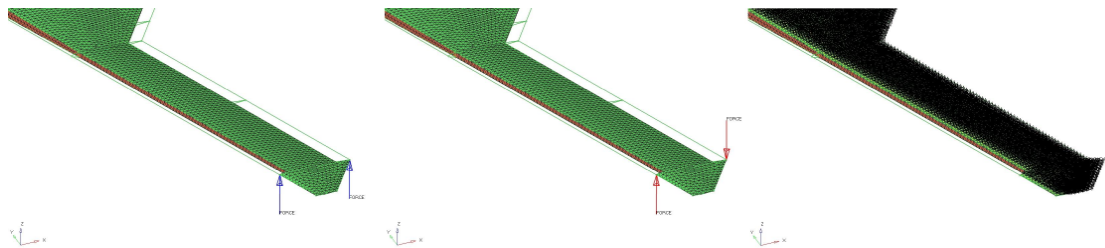
Figure 4.30 Three load cases applied to the UAV model. Bending (left), torsion (middle), and aerodynamic pressures (right).

4.2.2 Results

Figure 4.31 shows that the bending load case results in a similar outcome to the test case in Section 4.2.1. As expected, material is distributed in a single, spar-like structure, close to the upper and lower surfaces of the wing to improve bending stiffness. As in the earlier test case, the structure gradually widens in a chordwise direction along the length of the un-tapered wing section. This increase in spar thickness is due to the increased bending moment closer to the root. The use of more material in this area is an efficient way to reduce displacements, and therefore compliance. However, as the spar approaches the aircraft's centreline it becomes narrower due to the tight packaging constraints within the fuselage. Figure 4.32 shows how the spar joins the constrained centreline at the small space between the cargo bay and front landing gear, and the corresponding space along the top of the engine intake directly above. Although this is a basic preliminary study, it highlights the importance of correctly formulating an

optimisation problem, specifically the choice of operating conditions. Because the only load case defined is purely for bending of the wing, the resultant structure is only optimised for that condition. It is clear that the structure from this topology optimisation would perform very poorly for a different set of operating conditions, for example, torsional loading.
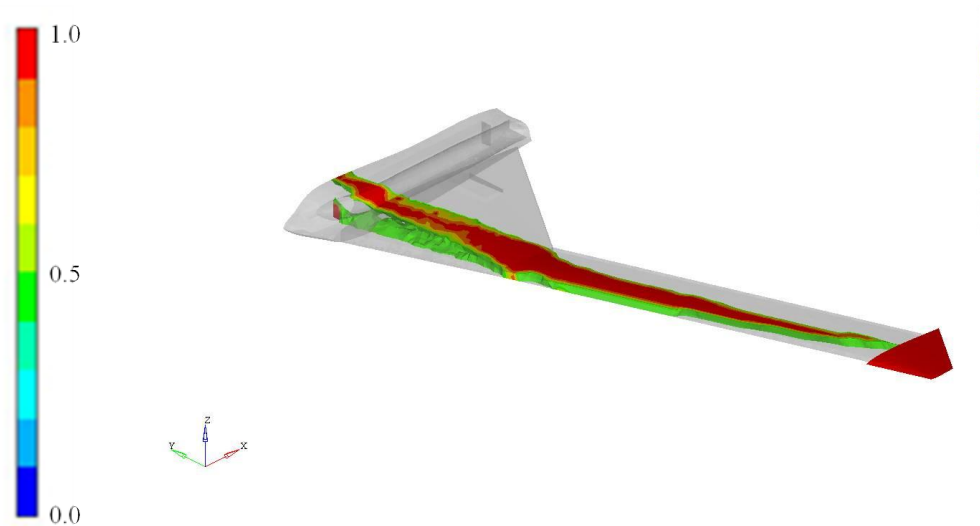
Figure 4.31 Contours of element density resulting from the bending load case, showing a single spar structure.
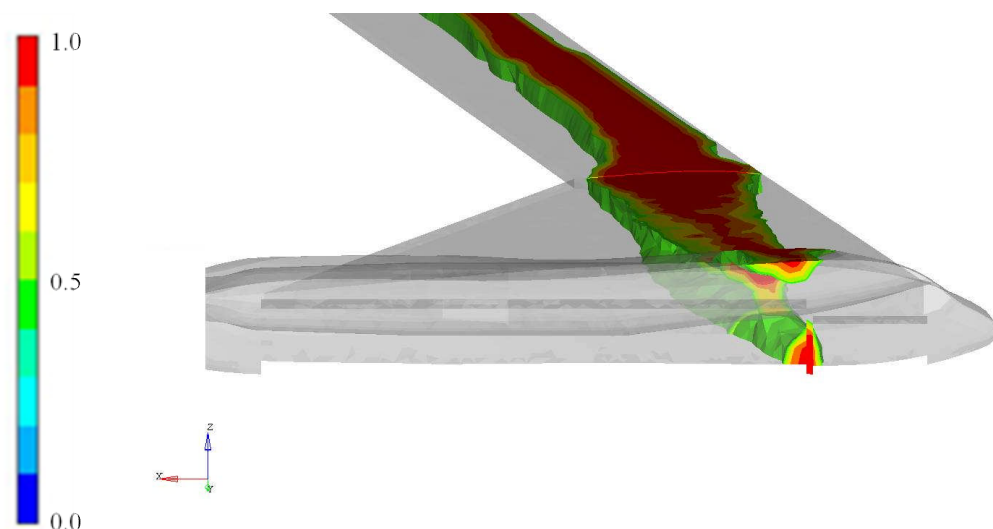
Figure 4.32 Single spar connecting to the aircraft centreline between the front landing gear and cargo bay.

The material distribution from the twisting load case, shown in Figure 4.33, reveals a

similar single, wide spar structure in the un-tapered section of wing, with most material at the upper and lower surfaces to increase the polar moment of inertia. However in the blended wing section the spar splits into two, with upper and lower sections of the spar joining the centreline of the aircraft at different points. The lower member attaches to the centreline of the aircraft at the same gap between the cargo bay and front landing gear that was utilised in the bending load case. The upper member, on the other hand, attaches above the engines approximately two thirds of the way down the fuselage. This second member gives the structure much better performance in torsion than that in Figure 4.31.
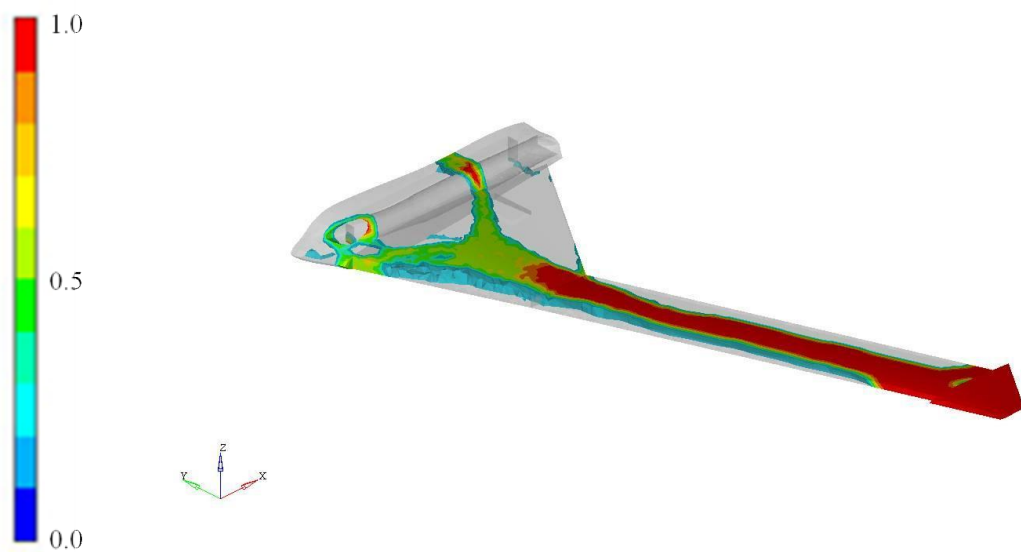
Figure 4.33 Contours of element density resulting from twisting load case, showing a single spar splitting into two before connecting to the aircraft centreline.
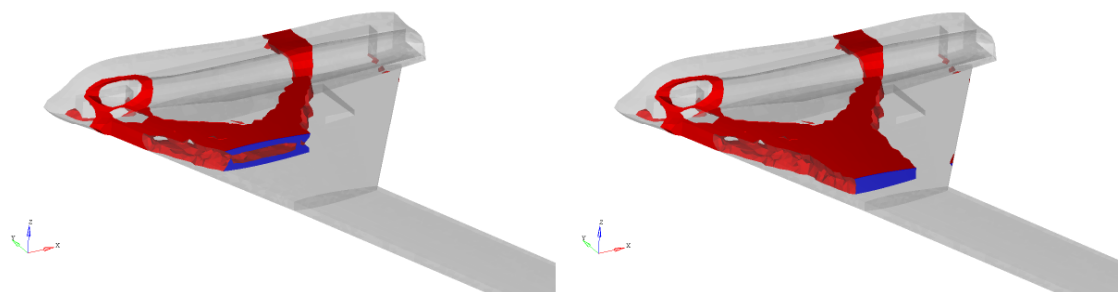
Figure 4.34 Section cuts of material distribution resulting from twisting load case. Material distributed at upper and lower surfaces in blended wing section, transitioning into a solid spar in the un-tapered section.

The third load case utilises pressure data calculated using CFD for a manoeuvre providing 3.5 vertical axis g-force. This is expected to exert large bending and twisting forces on the wing, as well as local deformation of the wing's skin due to pressure differences. The results from topology optimisation using the basic formulation described by (4.4) is shown in Figure 4.35. The structure is very similar to that produced with the bending load case. The only major difference is the additional material distributed around the nose of the aircraft. This is most likely to reduce deformation of the skin due to the high pressures exerted on this area of the aircraft. Also, there is a small, diagonal structural member close to the wing tip that should slightly reduce twisting of the wing. Despite these differences it is clear that, for this type of application, the minimum compliance formulation of the topology optimisation problem is dominated by the spanwise bending of the wing. There is no second spar to reduce twisting and, apart from in the nose, no material used to maintain the aircraft's cross sectional shape. This is due to the fact that compliance is a function of the nodal displacements. The displacements resulting from bending of the wing are of the order of 1m at the wing tip, whereas the displacements resulting from twisting of the wing are of the order of 1cm and local skin deformations are around 1mm at most.

The issue of increasing the significance of twisting of the wing can be dealt with quite simply with the inclusion of an additional constraint in the optimisation formulation. Again using the pressure data load case, the problem is reformulated as follows:

$$
\begin{aligned}
\text{minimise} \quad & \text{compliance} \\
\text{subject to} \quad & \text{volume fraction} \leq c_1 \\
& \text{twist angle}_{\text{wing tip}} \leq c_2 \\
& \rho_L \leq \rho_i \leq 1 \qquad i = 1,2,...,n
\end{aligned}
\qquad . \qquad (4.5)
$$

Typically, topology optimisation uses a large volume of material (in this case 25% of the aircraft's volume) and, due to the limiting factor of mesh resolution, the structural members defined by this material are unrealistically large. Therefore, the resultant structures have an equally unrealistically high stiffness. Because of this it is necessary to include overly strict upper limits when explicitly defining constraints on nodal displacements. Preliminary studies showed that a value of $0.25°$ for c_2 ensured that this constraint remained active so that its effects could be observed. The results for this new

formulation are shown in Figure 4.36. The same main spar structure remains, with material distributed along the quarter chord of the wing and joining the centreline of the aircraft in and above the gap between the cargo bay and landing gear. Additionally, the inclusion of a constraint on twist angle results in a second spar running close to the trailing edge of the blended wing section and passing through the fuselage in the space behind the cargo bay. The extra use of material in this second spar has caused material used to reduce local deformation due to the pressure loading in the nose to be removed.

The structural design shown in Figure 4.36 is now derived to resist the global bending and twisting of the wing, making it a useful tool in determining spar positions, however it neglects the smaller local deformation of the wing's skin. Due to the importance of the wing maintaining its aerodynamic shape, these local displacements cannot be overlooked. Also there is no second spar, like the ones existing in most commercial aircraft (Sensmeier and Samareh 2004), in the un-tapered wing section. A second spar would be expected to improve the structural performance of the wing under torsional loadings. However there may be other design requirements and loadings that dictate the need for this second spar. These issues are explored further in Section 4.4.
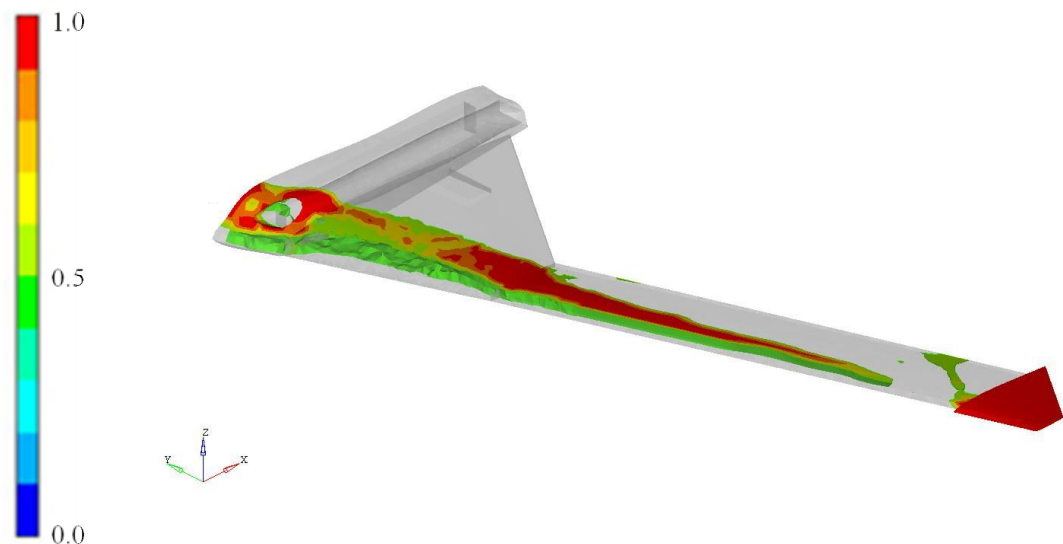
Figure 4.35 Contours of element density resulting from the aerodynamic pressures load case, showing a single spar structure.
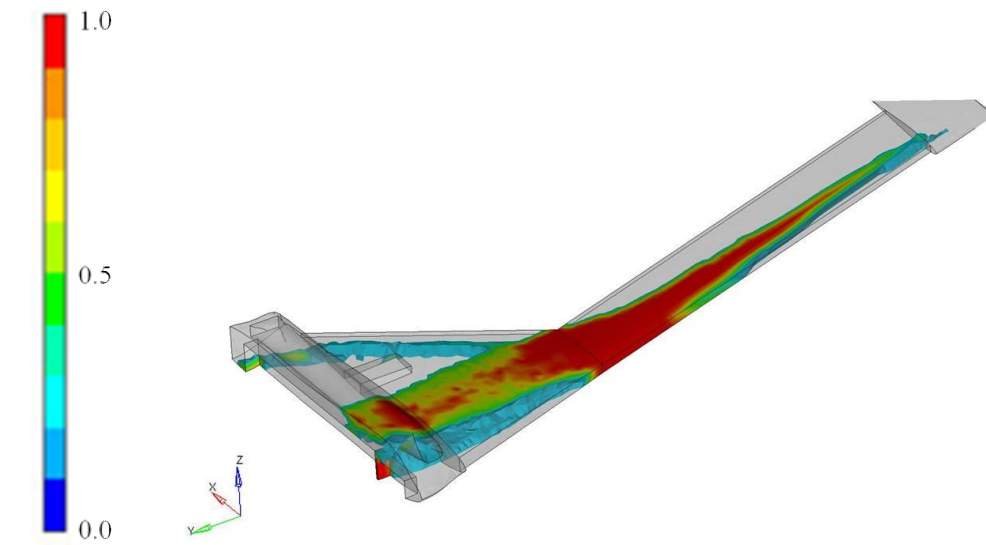
Figure 4.36 Additional spar structures in tapered wing section, resulting from the use of a wing twist constraint.

4.3   Further Investigation of the Aircraft Wing

Several approaches devised for overcoming the dominance of spanwise bending in the topology optimisation problem are presented below. To evaluate these approaches the UAV's fuselage section is ignored and optimisation is performed on the un-tapered and blended wing sections only. This allows more freedom for the optimiser as structural members are free to connect to the wing root at any location and are not restricted by the non-designable spaces within the fuselage such as engine, landing gear and cargo bay locations. A finite element model of the UAV's wing was constructed in a similar manner to that used earlier. A designable space is defined using 3D solid elements covered in a non-designable skin made of 2D shell elements, see Figure (4.37) (left).

4.3.1   Control Surface Loads

In order to determine the optimal layout of additional structural members, loads generated by the control surfaces are added to the finite element model. Initially these loads are estimated by integrating the pressure distributions over each control surface. The loads are then introduced to the finite element model as point forces at the upper and lower surfaces of the wing section at positions that represent potential connection points for the control surfaces (Figure 4.37 (right)). The topology optimisation problem is formulated using the same two constraint formulation given in (4.5). A penalisation factor of 2.0 is used along with a volume fraction constraint of 0.25. An additional extrusion constraint is applied with the assumption that all structural members should be uniform from the upper to lower surfaces of the wing. This approach makes it possible to optimise the locations of structural members, while computational expense can be reduced due to linking of design variables and a lower required mesh densities in the z-direction.
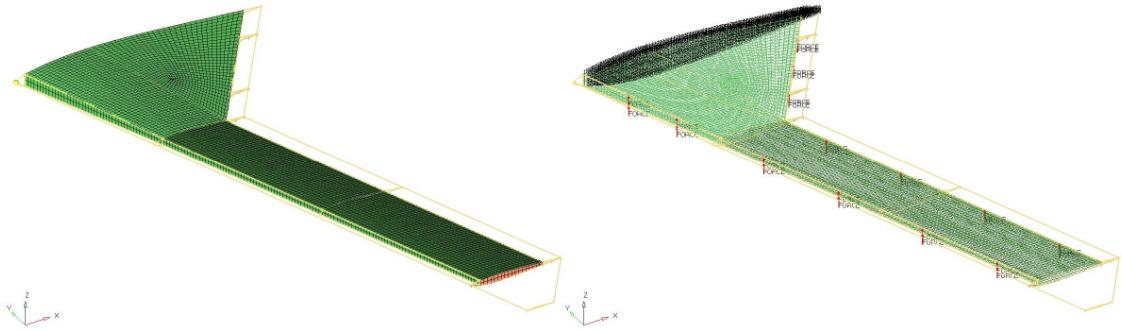
Figure 4.37 Finite element model of the UAV wing (left) with applied point forces at control surface connection points (right).

Initial optimisations shows these control surface loads to have little effect on the optimised topology. The main spar position is shifted slightly further towards the un-tapered wing section's leading edge, however no additional members are seen. To explore the optimised structure's sensitivity to the magnitude of the control surface loads, each load was increased by a factor of two. The penalisation factor was also relaxed to 1.0 to allow material with intermediate density to be used for additional structural members. Figure 4.38 shows very low density elements being used to connect the trailing edge loads to the main spar. Increasing the control surface loads further make no noticeable changes to the optimised topology. This confirms that even with these additional loads, the computation of compliance is still dominated by the global bending of the wing.
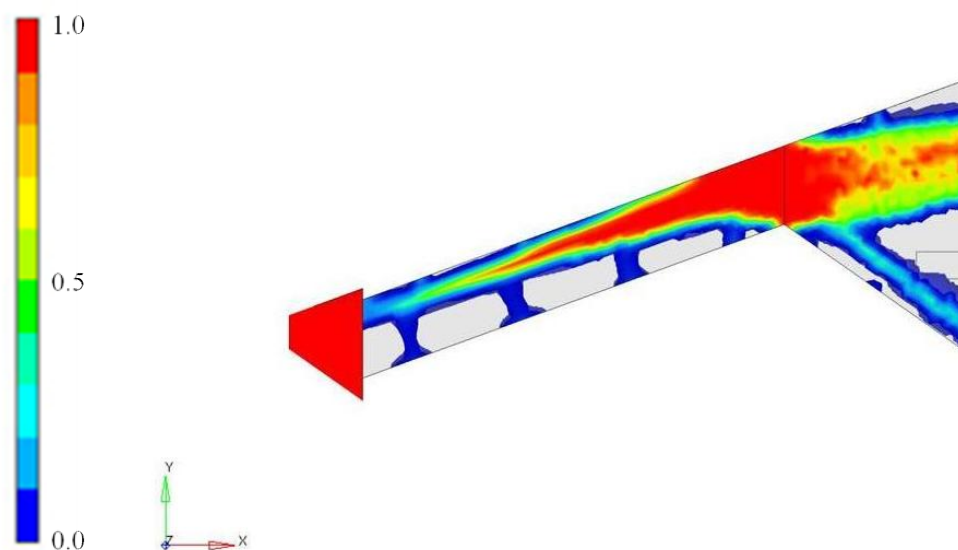
Figure 4.38 Contours of element density resulting from the inclusion of control surface loads, with low density material used to connect the control surface loads to the main spar.

4.3.2 Constraint on Change in Wing Thickness

An alternative approach is to place constraints on the difference in displacements between the upper and lower surfaces of the wing. This is achieved by applying constraints on the difference in displacements of a node on the upper surface and a corresponding node on the lower surface. The optimisation problem is formulated as follows:

$$
\begin{aligned}
&\text{minimise} && \text{compliance} \\
&\text{subject to} && \text{volume fraction} \leq c_1 \\
& && \text{twist angle}_{\text{wing tip}} \leq c_2 \\
& && \frac{\left| \Delta z_{j,upper} - \Delta z_{j,lower} \right|}{z_{j,upper} - z_{j,lower}} \leq c_3 \qquad j,upper = j,lower = 1,2,...,N \\
& && \rho_L \leq \rho_i \leq 1 \qquad i = 1,2,...,n
\end{aligned}
\qquad , \quad (4.6)
$$

where $z_{j,upper}$ are the z-coordinates of nodes on the upper surface of the wing, $z_{j,lower}$ are the z-coordinates of the nodes on the lower surface, and N is the number of nodes on each. Initially the displacement constraints are applied to all nodes on the upper surface and their corresponding nodes on the lower surface. Various values of c_3 are investigated. Using high values results in the constraints never being reached and the material distributions resembled those produced without the additional constraints. Any lower values of c_3 results in the optimiser finding no feasible solution, with material distributed in a seemingly random way in the design space and many of the displacement constraints violated. Changes in values for the first two constraints, penalisation factor and manufacturing constraints, fail to make any further improvement. The conclusion drawn from this is that the 9000 constraints involved cause difficulties for the optimiser.

Alternatively constraints can be applied to a small subset of the nodes. However, this encourages the optimiser to distribute material between the selected nodes in favour of all the others. This removes the main advantage of topology optimisation, i.e. its generality, as the locations of where material should be distributed are being pre-defined. This would be advantageous if there was prior knowledge of where structural members should be. However if that were the case, simple sizing optimisation could be

used and topology optimisation would not be necessary.

4.3.3 Rigid Beam Approach

Spanwise bending can be eliminated from the wing altogether, allowing local twisting and deformation of the wing's shape to be more influential in the compliance calculations. This is achieved using single point constraints to simulate a partially rigid beam running through the wing. The location of these constraints, shown in Figure 4.39, are selected using the topology optimisation results from earlier computations, shown in Figure 4.36, with the 'rigid beam' replacing the main spar. Nodes along this line are constrained in degrees of freedom 1, 3, 4 and 6, allowing only translation in the spanwise direction and rotation about the spanwise axis. The wing is loaded using the same pressure data and control surface loads from CFD as used earlier and the topology optimisation problem is formulated using the basic single constraint approach described by Equation (4.4). The twist constraint is neglected in this optimisation study as twisting of the wing should be sufficiently significant in the compliance. A penalisation factor of 2.0 is used and the volume fraction constraint is 0.25. An extrusion constraint is also included.
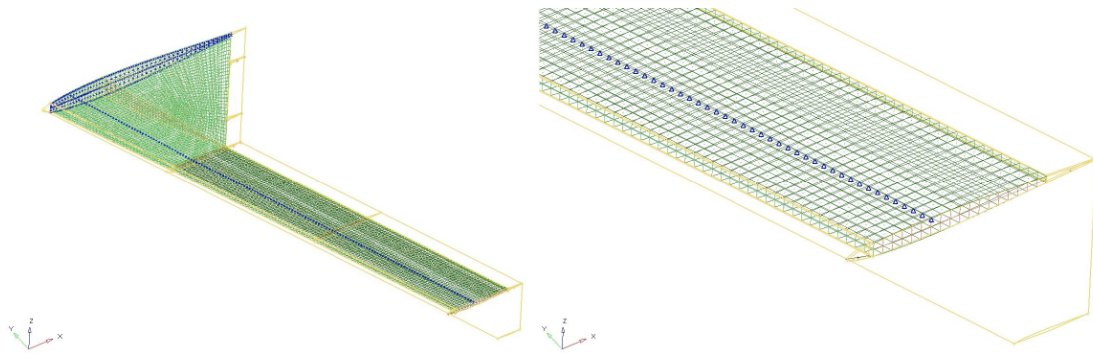
Figure 4.39 Finite element model of the UAV wing, showing a series of single point constraints used to represent a rigid beam.

An example of the results achieved using this method are shown in Figure 4.40. It is immediately clear that this approach has removed consideration for spanwise bending stiffness from the optimisation problem as there are no spar structures to resist this. The available material therefore, can be used to form additional structures to resist twisting

and local deformation of the wing's cross-sectional shape. The importance of control surface loads is demonstrated, as the majority of the material is used to connect the locations of these loads to each other and to the 'rigid beam'. However in the un-tapered, aft-swept wing section, the control surface connection points on the leading edge of the wing are not connected with the trailing edge loads opposite them (in the *y*-direction). Instead, most of the material is used to form diagonal, rib-like structures between these points. This is in contrast to what is usually seen in this type of aircraft wing, where ribs are aligned to the flow. It should be noted that buckling is not taken into account here, due to the difficulties associated with the inclusion of buckling constraints in topology optimisation, as discussed in Section 1.4.4. A major role of ribs is to prevent buckling, however the rib structures shown in Figure 4.40 are purely to improve the stiffness of the wing and minimise changes to its twist angle and aerodynamic shape. The issue of considering buckling requirements for conceptual aircraft architecture design is investigated further in Chapter 5. In the blended wing section there are rib structures very similar to what might be expected in conventional aircraft. As minimising compliance is the only objective of the optimiser, one of these ribs appears only in the front third of the wing section due to the higher aerodynamic pressures in this region.
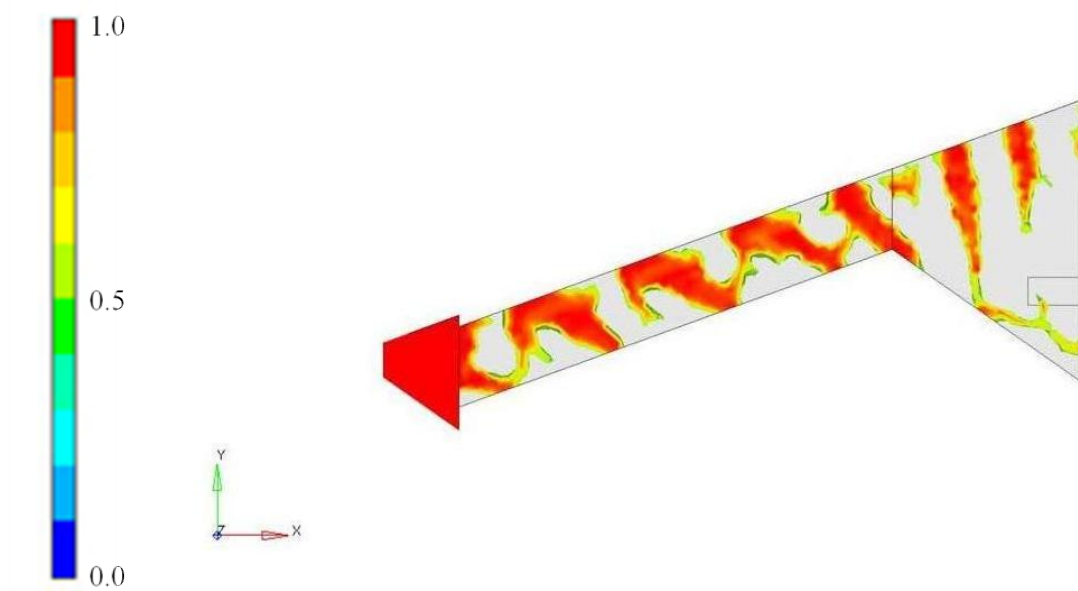
Figure 4.40 Contours of element densities resulting from the rigid beam approach. Material distribution shows multiple "riblets" used to link control surface loads to the rigid beam and each other.

4.3.4 Symmetrical Load Case

The final approach adopted to tackle the issue of maintaining the wing's aerodynamic shape is to investigate the inclusion of a symmetrical load case, as explored in Section 4.1.3. Pressures on the upper surface of the wing are made to correspond exactly to those on the lower surface. To achieve this the nodal pressure data from the wing's lower surface is extracted from the CFD computations. The *z*-coordinate of each node is then reflected in the *x-y* plane at the wing's mid-surface to create an additional data file containing pressures from the lower surface with coordinates corresponding to the upper surface. Control surface loads are neglected for this load case to maintain a neutral loading in the *z*-direction. An additional load case for the 3.5g manoeuvre contains the actual pressure loadings on the wing. Control surface loads are applied to this load case in a more realistic way than the point forces used previously. Control surfaces are included in the finite element model and joined to the wing at discrete points using rigid elements, as shown in Figure 4.41. Pressures on these surfaces, calculated from CFD, are then interpolated onto the finite element model. The addition of a second load case also results in the formulation of optimisation problem being more complex:

$$
\begin{aligned}
\text{minimise} \quad & \text{compliance}_{LC1} \\
\text{subject to} \quad & \text{volume fraction} \le c_1 \\
& \text{twist angle}_{\text{wing tip}_{LC2}} \le c_2 \\
& \text{displacement}_{\text{wing tip}_{LC2}} \le c_3 \\
& \rho_L \le \rho_i \le 1 \qquad i = 1,2,...,n
\end{aligned}
\qquad , \qquad (4.7)
$$

where *LC1* is the symmetrical load case and *LC2* is the 3.5g load case. The aim of this formulation is to keep the global bending and twisting of the wing within some predefined limits and allow the remaining material to be used to maximise resistance to local deformation of the wing skin due to the pressure loadings. As before, it is necessary to make the constraints on displacement and twist unrealistically strict due to the large volume of material being used to form solid aluminium structures. For this reason c_2 is 0.25°, c_3 is 150mm, c_1 remains 0.25 and a penalisation factor of 2.0 is used. Initially the only other constraint applied is for extrusion in the *z*-direction.
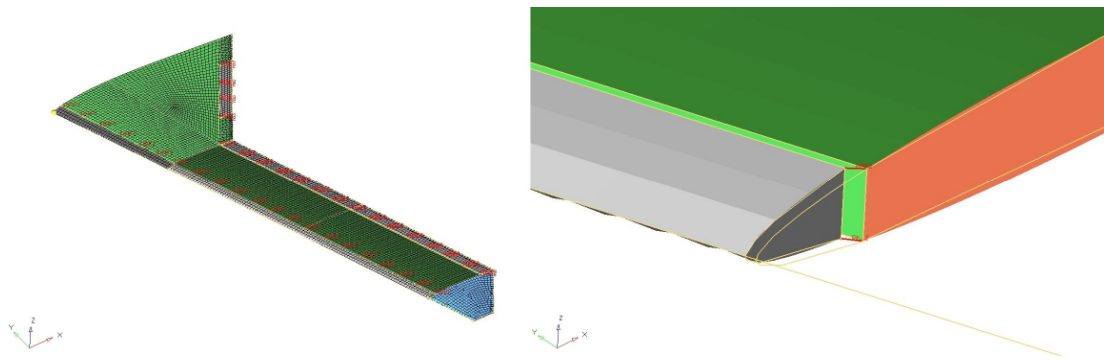
Figure 4.41 Finite element model of the UAV wing with control surfaces included (left). Rigid elements used to connect control surfaces to the main wing structure (right).

The approach results in several distinct structural members, as shown in Figure 4.42. Firstly there is a single spar structure in the tapered wing section running perpendicular to the flow. The main purpose of this is clearly to reduce bending of the wing, however its chordwise position should also be noted. The spar is located at approximately the quarter chord. In this area aerodynamic loadings are high and the wing is at its thickest. It is possible that the location of the spar is in some part driven by load case 1, as in this location the spar would resist localised deformation of the wing section at its most susceptible point. In the area where the tapered wing section meets the un-tapered section there is a member aligned to the flow. This part of the structure is of great importance in load case 2 as there are high stress concentrations due to the decreasing cross-sectional area of the wing. Displacement of the un-tapered wing section due to bending can be efficiently reduced with additional stiffness at this point. There are several members in the un-tapered wing section, mostly running perpendicular to the flow. This is assumed to be a result of load case 1, as usually only one spar has been seen in this section. The spacing of the members could indicate that they are serving the purpose of both reducing bending and twisting of the wing, and supporting the wing skin. It is also noticeable that the majority of the material used is distributed in the front third of the wing, possibly due to the higher aerodynamic pressures in these areas.
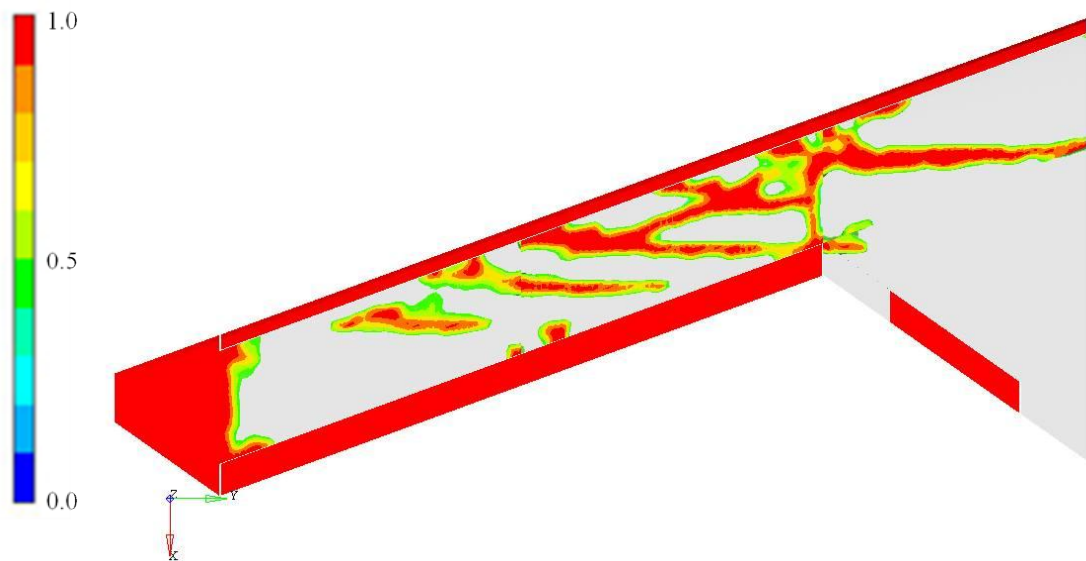
Figure 4.42 Contours of element density resulting from the symmetrical loading approach, showing multiple spars and a single rib to improve structural stiffness.

4.4   Topology Optimisation Study of the Fuselage

A topology optimisation study of the UAV's fuselage is also made, and in this case there are no large displacements dominating the compliance formulation like the ones associated with wing bending. However the tight packaging requirements of this part of the aircraft presented a different set of challenges. The layout of the fuselage is discussed in depth in Section 2.1. These requirements make this application ideally suited to topology optimisation. Firstly a finite element model of the fuselage was developed, consisting of 150000 tetrahedral elements. This is shown in Figure 4.43. As usual, the 3D elements are covered in a layer of 2D triangular shell elements representing the wetted surface where aerodynamic pressures can be applied. In addition to the aerodynamic pressure, the model is also loaded with a series of point forces at the wing root. These point forces are derived from the forces exerted on the fuselage by the wing when loaded with pressures from the 3.5g manoeuvre load case, by using a solid finite element model of the entire aircraft. Topology optimisation is performed using the basic minimum compliance formulation with a 0.25 volume fraction constraint. A penalisation factor of 2.0 is used alongside a maximum member size control of 200mm. This ensures material is used to form distinct structural members, rather than large sheets used to thicken the aircraft's skin in areas of high pressure.
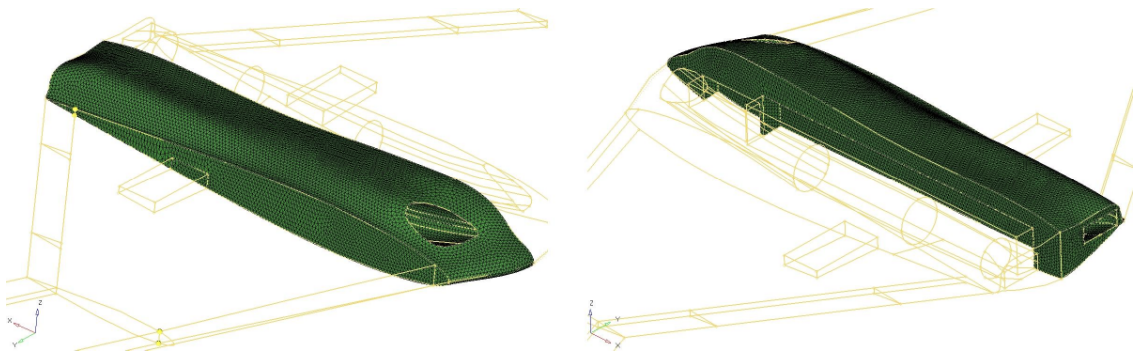
Figure 4.43 Finite element model of the UAV fuselage including non-designable voids.

Some results for topology optimisation of the fuselage are shown below. Figure 4.44 shows the series of stiffeners running along the upper surface of the fuselage. These give support to the skin as well as linking the top of the wing's root to the aircraft's centreline to reduce bending from the point forces applied there. In Figure 4.45 the locations where structural members attach to the symmetry plane can be seen. Apart

from the upper stiffeners, there is large amounts of material both behind and in front of the cargo bay. These are key locations for spars to prevent bending and twisting of the wing. Figures 4.46 and 4.47 show parts of the structure within the front and rear of the fuselage, respectively. Note the considerable volume of material used around the gap between the cargo bay and landing gear. Here there is space for members at the top (above the engine intake) and bottom of the fuselage. Therefore the material can be used efficiently in this area without excessive compromise due to the packaging constraints. The same is true at the rear of the aircraft, where structures can easily fit behind the cargo bay and above the engine's exhaust.
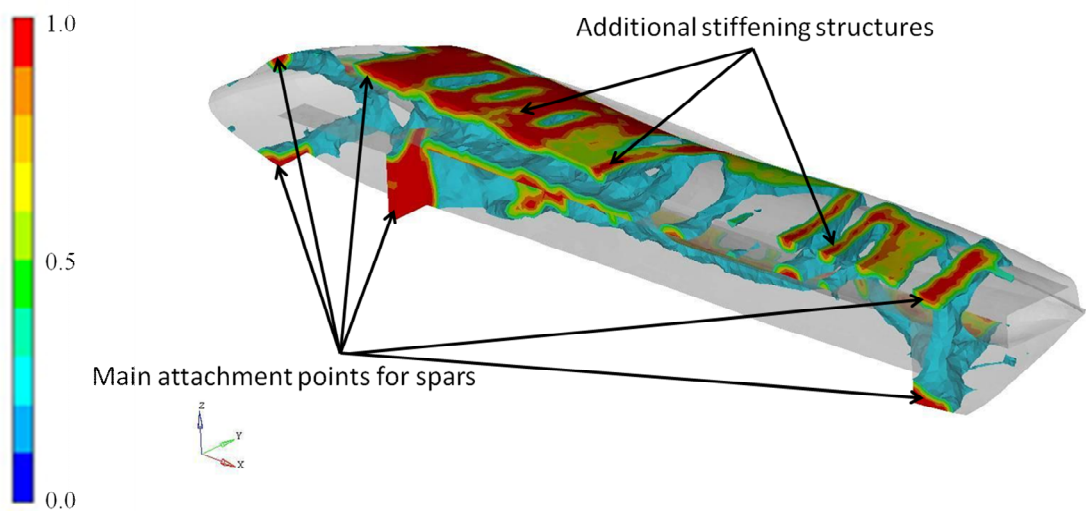
Figure 4.44 Contours of element density showing stiffening structures on the upper surface.
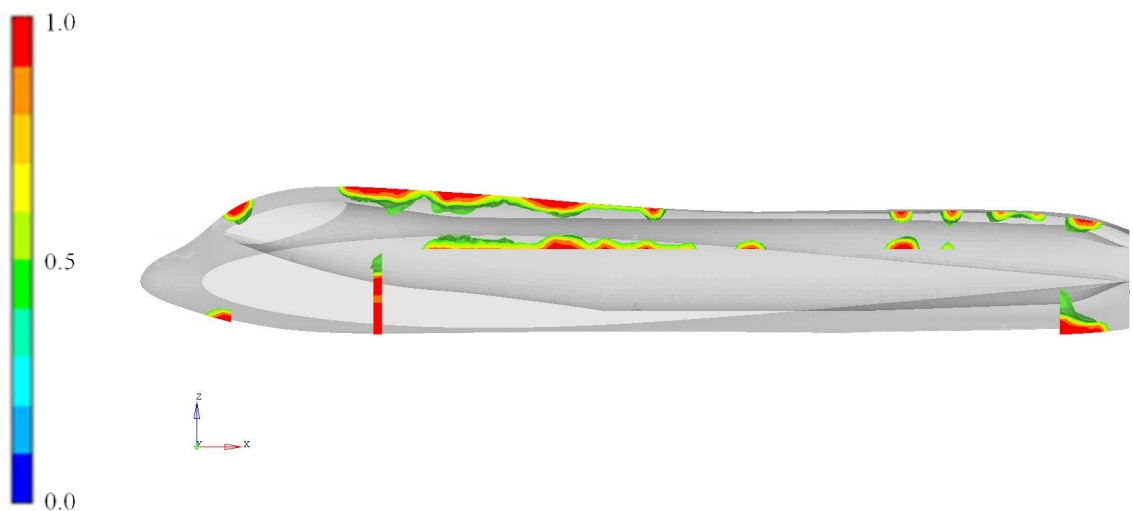
Figure 4.45 Contours of element density showing connection points of the stiffening structures to the aircraft centreline.
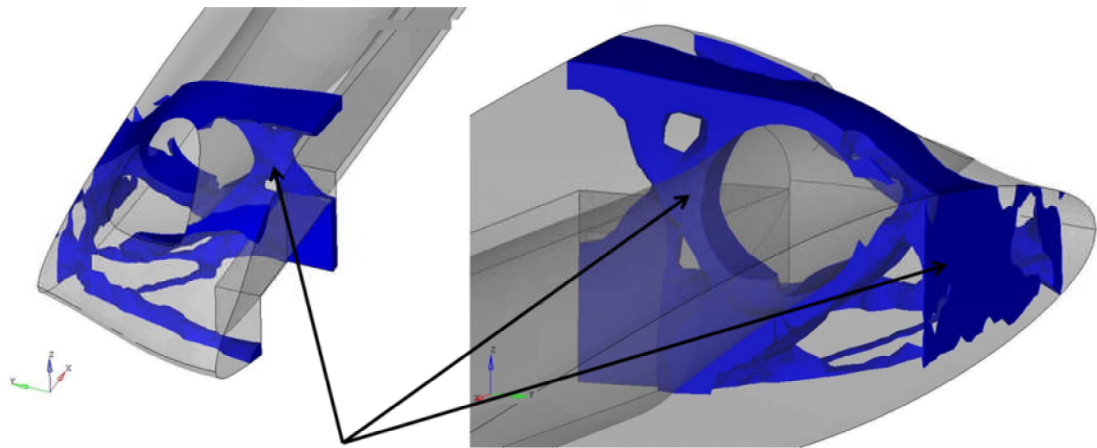
Large volumes of material used to link wing with aircraft's centreline

Figure 4.46 Material distribution in the front section of the fuselage, showing members located in spaces between the non-designable voids.
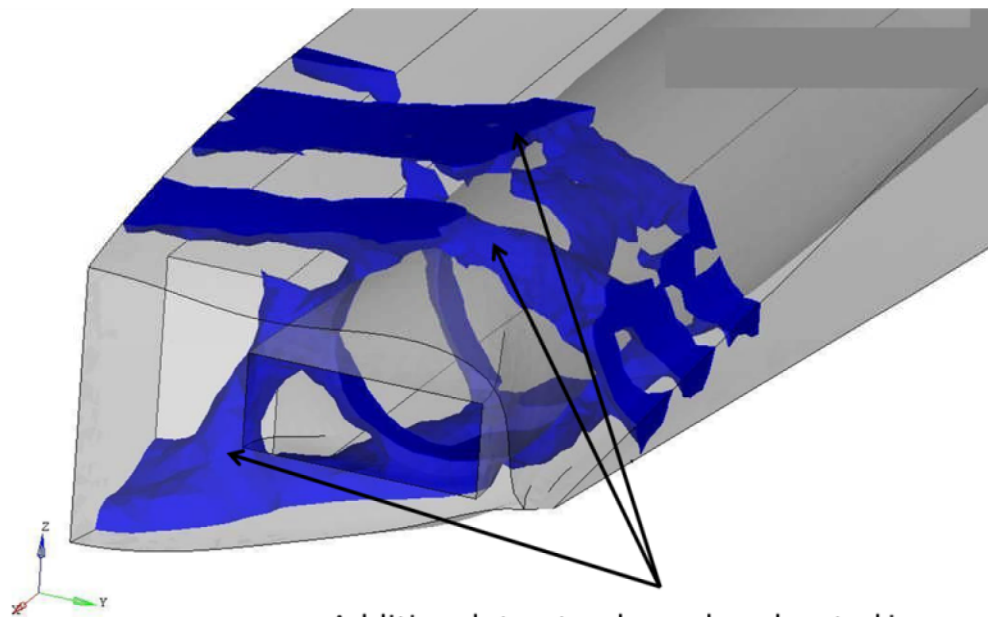
Additional structural members located in spaces that allow a rear spar to join the aircraft's centreline

Figure 4.47 Material distribution in the rear section of the fuselage, showing members located in spaces between the non-designable voids.

It is clear from the above figures that the material distributions could not be used as final designs that are feasible for manufacturing. However, the use of penalisation and

minimum member size constraints has made it possible to identify key structural members that are required, such as the structure seen between the cargo bay and front landing gear. In order for the results from topology optimisation to be of use in designing the internal structure of the fuselage, it is clearly necessary for an engineer to construct a more detailed finite element model containing these key structural members. The material distributions shown here could be used as a guide for where such members are required. The detailed model could then be used for further topology, shape and sizing optimisations in order to generate a manufacturable design.

4.5 Conclusion

A variety of test cases associated with topology optimisation in the design of aircraft architectures are presented in this chapter. The first of these is a simple un-tapered wing section. The dependence of an optimised structure on the type of applied loading is shown by comparing results from the wing section in bending and torsion. Several parameters involved in topology optimisation are investigated. The effects of insufficient mesh density on the optimised topology are established. The importance of a suitable penalisation factor in the SIMP formulation for aiding the production of designs with fewer elements with intermediate density is demonstrated. The implementation of stress constraints (or guidelines) in topology optimisation are shown to be of use, and capable of driving designs alongside other conventional design constraints. Manufacturing constraints can also be very important in generating useful designs. Extrusion constraints can be used to ensure the presence of continuous structural members such as spars, and member size controls can be useful in generating material distributions that can be interpreted as real structures for the creation of new CAD and FE models. An example of the need for checkerboard control is also demonstrated.

The difficulties involved with applying these approaches to an entire aircraft wing are demonstrated using a conceptual UAV design. Global bending of the wing is shown to dominate the computation of compliance making it necessary to employ additional constraints, loadings and other strategies. The simple addition of a constraint on the twist angle of the wing results in designs with greater torsional stiffness. A number of approaches for dealing with more localised deformation of the wing are explored. Control surface loads are found to have little influence in the compliance formulation. However, optimal locations for additional structures to support these can be determined with the use of single point constraints replacing the spar. The inclusion of large numbers of design constraints to conserve the wing's shape presents significant difficulties for the optimiser and is therefore an unfavourable approach. The use of an additional, artificial load case, where the wing is symmetrically loaded, is shown to give promising results. Designs using this approach include structural members that resist bending, twisting and local deformation of the wing's skin.

At this stage, all the methods used for determining optimal aircraft architecture have been concerned with improving stiffness. The issues of dealing with local as well as global stiffnesses are addressed, however the important design consideration of structural stability is neglected. Due to the difficulties associated with using buckling constraints in topology optimisation, these design requirements are usually considered later in the design process. However, ignoring these requirements at the concept stage can result in designs that are incompatible with requirements for structural stability. These issues are explored in Chapter 5.

Chapter 5

A Framework for Topology, Shape and Sizing Optimisation of Aircraft Structural Architectures

In Chapter 4 several implementations of topology optimisation were investigated for use in finding optimal structural layouts of aircraft. This involved ensuring that all aspects of linear static structural behaviour were accounted for, as opposed to merely the bending stiffness. In this chapter methods for combining topology optimisation with shape and sizing optimisation are investigated. The primary concern is in generating designs that improve both stiffness and structural stability. For aircraft layout design, conventional approaches for achieving this are not viable, therefore alternative approaches are explored. This begins with parameter studies of the sensitivity of buckling loads to the number of ribs, rib location, rib orientation and skin thickness. Shape and sizing optimisation is then used to find optimal rib pitches and skin thicknesses. A multi-level approach is proposed, where the optimal rib positions are included as non-designable structures in the topology optimisation problem. This is shown to significantly affect the resultant material distributions. Finally, the approaches developed in this and the previous chapters are applied to a conceptual UAV design and are shown to offer potential reductions in structural mass.

5.1 Shape and Sizing Optimisation Test Cases

The same test case used in Chapter 4 was modified to investigate of the effect of rib positions on buckling behaviour. The solid elements defining the designable space in the finite element model for topology optimisation are replaced with five uniformly spaced ribs as seen in most modern commercial aircraft (Sensmeier and Samareh 2004), one at both the root and tip of the wing, and three internal ribs. The ribs are all aligned with the flow and are defined with 2D shell elements, as shown in Figure 5.1 (right) highlighted in green; the leading and trailing edges of the wing are similarly defined, with shell elements representing front and rear spars, shown in yellow. Initially all ribs are allocated a thickness of 5mm, spars 10mm and a skin thickness of 4mm is specified.
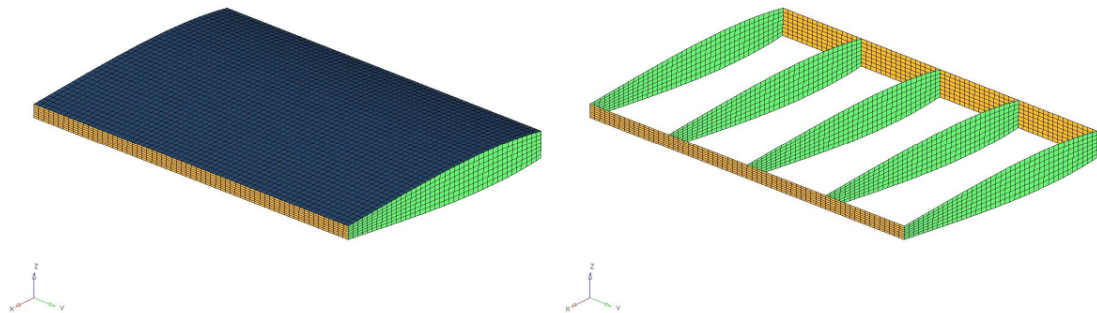
Figure 5.1 Finite element model of the wing section used for buckling analysis and shape optimisation, showing spars (yellow), ribs (green), and wetted surface (blue).

5.1.1 Buckling Analysis and Parametric Study
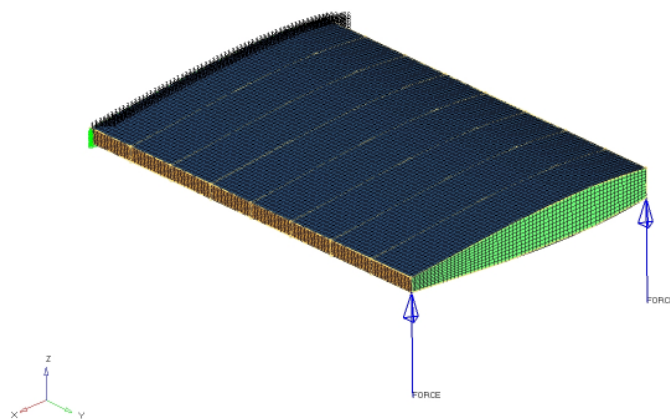
Figure 5.2 Bending load case applied to the wing section for buckling analysis and shape optimisation.

A single load case is used for studying the buckling behaviour, as shown in Figure 5.2. Two point forces, both with a magnitude of 2kN, are applied at the leading and trailing edges of the wing section's tip. Nodes at the root are constrained in all degrees of freedom. The first study conducted is of the buckling modes' mesh dependency. Five finite element meshes were produced. The number of shell elements in these meshes varies from 1936 to 46760, with the number of elements between each rib varying from 8 to 40. Buckling analysis is performed and the first five buckling modes are calculated for each mesh. On visual inspection the first three buckling modes appear similar for all meshes, as shown in Figures 5.3 to 5.5. There is some variation in the fourth and fifth modes in the coarsest mesh, shown in Figures 5.6 and 5.7. Despite the similarities in buckling modes, the buckling load factors show considerable variations in the two coarsest meshes when compared to the finer ones. Mesh independency is reached for meshes over 16440 shell elements, as is evident in Figure 5.8. This corresponds to a 96x60x10 element mesh.
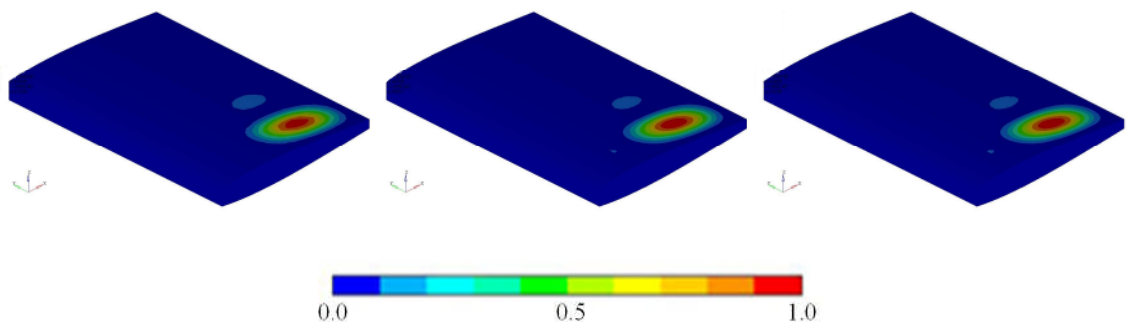
Figure 5.3 First buckling mode calculated on meshes of 1936 (left), 16440 (middle), and 46760 (right) elements. Buckling occurs close to the root and trailing edge.
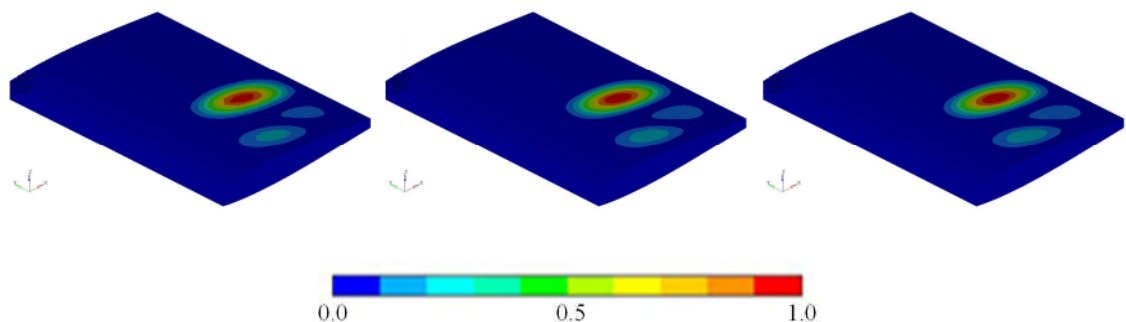
Figure 5.4 Second buckling mode calculated on meshes of 1936 (left), 16440 (middle), and 46760 (right) elements. Buckling occurs between the two internal ribs closest to the root.
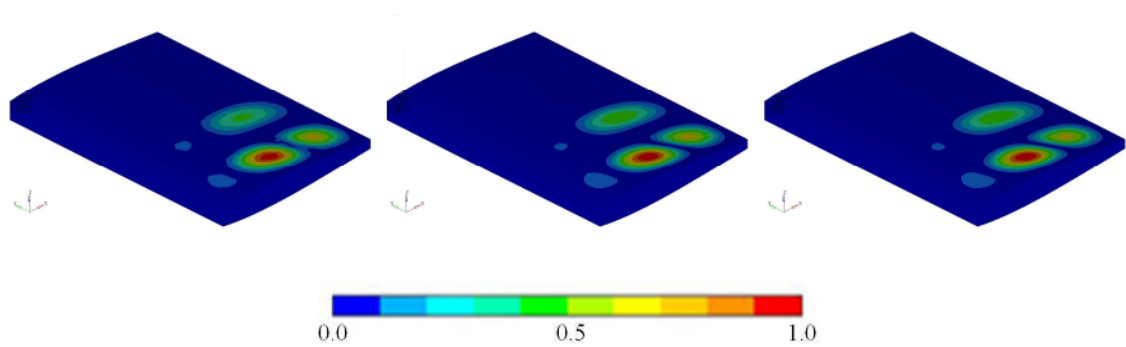
Figure 5.5 Third buckling mode calculated on meshes of 1936 (left), 16440 (middle), and 46760 (right) elements.
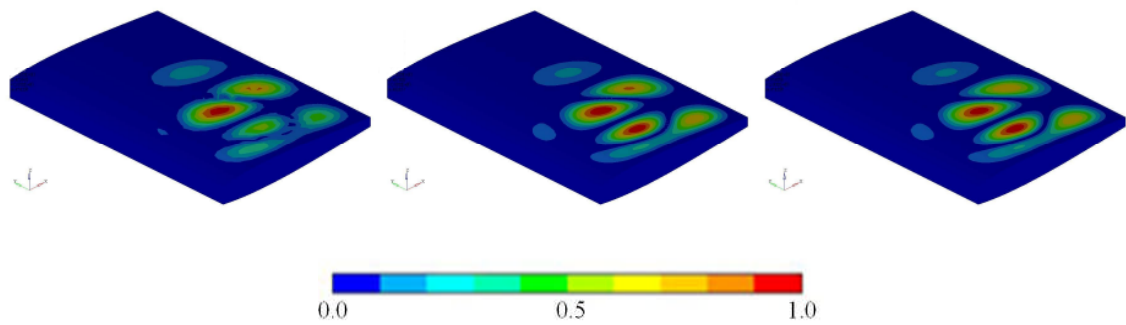
Figure 5.6 Fourth buckling mode calculated on meshes of 1936 (left), 16440 (middle), and 46760 (right) elements. Small differences between the modes seen on coarse and fine meshes.
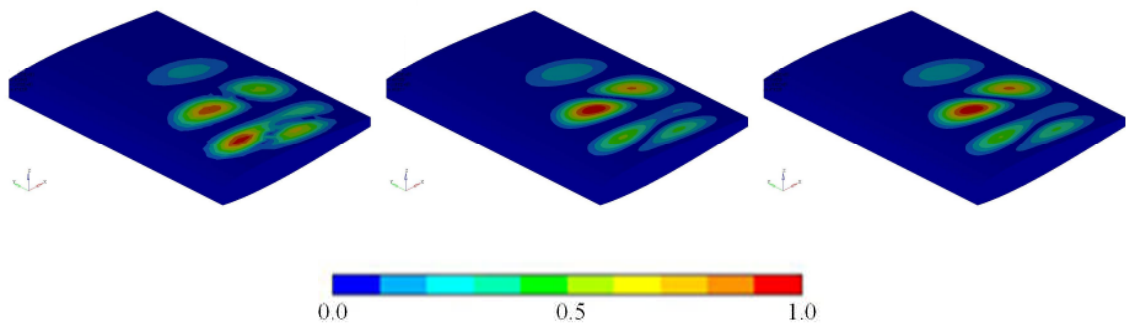
Figure 5.7 Fifth buckling mode calculated on meshes of 1936 (left), 16440 (middle), and 46760 (right) elements. Small differences between the modes seen on coarse and fine meshes.
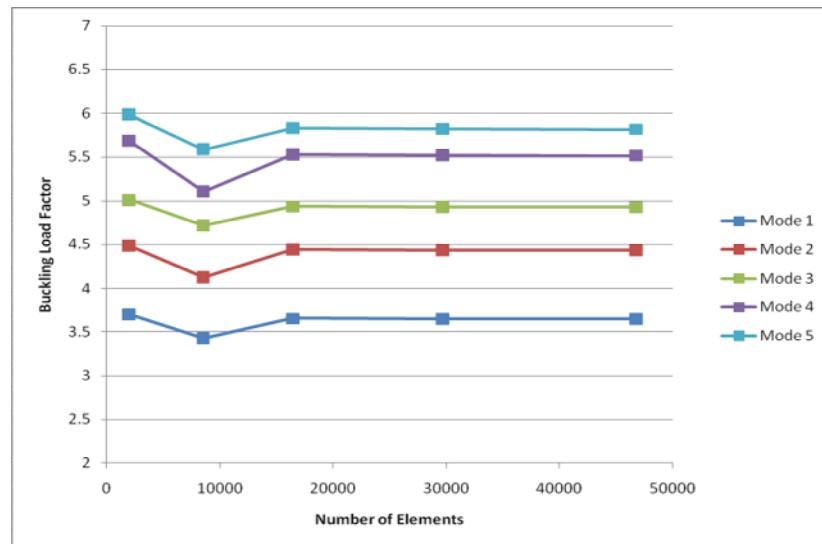
Figure 5.8 Variation in buckling load factors with finite element mesh resolution, with mesh independence reached at 16440 elements.

The second study conducted of this test case is the effect of skin thickness on buckling modes and load factors. The configuration and thicknesses of ribs and spars remains the same as in the previous study using the 16440 element mesh, however the skin thickness is varied between 1mm and 5mm. The same load case is applied and again, the first five buckling modes calculated for the different skin thicknesses. Increasing the skin thickness is shown to considerably increase the buckling load factors, shown in Figure 5.11, as expected. The analytical solution to buckling loads in flat plates states that buckling loads are proportional to the plate thickness cubed (Sun 2006). Figure 5.11 shows this not to be applicable to the wing section, with buckling loads severely overestimated. This could be due to the way in which the two point forces are applied at the leading and trailing edges along with the curvature of the wing section causing strain energy density to be unevenly distributed. The changes in skin thickness also results in changes to the buckling modes themselves. The first three modes are shown for a 1mm skin thickness in Figure 5.9, and a 5mm thickness in Figure 5.10.
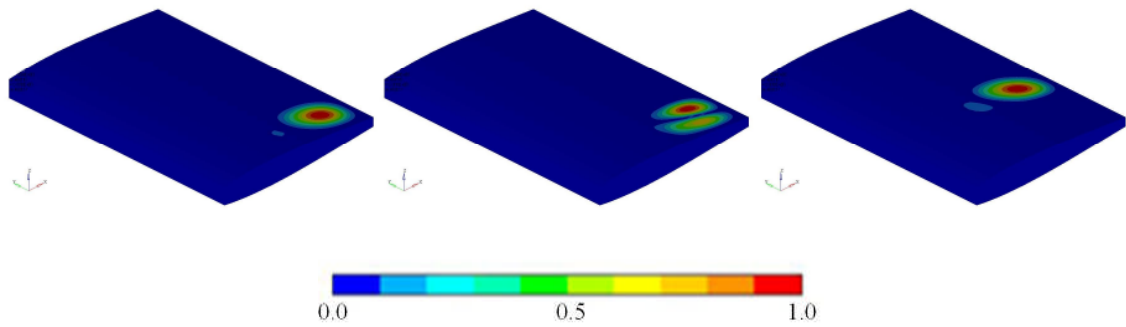
Figure 5.9 Buckling modes 1 to 3 (left to right) resulting from a skin thickness of 1mm, showing buckling occurring close to the root for the first two modes and after the first internal rib for the third mode.
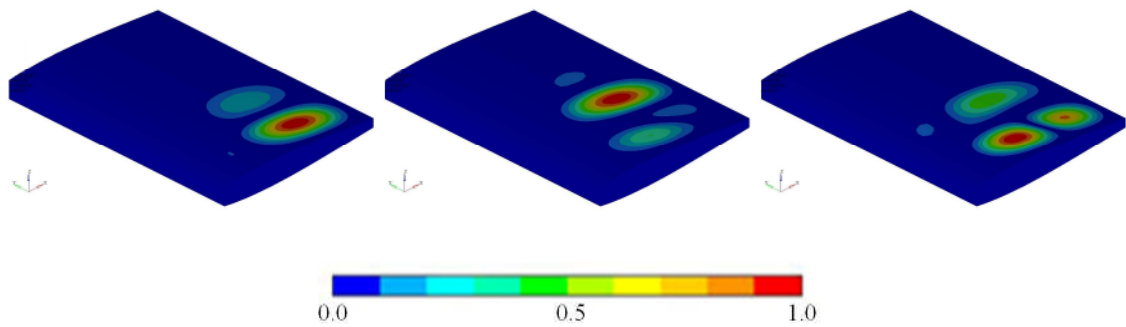
Figure 5.10 Buckling modes 1 to 3 (left to right) resulting from a skin thickness of 5mm, showing buckling occurring close to the root for the first and third mode and after the first internal rib for the second mode.
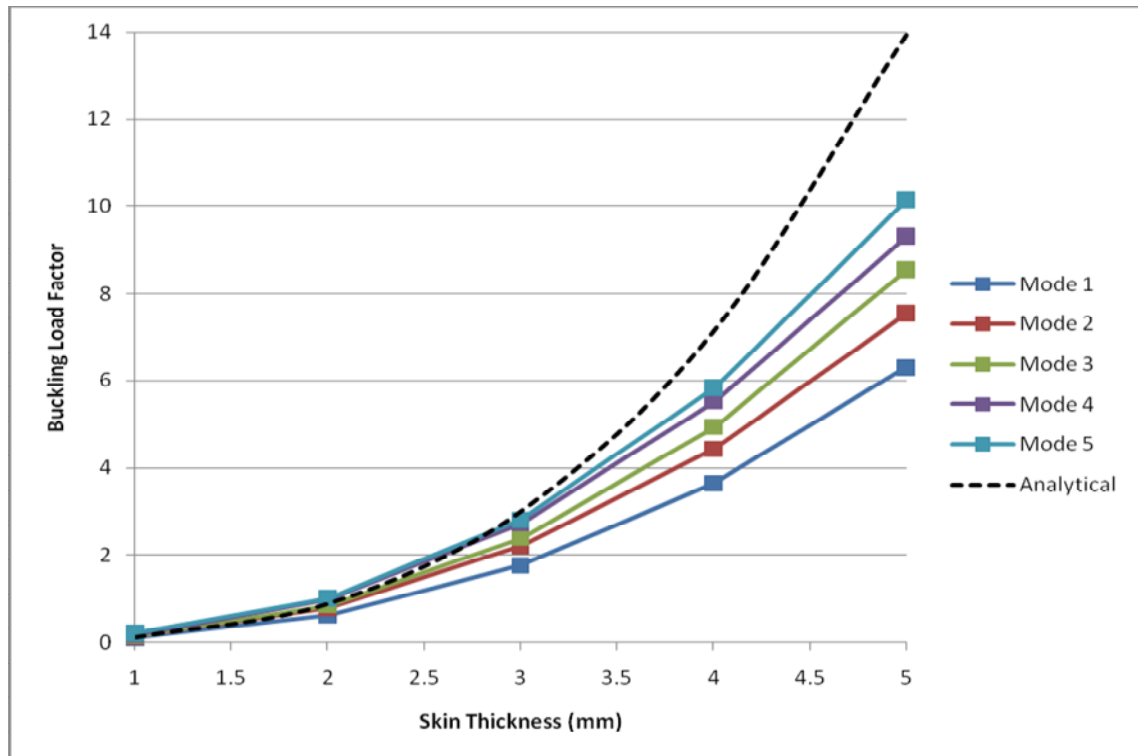
Figure 5.11 Increasing buckling load factors with increasing skin thicknesses. The analytical relationship for flat plates, which states that the buckling load factor is proportional to the thickness cubed, substantially over predicts the first mode.

The final part of this parametric study of buckling behaviour involves an investigation of the effects of rib pitch on buckling modes and load factors. Using the mesh density required for mesh independence identified above, three additional finite element models of the wing section were developed. These models have varying numbers of internal ribs, spaced uniformly along the wing section and aligned to the flow. The original model with three internal ribs was also included in the study. These four configurations are shown in Figure 5.12. The zero, one, three and seven internal rib models correspond to a rib spacing of 2m, 1m, 0.5m and 0.25m, respectively.
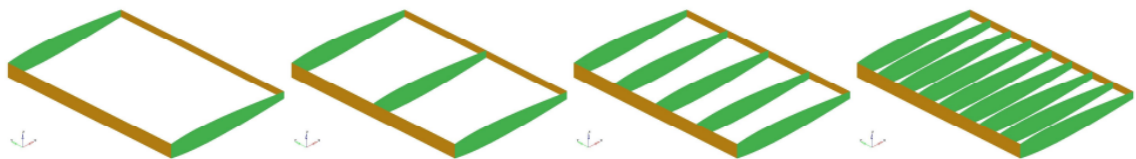
Figure 5.12 Models of wing sections with zero (far left), one (left), three (right), and seven (far right) internal ribs.

Buckling modes alter considerably depending on the rib spacing, as can be seen by comparing the first three buckling modes for 2m and 0.25m rib spacings shown in Figures 5.13 and 5.14, respectively. Additional ribs are also shown to considerably increase buckling load factors as expected. Another outcome of using a larger number of ribs is the more uniform spacing of buckling modes, as shown in Figure 5.15. At rib pitches of 2m and 1m there are different buckling modes occurring at very similar critical loads, however at smaller pitches these buckling modes are better separated. Similar buckling loads are undesirable, as at the sizing stage of the design process any additional material used to improve the critical loads needs to be distributed between the locations of multiple modes. Better separation of the buckling loads allows the first mode to be the primary concern.
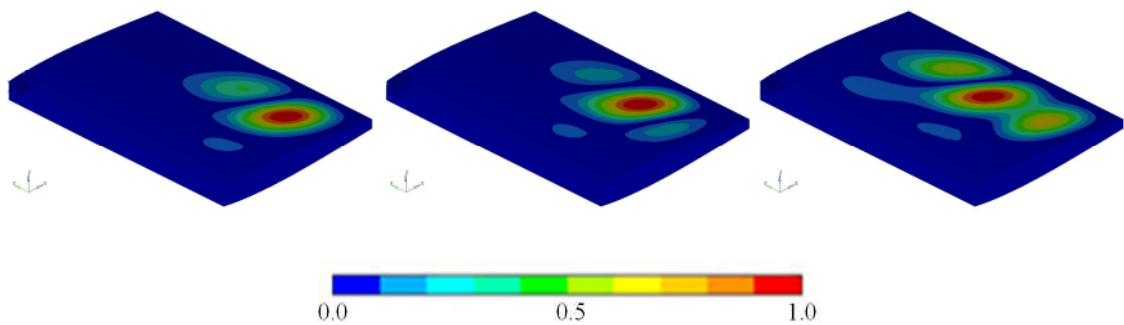
Figure 5.13 Buckling modes 1 to 3 (left to right) for a wing section with no internal ribs, showing buckling occurring close to the root for the first mode.
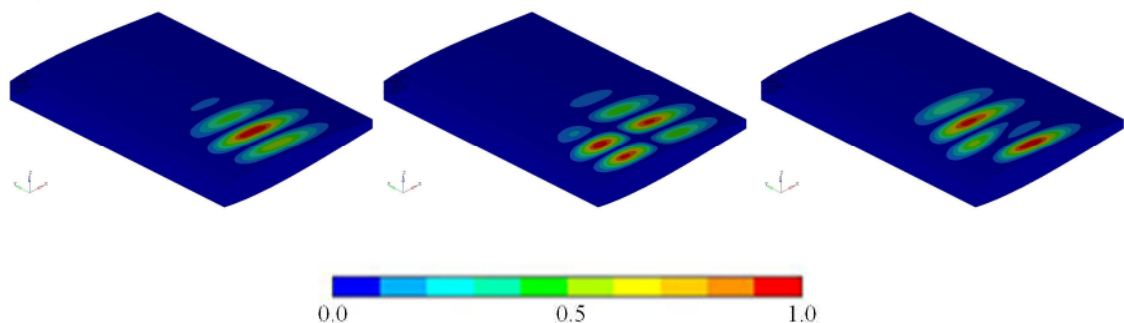
Figure 5.14 Buckling modes 1 to 3 (left to right) for a wing section with seven internal ribs, showing buckling occurring between ribs close to the root.
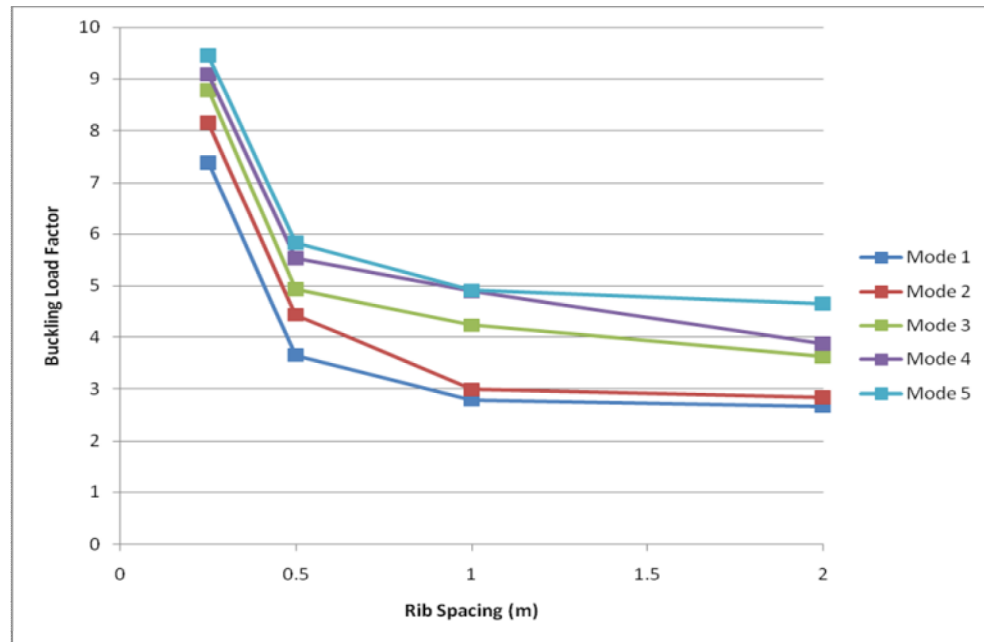
Figure 5.15 Decreasing buckling load factors with increasing rib spacing for the first five buckling modes.

5.1.2 Optimisation of Rib Pitch for Buckling Behaviour

A study into the use of shape optimisation for improving critical buckling loads is performed using the same test case. The same finite element models employed in the previous section, containing various numbers of ribs, are used. The aim of this study is to determine whether the uniform rib spacing found in most commercial aircraft is truly optimal, and also to investigate the use of shape optimisation in this role and how it may be combined with the results from topology optimisation. The design variables for shape optimisation, in this case the positions of each rib, are defined using the perturbation vector approach described in Section 2.4.1. The finite element meshes are morphed into new shapes so that nodal perturbation vectors can be calculated. Each design variable is then associated with a perturbation vector capable of describing the position of a wing rib. Results from this approach, applied in a number of ways, are presented below.

5.1.2.1 Optimisation of Rib Pitch with Uniform Skin Thickness

The first set of shape optimisations performed are to determine optimal rib positions, with all other parameters in the model remaining constant. This is achieved by using perturbation vectors of equal magnitudes at all nodes on a rib, so that any value of a particular design variable relates to a movement of the entire rib in a spanwise direction. This is shown in Figure 5.16. One perturbation vector is applied to each internal rib so that the number of design variable is equal to the number of internal ribs. Maximum and minimum values of the design variables are applied in order to prevent ribs crossing one another, which would cause problems for the finite element mesh. After each optimisation run, if a design variable reaches its limit, the mesh is rebuilt manually using the rib positions from the final iteration of the optimisation process. The model is then re-parameterised and the shape optimisation repeated. The optimisation problem was formulated as follows:

$$
\begin{aligned}
&\text{maximise} && BLF_{\text{Mode 1}} \\
&\text{subject to} && x^L \le x_i \le x^U && i = 1,2,...,n
\end{aligned}
\qquad , \qquad (5.1)
$$

where in this case, $\mathbf{x}$ are the shape variables, L and U denote the upper and lower limits on each variable, and BLF stands for buckling load factor.. No constraints other than those placed on the design variables are used at this stage.
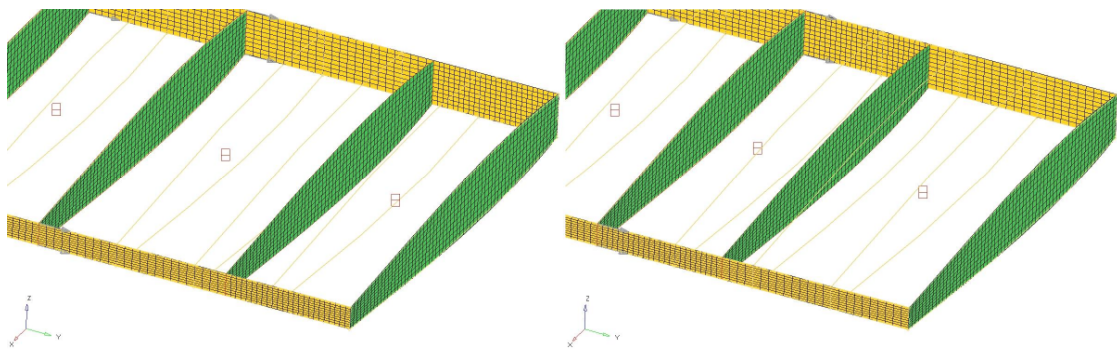
Figure 5.16 The effect of shape variables on the finite element model for rib pitch optimisation, with ribs moving in a spanwise direction.

An example of the results from this approach, applied to the model with three internal ribs, are shown in Figures 5.17 and 5.18. Optimising the rib pitch results in the buckling

load factor for mode one increasing by 28%. This is due to the location of the first buckling mode after optimisation being further towards the wing tip, where loadings are smaller. Obviously, this improvement in structural stability comes at no cost as far as additional mass is concerned. However the increased rib spacing in some parts of the wing may leave it more prone to localised shape deformation due to aerodynamic loadings, the prevention of which was addressed in Chapter 4. Approaches to the consideration of both structural stability and linear static behaviour within the optimisation process are discussed later in this chapter.
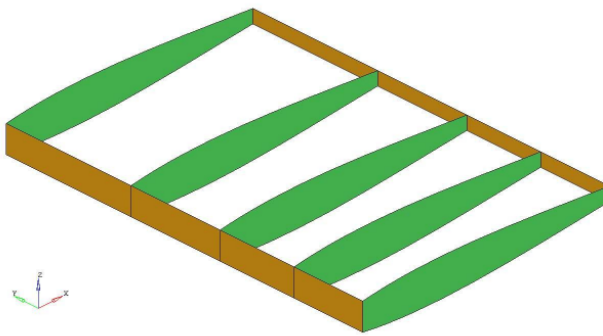
Figure 5.17 Optimised rib locations for maximum buckling load, with rib spacing decreased close to the root.
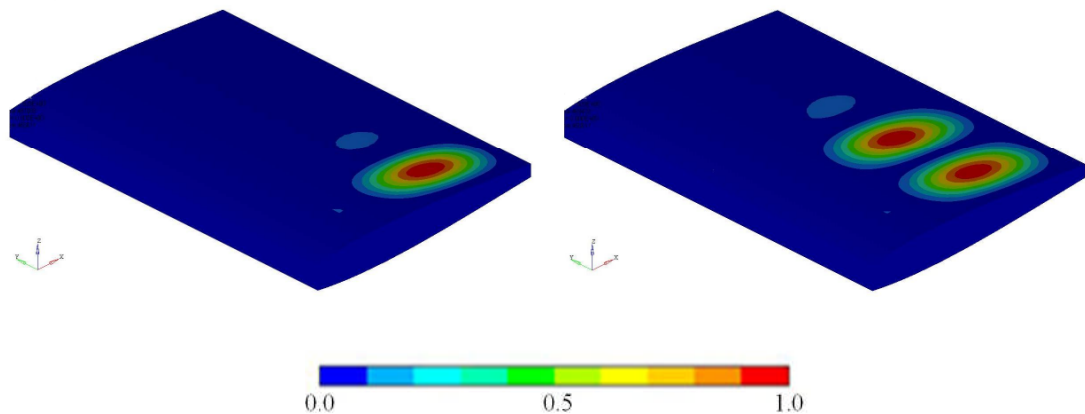
Figure 5.18 First buckling mode before (left) and after (right) optimisation, resulting in buckling occurring either side of rib closest to the root, and the buckling load factor increasing from 3.65 to 4.67.

5.1.2.2   Optimisation of Rib Pitch and Orientation

Next both the rib pitch and orientation are optimised for maximum buckling loads. Wing ribs are usually aligned with the air flow, as other orientations can cause changes in the wing's shape under aerodynamic loading which result in boundary layer separation. This test case examines whether this is the most structurally efficient orientation of the ribs. This is achieved in a similar way to the previous study, however this time the leading and trailing edges of each rib are assigned separate design variables and corresponding perturbation vectors. The same maximum and minimum values are applied to the design variables as used earlier allowing the ribs to be orientated between ±20° to the chordwise axis, as shown in Figure 5.19, where a negative angle corresponds to the leading edge being located further from the wing tip than the trailing edge (left) and the reverse for a positive angle (right). The optimisation problem is formulated in the same way as in Section 5.1.2.1, with a single objective and constraints only on the design variables.
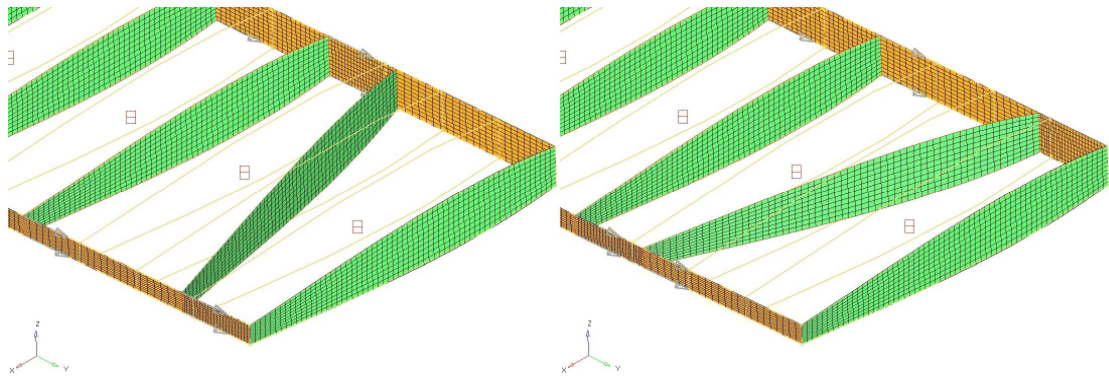
Figure 5.19 The effect of shape variables on the finite element model for rib pitch and orientation optimisation, showing ribs at negative (left) and positive (right) angle.

This approach results in no further improvements to the critical buckling loads over the optimisation of only the rib pitch. The angle of the ribs remains close to their original orientation, perpendicular to the leading and trailing edge spars, as shown in Table 5.1. Figure 5.20 shows the first five buckling modes for the original test case along with the results from the two shape optimisation approaches. As the only objective in the optimisation problem was the maximisation of the first buckling load factor, the increase in this critical load for both approaches is unsurprising. For the optimisation of only the rib pitch the buckling load factors for all five modes was increased, however the improvements at modes two to five are generally more modest. Optimisation of

pitch and orientation, on the other hand, results in a decrease in buckling loads at all modes when compared with the first shape optimisation. There is also a decrease in buckling load factors of modes four and five compared to the original model with uniform rib spacing. Clearly the increased number of design variables results in the optimisation problem being more difficult to solve. The optimised rib locations are similar for both shape optimisation approaches, therefore it is unlikely that these non-optimal solutions are caused by local optima. The only explanation is that the convergence criteria are allowing the optimisation process to be stopped at near-optimal solutions for the more complex optimisation problem.

Table 5.1 Optimised rib orientations for a test case with three internal ribs, with ribs numbered from root to tip.

Rib Number	1	2	3
Rib Angle (degrees)	-0.953	0.000	-1.377
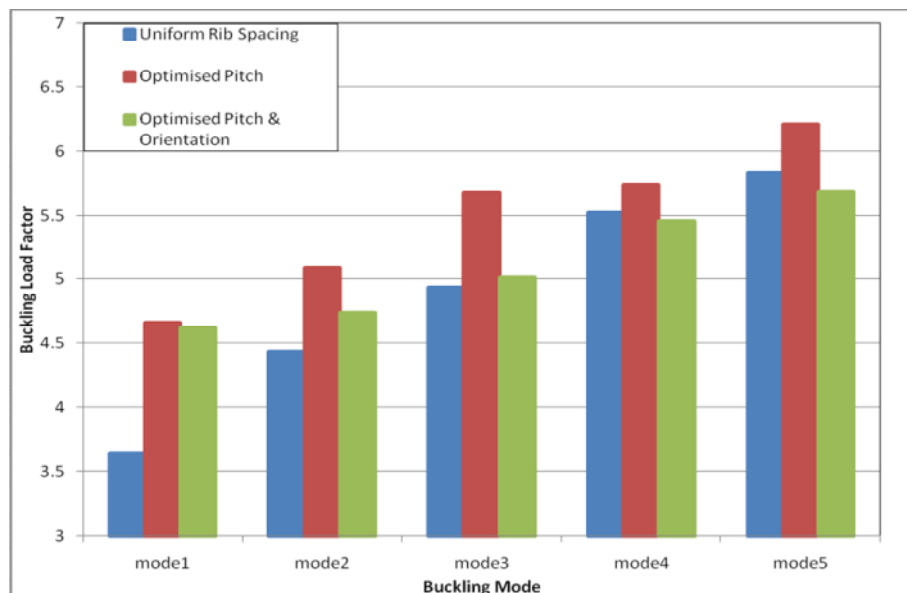
Figure 5.20 First five buckling load factors of wing sections with uniform rib pitch, optimised pitch, and optimised pitch and orientation.

A similar study investigated the optimal rib orientation's sensitivity to torsional loads. The trailing edge point force was reduced to 1kN while the leading edge point force remained at 2kN to introduce an element of torsion as well as bending. Again, this resulted in rib orientation remaining near-aligned to the flow.

5.1.2.3   Variation of the Number of Ribs

The approach to optimising rib positions used in Section 5.1.2.1 is adopted for further shape optimisation studies. This approach is applied to finite element models of the wing section, containing one, three, five and seven internal ribs. In all cases the rib spacing is reduced close to the root of the wing, where the first buckling modes occur. This can be seen in Figures 5.21 and 5.22 for one rib, and in Figures 5.23 and 5.24 for seven ribs. The result of using three ribs was shown earlier in Figure 5.17 and 5.18. Optimisation of the rib pitch using this approach gives substantial improvements in critical buckling loads over uniform rib spacing for all models, as shown in Figure 5.25. The locations of two ribs closest to the tip in Figure 5.23 are most likely arbitrary as the critical buckling load is insensitive to the design variables describing them.
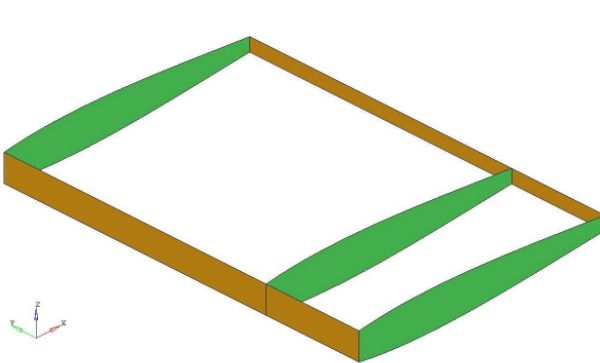
Figure 5.21 Optimised location of a single rib for maximum buckling load, with rib shifted towards the root.
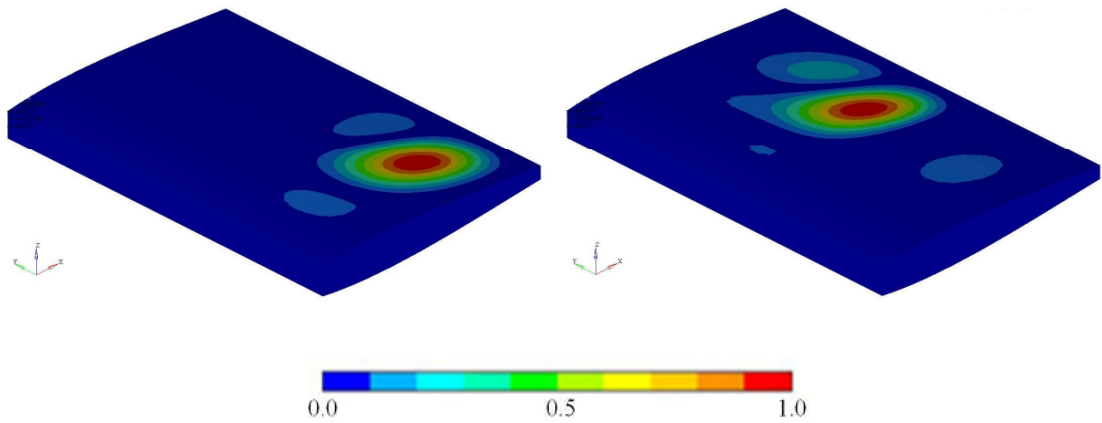
Figure 5.22 First buckling mode before (left) and after (right) optimisation. Before optimisation buckling occurs near the root, and after optimisation between the internal rib and wing tip.
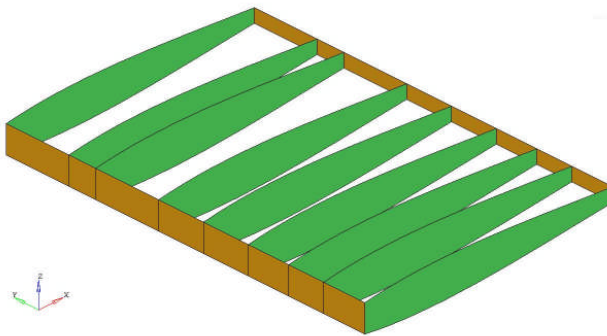
Figure 5.23 Optimised locations of seven internal ribs for maximum buckling loads. Rib spacing is reduced close to the root, and the two ribs closest to the tip are positioned arbitrarily.
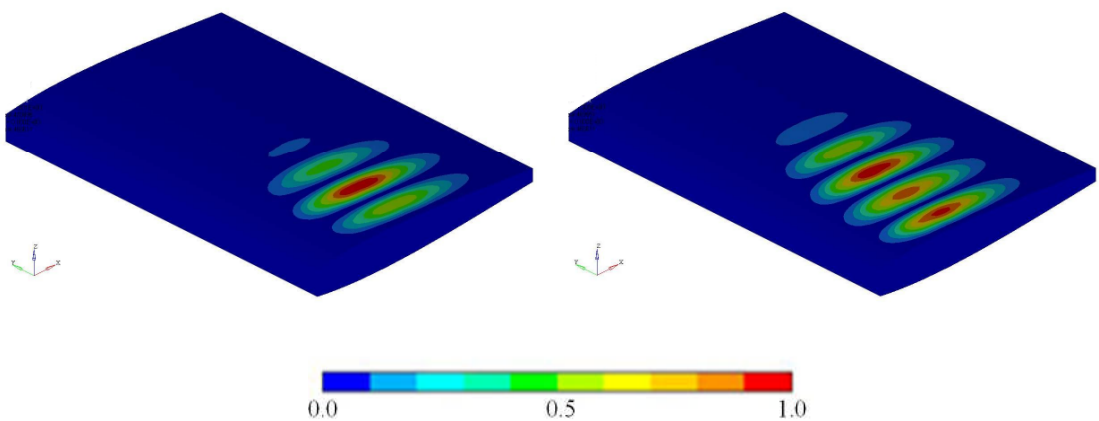
Figure 5.24 First buckling mode before (left) and after (right) optimisation. Optimisation results in a less localised buckling mode.
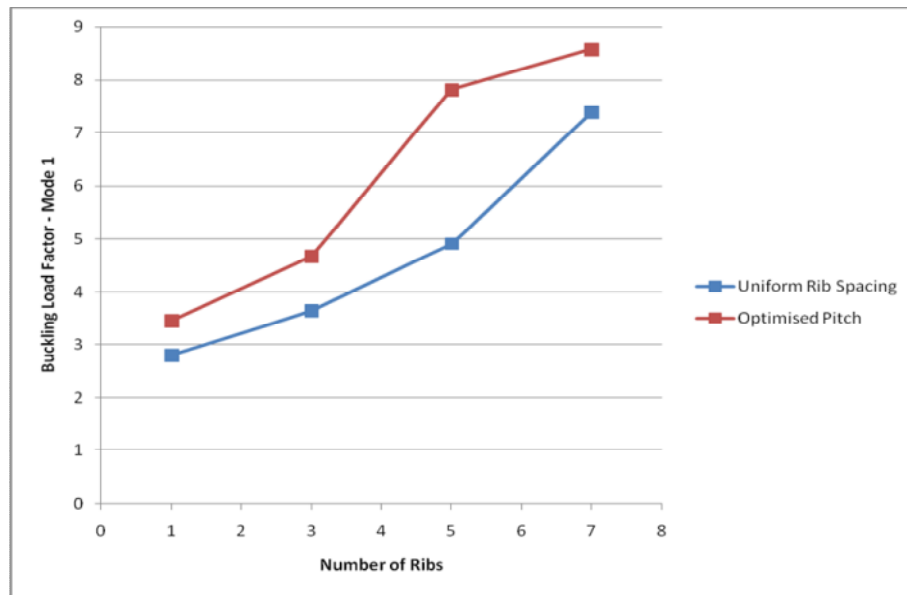
Figure 5.25 Increasing buckling load factor with increased numbers of ribs, showing improvements in structural stability resulting from shape optimisation.

5.1.2.4   Optimisation of Rib Pitch and Skin Thickness

The next stage of this optimisation study is to combine shape optimisation with sizing optimisation. This allows the skin thickness to be optimised as well as the rib positions. The optimisation is reformulated as follows:

$$
\begin{array}{lll}
\text{minimise} & \text{mass} & \\
\text{subject to} & BLF \geq 1.0 & , \qquad (5.2) \\
& x^L \leq x_i \leq x^U & i = 1,2,...,n
\end{array}
$$

where **x** now contains the shape variables, as used earlier, along with the skin thicknesses. This method is then applied to wing sections containing various numbers of ribs. The resulting skin thicknesses and rib spacings are shown in Figure 5.26. As expected, a larger number of ribs results in a smaller required skin thickness. The general pattern of rib spacing increasing towards the tip is similar to that seen when only optimising the rib pitch. This coincides with the locations of the first buckling modes. The only exception to this is in the seven-ribbed model, where the last three ribs are closer together. It is likely that these spacings are arbitrary as the buckling response

is quite insensitive to rib spacing in this part of the wing when the skin thickness is uniform and the average rib spacing is high.
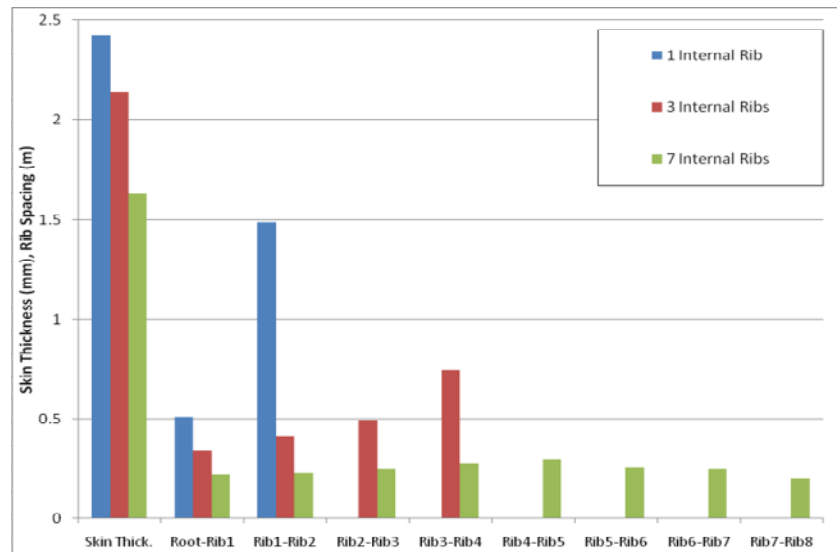
Figure 5.26 Optimised skin thicknesses and rib spacings for a uniform skin thickness and various numbers of ribs, with ribs numbered from root to tip.

Table 5.2 Optimised skin thicknesses and rib spacings for various numbers of ribs.

No. of Internal Ribs	1	3	7
Skin Thickness (mm)	2.42	2.14	1.63
Root - Rib1 (m)	0.51	0.34	0.22
Rib1 - Rib2 (m)	1.49	0.41	0.23
Rib2 - Rib3 (m)		0.50	0.25
Rib3 - Rib4 (m)		0.75	0.28
Rib4 - Rib5 (m)			0.30
Rib5 - Rib6 (m)			0.26
Rib6 - Rib7 (m)			0.25
Rib7 - Rib8 (m)			0.2

Up to this point all shape optimisation runs have been performed under the assumption that the wing has a uniform skin thickness. However it is more usual for the skin thickness to decrease toward the wing tip (as stresses are higher near the root) either by

selection of aluminium skin of varying thicknesses or varying the number of composite layers in the skin (Niu 1992). In order to examine this the wing's skin is split into four sections, corresponding to the spaces between ribs in the three ribbed model. The optimisation problem remains the same as in (5.2), however now the design variables y_j define the thicknesses of each section of the skin. The results from applying this method to the wing section with three ribs are shown below in Figures 5.27 and 5.28.
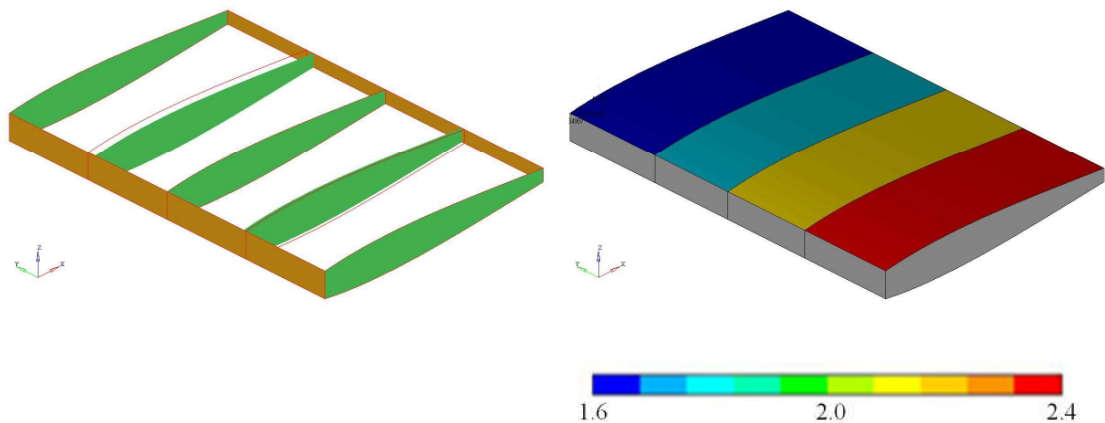
Figure 5.27 Optimised skin thicknesses and rib spacings for a uniform skin thickness and various numbers of ribs, with ribs numbered from root to tip.
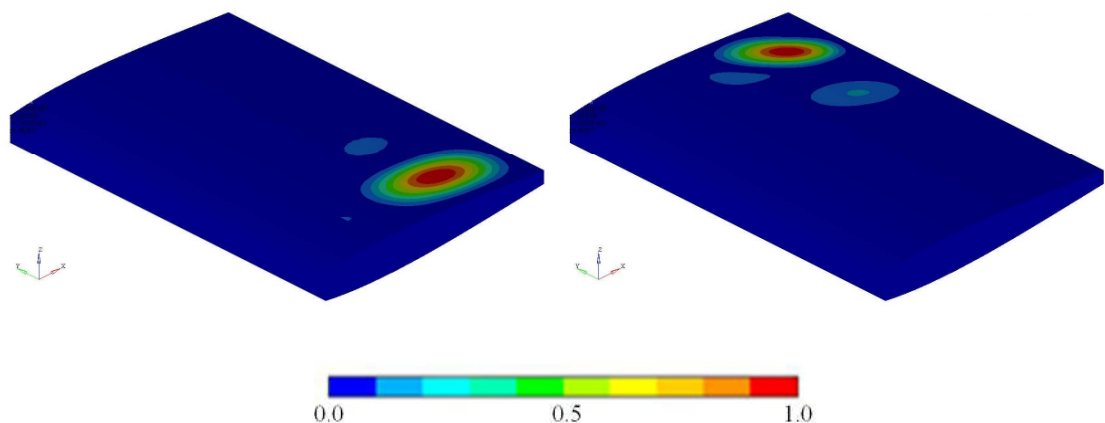
Figure 5.28 First buckling mode before (left) and after (right) optimisation, with buckling occurring at the wing tip after optimisation.

Figure 5.27 (left) shows the optimised rib positions with the red outlines indicating the original, uniformly spaced rib locations. The changes in rib pitch are much smaller than when using purely shape optimisation, however the same pattern exists, with rib

spacings increasing slightly towards the wing tip. Figure 5.27 (right) shows the optimised skin thicknesses, which are clearly thicker towards the root, as expected. The first buckling modes before and after optimisation are shown in Figure 5.28. The buckling load factor is decreased from 3.65 to 1.0 satisfying the constraint in (5.2). Mass is decreased by 35% compared to the baseline design and 5.8% compared to the optimised uniform skin thickness. This method was repeated on models with varying numbers of ribs. In all cases rib pitch remains almost uniform. The resulting skin thicknesses are shown in Figure 5.29. Obviously the higher number of ribs reduces the required skin thicknesses and therefore the mass of the skin. However the total structural mass is dependent on the mass of each rib, which is not considered here.
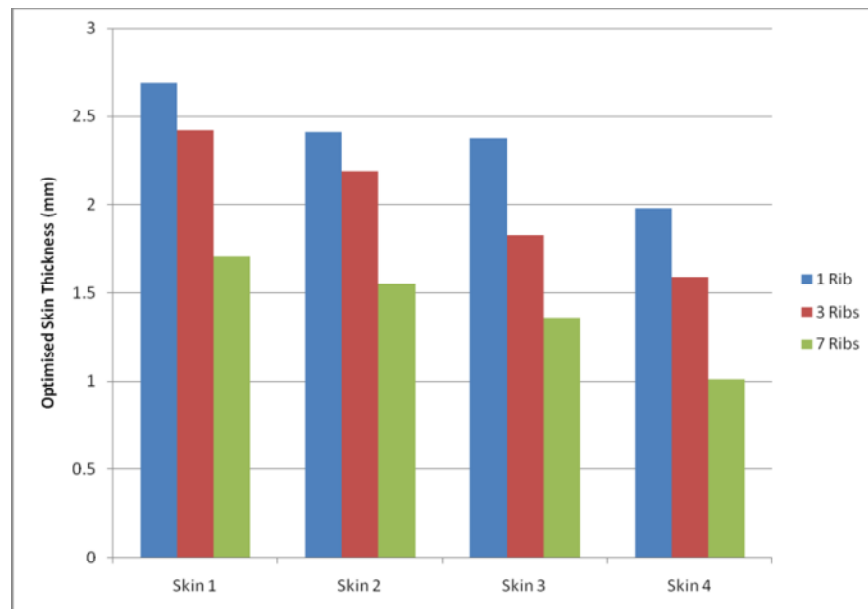
Figure 5.29 Optimised skin thicknesses for wing sections with various numbers of ribs, with skin sections numbered from root to tip.
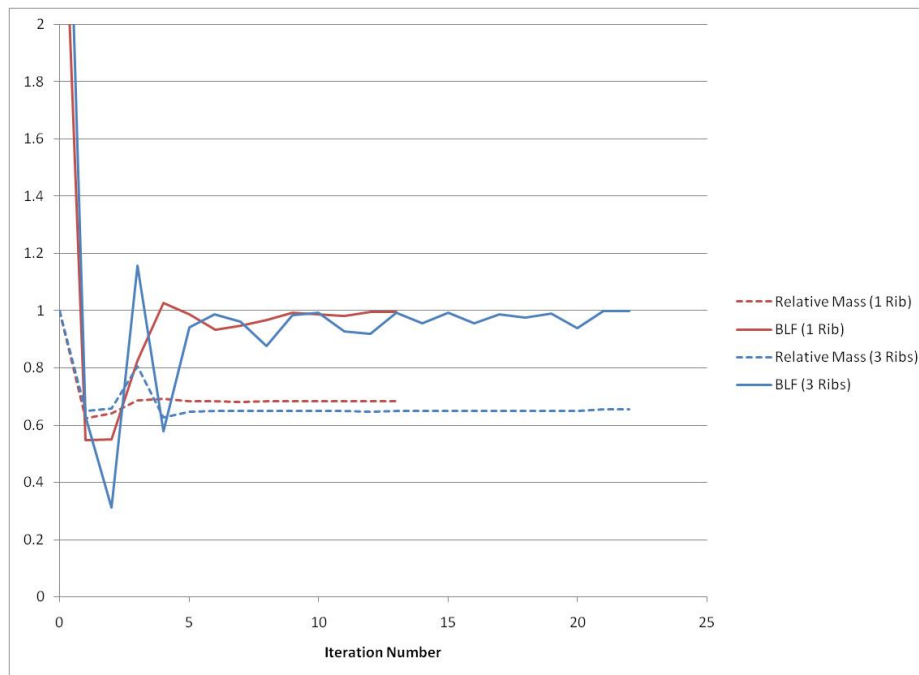
Figure 5.30 Convergence curves showing the increased number of iteration required to reach an optimal solution for a higher number of design variables (number of ribs).

5.2 Interactions Between Shape and Topology Optimisation

Although in some applications it can be possible to combine shape and topology optimisation into a single optimisation problem (Zhou, Pagaldipti et al. 2004), the difficulties with buckling constraints remain. Therefore it is necessary to look at this application of structural optimisation as a multi-level process. The approach usually adopted to get around these issues is to start with a minimum compliance design from topology optimisation and then interpret the results as shell structures for shape optimisation where buckling can be considered (Schramm, Zhou et al. 2004). However it may also be necessary to consider the effect of the structural layouts derived from shape optimisation at the topology optimisation stage. This is the focus of the following investigation.

5.2.1 Test Cases

The first test case used for this investigation is the un-tapered wing section used in the previous sections. Five uniformly spaced ribs with front and rear spars are represented with 2D shell elements. The wing skin is also defined with shell elements, with thicknesses taken from the results of size optimisation with buckling constraints performed in Section 5.1.2.4. The internal spaces within the wing section are defined with designable 3D solid elements, whose relative densities act as design variables in the topology optimisation problem. Two load cases are applied to the wing section, both constraining nodes in all degrees of freedom at the root. The first is a simple bending case with 2kN point forces applied in an upward direction at the leading and trailing edges of the wing tip, as shown in Figure 5.31 (left). The second is a twisting cases with opposing 2kN point forces at the leading and trailing edges of tip, as shown in Figure 5.31 (right). These point forces could, for example, represent attachment points for control surfaces.
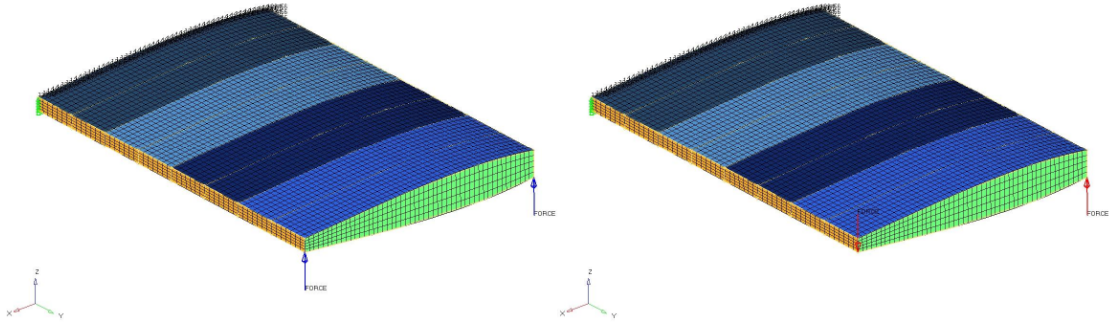
Figure 5.31 Bending (left) and torsional (right) load cases used for investigating the effect of ribs on topology optimisation.

In order to evaluate the sensitivity of optimal topologies to the presence of the ribs, rib thicknesses are varied from 25mm to 250mm. As mentioned in Chapter 4 when dealing with explicit displacement constraints, limits on mesh resolution result in topology optimisation forming unrealistically large structural members. It is therefore necessary to use rib thicknesses of a comparable size if they are to make any significant contribution to the structural behaviour of the wing section. At this stage in the design process it is more useful to define the rib thicknesses in relation to the minimum member size constraint. Initially, optimisation is performed using only the first (bending) load case. The optimisation problem is formulated as follows:

$$
\begin{aligned}
\text{minimise} \quad & \text{compliance}_{LC1} \\
\text{subject to} \quad & \text{volumefraction} \leq 0.25 \\
& \text{membersize} \geq 100\text{mm} \\
& \rho_L \leq \rho_i \leq 1 \qquad i = 1,2,...,n
\end{aligned}
\qquad , \qquad (5.3)
$$

where *LC1* denotes the first load case. An extrusion constraint is also applied in the z-direction in order to force the optimiser to distribute material in continuous structural members. The effect of ribs on the topologies of designs optimised for bending compliance is found to be negligible, as can be seen in Figure 5.32. This is expected as the ribs, orientated in this way, provide very little resistance to spanwise bending.
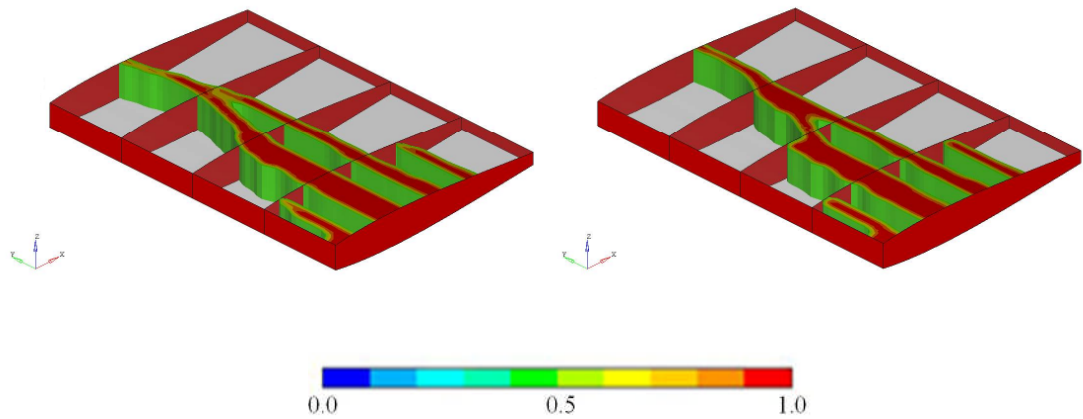
Figure 5.32 Contours of element density optimised for bending compliance with 25mm (left) and 200mm (right) non-designable ribs included, showing multiple spars at the root decreasing to a single spar at the tip.

The study is repeated using the second (torsional) load case, with the optimisation problem formulated in the same manner:

$$
\begin{aligned}
&\text{minimise} &&\text{compliance}_{LC2} \\
&\text{subject to} &&\text{volumefraction} \leq 0.25 \\
&&&\text{membersize} \geq 100\text{mm} \\
&&&\rho_L \leq \rho_i \leq 1 &&i = 1,2,...,n
\end{aligned}
\qquad . \qquad (5.4)
$$

In this case, the presence and thickness of the ribs have a much greater effect. At low rib thicknesses the material is distributed to form diagonal members, similar to those seen in Section 4.12 where no ribs are present. This can be seen in Figure 5.33. At higher rib thicknesses, where thicknesses are close to the minimum member size, these diagonal members are no longer seen. Instead material is used to form two spars perpendicular to the ribs, one at the leading edge and one at the trailing edge, as shown in Figure 5.34. It is clear that the ribs allow forces to be transmitted from leading to trailing edges without the need for additional structural members. This two spar configuration is typical of most high aspect ratio wing (Sensmeier and Samareh 2004) but was not seen in the topology optimisation of the wing presented by Rao, Kiran et al. (2008), as ribs were not included at this stage of the optimisation process.
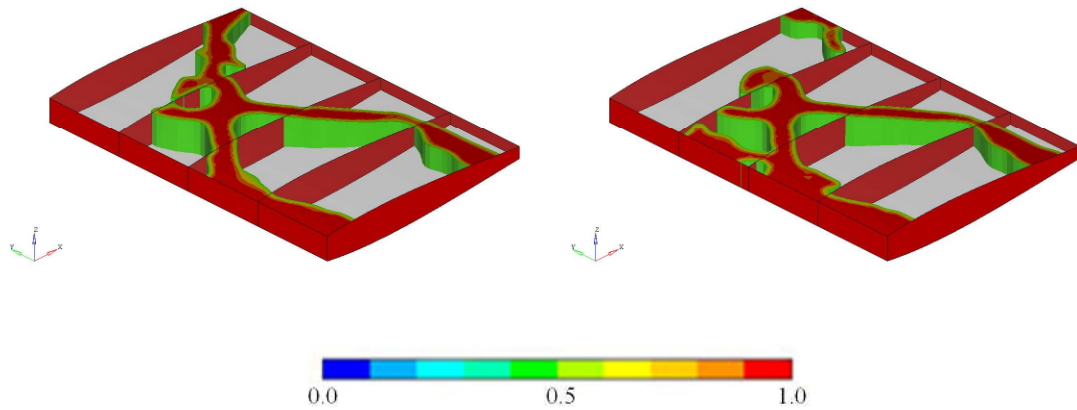
Figure 5.33 Contours of element density optimised for torsional compliance with 25mm (left) and 50mm (right) non-designable ribs included, showing diagonal spars connecting to the root at two points.
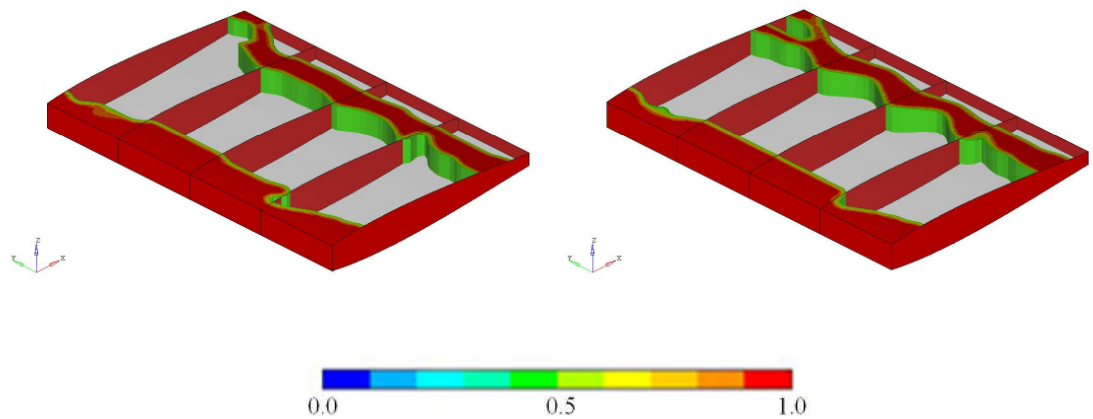
Figure 5.34 Contours of element density optimised for torsional compliance with 100mm (left) and 200mm (right) non-designable ribs included, showing two spanwise spars near the leading and trailing edges.

Next the two load cases are combined to generate designs that improve both bending and twisting stiffness. This is achieved using a weighted compliance, with the optimisation problem formulated as follows:

minimise $\qquad C_{\mathrm{W}} = W_1 C_1 + W_2 C_2$

subject to $\qquad$ volumefraction ≤ 0.25

$\qquad\qquad$ membersize $\geq 100\mathrm{mm}$ $\qquad\qquad\qquad\qquad$, $\qquad$ (5.5)

$\qquad\qquad \rho_L \leq \rho_i \leq 1 \qquad\qquad i = 1,2,...,n$

where C are the compliances, W are weighting factors, and the indices 1 and 2 refer to the bending and torsional load cases, respectively. The ratio of theses weighting factors W_2/W_1 is varied from 1 to 10 in order to find a value that gave both load cases equal significance in the objective function, i.e. $W_1 C_1 \approx W_2 C_2$. Initially no ribs are included in the finite element model. The results from this study are shown in Figures 5.35 and 5.35. With equal weightings, material distribution is dominated by the structural members clearly used to increase bending stiffness, as in Figure 5.35 (left). A ratio of ten produces predominantly diagonal members for increasing torsional stiffness, shown in Figure 5.36. A weighting of 1:3 is found to be a good compromise, resulting in a combination of the members seen in both the bending and twisting test cases used earlier (Figure 5.35 (right)). Using these weightings results in the optimised bending compliance being approximately three times larger than the twist compliance (shown in Figure 5.37) making the two load cases of equal importance in the weighted compliance.
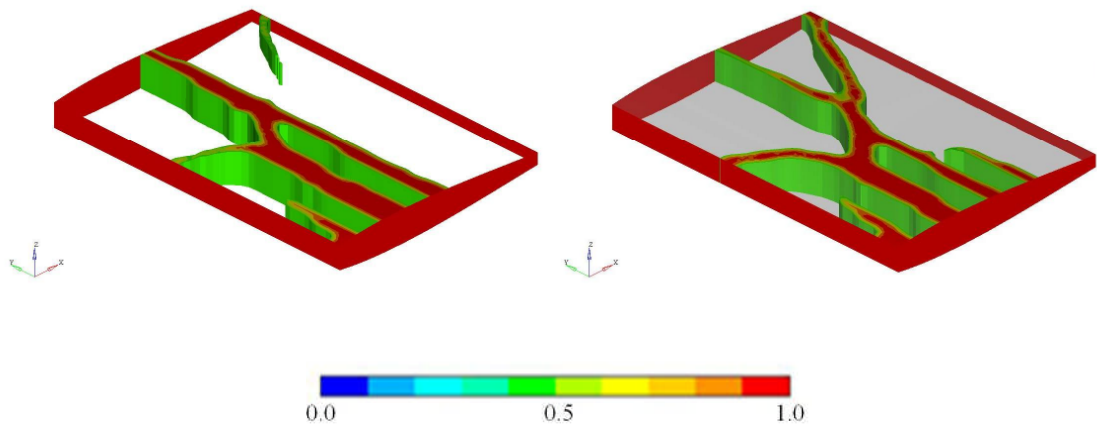
Figure 5.35 Contours of element density optimised for weighted compliance with weighting factors of 1:1 (left) and 1:3 (right) on bending and twisting compliances, respectively. A weighting of 1:1 results in structures for bending stiffness, and 1:3 results in members that improve both bending and torsional stiffness.
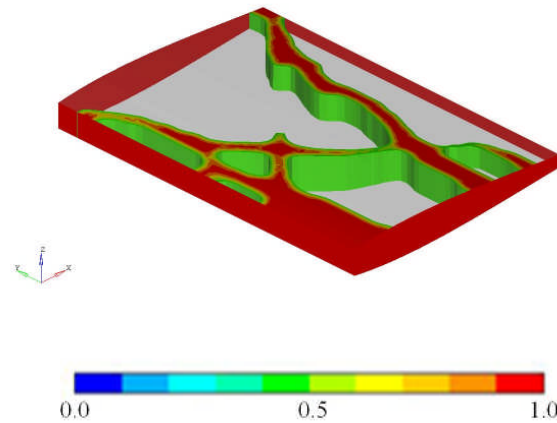
Figure 5.36 Contours of element density optimised for weighted compliance with weighting factors of 1:10, resulting in members that predominantly improve torsional stiffness.
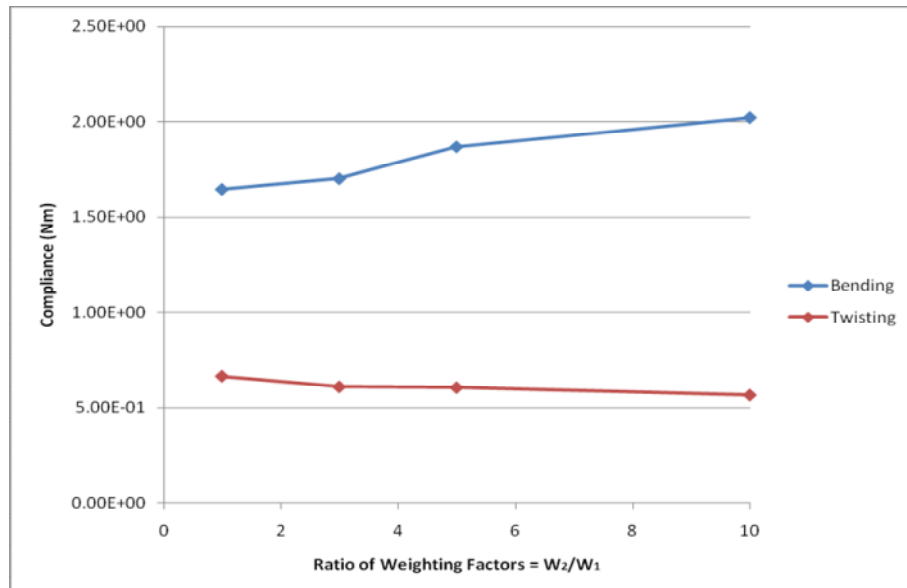
Figure 5.37 The effect of weighting factors on optimised compliances of bending (C_1) and torsional (C_2) load cases.

The same study of design sensitivity to rib thicknesses is repeated using the new weighted compliance formulation in (5.5) and the weighting selected in the previous study. Again, rib thickness is varied from 25mm to 250mm. The presence of the ribs has little effect on the material distributions when the rib thickness is lower than the minimum member size. The only noticeable effect is that all structural members end at a rib, never in between, as shown in Figure 5.38, as the ribs allow loads to be transferred

from the shorter spars to the longer ones running all the way to the wing tip. At a thickness of 100mm (Figure 5.39 (left)) the optimised designs begin to differ quite significantly, with several additional members, some diagonal some spanwise. At even higher rib thicknesses the resultant topologies return to the two spar configuration shown in Figure 5.34, but with the addition of small spanwise spars between the root and first rib, as shown in Figure 5.40, which are beneficial to bending stiffness.
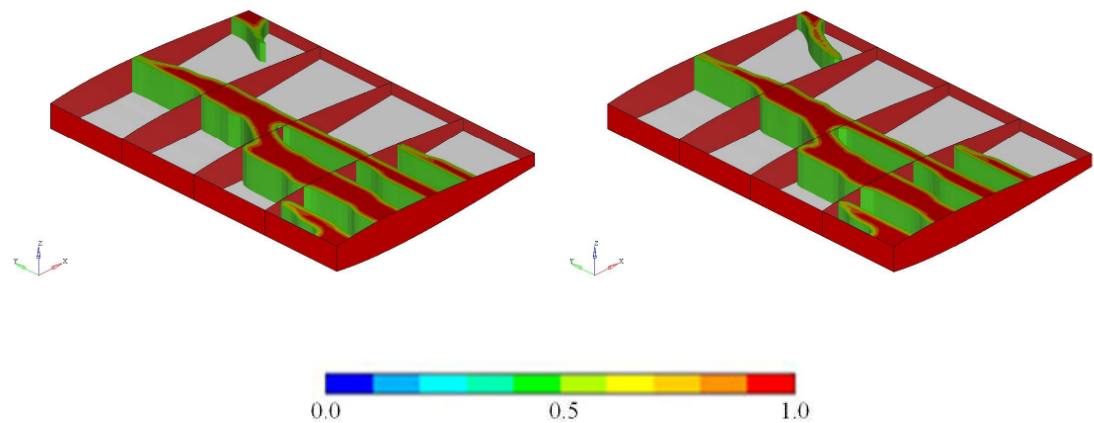
Figure 5.38 Contours of element density optimised for weighted compliance with 25mm (left) and 50mm (right) non-designable ribs included.
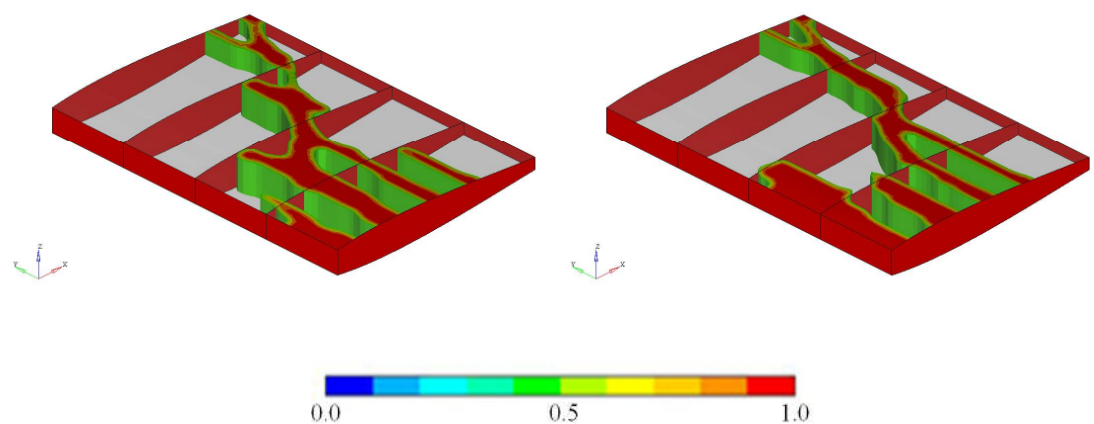
Figure 5.39 Contours of element density optimised for weighted compliance with 100mm (left) and 150mm (right) non-designable ribs included.
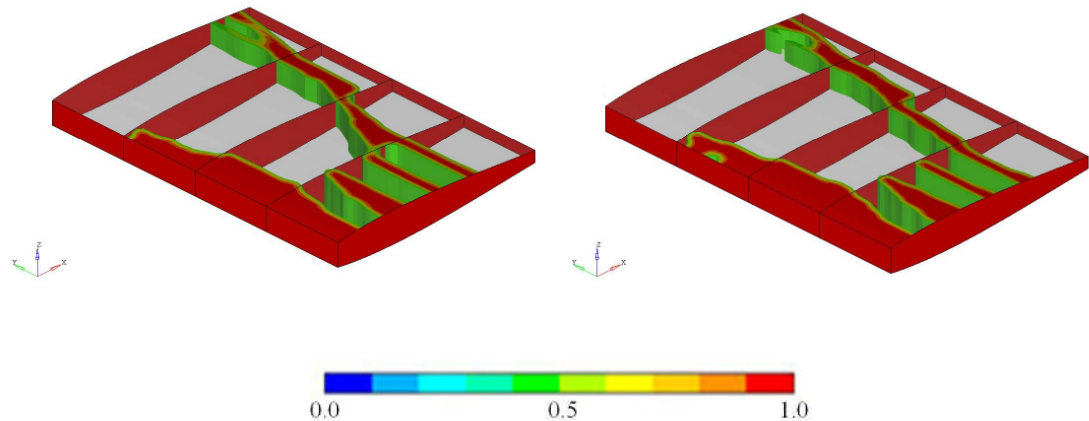
Figure 5.40 Contours of element density optimised for weighted compliance with 200mm (left) and 250mm (right) non-designable ribs included.

The results from all rib thickness sensitivity studies are compared in Figure 5.41. It is clear that the effect of the ribs on torsional compliance is much greater than the effect on bending compliance. This is expected, as ribs play no part in improving the spanwise bending stiffness of a wing. The only notable improvement in bending compliance due to increased rib thickness occurs in the case where only torsional compliance is optimised, see Figure 5.41 *(Bending (Twisting Load Case))*. This is due to the considerable change in the optimised topologies from Figure 5.33 to Figure 5.34, i.e. the transition from diagonal spars to spanwise spars. Clearly the spanwise spars are better suited to improving bending stiffness than the diagonal ones. There is one other obvious point to be observed in Figure 5.41. As is to be expected, the lowest compliance for either load case occurs when only the compliance for that load case is used as the objective function. However, optimising for the compliance of one load case results in a higher compliance for the other. The weighted compliance formulation offers a compromise, and allows the generation of design concepts that perform satisfactorily for both cases.
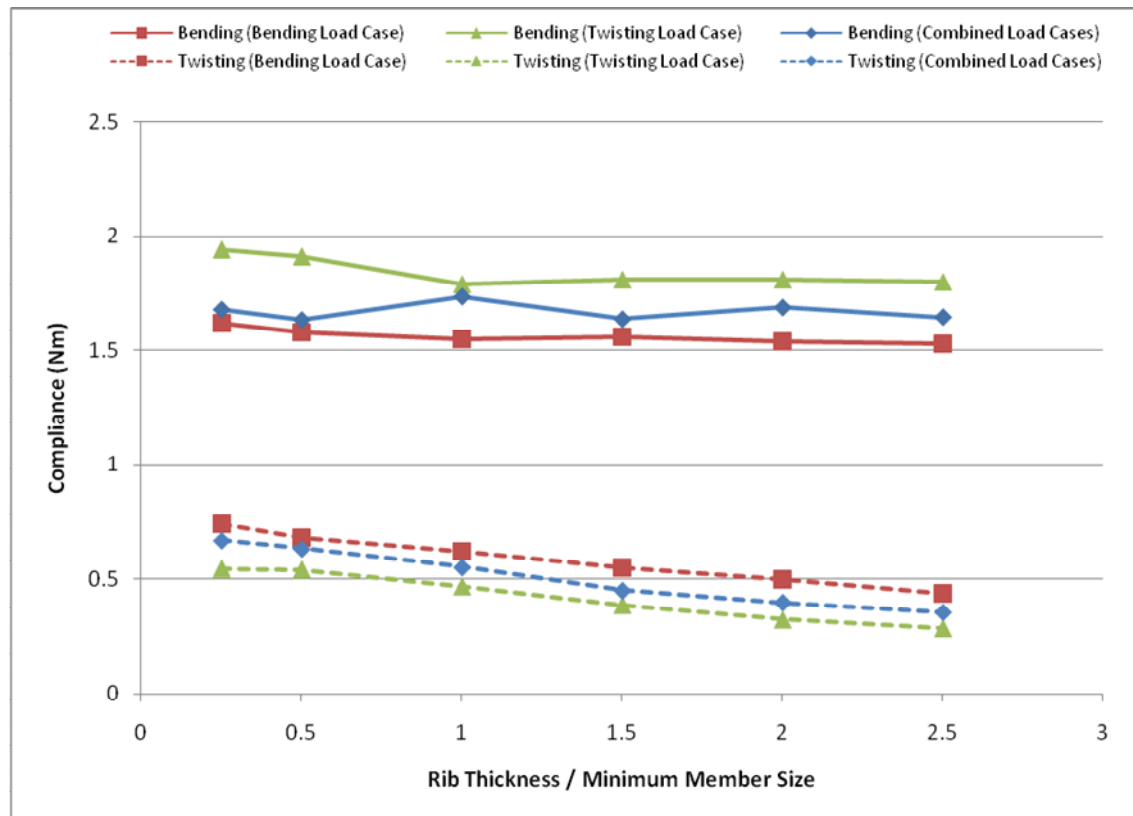
Figure 5.41 The effects of rib thicknesses on bending and torsional compliances for various formulations of the topology optimisation problem.

5.3 Application to UAV Design

In order to demonstrate how the methods and techniques explored in this work might be applied to optimising an aircraft's structural architecture, a final optimisation study is performed on the entire UAV wing. The aim of this study is to combine methods for determining: optimal spar positions to reduce bending and twisting; the location of additional structural reinforcement to maintain the wings aerodynamic shape; and rib positions to improve structural stability.

5.3.1 Methodology

The optimisation frameworks used to achieve these aims are shown in Figure 5.42. Both approaches start with a finite element model of the UAV wing made up of shell elements representing the wing skin, front and rear spars at the leading and trailing edges, uniformly spaced ribs, and control surfaces. Pressure loads derived from CFD for the 3.5g manoeuvre are applied to the skin and control surfaces. The positions of each rib are linked to a design variable via the perturbation vector approach used in Section 5.1.2. Control surfaces are attached to the spars using rigid elements at the location of fixed ribs whose positions are not to be optimised. These fixed points are located at the root of the wing, where the wing transitions from tapered to un-tapered, half way along the un-tapered wing and finally, at the tip. The reason for this is that if the location of control surface connection points are allowed to move, the optimiser will always move these points towards the aircraft's centreline to reduce bending moments. The optimised rib positions would then not truly represent the optimal locations to increase buckling loads, and solutions would become trivial. The positions of the moveable ribs are then optimised to maximise the buckling load factor.

Method 1

Method 2

Topology Optimisation
(Optimise locations of structural
members to minimise compliance)

Shape Optimisation
(Optimise rib pitch to maximise critical
buckling load)

Shape Optimisation
(Optimise rib pitch to maximise critical
buckling load)

Topology Optimisation
(Optimise locations of structural
members to minimise compliance,
with non-designable ribs included)

Interpret Material Distribution as
Shell Structures
(Combine with optimised ribs then
optimise thicknesses of all shell
structures)

Interpret Material Distribution as
Shell Structures
(Optimise thicknesses of all shell
structures)

Figure 5.42 Two approaches to combining topology, shape and sizing optimisation for designing the structural architecture of a UAV wing.

The next step in the optimisation process is to define designable space within the aircraft using 3D elements. These designable elements are covered in non-designable 2D shell elements on which the aerodynamic pressure loads are applied. Two load cases are applied to the model, the 3.5g flight loads along with the symmetrical loading explored in Section 4.4.4. Topology optimisation is performed with constraints on tip deflection, twist and volume fraction, with an objective of minimising the compliance of the symmetrical load case. The rationale behind this is to allow the optimal positions of the spars to be located, in order to satisfy the displacement and twist constraints. Once these constraints are satisfied, additional material can then be used to reinforce the wing in areas of high aerodynamic pressures, in order to minimise the objective function. This helps maintain the wing's cross-sectional shape. So, assuming the wing has been designed for a specific lift-drag ratio, minimising the deformation of its cross-sectional shape is considered equivalent to maintaining a similar lift-drag ratio. This assumption is highly idealised but it enables the consideration of aerodynamic performance without the need for expensive flow analyses.

The difference in the two approaches, shown in Figure 5.42, is in the way shape and

topology optimisation are combined. In Method 1 shape and topology optimisations are performed independently. Optimised rib positions from the shape optimisation are then combined with discrete structural members, interpreted from the material distribution from topology optimisation. In Method 2 the optimised rib positions from the shape optimisation are included as non-designable structures in the FE model used for topology optimisation. Rib thicknesses are made equal to the minimum member size constraint in the topology optimisation problem, as in Section 5.2; values lower than this were found to make the effect of their presence negligible. The resultant material distribution, including the non-designable material, is then interpreted as discrete structural members.

Finally, new FE models are constructed, representing all structural members with 2D shell elements. The thicknesses of all members in the new models, along with each section of the wing's skin are then defined as design variables for sizing optimisation. At this stage it is possible to include a range of design constraints such as buckling loads, local stresses, tip deflection and twist, and global compliances. The final objective of the optimisation procedure is to minimise the structural mass of the UAV subject to these design constraints.

5.3.2   Baseline Architecture Design

In order to carry out shape optimisation on the UAV a baseline design was required whose geometry could then be parameterised into design variables. This baseline geometry is shown in Figure 5.43. It consists of front and rear spars at the leading and trailing edges with twenty ribs spaced uniformly with a 0.6m pitch, as is commonly seen in most modern transport aircraft (Sensmeier and Samareh 2004). This baseline architecture is not only used as a starting point for the shape optimisation, but also to assess any advantages of the proposed optimisation methodology. The baseline design underwent the same sizing optimisation as described above so that the benefits of additional structural members derived from topology optimisation could be investigated.
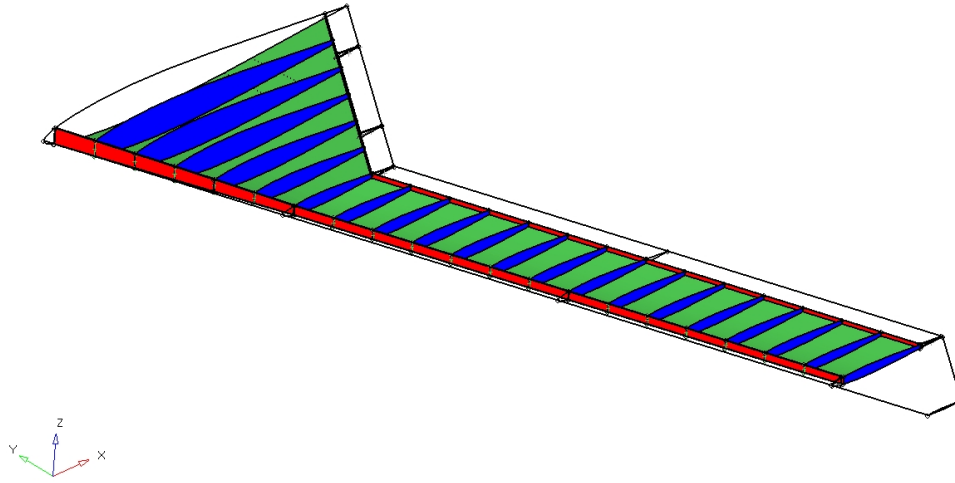
Figure 5.43 Baseline UAV structural architecture showing spars (red), ribs (blue) and wetted surface (green).

5.3.3 Shape Optimisation

As described earlier, the spanwise position of each rib in the baseline model is defined as a design variable. The position of leading and trailing edges of each rib are allowed to vary independently, as in the earlier test case in Section 5.1.2.2. The test case suggests that orientation of the ribs will remain aligned to the flow, however these additional degrees of freedom are included as this may not be true for all wing shapes and loadings. Three of the ribs were fixed for the connection of control surfaces, resulting in thirty four design variables. At this stage a uniform skin of thickness of 2mm was used and front and rear spars were both 20mm thick. The wing was constrained in all degrees of freedom at the root, with the 3.5g flight loads from CFD applied to the skin. The shape optimisation problem was formulated as follows:

$$
\begin{aligned}
\text{maximise} \quad & BLF_{\text{Mode 1}} \\
\text{subject to} \quad & -200mm \leq x_i \leq 200mm \qquad i = 1,2,...,34
\end{aligned}
\qquad , \qquad (5.6)
$$

where x_i are the changes in the spanwise location of the ribs, and the limits are imposed to prevent highly deformed elements in the FE mesh.
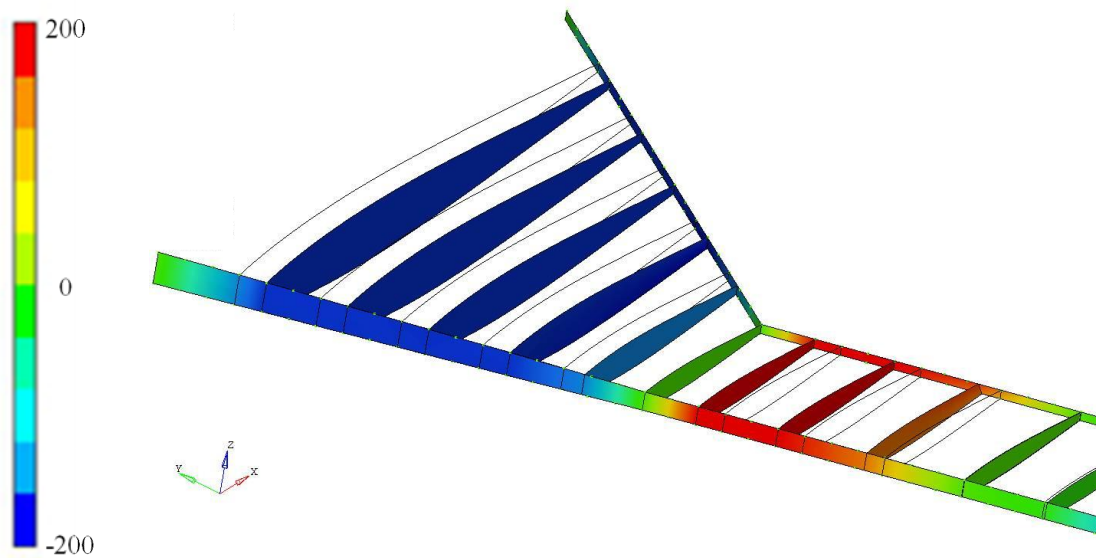
Figure 5.44 Changes in spanwise location of ribs optimised for maximum buckling loads.
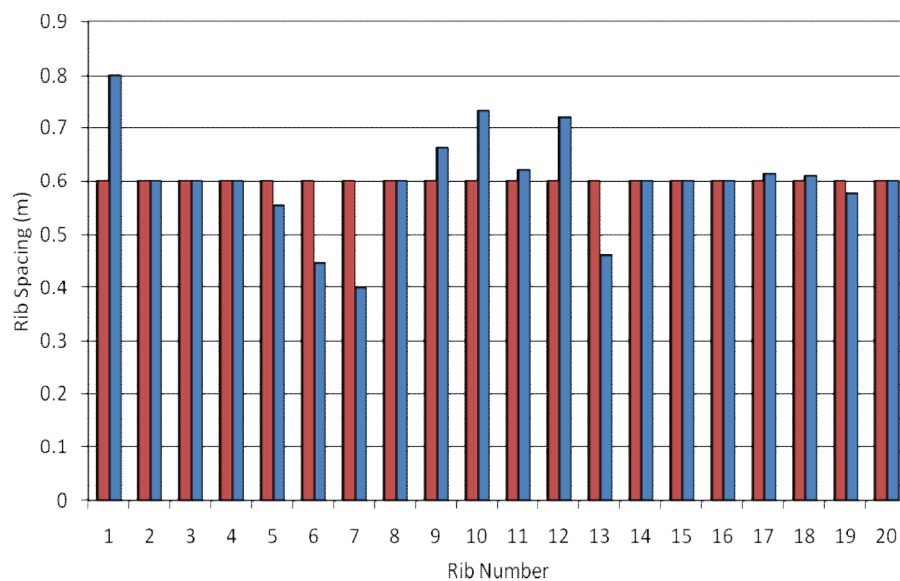
Figure 5.45 Rib spacings before (red) and after (blue) shape optimisation, with ribs numbered from root to tip and the tapered wing section ending at rib six.

Figure 5.46 (left) shows the first buckling mode before optimisation, with uniform rib spacing. Unlike in the earlier case studies this first mode does not occur at the root of the wing but in the area where the wing transitions from tapered to un-tapered. Figure 5.44 shows the displacements of the ribs from their original positions and Figure 5.45 shows the original and optimised rib spacings. As would be expected, rib spacing in the

area where the first mode occurs is reduced, with rib spacing increasing in both directions from this area. Rib orientation has remained aligned with the flow, as seen in the earlier test case. The first buckling mode resulting from the optimised rib positions is shown in Figure 5.46 (right). The first buckling mode is now less localised, resulting in the buckling load factor being increased from 0.96 to 1.14. Although the aircrafts mass was not taken into consideration at this stage, the repositioning of the ribs in the tapered wing section actually led to the UAV's structural mass decreasing, as the cross sectional area of the ribs was reduced.
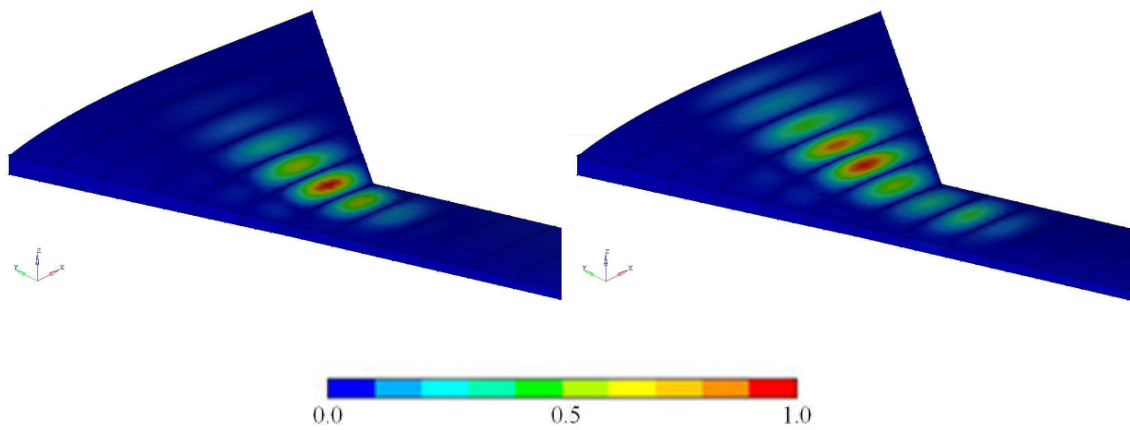
Figure 5.46 First buckling mode before (left) and after (right) shape optimisation, resulting in the buckling mode becoming less localised and the buckling load factor increasing from 0.96 to 1.14.
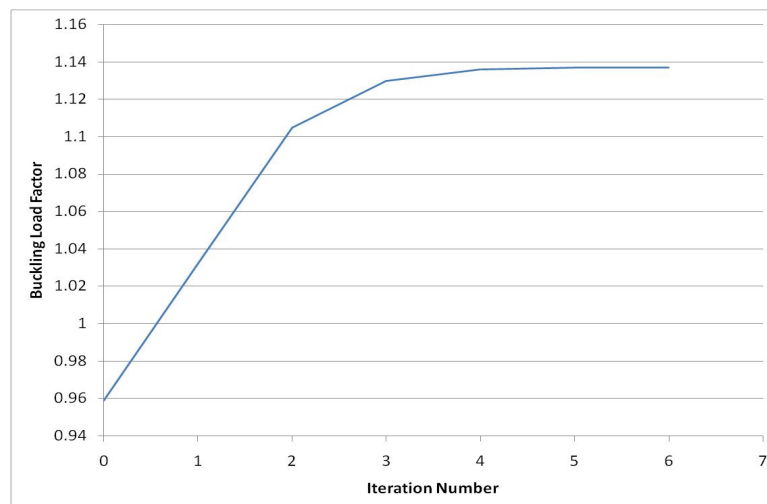
Figure 5.47 Convergence curve showing buckling load factor increasing from 0.96 to 1.14 throughout the optimisation process.

5.3.4 Topology Optimisation

The second stage of the optimisation process is to use topology optimisation for determining the optimal layout of additional structural members. Here, two methods are adopted for combining the results of shape and topology optimisations, as described in Section 5.3.1. Method 1 involves interpretation of the optimised material distribution from Section 4.3.4 (Figure 5.48), where ribs were not considered, as discrete structural members. These members are then combined with the optimised rib positions calculated above. Method 2 adopts the approaches investigated in Section 5.2 where ribs are included in the topology optimisation problem as non-designable elements. Designable material is added to the finite element model resulting from the preceding shape optimisation. Two load cases are applied, the first using the 3.5g flight loads, the second using the symmetrical load case investigated in the previous chapter. A rib thickness of 150mm is used, which corresponds to a minimum member size constraint, and the topology optimisation problem formulated as follows:

$$
\begin{aligned}
&\text{minimise} &&\text{compliance}_{LC2} \\
&\text{subject to} &&\text{volumefraction} \leq 0.25 \\
& &&\text{displacement}_{\text{wingtip } LC1} \leq 150mm \\
& &&\left|\text{twist}_{\text{wingtip } LC1}\right| \leq 0.25° \\
& &&\text{membersize} \geq 150\text{mm} \\
& &&\rho_L \leq \rho_i \leq 1 &&i = 1,2,...,n
\end{aligned}
\qquad . \qquad (5.7)
$$

The material distribution resulting from this approach is shown in Figure 5.49. The inclusion of the ribs has a clear effect on the resulting design. When ribs are not included most of the structural members connect the leading and trailing edges, most likely to transmit torsional forces between the two spars and reduce twisting angle. The presence of the ribs removes the need for this. A great deal of the material is now positioned in the front third of the wing, with members altering orientation between each rib. This helps to reduce the compliance of the second load case, as the aerodynamic loadings are much higher towards the wing's leading edge.
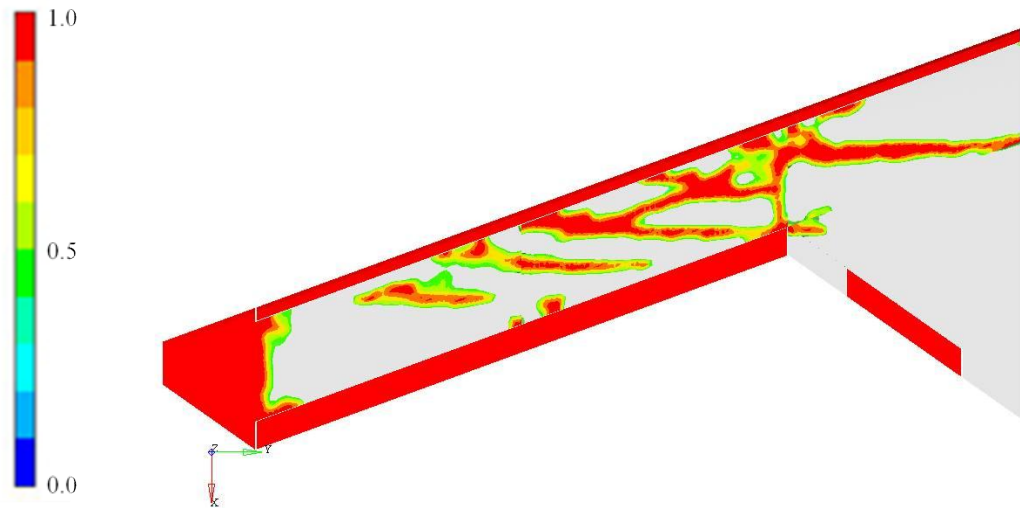
Figure 5.48 Contours of element density optimised using Method 1 (Figure 5.42) with no ribs included as non-designable structures.
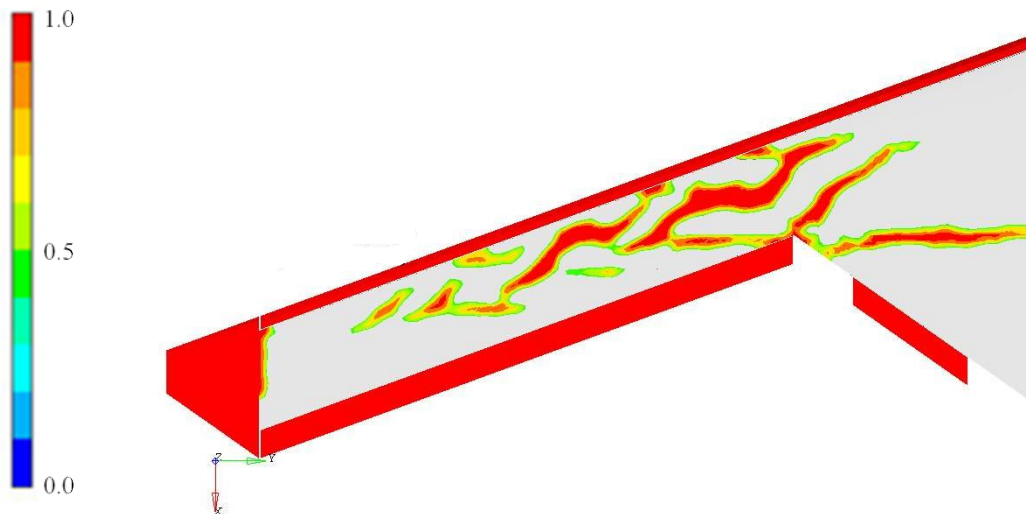
Figure 5.49 Contours of element density optimised using Method 2 (Figure 5.42) with non-designable ribs included.

In order to investigate the material distribution's sensitivity to the prescribed rib thicknesses, the optimisation problem is repeated with rib thicknesses reduced from 150mm to 100mm and then 50mm. All other design parameters, including the minimum member size remain the same. Figure 5.50 shows the material distribution resulting

from the use of a 50mm rib thickness. On comparison with Figure 5.49 it is clear that there is very little change in the design. Any changes do not affect the general topology of the structure. This suggests that, in this case, the designs are reasonably insensitive to the rib thickness used. The important factor is whether the ribs are included at all.
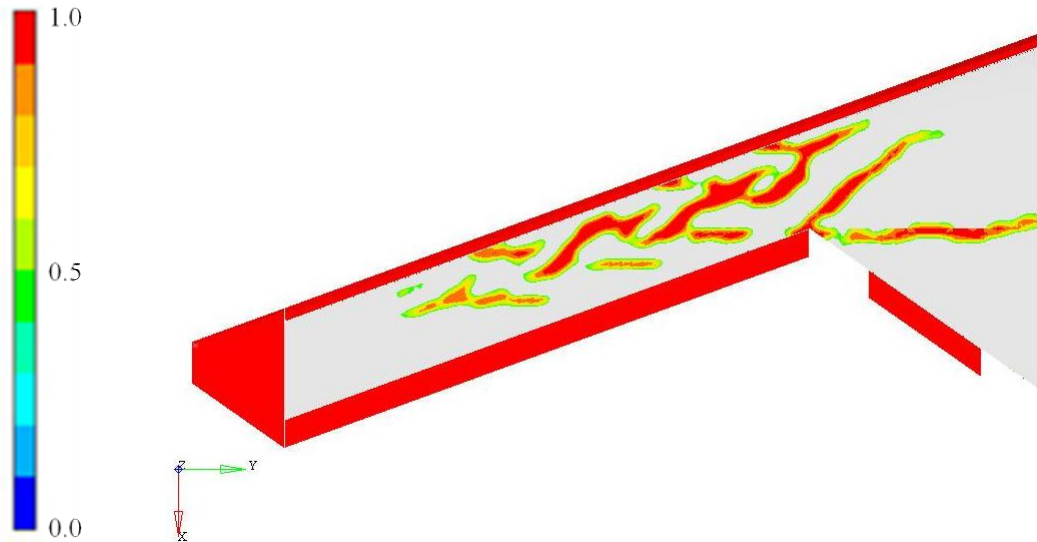
Figure 5.50 Material distribution resulting from a reduced rib thickness of 50mm in the finite element model.

5.3.5 Assessment of Potential Advantages of New Approaches

The final stage of the optimisation procedure is to use sizing optimisation on the baseline UAV architecture, as well as the optimised architectures resulting from both methods described above. This allows the potential benefits of the approaches used to be evaluated. In order to achieve this the material distributions from the topology optimisation stage had to be interpreted as shell structures. This is performed manually, using 2D shell elements to represent structural members with the same connectivity as the material distributions. The finite element model resulting from Method 1 is shown in Figure 5.51, and that from Method 2 in Figure 5.52.
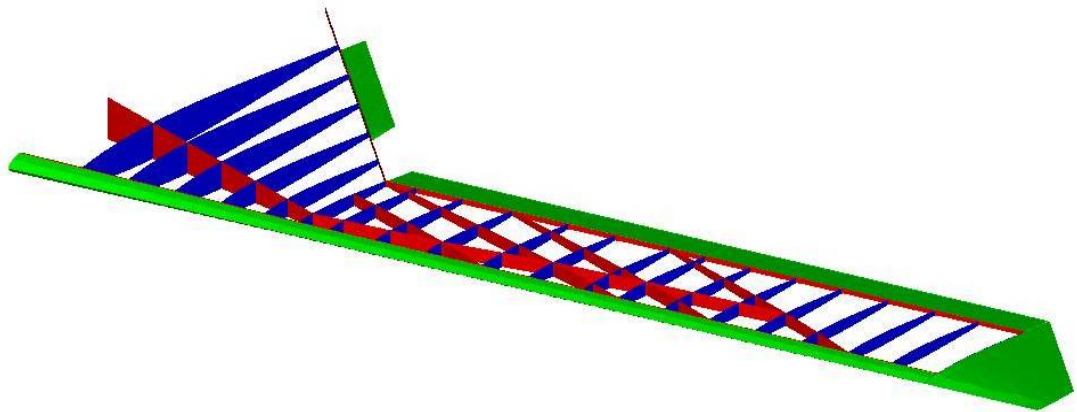
Figure 5.51 Finite element model resulting from Method 1 (Figure 5.42), with optimised rib locations and spars interpreted from Figure 5.48.
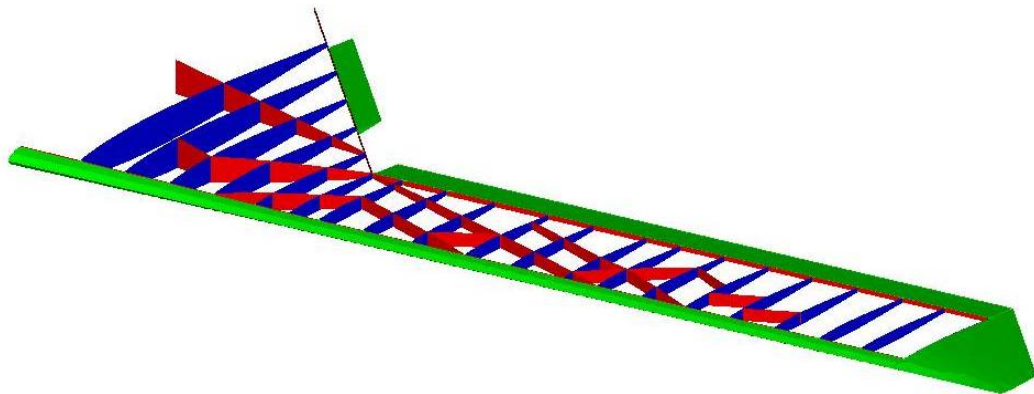
Figure 5.52 Finite element model resulting from Method 2 (Figure 5.42), with optimised rib locations and spars interpreted from Figure 5.49.

The resulting models result in structures which are considerably more manufacturable than the raw material distributions produced after topology optimisation. However some issues still remain regarding the manufacturability of these designs. For example there are a large number of structural members, which would make manufacturing expensive. There are also areas where structural members create small spaces and acute angles that could be difficult to manufacture. These factors cannot currently be considered using topology optimisation, therefore the responsibility of avoiding such issues would belong to the structural and manufacturing engineers interpreting the designs.

Next, the thicknesses of each section of spar and of each rib are defined as design

variables, along with the thicknesses of the wing skin between each rib. The thicknesses of the upper and lower skins for each section are kept equal. Because of the symmetrical nature of the aircraft, this allows the generation of designs capable of withstanding negative loadings without the need for considering an additional load case. The number of design variables in each model are shown in Table 5.3.

Table 5.3 Number of design variables used in sizing optimisation for the finite element models representing three UAV architectures.

Model	Skin Thicknesses	Rib Thicknesses	Spar Thicknesses	Total
Baseline (Fig. 5.35)	20	20	6	46
Method1 (Fig. 5.39)	20	20	18	58
Method2 (Fig. 5.40)	20	20	22	62

The objective of the sizing optimisation is to minimise the structural mass of the UAV. The selection of some constraints is obvious, for example the buckling load factor must be greater than one. However, it is desirable to apply a constraint on global compliance for the symmetrical load case, where the choice of the limiting value in this constraint is not trivial. A parametric study is carried out on the baseline geometry with the optimisation problem formulated in the following way:

$$
\begin{aligned}
&\text{minimise} && \text{mass} \\
&\text{subject to} && \left| \text{twist}_{wingtip\,LC1} \right| \leq 1° \\
& && BLF \geq 1 \\
& && \text{compliance}_{LC2} \leq c_U \\
& && 1mm \leq x_i \leq 100mm \qquad i = 1,2,...,n
\end{aligned}
\qquad , \qquad (5.8)
$$

where c_U is the constraint on compliance which was varied from 60Nm to 100Nm. The problem is also solved using no compliance constraint for comparison. Preliminary studies showed all but the strictest constraints on the wing tip displacement are inactive, as sufficient bending stiffness is achieved as a by product of the other constraints. For this reason no constraint on tip displacement is applied in this study.
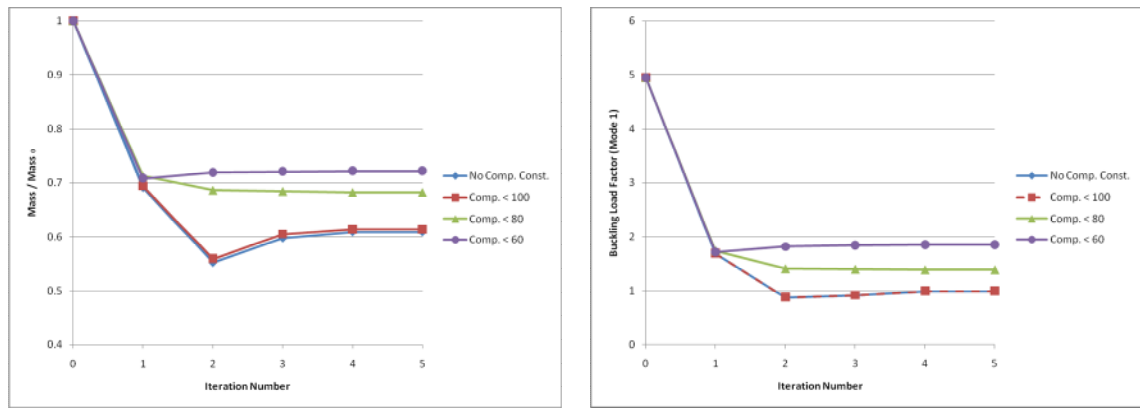
Figure 5.53 Mass normalised by initial design point (left), and buckling load factor (right) throughout the optimisation process, resulting from various compliance constraints.

The effects of the additional compliance constraint on the optimisation process are shown in Figure 5.50. At 100Nm, the compliance constraint remains inactive throughout optimisation. The skin thicknesses required to satify the buckling constraint are greater than those needed to achieve a compliance of under 100Nm, as is demonstrated in Figure 5.53 (right), with the optimiser reaching a buckling factor of 1.0. Stricter compliance constraints, on the other hand, are active during optimisation and have a significant result on the other optimisation responses. Figure 5.53 (left) shows the increased structural mass required to satisfy lower compliance constraints, and Figure 5.53 (right) shows that the lower compliance requirements result in the optimised buckling load factor increasing above its lower limit. It would be desireable to be able to somehow associate the wing's compliance under this symmetrical loading with a loss in aerodynamic efficiency. This would make the choice of a value for this constraint less arbitrary. However in this work, the sizing optimisation stage of the methodology is used purely to illustrate any benefits of the additional structural members derived from topology optimisation. For this reason a constraint of 60Nm is selected for further studies, as at this value the constraint is active but does not negate buckling requirements.
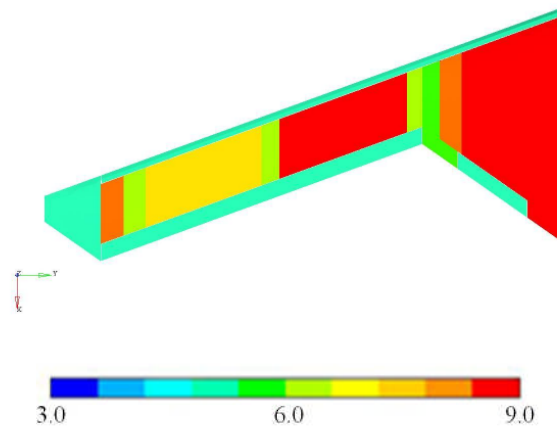
Figure 5.54 Optimised skin thicknesses for the baseline architecture.
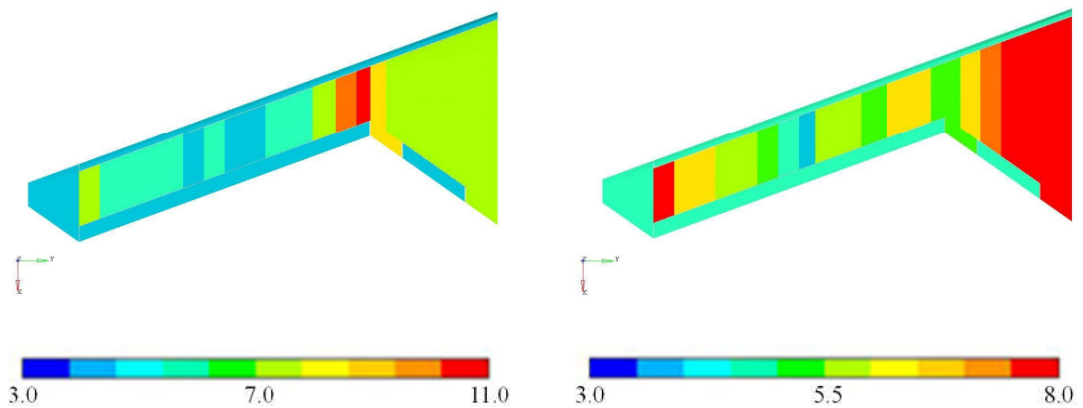
Figure 5.55 Optimised skin thicknesses for architectures resulting from Method 1 (left) and Method 2 (right) of combining shape and topology optimisation.

Sizing optimisation is then applied to all three structural architectures, those shown in Figures 5.43, 5.51 and 5.52. The optimisation problem is formulated as in (5.8), with c_U assigned the 60Nm value selected in the previous study. The design variables used for each optimisation are those set out in Table 5.2. The optimised skin thicknesses are shown in Figures 5.54 to 5.56, with the values of responses at each iteration of the optimisation shown in Figures 5.57 and 5.58. The first thing that is evident (in Figure 5.57 (left)) is that despite their initially higher structural mass, both Method 1 and Method 2 offer reductions in mass compared to the baseline; 6% and 10% respectively. Method 2, where the ribs are defined as non-designable elements at the topology optimisation stage, results in the lowest structural mass. This clearly shows the potential

advantages of considering structural stability at an early stage in the design process. Examining the behaviour of the constrained responses throughout the optimisations gives a better idea of why this is the case. Figure 5.58 (right) shows that the compliance constraint is reached in all cases, indicating that structural mass has to be used to satisfy this requirement. Figure 5.57 (left), on the other hand, shows that the buckling load factor is always comfortably higher than the defined lower limit in the baseline model. For the baseline architecture, the only way in which to reduce compliance due to the symmetrical loads used in load case 2 is to increase skin thicknesses. This appears to be an inefficient way of achieving this. Also, as a by-product, the thick skin sections increase the critical buckling loads beyond their required limit. The other two architectures contain additional structural members which, in some part, are designed to reduce deformation of the symmetrically loaded wing and maintain its aerodynamic shape. The presence of these members allows the skin thickness to be (on average) significantly lower, to the point where their thickness is limited by structural stability requirements.
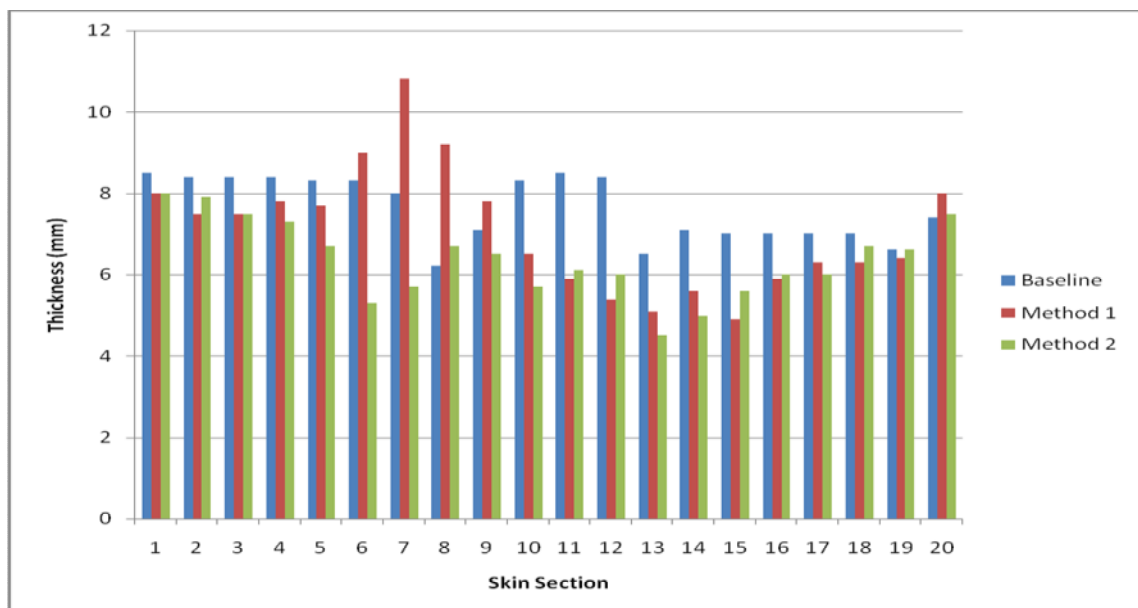
Figure 5.56 A comparison of optimised skin thicknesses for the three UAV structural architectures. Skin sections are numbered from root to tip, with the tapered wing section ending after skin six.

Table 5.4 Optimised skin thicknesses for the three UAV structural architectures. Skin sections are numbered from root to tip, with the tapered wing section ending after skin six.

Skin No.	Baseline	Method 1	Method 2
		Thickness (mm)	
1	8.71	7.96	8
2	8.63	7.45	7.87
3	8.58	7.54	7.54
4	8.48	7.82	7.31
5	8.12	7.68	6.74
6	6.1	9.02	5.28
7	6.59	10.83	5.74
8	8.38	9.21	6.65
9	8.97	7.82	6.53
10	8.94	6.48	5.68
11	8.5	5.89	6.08
12	8.32	5.4	5.97
13	6.75	5.08	4.51
14	7.16	5.63	5.03
15	7.45	4.92	5.63
16	7.14	5.86	5.96
17	7.13	6.25	6.04
18	7.17	6.31	6.69
19	6.86	6.45	6.59
20	7.88	8.06	7.45
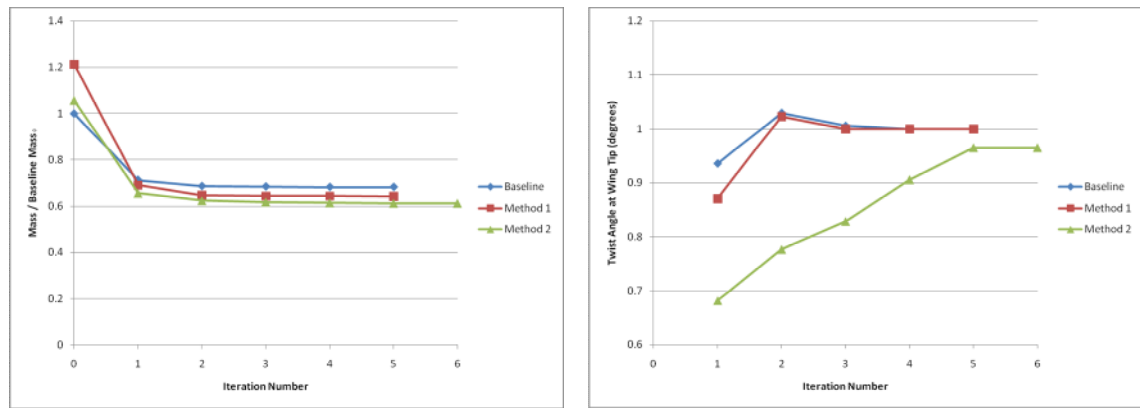
Figure 5.57 Mass normalised by initial design point (left), and twist angle (right) throughout the sizing optimisation process, for three UAV architectures.
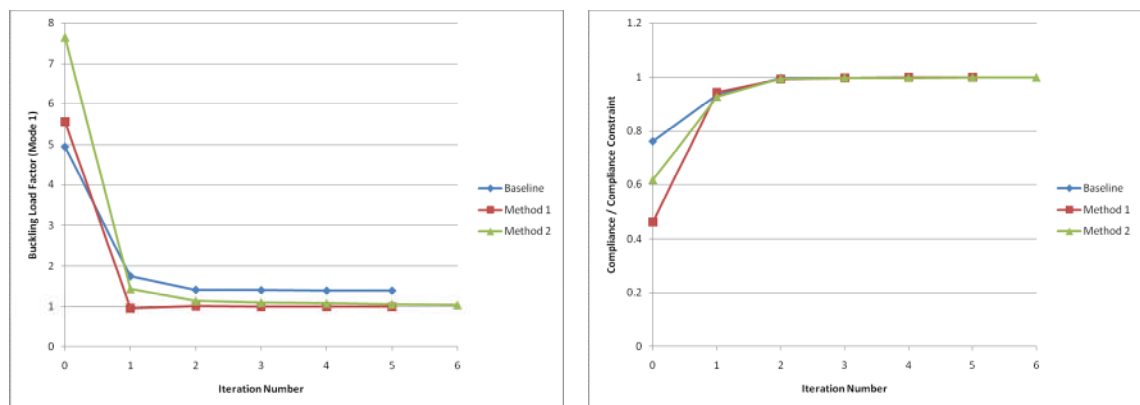
Figure 5.58 Buckling load factor (left), and compliance normalised by its allowable value (right) throughout the sizing optimisation process, for three UAV architectures.

5.4   Conclusion

In this chapter new methods are proposed for incorporating topology optimisation into a framework with shape and sizing optimisation, for designing the structural architectures of aircraft wings. This is investigated using a basic un-tapered, un-swept wing section test case. Firstly parameter studies are performed investigating the effects of mesh density, skin thickness and rib pitch on the structural stability of the wing section. The use of sizing and shape optimisation for optimising rib spacing and skin thicknesses in order to improve buckling behaviour is then studied. Methods for incorporating topology optimisation into this design process is then explored. Finally the approaches developed in this and the previous chapter are applied to the wing of a Blended Wing Body aircraft.

The initial parameter studies demonstrated how increasing skin thickness and the number of ribs within the wing increases critical buckling loads. High numbers of ribs are also shown to produce a more uniform spacing of these critical loads for different buckling modes. The finite element model of the wing section was then parameterised using nodal perturbation vectors, which allowed the location of ribs within the wing to be defined as design variables. Various formulations of the shape and sizing optimisation problem are investigated. Initially only rib locations were optimised with uniform skin thickness. The optimal spacing of ribs is shown to increase towards the wing tip, with the smallest spacings at the root where the first buckling mode occurs. Ribs aligned with the flow are shown to be optimal, with negligible changes in rib orientations when these are included as additional design variables in the optimisation problem. Introducing skin thickness variables to the problem is shown to result in almost uniform rib spacing, with buckling constraints being satisfied by a thicker skin closer to the root.

A conventional approach to considering buckling behaviour in problems involving topology optimisation is described. This involves optimising topologies for minimum compliance. The resultant material distributions are then interpreted as shell structures for shape and size optimisation, where buckling constraints may be included. Here it is suggested that this method is not appropriate for the optimisation of aircrafts' structural architecture, as the structural members used for reducing bending of the wing, i.e. spars,

are distinct from those used to increase buckling loads, i.e. ribs. Therefore a new method is presented for using topology optimisation within a structural optimisation framework for this type of application, where both linear static and buckling behaviours must be considered. This new approach involves optimising the location and orientation of members needed to increase buckling loads, using the shape optimisation of shell structures. These members are then included as non-designable shell elements within the design space used for topology optimisation. The inclusion of these members is shown to significantly influence the results of the topology optimisation. The thicknesses of the non-designable members is also shown to be of importance in some cases. Mesh density restrictions may mean that the size of members resulting from topology optimisation are larger than what would realistically be used in a final design. If this is the case then using a 'realistic' thickness for the non-designable structures could make them irrelevant. For this reason it is proposed to use thicknesses equal to a minimum member size constraint imposed on the optimiser. In the application used here, this is shown to make the rib structures significant in the topology optimisation problem.

This approach, along with the symmetrical loading method for constraining deformation of a wing's aerodynamic shape (5.7), proposed in the previous chapter, are applied to optimising the structural layout of a Blended Wing Body UAV. The use of shape optimisation to optimise rib positions is shown to increase the critical buckling load by 19%. Again, rib spacing is smallest close to the location of the first buckling mode, in this case in the area where the wing transitions from tapered to un-tapered. Topology optimisation is performed using a new formulation that takes into consideration bending, twisting and preservation of the wing's shape. This is applied to models both with and without the non-designable rib structures from the earlier shape optimisation, where the presence of the ribs is again showed to influence the optimal material distributions. How the resultant material distributions may be interpreted as shell structures is illustrated, and sizing optimisation is performed on them. The compliance of the wing under a symmetrical loading remains a part of the optimisation problem at this stage.

The sensitivity of designs to an applied compliance constraint is explored, and it is suggested that it would be advantageous to be able to better relate the compliance to a

loss in aerodynamic efficiency. In fact at this stage of the optimisation, where the number of design variables is significantly lower than in topology optimisation, it would be possible to implement a multidisciplinary approach where the aerodynamic performance of the wing is evaluated using CFD. This approach is often used in the shape and size optimisation of wing layouts (Venter and Sobieszczanski-Sobieski 2004; Paiva, Carvalho et al. 2009), but remains prohibitively computationally expensive for the large number of design variables involved in topology optimisation of 3D structures. For this reason, assuming changes in the shape of the wing will reduce aerodynamic efficiency provides a reasonable estimate at the concept stage of the design process.

Finally, and most importantly, the topology optimisation approaches adopted are compared to a baseline structural architecture and are shown to offer potential weight reductions of up to 10%.

Chapter 6

Conclusions

The primary aim of this thesis has been to investigate the potential use of topology optimisation for determining optimal structural architectures of aircraft. A review of the literature in this field revealed that very few such studies have been published to date. There are several publications on recent academic research with a focus on multidisciplinary topology optimisation with aeroelastic coupling; however, this approach is prohibitively expensive for use in most real-world aerospace applications. Published literature from the aerospace industry focuses predominantly on the topology optimisation of individual structural components, e.g. wing ribs. The small amount of literature on applications involving entire aircraft or entire wing layouts, along with some preliminary studies, indicate several key obstacles that stand in the way of the use of topology optimisations in this field. These obstacles were identified as:

- The usual minimum compliance formulation of the topology optimisation problem is not well suited for optimisation of an entire wing. Spanwise bending of the wing creates large displacements compared to twisting, however compliance is calculated using the global displacement vector. This results in the optimisation algorithm favouring structures which resist bending, with little

consideration for twisting. This is also true for displacements due to local loadings such as control surface loads.

- The consideration of aeroelastic effects in topology optimisation is prohibitively expensive. However if the wing is to remain aerodynamically efficient under flight loads, there needs to be some consideration for the wing's aerodynamic shape. This problem is in many ways related to the first. The small displacements of the wing skin, which result in deformation of its cross-sectional shape, are negligible in the compliance calculations when compared to both bending and twisting.

- Methods for applying buckling constraints in topology optimisation are not yet mature enough for general applications. Additionally, the typical practical design optimisation approach that is: topology optimisation for improved stiffness, followed by sizing and shape optimisation to account for buckling, is not well suited to optimising wing architectures. This is due to wings having distinct structural members for improving bending and torsional stiffness, i.e. spars together with the skin, and improving buckling loads, i.e. ribs.

Therefore, the objectives of this thesis were to propose and apply methods for overcoming these obstacles, and to evaluate the potential of these methods for implementation using commercially available topology optimisation software. All of the proposed methods can be applied without access to source code and are achieved by reformulation of the topology optimisation problem, i.e. definition of designable and non-designable spaces, selection of objectives and constraints and application of load cases.

6.1   Achievement of Objectives

The achievements reported in this thesis, along with a summary of the approaches applied in reaching them are discussed below.

6.1.1   Incorporation of Wing Twisting Control Requirements in the Topology Optimisation Problem

In order to generate structural layouts that resist twist as well as spanwise bending several approaches were investigated.

- Aerodynamic loadings on the wing were replaced with idealised load cases, consisting of point forces and moments applied at the wing tip. This approach allowed the bending and twisting of the wing to be considered separately, hence removing the dominance of one over the other. Topology optimisation using the standard minimum compliance formulation was performed on a simple test case for each loading. The bending load case resulted in a single spanwise spar structure with the majority of the material at the upper and lower wing surfaces to increase the second moment of area. A minimum mass formulation with stress constraints produced similar results. The twisting load case resulted in diagonal members, with a large amount of the material distributed at the upper and lower surfaces and towards the leading and trailing edges to increase the polar moment of inertia.

- The difference in layouts resulting from the two idealised load cases is evident. Therefore it was necessary to combine the considerations for bending and twisting. The use of a weighted compliance formulation enabled this, while maintaining separability of the load cases. Weighting factors were shown to have significant effects on the resulting structures, and an appropriate choice could produce layouts that appear to be well suited for both bending and torsional stiffness.

- The accuracy of the highly idealised load cases representing the real aerodynamic loadings may not be sufficient for all but the earliest of preliminary optimisations. Therefore it was necessary to improve the wing's torsional performance under aerodynamic pressure loads derived from CFD. The addition of a constraint on the twist angle of the wing tip to the topology optimisation problem proved a simple way of achieving this. This approach resulted in a main spar, as was seen for bending considerations only, with an additional spar to improve torsional stiffness.

6.1.2 Determining Optimal Locations and Orientations of Additional Structural Members for Control Surface Loads

In order to find optimal structures to support control surface loads the following approaches were employed:

- Control surface loads were applied using point forces at discrete locations along the wing's leading and trailing edges. Using realistic load magnitudes resulted in no change to the structure due to the dominance of bending in the compliance calculations. Increasing the magnitudes resulted in a small amount of material being used to connect trailing edge loads to the main spar. However, any increase to these local loadings also increased the displacement or twist at the wing tip. Therefore local displacements due to these loads had an insignificant effect on the global compliance.

- Optimal layouts of additional structures were obtained through the use of a pseudo rigid beam running along the quarter chord of the wing, in a similar position to the main spar. This removed all spanwise bending from the wing so that local displacements and twisting due to the control surface loads could be considered independently. The optimal configuration for these members was shown to be a series of diagonal "riblets" linking the control surface connection points. However it was noted that these "riblets" were only optimal for stiffness. There were no considerations for improving buckling loads, which is usually a major role of an aircrafts wing ribs.

6.1.3 Accounting for Deformation of a Wing's Aerodynamic Cross-Sectional Shape in Topology Optimisation

Consideration for the deformation of the wing's cross-sectional shape was one of the most difficult challenges. Load cases could not be idealised into simple point forces or moments as the deformation is caused by pressure loads over the entire wing skin.

- In order to isolate the effects of the pressure loads on the wing's cross-sectional shape from the larger displacements from bending and twisting an additional load case was introduced. The load case consisted of identical pressure distributions on the upper and lower surfaces of the wing. This symmetrical loading was applied to a simple test case and was shown, with the use of manufacturing constraints, to be capable of producing coherent structures that resisted deformation of the cross-sectional shape.

- Symmetrical loading, along with more realistic flight loads, were used to optimise the structural layout of a wing. Applying displacement and twist constraints to the "real" load case, while minimising compliance for the symmetrical load case, was shown to result in a large number of structural members. Some of these appeared well suited to resist spanwise bending while others were likely to improve torsional stiffness. The majority of material was positioned in areas where the aerodynamic loadings were high, and therefore the deformation of the wing's shape was likely to be high.

- An approach to maintaining the wing's shape was investigated that involved a large number of constraints that related the displacement of the wing's upper surface to the displacement of its lower surface. The cross-sectional shape could then be maintained by constraining the differences between the two. This meant applying constraints at every node on the wing skin. The huge number of constraints involved, along with the even larger number of design variables associated with topology optimisation, resulted in failure of the optimiser to converge to a feasible solution. Therefore, with the current topology optimisation techniques and available software, this approach was unsuccessful.

6.1.4 Quantifying the Effect of Structural Topology on Buckling Loads

Although it was not viable to account for buckling behaviour as part of the topology optimisation problem, it was possible to carry out a parameter study into the effect of structural topology, i.e. the number and spacing of ribs, on buckling modes and their critical loads.

- Linear buckling analyses were conducted on wing sections with uniform rib spacings ranging from 0.25m to 2m. Reducing rib spacing was shown to have dramatic effects on both the location of buckling modes and the critical buckling loads. This highlights the need to consider buckling early on in the conceptual design process.

- Shape optimisation was used to find optimal rib positions and orientation for a predefined number of ribs, and therefore fixed topology. Optimal rib spacing was reduced in areas surrounding the first buckling mode if the skin thickness was uniform. Optimal rib orientations were found to remain aligned with the flow. When skin thicknesses were also included as design variables, the optimal rib spacing was shown to be near-uniform.

6.1.5 Combining Topology, Shape and Sizing Optimisation into a Framework for Wing Architecture Design

In order to combine the optimisation of topology for stiffness with the optimisation of rib positions for buckling requirements the following approaches were proposed and investigated:

- The material distributions resulting from topology optimisation were interpreted as 2D shell structures. These structures were then combined with the optimal rib positions resulting from shape optimisation. This approach relies on the assumption that the bending and twisting load-carrying capacity of the ribs is negligible, and therefore have no effect on the optimised material distributions from topology optimisation. Even so, this approach was shown to offer a small

potential reduction in mass.

- Ribs were included as non-designable structures in the finite element models used for topology optimisation. The inclusion of the ribs was shown to have little effect on the optimised material distributions when realistic rib thicknesses were used. This is presumably because unrealistically large structural members are created by topology optimisation due to restrictions imposed by the element sizes. Using thicker ribs was shown to have significant effects on the resultant topologies for problems that included considerations for wing twist angle. The ribs were able to transfer loads from the leading edge to trailing edge spars making diagonal members unnecessary. There was negligible effect on topologies optimised for bending compliance only. A rib thickness equal to the minimum member size constraint was found to be an appropriate choice.

- Rib positions and orientations were optimised to maximise buckling load factors. The ribs, in their optimal positions, were then included as non-designable structures in a finite element mesh. Topology optimisation was performed using the 'real' and 'symmetrical' load cases mentioned earlier. The effect of including the ribs was confirmed. The optimised material distribution was interpreted as a 2D shell structure and was shown to offer up to 10% potential reductions in structural mass. This was an improvement over the alternative approach where ribs were assumed not to carry structural loads.

6.2   Outlook

Despite the advances resulting from the work contained in this thesis, with respect to the applicability of topology optimisation for determining optimal structural architectures of aircraft, several issues remain to be addressed.

- The symmetrical loading used in this work, that removes bending and twisting of the wing from the optimisation problem, is only applicable to wings with symmetrical aerofoil sections. If this was not the case, as is common in the majority of aircraft, alternative approaches would be necessary. This may include an extension of the rigid beam method used in this work. A rigid mid-surface could be applied between the upper and lower surfaces of the wing. All displacements would then represent deformation of the wing's cross-sectional shape.

- Throughout this work an assumption is made that the wing has been designed for a required lift-drag ratio and that minimising the compliance of the wing is analogous to maintaining this aerodynamic performance. Of course the intuitive way to remove this assumption is through topology optimisation with aeroelastic coupling, but as already stated this is not practical for large-scale problems. It is also not possible to directly relate a global metric like compliance to another global metric like aerodynamic efficiency, due to both of these being a function of local displacements. However, it may be possible to form some loose relationship between the two by some statistical means. This would involve a thorough study of the sensitivity of aerodynamic performance to displacement fields.

- Current restrictions on finite element mesh densities mean that the structural members resulting from topology optimisation are unrealistically large. The result of this is that displacements and stresses are unrealistically small. This is not an issue when using a typical minimum compliance formulation with a single constraint on volume fraction. However, when additional displacement and stress constraints are to be included the question of what values to use for these constraints arises. The choice of these values has been investigated in this

work, through a series of parameter studies. It would be beneficial to have a more efficient way of making these choices rather than using trial and error.

- The effect of non-designable ribs on optimal material distributions has been demonstrated. On the other hand, the effect of structural members derived from topology optimisation on the optimal rib positions is still unclear. The next stage of this investigation could be to repeat the shape optimisation, with these additional structural members included. The large number of members, crossing each other at multiple points, may however present a challenge when parameterising the finite element model for shape optimisation. If this was found to affect optimal rib positions then an iterative shape optimisation – topology optimisation approach could be adopted, although this would involve a large increase in computational cost.

- In the work presented, the material distributions resulting from topology optimisation have been interpreted as shell structures manually. Although this approach maintains the general topology of the structure it is not highly accurate. There is scope for the incorporation of an automated approach to relating these distributions to new geometric models, such as that proposed by Sienz, Szarvasy et al. (2000). These models could then be used for the generation of new finite element meshes for a second stage of shape optimisation and sizing.

6.3 Concluding Remarks

At first glance topology optimisation seems the ideal tool for designing the structural architectures of next-generation aircraft. There is little knowledge on what these architectures may look like and using only shape optimisation and sizing would require assumptions to be made based on the paradigms applied to conventional aircraft. The generality of topology optimisation removes the need for such assumptions. Therefore, the first question that needed to be answered in this work was:

'Can topology optimisation software simply be installed on a computer and used to optimise the structural layout of an entire aircraft at the click of a button?'

On closer inspection, the answer to this question is quickly revealed. It is evident that topology optimisation has not yet reached the level of maturity required to achieve this goal and the difficulties associated with using it in this type of application are more numerous than first appears. These issues have been identified and discussed in detail within this thesis and methods for circumventing them have been suggested.

Of course, the ever increasing availability of high performance computing may remove many of these issues. It is likely that at some time in the future multidisciplinary topology optimisation with aeroelastic coupling will be commonplace. It will then not be necessary to make assumptions on the relationship between compliance and aerodynamic metrics such as lift-drag ratio. It is also likely that advances in how buckling constraints are applied to topology optimisation problems will be made. This will allow consideration of stiffness, stress and buckling to made within a single optimisation problem. However, the research presented here has made suggestions that are applicable to industrial problems in the here-and-now, and the findings will hopefully aid the next group of researchers that attempt to tackle this fascinating problem.

Bibliography

ACARE (2001). European Aeronautics: A Vision for 2020. Brussels, Belgium, Advisory Council for Aeronautics Research in Europe.

Allaire, G., Belhachmi, Z. and Jouve, F. (1996). "The homogenization method for topology and shape optimization. single and multiple load cases." European Journal of Finite Elements **15**(5-6): 649-672.

Allaire, G., Jouve, F. and Toader, A.M. (2004). "Structural optimization using sensitivity analysis and a level-set method." Journal of Computational Physics **194**(1): 363-393.

Altair (2009 i). HyperMesh and BatchMesher 10.0, User's Manual, Altair Engineering Inc. Troy, MI.

Altair (2009 ii). Radioss, MotionSolve, and OptiStruct 10.0, User's Manual, Altair Engineering Inc. Troy, MI.

Altair. (2010). "Contour Premium Aircraft Seating Reaps the Benefits of HyperWorks Enterprise Simulation Suite to Reduce Development Costs and Drive Innovation." from http://www.altairhyperworks.com/NewsDetail.aspx?news_id=10438.

ANSYS (2009). Fluent 12.0, User's Manual, ANSYS, Inc. Canonsburg, PA.

Balabanov, V.O. and Haftka, R.T. (1996). "Topology optimization of transport wing internal structure." Journal of Aircraft **33**(1): 232-233.

Barnstorff, K. (2006). "The X-48B Blended Wing Body." 2010, from http://www.nasa.gov/vision/earth/improvingflight/x48b.html.

Bates, S.J., Sienz, J. and Toropov, V.V. (2004). Formulation of the Optimal Latin Hypercube Design of Experiments Using a Permutation Genetic Algorithm. 45th AIAA/ASME/ASCE/AHS/ASC Structures, Structural Dynamics & Materials Conference. Palm Springs, CA, AIAA.

Bendsoe, M.P. (1989). "Optimum shape design as a material distribution problem." Structural Optimization **1**: 193-202.

Bendsoe, M.P. and Kikuchi, N. (1988). "Generating Optimal Topologies in Structural Design Using a Homogenization Method." Computer Methods in Applied Mechanics and Engineering **71**(2): 197-224.

Bendsoe, M.P. and Sigmund, O. (1999). "Material interpolation schemes in topology optimization." Archive of Applied Mechanics **69**(9-10): 635-654.

Bendsoe, M.P. and Sigmund, O. (2004). Topology Optimization: Theory, Methods and Applications. Berlin, Heidelberg, New York, Springer-Verlag.

Boeing. (2010). "787 Dreamliner: Program Fact Sheet." 2010, from http://www.boeing.com/commercial/787family/programfacts.html.

Borrvall, T. and Petersson, J. (2003). "Topology optimization of fluids in Stokes flow." International Journal for Numerical Methods in Fluids **41**(1): 77-107.

Braibant, V. and Fleury, C. (1984). "Shape Optimal-Design Using B-Splines." Computer Methods in Applied Mechanics and Engineering **44**(3): 247-267.

Buchanan, S. (2007). Development of a Wingbox Rib for a Passenger Jet Aircraft using Design Optimization and Constrained to Traditional Design and Manufacture Requirements. 5th Altair CAE Technology Conference. Gaydon, UK.

Bulman, S., Sienz, J. and Hinton, E. (2001). "Comparisons between algorithms for structural topology optimization using a series of benchmark studies." Computers & Structures **79**(12): 1203-1218.

Burnelli, V.J. (1930). Airplane. United States, R B PATENT CORP.

Challis, V.J. (2010). "A discrete level-set topology optimization code written in Matlab." Structural and Multidisciplinary Optimization **41**(3): 453-464.

Cheng, G.D. and Guo, X. (1997). "epsilon-relaxed approach in structural topology optimization." Structural Optimization **13**(4): 258-266.

Deb, K. and Gulati, S. (2001). "Design of truss-structures for minimum weight using genetic algorithms." Finite Elements in Analysis and Design **37**(5): 447-465.

Desktop_Aeronautics (2007). Applied Aerodynamics: A Digital Textbook, Desktop Aeronautics, Inc.

Ding, Y.L. (1986). "Shape Optimization of Structures - a Literature Survey." Computers & Structures **24**(6): 985-1004.

Dorn, W.S., Gomory, R.E. and Greenberg, H.J. (1964). "Automatic design of optimal structures." Journal de Mechanique **3**: 25-52.

Duysinx, P. and Sigmund, O. (1998). New develoments in handling stress constraints in optimal material distributions. 7th Symposium on Multidisciplinary Analysis and Optimisation AIAA/USAF/NASA/ISSMO. Saint Louis, MO.

Eschenauer, H.A., Kobelev, V.V. and Schumacher, A. (1994). "Bubble Method for Topology and Shape Optimization of Structures." Structural Optimization **8**(1): 42-51.

Eves, J., Toropov, V.V., Thompson, H.M., Gaskell, P.H., Doherty, J.J. and Harris, J.C. (2009). Topology optimization of aircraft with non-conventional configurations. 8th World Congress on Structural on Multidisciplinary Optimization. Lisbon, Portugal.

Fan, J., Eves, J., Thompson, H.M., Toropov, V.V., Kapur, N., Copley, D. and Mincher, A. (2011). "Computational fluid dynamic analysis and design optimisation of jet pumps." Computers and Fluids **In Press**.

Fletcher, R. and Reeves, C.M. (1964). "Function Minimization by Conjugate Gradients." Computer Journal **7**(2): 149-&.

Fleury, C. (1989). "CONLIN: an efficient dual optimizer based on convex approximation concepts." Structural Optimization **1**: 81-89.

Flight_International (2006). Airbus A380 Clears European and US Certification Hurdles for Evacuation Trial. Flight International. **March 2006**.

Fuchs, M.B. and Shemesh, N.N.Y. (2004). "Density-based topological design of structures subjected to water pressure using a parametric loading surface." Structural and Multidisciplinary Optimization **28**(1): 11-19.

Galea, E.R., Filippidis, L., Wang, Z., Lawrence, P.J. and Ewer, J. (2010). Evacuation analysis of 1000+ seat Blended Wing Body aircraft configurations: computer simulations and full-scale evacuation experiment. 12th NASA-ESA Workshop on Product Data Exchange. Oslo, Norway.

Gomes, A.A. and Suleman, A. (2008). "Topology optimization of a reinforced wing box for enhanced roll maneuvers." Aiaa Journal **46**(3): 548-556.

Grihon, S. and Krog, L. (2009). Numerical optimisation applied to structure sizing at Airbus: a multi-step process. 8th World Congress on Structural and Multidisciplinary Optimization. Lisbon, Portugal.

Haber, R.B., Jog, C.S. and Bendsoe, M.P. (1996). "A new approach to variable-topology shape design using a constraint on perimeter." Structural Optimization **11**(1): 1-12.

Haftka, R.T. and Grandhi, R.V. (1986). "Structural Shape Optimization - a Survey." Computer Methods in Applied Mechanics and Engineering **57**(1): 91-106.

Haftka, R.T. and Gurdal, Z. (1992). Elements of Structural Optimization, Kluwer Academic Publishers.

Haftka, R.T. and Starnes, J.H. (1976). "Applications of a Quadratic Extended Interior Penalty Function for Structural Optimization." AIAA Journal **14**(6): 718-724.

Hammer, V.B. and Olhoff, N. (2000). "Topology optimization of continuum structures subjected to pressure loading." Structural and Multidisciplinary Optimization **19**(2): 85-92.

Hansen, L.U., Heinze, W. and Horst, P. (2008). "Blended wing body structures in multidisciplinary pre-design." Structural and Multidisciplinary Optimization **36**(1): 93-106.

Harzheim, L. and Graf, G. (2006). "A review of optimization of cast parts using topology optimization - II - Topology optimization with manufacturing constraints." Structural and Multidisciplinary Optimization **31**(5): 388-399.

Hawk, J. (2005). Boeing 787 Dreamliner: More than an Airplane. AIAA/AAAF Aircraft Noise and Emissions Reduction Symposium. Monterey, CA, AIAA.

Hileman, J.I., Spakovszky, Z.S., Drela, M., Sargeant, M.A. and Jones, A. (2010). "Airframe Design for Silent Fuel-Efficient Aircraft." Journal of Aircraft **47**(3): 956-969.

Holland, J.H. (1992). Adaptation in natural and artificial systems: an introductory analysis with applications to biology, control, and artificial systems, MIT Press.

Inoyama, D., Sanders, B.P. and Joo, J.J. (2007). "Topology synthesis of distributed actuation systems for morphing wing structures." Journal of Aircraft **44**(4): 1205-1213.

Inoyama, D., Sanders, B.P. and Joo, J.J. (2008). "Topology Optimization Approach for the Determination of the Multiple-Configuration Morphing Wing Structure." Journal of Aircraft **45**(6): 1853-1862.

Junkers, H. (1914). Flying-Machine. United States, United States Patent Office.

Kang, B.S., Choi, W.S. and Park, G.J. (2001). "Structural optimization under equivalent static loads transformed from dynamic loads based on displacement." Computers & Structures **79**(2): 145-154.

Kang, B.S., Park, G.J. and Arora, J.S. (2006). "A review of optimization of structures subjected to transient loads." Structural and Multidisciplinary Optimization **31**(2): 81-95.

Kang, Z., Wang, X.M. and Wang, R. (2009). "Topology optimization of space vehicle structures considering attitude control effort." Finite Elements in Analysis and Design **45**(6-7): 431-438.

Keane, A.J. and Nair, P.B. (2005). Computational Approaches for Aerospace Design: The Pursuit of Excellence. Chichester, UK, John Wiley & Sons Ltd.

Kennedy, J. and Eberhart, R. (1995). "Particle swarm optimization." 1995 Ieee International Conference on Neural Networks Proceedings, Vols 1-6: 1942-1948.

Kharmanda, G., Olhoff, N., Mohamed, A. and Lemaire, M. (2004). "Reliability-based topology optimization." Structural and Multidisciplinary Optimization **26**(5): 295-307.

Krog, L., Grihon, S. and Marasco, A. (2009). Smart design of structures through topology optimisation. 8th World Congress on Structural and Multidisciplinary Optimization. Lisbon, Portugal.

Krog, L., Tucker, A., Kemp, M. and Boyd, R. (2004). Topology Optimization of Aircraft Wing Box Ribs. 10th AIAA/ISSMO Multidisciplinary Analysis and Optimization Conference. Albany, NY.

Krog, L., Tucker, A. and Rollema, G. (2002). Application of Topology, Sizing and Shape Optimisation to Optimal Design of Aircraft Components. 4th Altair CAE Technology Conference. Gaydon, UK.

Ledermann, C., Ermanni, P. and Kelm, R. (2006). "Dynamic CAD objects for structural optimization in preliminary aircraft design." Aerospace Science and Technology **10**(7): 601-610.

Lencus, A., Querin, O. and Steven, G. (2002). "Aircraft wing design automation with ESO and GESO." International Journal of Vehicle Design **28**(4): 356-369.

Lencus, A., Querin, O., Steven, G. and Xie, Y.M. (1999). Group ESO with Morphing. 1st ASMO/ISSMO Conference on Engineering Design Optimization. Ilkley, UK.

Leonard, B.P. (1979). "Stable and Accurate Convective Modeling Procedure Based on Quadratic Upstream Interpolation." Computer Methods in Applied Mechanics and Engineering **19**(1): 59-98.

Li, P., Seebass, R. and Sobieczky, H. (1998). Manual Aerodynamic Optimization of an Oblique Flying Wing. 36th AIAA Aerospace Sciences Meeting and Exhibit. Reno, NV, AIAA.

Liebeck, R.H. (2004). "Design of the blended wing body subsonic transport." Journal of Aircraft **41**(1): 10-25.

Liebeck, R.H., Page, M.A. and Rawdon, B.K. (1998). Blended-Wing-Body Subsonic Commercial Transport. 36th AIAA Aerospace Sciences Meeting and Exhibit. Reno, NV, AIAA.

Ling, Q.Q. and Steven, G. (2002). "A performance-based optimization method for topology design of continuum structures with mean compliance constraints."

Computational Methods in Applied Mechanics and Engineering **191**: 1471-1489.

Lund, E. (2009). "Buckling topology optimization of laminated multi-material composite shell structures." Composite Structures **91**(2): 158-167.

Luo, Z., Yang, J.Z. and Chen, L.P. (2006). "A new procedure for aerodynamic missile designs using topological optimization approach of continuum structures." Aerospace Science and Technology **10**(5): 364-373.

Maute, K. and Allen, M. (2004). "Conceptual design of aeroelastic structures by topology optimization." Structural and Multidisciplinary Optimization **27**(1-2): 27-42.

Maute, K. and Reich, G.W. (2004). An Aeroelastic Topology Optimization Approach for Adaptive Wing Design. 45th AIAA/ASME/ASCE/AHS/ASC Structures, Structural Dynamics and Materials Conference. Palm Springs, CA, AIAA.

Maute, K. and Reich, G.W. (2006). "Integrated multidisciplinary topology optimization approach to adaptive wing design." Journal of Aircraft **43**(1): 253-263.

Metropolis, N., Rosenbluth, A.W., Rosenbluth, M.N., Teller, A.H. and Teller, E. (1953). "Equation of State Calculations by Fast Computing Machines." Journal of Chemical Physics **21**(6): 1087-1092.

Mialon, B., Fol, T. and Bonnaud, C. (2002). Aerodynamic Optimization of Subsonic Flying Wing Configurations. 20th AIAA Applied Aerodynamics Conference. Saint Louis, MO, AIAA.

Min, S., Kikuchi, N., Park, Y.C., Kim, S. and Chang, S. (1999). "Optimal topology design of structures under dynamic loads." Structural Optimization **17**(2-3): 208-218.

Mukhopadhyay, V., Sobieszczanski-Sobieski, J., Kosaka, I., Quinn, G. and Vanderplaats, G.N. (2004). "Analysis, design, and optimization of noncylindrical fuselage for blended-wing-body vehicle." Journal of Aircraft **41**(4): 925-930.

Neves, M.M., Rodrigues, H. and Guedes, J.M. (1995). "Generalized Topology Design of Structures with a Buckling Load Criterion." Structural Optimization **10**(2): 71-78.

Niu, M.C.Y. (1992). Composite Airframe Structures: Practical Design Information and Data. Hong Kong, Conmilit Press Ltd.

Niu, M.C.Y. (1997). Airframe Stress Analysis and Sizing. Hong Kong, Conmilit Press Ltd.

Olhoff, N. and Enschenauer, H.A. (2001). "Topology optimisation of continuum structures: A review." Applied Mechanics Reviews **54**(4): 331-391.

Onwubiko, C. (2000). Introduction to Engineering Design Optimization. Upper Saddle River, NJ, Pretice-Hall, Inc.

Osher, S. and Sethian, J.A. (1988). "Fronts Propagating with Curvature-Dependent Speed - Algorithms Based on Hamilton-Jacobi Formulations." Journal of Computational Physics **79**(1): 12-49.

Paiva, R.M., Carvalho, A., Crawford, C. and Suleman, A. (2009). A Comparison of Surrogate Models Using an MDO Tool for Wing Design. 8th World Congress on Structural and Multidisciplinary Optimization. Lisbon, Portugal.

Park, G.J.G.-d., KR) (2010). TOPOLOGY OPTIMIZATION METHOD USING EQUIVALENT STATIC LOADS. United States, IUCF-HYU (Industry-University Cooperation Foundation Hanyang University) (Seoul, KR).

Patankar, S.V. and Spalding, D.B. (1972). "Calculation Procedure for Heat, Mass and Momentum-Transfer in 3-Dimensional Parabolic Flows." International Journal of Heat and Mass Transfer **15**(10): 1787-&.

Petersson, J. and Sigmund, O. (1998). "Slope constrained topology optimization." International Journal for Numerical Methods in Engineering **41**(8): 1417-1434.

Petiau, C. (1991). "Structural Optimization of Aircraft." Thin-Walled Structures **11**(1-2): 43-64.

Pickett, R.M., Rubinste, M. and Nelson, R.B. (1973). "Automated Structural Synthesis Using a Reduced Number of Design Coordinates." Aiaa Journal **11**(4): 489-494.

Pingen, G., Evgrafov, A. and Maute, K. (2007). "Topology optimization of flow domains using the lattice Boltzmann method." Structural and Multidisciplinary

Optimization **34**(6): 507-524.

Pingen, G., Waidmann, M., Evgrafov, A. and Maute, K. (2010). "A parametric level-set approach for topology optimization of flow domains." Structural and Multidisciplinary Optimization **41**(1): 117-131.

PLATO-N. (2010). "A PLAtform for Topology Optimisation incorporating Novel, Large-Scale, Free-Material Optimisation and Mixed Integer Programming Methods." 2010, from www.plato-m.org.

Potsdam, M.A., Page, M.A. and Liebeck, R.H. (1997). "Blended Wing Body Design and Analysis." AIAA Paper(AIAA-97-2317).

Qin, N., Vavalle, A. and Le Moigne, A. (2005). "Spanwise lift distribution for blended wing body aircraft." Journal of Aircraft **42**(2): 356-365.

Qin, N., Vavalle, A., Le Moigne, A., Laban, M., Hackett, K. and Weinerfelt, P. (2004). "Aerodynamic considerations of blended wing body aircraft." Progress in Aerospace Sciences **40**(6): 321-343.

Querin, O.M., Steven, G.P. and Xie, Y.M. (1998). "Evolutionary structural optimisation (ESO) using a bidirectional algorithm." Engineering Computations **15**(8): 1031-+.

Rao, J.S., Kiran, S., Kamesh, J.V., Padmanabhan, M.A. and Chandra, S. (2008). Topology Optimization of Aircraft Wing. Proceedings of the Altair India/S.Asia HyperWorks Technology Conference. Bangalore, India.

Rao, S.S. (2009). Engineering Optimization: Theory and Practice. Hoboken, NJ, John Wiley & Sons, Inc.

Rodriguez, D.L. (2009). "Multidisciplinary Optimization Method for Designing Boundary-Layer-Ingesting Inlets." Journal of Aircraft **46**(3): 883-894.

Roskam, J. (2003). Airplane Design: Part V Component Weight Estimation. Lawrence, USA, DARcorporation.

Rossow, M.P. and Taylor, J.E. (1973). "Finite-Element Method for Optimal Design of Variable Thickness Sheets." Aiaa Journal **11**(11): 1566-1569.

Rozvany, G.I.N. (1996). "Difficulties in truss topology optimization with stress, local buckling and system stability constraints." Structural Optimization **11**(3-4): 213-217.

Rozvany, G.I.N. (2000). "Problem classes, solution strategies and unified terminology of FE-based topology optimization." Topology Optimization of Structures and Composite Continua **7**: 19-35.

Rozvany, G.I.N. (2001). "Aims, scope, methods, history and unified terminology of computer-aided topology optimization in structural mechanics." Structural and Multidisciplinary Optimization **21**(2): 90-108.

Rozvany, G.I.N. (2009). "A critical review of established methods of structural topology optimization." Structural and Multidisciplinary Optimization **37**(3): 217-237.

Rozvany, G.I.N. and Birker, T. (1994). "On Singular Topologies in Exact Layout Optimization." Structural Optimization **8**(4): 228-235.

Rozvany, G.I.N. and Querin, O.M. (2002). "Combining ESO with rigorous optimality criteria." International Journal of Vehicle Design **28**(4): 294-299.

Rozvany, G.I.N. and Zhou, M. (1991). "The Coc Algorithm .1. Cross-Section Optimization or Sizing." Computer Methods in Applied Mechanics and Engineering **89**(1-3): 281-308.

Rozvany, G.I.N. and Zhou, M. (1992). COC methods for additional geometrical constraints. Shape and Layout Optimization of Structural Systems and Optimality Criteria Methods. G. I. N. Rozvany. Wien - New York, Springer Verlag.

Rozvany, G.I.N., Zhou, M. and Birker, T. (1992). "Generalized Shape Optimization without Homogenization." Structural Optimization **4**(3-4): 250-252.

Saleem, W., Hu, L., Fan, Y.Q. and Yong, Y. (2009). "Realization of Nonparametric Structural Optimization in Design of Aircraft Components." Proceedings of the 2nd International Conference on Advanced Computer Theory and Engineering (Icacte 2009), Vols 1 and 2: 185-192.

Saleem, W., Yuqing, F. and Yunqiao, W. (2008). "Application of topology optimization

and manufacturing simulations - A new trend in design of Aircraft components." Imecs 2008: International Multiconference of Engineers and Computer Scientists, Vols I and Ii: 1791-1796.

Samareh, J.A. (2001). "Survey of shape parameterization techniques for high-fidelity multidisciplinary shape optimization." Aiaa Journal **39**(5): 877-884.

Schmit, L.A. and Farshi, B. (1974). "Some Approximation Concepts for Structural Synthesis." Aiaa Journal **12**(5): 692-699.

Schramm, U. (2009). Optimization processes for aerospace structures. 8th World Congress on Structural and Multidisciplinary Optimization. Lisbon, Portugal.

Schramm, U., Zhou, M., Tang, P.S. and Harte, C.G. (2004). Topology Layout of Structural Designs and Buckling. 10th AIAA/ISSMO Multidisciplinary Analysis and Optimization Conference. Albany, NY, AIAA.

Sensmeier, M.D. and Samareh, J.A. (2004). A Study of Vehicle Structural Layouts in Post-WWII Aircraft. 45th AIAA/ASME/ASCE/AHS/ASC Structures, Structural Dynamics, & Materials Conference. Palm Springs, CA, AIAA.

Sethian, J.A. and Wiegmann, A. (2000). "Structural boundary design via level set and immersed interface methods." Journal of Computational Physics **163**(2): 489-528.

Sherif, K., Witteveen, W., Puchner, K. and Irschik, H. (2010). "Efficient Topology Optimization of Large Dynamic Finite Element Systems Using Fatigue." Aiaa Journal **48**(7): 1339-1347.

Sienz, J., Szarvasy, I., Hinton, E. and Andrade, M.L. (2000). "Computational modelling of 3D objects by using fitting techniques and subsequent mesh generation." Computers & Structures **78**(1-3): 397-413.

Sigmund, O. (2000). "Topology optimization: a tool for the tailoring of structures and materials." Philosophical Transactions of the Royal Society a-Mathematical Physical and Engineering Sciences **358**(1765): 211-227.

Sigmund, O. (2001). "A 99 line topology optimization code written in Matlab." Structural and Multidisciplinary Optimization **21**(2): 120-127.

Sigmund, O. and Clausen, P.M. (2007). "Topology optimization using a mixed formulation: An alternative way to solve pressure load problems." Computer Methods in Applied Mechanics and Engineering **196**(13-16): 1874-1889.

Silva, M., Tortorelli, D.A., Norato, J.A., Ha, C. and Bae, H.R. (2010). "Component and system reliability-based topology optimization using a single-loop method." Structural and Multidisciplinary Optimization **41**(1): 87-106.

Spalart, P.R. and Allmaras, S.R. (1994). "A One-Equation Turbulence Model for Aerodynamic Flows." Recherche Aerospatiale(1): 5-21.

Stadler, W. (1986). "Nonexistence of Solutions in Optimal Structural Design." Optimal Control Applications & Methods **7**(3): 243-258.

Stanford, B. and Beran, P. (2010). Optimal Structural Topology of a Plate-Like Wing for Subsonic Aeroelastic Stability. 51st AIAA/ASME/ASCE/AHS/ASC Structures, Structural Dynamics and Materials Conference. Orlando, FL, AIAA.

Stanford, B. and Ifju, P. (2009). "Aeroelastic topology optimization of membrane structures for micro air vehicles." Structural and Multidisciplinary Optimization **38**(3): 301-316.

Steven, G., Querin, O. and Xie, M. (2000). "Evolutionary structural optimisation (ESO) for combined topology and size optimisation of discrete structures." Computer Methods in Applied Mechanics and Engineering **188**(4): 743-754.

Stolpe, M. and Svanberg, K. (2001). "On the trajectories of penalization methods for topology optimization." Structural and Multidisciplinary Optimization **21**(2): 128-139.

Sun, C.T. (2006). Mechanics of Aircraft Structures. Hoboken, NJ, John Wiley & Sons.

Svanberg, K. and Stolpe, M. (2000). "Some intrinsic difficulties with relaxation- and penalization methods in topology optimization." Topology Optimization of Structures and Composite Continua **7**: 161-175.

Szabo, B.A. and Babuska, I. (1991). Finite Element Analysis, John Wiley & Sons, Inc.

Vanderplaats, G.N. (1973). CONMIN - A Fortran Program for Constrained Function

Minimization User's Manual, NASA. **TM X-62,282**.

Venter, G. and Sobieszczanski-Sobieski, J. (2004). "Multidisciplinary optimization of a transport aircraft wing using particle swarm optimization." <u>Structural and Multidisciplinary Optimization</u> **26**(1-2): 121-131.

Wakayama, S. and Kroo, I. (1995). "Subsonic Wing Planform Design Using Multidisciplinary Optimization." <u>Journal of Aircraft</u> **32**(4): 746-753.

Wang, G.G. and Shan, S. (2007). "Review of metamodeling techniques in support of engineering design optimization." <u>Journal of Mechanical Design</u> **129**(4): 370-380.

Xie, Y.M. and Steven, G.P. (1993). "A Simple Evolutionary Procedure for Structural Optimization." <u>Computers & Structures</u> **49**(5): 885-896.

Zhou, M. (1989). "Geometrical optimization of trusses by a two-level approximation concept." <u>Structural Optimization</u> **1**: 235-240.

Zhou, M. (1996). "Difficulties in truss topology optimization with stress and local buckling constraints." <u>Structural Optimization</u> **11**(2): 134-136.

Zhou, M. (2004). "Topology optimization for shell structures with linear buckling responses." <u>Computational Mechanics, Proceedings</u>: 795-800.

Zhou, M., Fleury, R., Shyy, Y.K., Thomas, H. and Brennan, J.M. (2002). Progress in Topology Optimization with Manufacturing Constraints. <u>9th AIAA Symposium on Multidisciplinary Analysis and Optimization</u>. Atlanta, GA.

Zhou, M., Pagaldipti, N., Thomas, H.L. and Shyy, Y.K. (2004). "An integrated approach to topology, sizing, and shape optimization." <u>Structural and Multidisciplinary Optimization</u> **26**(5): 308-317.

Zhou, M. and Rozvany, G.I.N. (1991). "The Coc Algorithm .2. Topological, Geometrical and Generalized Shape Optimization." <u>Computer Methods in Applied Mechanics and Engineering</u> **89**(1-3): 309-336.

Zhou, M. and Rozvany, G.I.N. (1992). "Dcoc - an Optimality Criteria Method for Large Systems .1. Theory." <u>Structural Optimization</u> **5**(1-2): 12-25.

Zhou, M. and Rozvany, G.I.N. (1993). "Dcoc - an Optimality Criteria Method for Large Systems .2. Algorithm." Structural Optimization **6**(4): 250-262.

Zhou, M. and Rozvany, G.I.N. (2001). "On the validity of ESO type methods in topology optimization." Structural and Multidisciplinary Optimization **21**(1): 80-83.

Zhou, M., Shyy, Y.K. and Thomas, H.L. (2001). "Checkerboard and minimum member size control in topology optimization." Structural and Multidisciplinary Optimization **21**(2): 152-158.

Appendix

Topology Optimization of Aircraft with Non-Conventional Configurations

J. Eves, V.V. Toropov, H.M. Thompson, P.H. Gaskell, J.J. Doherty, J.C. Harris

Topology Optimization of Aircraft with Non-Conventional Configurations

J. Eves[1], V.V. Toropov[2], H.M. Thompson[1], P.H.Gaskell[1], J.J.Doherty[3], J.C. Harris[3]

[1]School of Mechanical Engineering, [2]School of Civil Engineering, University of Leeds, Leeds, UK, men3je@leeds.ac.uk
[3]QinetiQ Ltd., Farnborough, UK, jcharris@qinetiq.com

1. Abstract

The optimal structural layouts of new aircraft configurations such as the flying wing and blended wing body (BWB) are not yet understood. These new configurations may require quite different design methods from those used conventionally and one promising alternative that is attracting increasing levels of interest is topology optimization, an approach which is significantly different from conventional approaches and valuable in applications where there is little or no collective knowledge on what an optimal structure may be. This paper proposes a new approach for using topology optimization for developing conceptual designs of an aircraft's structural layout. Its aim is to overcome some of the problems associated with the inclusion of local displacement and buckling constraints. The approach is applied to the design of a BWB UAV's wing and is shown to offer significant advantages over a baseline design.

2. Keywords: Topology Optimization, Aircraft Wing, Blended Wing Body

3. Introduction

Almost all aircraft since WWII have used the conventional 'tube with wings' configuration. However because of financial and environmental factors new aircraft configurations such as the blended wing body (BWB) are becoming increasingly attractive. These low drag aircraft offer potential reductions in running costs and CO_2 emissions due to increased fuel economy. The drawback of using these configurations is that their structures are not well understood and there are still many possibilities to explore in order to find an optimal structural layout. The layout of wings with conventional configurations has been extensively investigated and is well understood. There is very little variation in the layouts of high aspect ratio wings found on the commercial transport jets from major airframe manufacturers since WWII [1]. These wings usually consist of two primary spars positioned at approximately 25% and 75% of the chord width. In some cases a third spar is found between these two in the wing section closest to the fuselage. Ribs usually have a uniform spacing of approximately 2 feet [1].

The use of optimization in exploring the structural layouts of these new configurations has predominantly concentrated on the established approaches of parameterizing the aircraft's geometry and performing size and shape optimizations [2]. These approaches require a good first design point, however what this initial design should be is not yet known. An alternative to these conventional optimization approaches is topology optimization, a valuable tool when there is little or no collective knowledge on what the optimal structure may be. Topology optimization is used to determine the optimal distribution of material within a design space. It is widely used in the aerospace industry. However, at the present time its use has mostly been confined to the design of individual aircraft components such as wing ribs [3,4]. Its use in determining optimal structural configurations of wings has been minimal. It has been used with some success to determine the optimum position of primary spars [5] and also the optimum position of spars & ribs so that the wing's aerodynamic shape is maintained [6]. However both of these cases were confined to a conventional wing. It is also still unclear how these approaches should best be incorporated into a complete optimization methodology that considers all the requirements of the wing's design. Topology optimization has also been used to determine the optimal distribution of laminate reinforcement in the wings of non-conventional aircraft [7].

Another use of topology optimization that is currently being explored is in the design of mechanisms for morphing wing structures. Its use here is predominantly confined to the selection of structural members and mechanisms to be used in a predefined layout [8]. This approach does not have the same freedom to distribute material as the density method described below, so is therefore a less desirable option for simply optimizing a wing's structural configuration.

This paper discusses a proposed methodology for incorporating topology optimization into the process of designing the structural layout of a BWB aircraft's wing. Its aim is to overcome some of the limitations of the approach such as the inclusion of buckling constraints and the consideration of local displacements as discussed below. The design process should generate solutions that consider both global and local deformation of the wing and buckling load factors.

4. Topology Optimization

The density method of topology optimization used in this paper can be described using the following formulation:

$$Minimize \quad f(\mathbf{\rho})$$
$$Subject\ to \quad g_i(\mathbf{\rho}) \le g_i^{constraint} \tag{1}$$
$$0 \le \rho_j \le 1$$

Where $f(\mathbf{\rho})$ is the objective function, $g_j(\mathbf{\rho})$ are a series of responses such as static displacements and ρ_j is the relative density of each element in a finite element model. The elemental densities are related to the elastic modulus using the SIMP (solid isotropic material with penalization) approach [9]:

$$E_j = \rho_j^P \tag{2}$$

Where E_j is the relative elastic modulus of each element and P is the penalization factor. Using a value of P greater than 1 penalizes elements with intermediate densities and helps ensure solutions where most elements have densities close to either 0 or 1. A common approach is to define a 'minimize compliance' objective and a constraint on volume fraction of a designable space. Sensitivities are calculated using a finite element solver and material is removed from regions where it is not needed and added to regions where it is.

Topology optimization is usually used at the concept stage of the design process [10] where its main concern is with global compliance or displacements. The results of the topology optimization must then be interpreted to develop a CAD model of the initial design, which can then be used for further analysis and more conventional shape and size optimization, where additional constraints can be considered. Its place in the design process is shown in Figure 1.
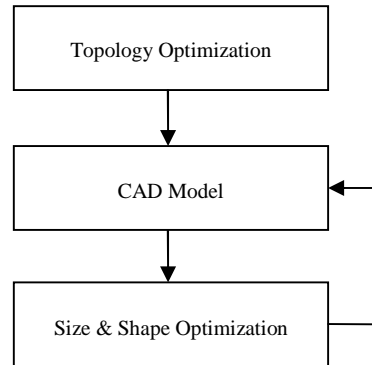
Figure 1: Optimization process

Due to this method of variable densities, topology optimization is not well suited to dealing with the eigenvalue responses required to generate stable designs [11]. Buckling constraints are usually considered later in the design process during size and shape optimization [10]. However, ignoring these responses at the concept stage can result in designs that are incompatible with requirements for structural stability. This highlights the requirement for a methodology that combines the structure needed to improve stiffness with that required to prevent buckling.

5. Methodology & Results

The proposed methodology will be applied to a conceptual UAV design with a BWB configuration provided by QinetiQ Ltd.
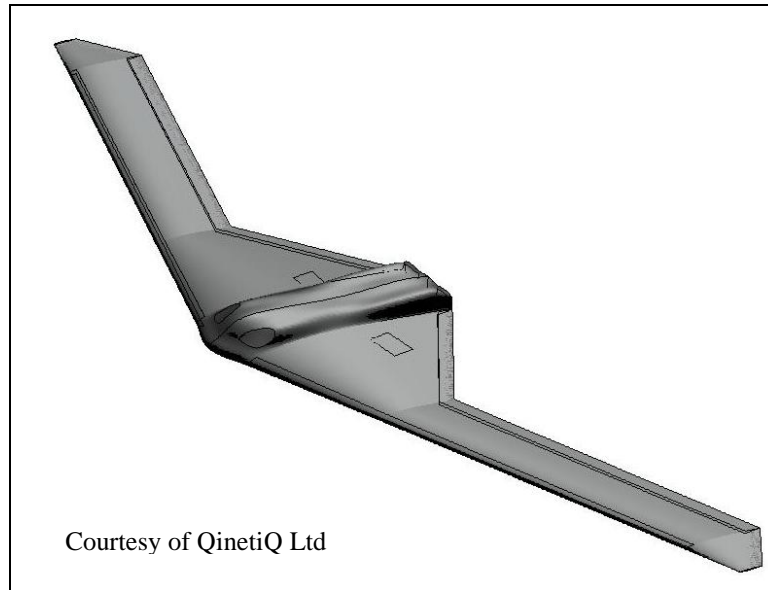
Courtesy of QinetiQ Ltd

Figure 2: QinetiQ Conceptual UAV design

In the current study the UAV's centre section will be removed and optimization will be performed on the wing only. This allows more freedom for the topology optimization as structural members are free to connect to the wing root at any location, they are not restricted by the non-designable spaces within the fuselage such as engine, landing gear or load bay locations. A 3.5g 'pulling out of a dive' load case will be used in the optimization process. This was chosen as it provides considerable bending and twisting of the wing so that robust designs can be developed. Due to the symmetrical nature of the wing a negative load case will not be necessary. Aerodynamic loadings are calculated using the CFD software, Fluent [12].

A finite element model of the UAV's wing is constructed using a designable space made of 3D solid elements covered in a non-designable skin made of 2D shell elements. The skin is necessary to allow pressures to be applied to the model however a thickness of 2mm is used so that its effect in comparison to material in the designable space is negligible. Control surfaces at the leading and trailing edges are made of non-designable shell elements and are attached to the wing's upper and lower surfaces at discrete points using rigid elements. Aluminium is used for all structural components. Pressures from the 3.5g load case described above are applied to the skin and the wing is constrained in all degrees of freedom at the root. Initially, a simple minimum compliance problem formulation is used with a constraint of 0.3 on maximum volume fraction and 0.25° constraint on the wing's twist at the tip. An extrusion manufacturing constraint is included which forces all structure to remain uniform through the thickness of the wing. This is to prevent all material being used to thicken the wing's skin and improve bending stiffness, and instead, be used to indicate the optimum position of structural members. Optimization is carried out using Altair's Optistruct [13] and the results are illustrated in Figure 3.
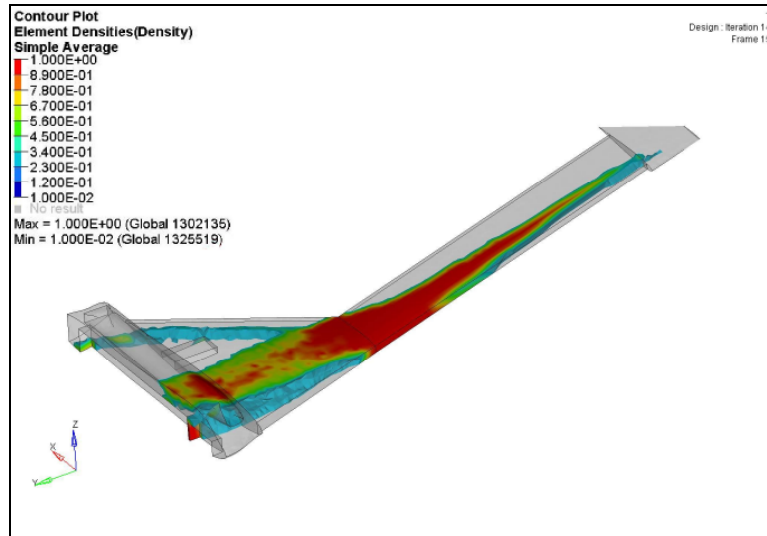
Figure 3: Material distribution after initial topology optimization

The topology optimization process for this minimum compliance formulation is dominated by the global bending and twisting of the wing, making it a useful tool in determining primary spar positions, however it neglects the smaller local deformation of the wing's skin. Due to the importance of the wing maintaining its aerodynamic shape, these local displacements cannot be overlooked. Also, because of the difficulties associated with buckling analysis within topology optimization, methods for including local buckling constraints into the optimization process must be explored.

5.1. Local Deformation of Wing Skins

To allow the wing's design to be driven by both local and global displacements, the following problem formulation is proposed for topology optimization. In addition to the 3.5g load case, a second load case in which pressures on the upper and lower surfaces of the wing are identical is included, therefore there is no bending or twisting of the wing. Constraints of 150mm maximum tip displacement and 0.25° maximum twist are applied to the 3.5g load case with an objective of minimizing compliance for the symmetrical load case. The volume fraction of the designable space is again constrained to 0.3. The aim of this formulation is to ensure just enough material is used to keep the wing's global deformation within some predetermined limits, and allow the rest of it to be used to minimize the local deformation of the wing (Figure 4). The constraints on the wing's global deflection and twist are made artificially strict. This is necessary because, due to limitations on mesh density, unrealistically large, solid aluminium structural members are being distributed in the design space. Note that it is possible to use more realistic values later in the design process.
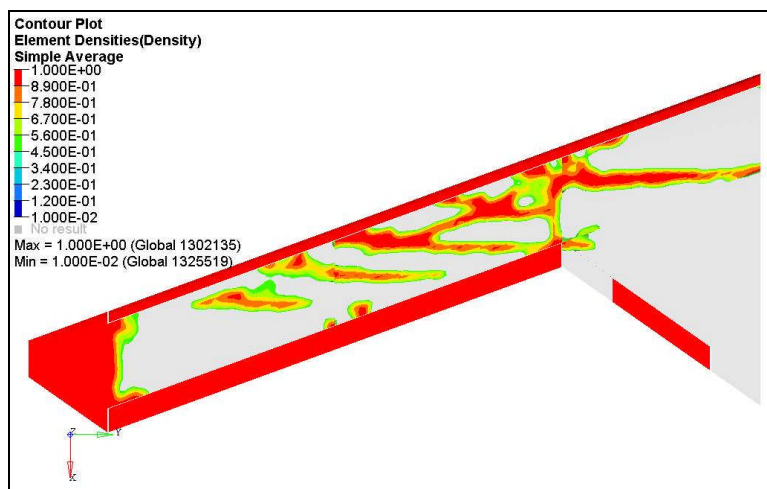

Figure 4: Material distribution after topology optimization

5.2. Wing Skin Buckling

Two methods are proposed to deal with buckling in the topology optimization process. Both methods include the topology optimization step described earlier and a separate shape optimization step using buckling constraints to determine rib positions. Both methods also assume an average rib spacing of approximately 2 feet as indicated in the literature [1].

5.2.1. Approach 1

Firstly the topology optimization described above is carried out and then a shape optimization is performed to determine rib pitch. The shape optimization process starts with an estimate of the average rib pitch. A finite element model of the aircraft with ribs is then created using 2D shell elements. The maximum range of movement for the ribs is set by morphing the finite element mesh using Altair's HyperMorph tool. In this case a range of $\pm 1/3$ of the average rib pitch is used, allowing maximum movement of the ribs without creating very high aspect ratio elements. The junctions of the ribs with the front and rear spars are allowed to move independently so that rib orientation can also be optimized. A shape optimization is then performed to maximize the buckling load factor. The repositioning of ribs (Figure 5) results in the buckling load factor being increased by 18% as well as being more uniformly spread over the section of the wing closest to the root (Figure 6). All ribs remain parallel to the centerline of the aircraft.
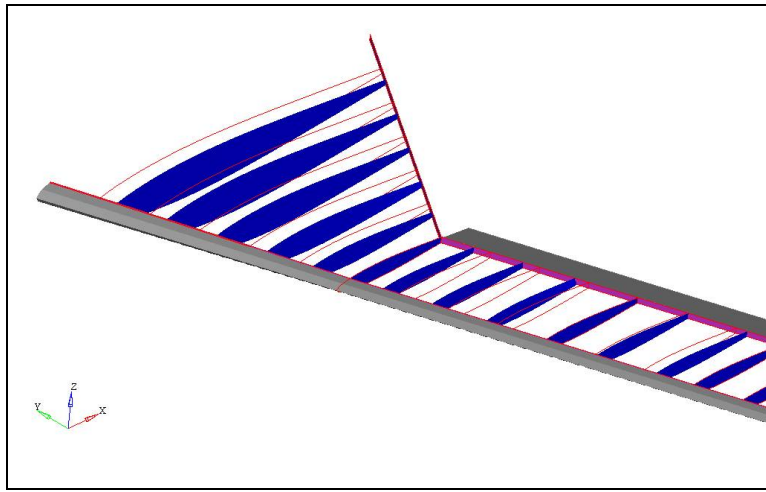

Figure 5: Optimized (blue) and original (red) rib positions
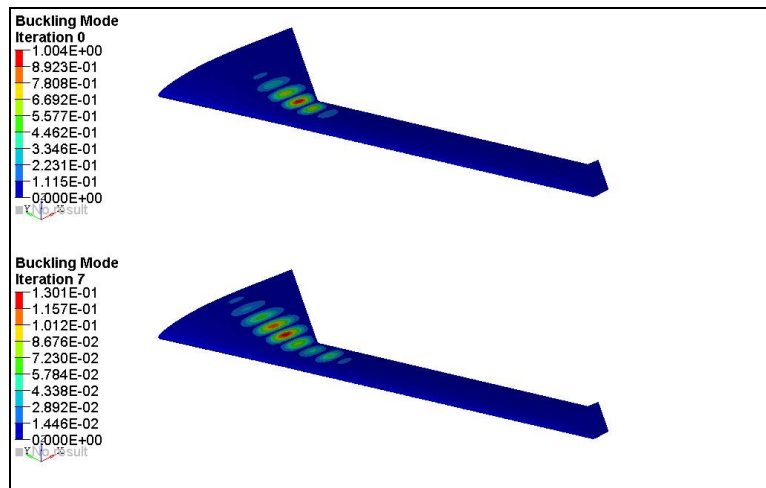

Figure 6: Buckling load factor before (top) and after (bottom) shape optimization

The results from the topology optimization are then interpreted as spars made of 2D shell elements. These are combined with the rib positions from the shape optimization step to provide a final finite element model to be used for further analysis and optimization (Figure 7).
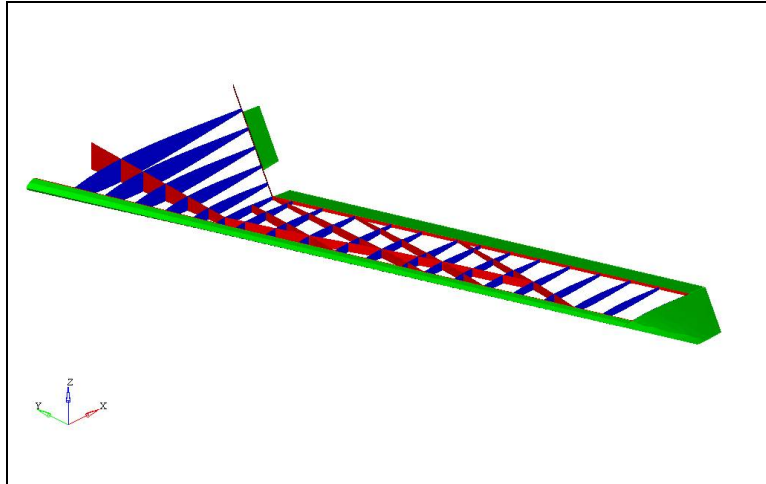
Figure 7: Interpretation of topology and shape optimization (approach 1)

5.2.2. Approach 2

The second method differs from conventional approaches using topology optimization as discussed so far. Rather than topology optimization being the first step in the design procedure, a shape optimization is initially conducted to determine the optimum rib pitch for maximum buckling load factor. The ribs are then included in the finite element model as non-designable 2D shell elements, separating a series of 3D designable spaces. A rib thickness equal to the average element size is used so that the ribs do not become negligible when compared to the material distributed within the designable space. Topology optimization is performed (Figure 8) and the results are interpreted as 2D shell elements and, along with the optimized rib positions, give a final finite element model (Figure 9) to be compared to the one from the first method.
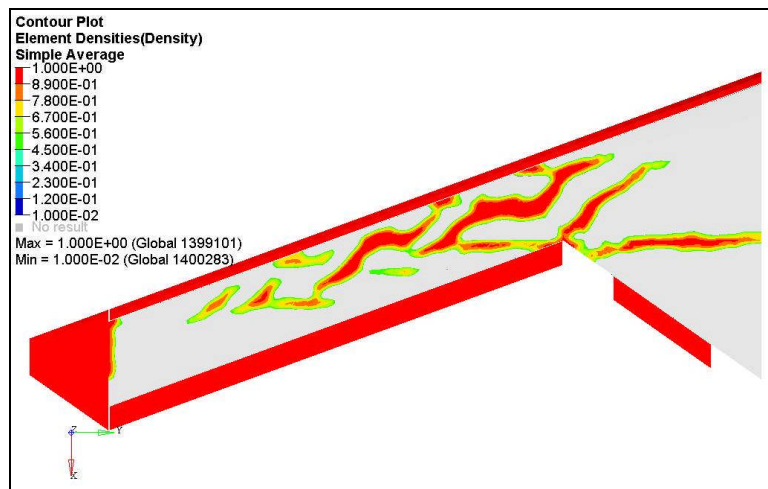

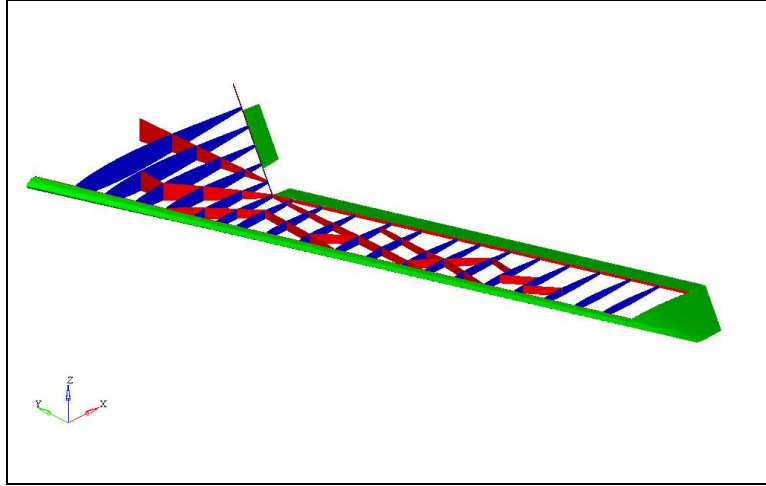Figure 8: Material distribution after topology optimization (approach 2)

Figure 9: Interpretation of topology optimization (approach 2)

5.3 Discussion of Approaches Applied

Approach 1 allows complete freedom at the topology optimization stage, so that material can be distributed in the best way to reduce skin deformation while keeping global displacements at a desired level. However, the solver has no knowledge of the rib positions and therefore may use material that is later made obsolete by the presence of ribs. Also, because the optimum position and orientation of structural members to reduce local deformations differs from that required to prevent buckling, it may prove difficult to satisfy both criteria and provide a minimum mass configuration. Approach 2 is a little more restrictive at the topology optimization stage because of the pre-imposed rib positions. The method's primary concern is with buckling, other design considerations are then incorporated around this. However all the material used in the designable spaces is working with the ribs to reduce local deformations and will not be made obsolete later in the design process.

To compare the two methodologies, a sizing optimization is performed on both finite element models. The skin is separated, by the ribs, into 20 sections. The spars are also split into sections. The thicknesses of each of these along with the thicknesses of each rib are the design variables (table 1) and the following problem formulation is used (table 2).

Table 1: Design variables

Component	Design variables	Start value	Min. value	Max. value
Skin thickness/mm	20	10	2	25
Spar thickness/mm	18	10	5	50
Rib thickness/mm	20	10	5	50

Table 2: Problem formulation

3.5g Load case	Symmetrical load case
Objective = minimize mass	
Twist angle < 1°	
Von Misses stress < 50MPa	
Buckling load factor > 1	
	Compliance < 80

At this point, the constraint on the wing twist angle is relaxed, a stress constraint is introduced and no constraint is applied to the wing tip deflection. To assess the methodologies the same optimization is also performed on a baseline design, without the additional spars derived from topology optimization, having only the front and rear spars where the control surfaces are attached. A uniform spacing of 2 feet is used for the ribs. The constraint on compliance for the symmetrical loading case is determined from initial analysis of both models (Figures 9 & 10). The value used is achievable by both layouts and offers an improvement over the baseline deign.
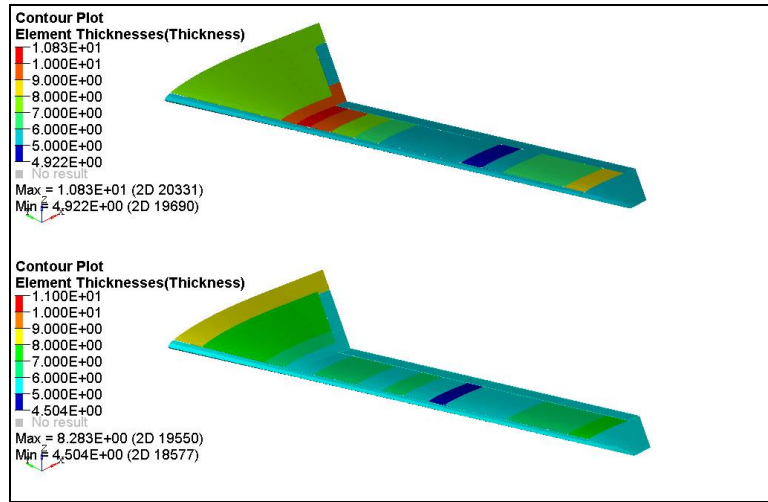
7

Figure 10: Skin thickness after size optimization for approach 1 (top) and approach 2 (bottom)
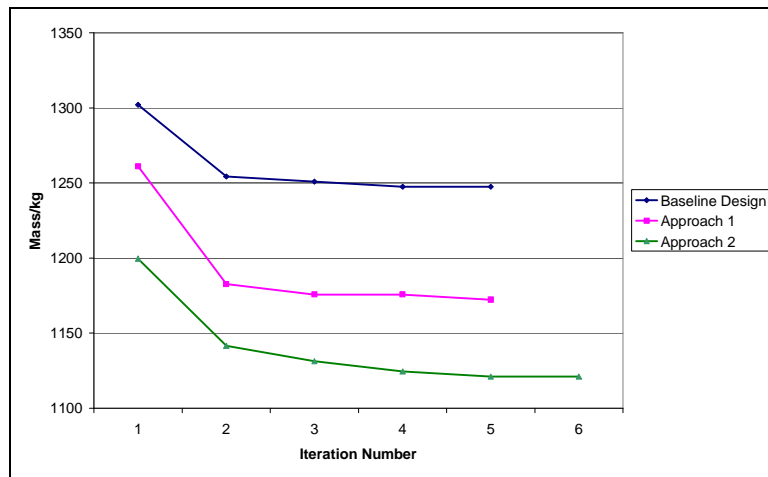

Figure 11: Reduction of mass during size optimization for both methodologies and baseline model

Both topology optimization methods offer a reduction in mass compared to the baseline design, 6% and 10% for methods 1 and 2 respectively. However, as predicted some of the structural members included in method 1 are under-utilized due to the presence of the ribs. Their thicknesses are reduced to the lowest value possible without buckling. It should be noted that for the baseline design buckling is not a driving factor, the buckling load factor remained at 1.2. This is because for this design the only method for improving compliance for the symmetrical load case is to increase skin thickness. The skin thicknesses required to satisfy the compliance constraint are greater than those required to prevent buckling.

6. Conclusions

A new approach for the use of topology optimization in wing design is introduced where structural stability and local displacements are considered at the concept stage. The methodology combines the use of topology, size and shape optimization. This approach is applied to the structural optimization of a BWB aircraft wing in two ways. Both methods show significant improvement in the form of a mass reduction when compared to a baseline design. The addition of buckling responses at the topology optimization stage remains a problem, however the importance of considering buckling at early stage in the design process is shown. The proposed approach requires selection of a compliance constraint at the size optimization stage. The value used is important as it can determine whether the design is driven by constraints on buckling or local deformation of the wing. A study of the effect of a symmetrically loaded wing's compliance on the aerodynamic performance will be conducted so that suitable values can extracted for future work.

7. Acknowledgments

8. References

[1] M.D. Sensmeier and J.A. Samareh, A study of vehicle structural layouts in post-WWII aircraft, *45th AIAA/ASME/ASCE/AHS/ASC Structures, Structural Dynamics & Materials Conference,* Palm Springs, California, 2004.

[2] L.U. Hansen and P. Horst, Multilevel optimization in aircraft structural design evaluation, *Computers & Structures,* 86, 104-118, 2007.

[3] S. Buchanan, Development of a wingbox rib for a passenger jet aircraft using design optimization and constrained to traditional design and manufacture requirements, *Altair CAE Technology Conference,* Gayton, UK, 2007.

[4] L. Krog, A. Tucker, M. Kemp and R. Boyd, Topology optimization of aircraft wing box ribs, *10th AIAA/ISSMO Multidisciplinary Analysis and Optimization Conference,* Albany, New York, 2004.

[5] J.S. Rao, S. Kiran, J.V. Kamesh, M.A. Padmanabhan and S. Chandra, Topology optimization of aircraft wing, *Proceedings of the Altair India/S.Asia HyperWorks Technology Conference,* Bangalore, India, 2008.

[6] K. Maute and M. Allen, Conceptual design of aeroelastic structures by topology optimization, *Structural and Multidisciplinary Optimization,* 27, 27-42, 2004.

[7] B. Stanford and P. Ifju, Aeroelastic topology optimization of membrane structures for micro air vehicles, *Structural and Multidisciplinary Optimization,* 38, 301-316, 2009.

[8] D. Inoyama, B.P. Sanders and J.J. Joo, Topology optimization approach for the determination of the multiple-configuration morphing wing structure, *Journal of Aircraft,* 45 (6), 1853-1862, 2008

[9] M.P. Bendsoe and O. Sigmund, *Topology Optimization: Theory, Methods and Applications*, Springer-Verlag, Berlin, 2003.

[10] U. Schramm, M. Zhou, Poh-Soong Tang and Cathal G. Harte, Topology layout of structural designs and buckling, *10th AIAA/ISSMO Multidisciplinary Analysis and Optimization Conference,* Albany, New York, 2004.

[11] N. Neves, H.C. Rodrigues and J.M. Guedes, Generalized topology design of structures with a buckling load criterion, *Structural Optimization,* 10, 71-78, 1995.

[12] Fluent Version 6.3: Users manual, ANSYS Fluent, 2006

[13] Altair Optistruct Version 9.0: Users manual, Altair Engineering, 2008